Asteroseismology from the Main Sequence to Giant Stars

by

Neil James Tarrant

A thesis submitted to
The University of Birmingham
for the degree of
DOCTOR OF PHILOSOPHY

HiROS Research Group
School of Physics and Astronomy
The University of Birmingham
April 2010

Abstract

The thesis focuses on the use of asteroseismology to probe the structure of stellar sources. By observing pulsational variability, a detailed description of the interior of stars, and the determination of stellar parameters can be obtained.

An extensive sample of bright K and M class giant stars were surveyed to detect the presence of any noticeable variability. Three giant stars have been studied in detail. In Arcturus (α Boo), no oscillations at a significant amplitude were detected. In β UMi (Kochab) multiperiodic oscillations have been observed for the first time, allowing an asteroseismic estimate for the mass. In γ Crucis (Gacrux) previously observed frequencies have been confirmed, and the modes shown to be sinusoidal in nature.

Two main-sequence stars have been studied in detail. In the first, γ Dor, prototype star of the class of γ Doradus variable stars, three oscillations further to those previously known were unambiguously detected in the star. In the second, ν Eri, a β Cephei class variable star, modes detected by an extensive previous campaign were confirmed, with determined frequencies in excellent agreement between the two studies.

All results gathered should provide a valuable input to future models of these stars, and provide an interesting starting point for further, detailed studies.

To my parents.

Without your love and support none of this would have been possible.

Acknowledgements

Without my two supervisors, Professor Yvonne Elsworth and Doctor Bill Chaplin, none of this thesis could have been achieved. I feel that I have been dealt a very lucky hand in having had the privilege of having worked with such devoted and inspirational scientists. Doctors Ian Stevens and Steven Spreckley must also be thanked (or possible blamed!) for opening up the world of SMEI data for me to play with.

I would also like to thank my mother, Carola Tarrant and my colleagues Bill Chaplin and Saskia Hekker for their proof reading skills and other helpful comments. Especially in the light of an individual who insists on spelling words in an archaic manner. Brek Miller, my LaTeX guru, should also receive a great deal of praise for helping with some of the more interesting challenges that writing a thesis presents.

To my many house mates over the years; thank you for putting up with my moods when research has not been as successful as I would like. Special thanks go to Ana-Maria Andritoiu, Howie Carson, Thomas Massey, James Saady, Hannah Scott, and Ben Spanton. I also must comment on the kindness and consideration of Sam George, Kym Goss, and Marianne Beecroft who put me up when I had nowhere else to go.

I would also like to offer my thanks to everyone in the HiROS group, both those who are still here, and those who have moved on to pastures new, not only for the help and support in matter academic, but also for the great times and conversations I have had during my time here: John Allison, Alexandra Andric, Ian Barnes, Guy Davies, Stephen Fletcher, Kym Goss, Steve Hale, Saskia Hekker, Barry Jackson, Lizzie Jarvis, Christoffer Karoff, Brek Miller, and Graham Verner.

Contents

List of Figures

List of Tables

Chapter 1

Introduction

From the time that scientists first realised that the Sun was not merely a celestial manifestation of divine providence, but rather an object subject to the same physical laws as any other, the question of what processes occurred within the body has been fiercely debated:

> *At first sight it would seem that the deep interior of the sun and stars is less accessible to scientific investigation that any other region of the universe. Our telescopes may probe farther and farther into the depths of space; but how can we ever obtain certain knowledge of that which is hidden beneath substantial barriers? What appliance can pierce through the outer layers of a star and test the conditions within?*

The above quotation was made in 1926 by the eminent physicist Sir Arthur Eddington, who laid down many of the foundations for our understanding of stars (Eddington 1926). He later went on to show how even without a direct probe it is possible to make predictions on the likely structure found inside stars by using the equations of stellar structure. However, these predictions were based upon untested assumptions, indeed before the second world war a primary contender for a model of the solar interior consisted of approximately 65% iron by mass, with the remainder primarily hydrogen. This is in contrast to the contemporary determinations, in which the Sun consists of around 74% hydrogen, 24% helium, and less than 0.2% iron.

The phenomenon of pulsating stars offers a means to directly probe the interior of stars, and therefore to test these assumptions, a fact which Eddington himself would note (Eddington 1927):

> *Ordinary stars must be viewed respectfully like objects in glass cases in museums; our fingers are itching to pinch them and test their resilience. Pulsating stars are like those fascinating models in the Science Museum provided with a button which*

> *can be pressed to set the machinery in motion. To be able to see the machinery of a star throbbing with activity is most instructive to the development of our knowledge.*

Studying stellar interiors does not merely present an academic curiosity. The Sun itself is a star, and helioseismology, the study of solar pulsations, has helped to answer questions about the age and future evolution of the Sun. A detailed knowledge of processes occurring at the solar surface through helioseismology may also allow the prediction of violent solar events such as coronal mass ejections. In recent years helioseismology has helped to answer questions on whether temperature rises observed on Earth have an origin in the Sun (Goode 2007), and if the lack of solar activity is simply skin deep (Broomhall et al. 2009c).

1.1 Asteroseismology

As a science it can be argued that asteroseismology can trace its origins to the discovery of the variability of Mira in the early 17th century by the astronomers David Fabricius and Johannes Holwarda. This was the first unequivocal detection of a variable star (in fact a Mira-class variable on the asymptotic Giant Branch), and showed that the stars were not the exotic, unchanging objects which the ancients had imagined them to be.

The development of photographic techniques for determining the relative magnitude of stars in the 1890's caused knowledge of the number and types of variable stars to increase rapidly, however it was not until the 1930's that Arthur Eddington provided the first physical explanations for stellar variability. The first varieties of variable star typically had very large oscillations and would only vary in one or two modes.

However, even these simple oscillators were able to provide scientifically useful information. A relationship between the period of oscillation and luminosity of a class of stars known as cepheid (or δ cephei) variables was discovered by Leavitt and Pickering (1912). This relationship (which may be predicted from Equation 3.25 on page 52 by assuming all cepheids to have the same mass and temperature) allowed exploration of the cosmic distance scale, both within our galaxy and across the Universe, leading eventually to the cosmologically significant Hubble law.

The discovery of periodic oscillations of the Sun's surface by Leighton et al. (1962) and the confirmation of these as manifestations of global modes by Deubner (1975) enabled scientists to see into the interior of the Sun in a similar manner to these oscillating stars. The mean speed of sound within the region a mode penetrates can be found from properties of the mode, and therefore by consideration of a number of modes which traverse different depths of the solar interior one can perform a ‘helioseismological inversion’, giving the radial profile of the sound speed. In combination with models of the composition, this can return a reconstruction of the temperature, pressure and density as a function of radius.

The inferences from helioseismology have not been restricted to the field of stellar physics, but also aided in the discovery of neutrino oscillations. During the mid 1980’s the internal structure found by helioseismic inversions revealed the solar core was too hot for attempts to reconcile implied nuclear reaction rates with the observed neutrino flux. Various exotic explanations were proposed to explain this anomaly, for instance including the addition of weakly interacting massive particles’ (WIMPs) in the solar core. Helioseismology was vindicated as ever more precise data remained consistent with the value returned by standard solar models without WIMPs (Elsworth et al. 1990), and it was not until the earth twenty-first century that an explanation for the observed neutrino flux came from the realm of particle physics, specifically the oscillation of neutrinos between flavours during their transit to Earth.

The last years of the twentieth, and early years of the twenty-first century saw a further rapid expansion in the number of known variable stars, and the known types of variability, including the first detections of solar-like oscillations in stars other than the Sun. This can be put down to the rising precision of observations, the increasing number of automated observation systems, and the first space based observatories. It is now thought that a majority of all stars manifest some form of variability, and therefore asteroseismology provides a key to unlock stellar structure across the entire colour-magnitude diagram.

1.2 Thesis Synopsis

The main focus of this thesis is to explore the use of data from the Solar Mass Ejection Imager (SMEI) instrument aboard the Coriolis satellite to detect and characterise oscillatory power in a number of stars.

Chapter 2 provides a basic introduction to stellar physics as it applies to the objectives of the thesis. It starts by showing how stars are broadly characterised in groups on the Hertzsprung-Russell (HR) diagram, and how the internal structure of stars varies, both between and within these groups. The chapter continues to show how these structures arise as a consequence of the equations of stellar structure, and briefly discusses some important aspects of physics as they apply to stars.

The chapter ends by categorising stellar variability. In the case of pulsational variability which is of interest for asteroseismology, the forces which excite, maintain and damp modes is presented. Finally, details of oscillations for specific types of variable star which are relevant to the remainder of the thesis are discussed in more detail.

Chapter 3 introduces the sciences of helio- and asteroseismology, beginning with the characterisation of stellar oscillations as resonant modes, and how the twin sciences can be used to determine the internal structure of the bodies under study.

The chapter continues in a more practical light on how modes are observed, and which modes may be visible in any single star, considering both stellar and observational (e.g. inclination and instrumentational) effects. Scaling laws for the most important parameters which characterize an oscillation spectrum are presented. The chapter concludes with a brief description of a number of helio- and asteroseismic observatories.

Chapter 4 discusses the Solar Mass Ejection Imager instrument. This instrument was designed to detect coronal mass-ejections in transit to Earth, and the adaptation of the data for the purposes of asteroseismology has presented some unique challenges for the development of the analysis pipeline. The quality of the SMEI data is presented, and the origins of certain peculiarities are discussed. A brief description of studies of stars with SMEI undertaken by others is then presented.

Chapter 5 presents the analysis techniques which have been used for the studies undertaken in this thesis. There are a number of different means of extracting a periodogram from timeseries data, and these are compared and contrasted in the light of data which has not been gathered at regular intervals.

The chapter concludes by describing statistical tests which may be undertaken on a power spectrum to determine the significance of any features, and the impact which oversampling the power spectrum will have on this analysis. The theoretical justification for, and relevance of the canonical 4.0 signal-to-noise test is discussed.

Chapter 6 shows the results which have been gathered with SMEI on giant stars. Three stars in particular are studied, Arcturus, β UMi and γ Crucis. In the first of these no notable variability over periods less than 5 days is detected, while the second and third have had modes detected.

Chapter 7 reveals SMEI results on main-sequence stars. Two stars in particular have been subject to analysis, γ Doradus and ν Eri. Studies of the two stars have confirmed the presences of modes previously noted by others, and added additional modes in the case of γ Dor.

Chapter 8 provides a brief overview of the thesis as a whole and discusses what conclusions may be drawn.

Chapter 2

Stellar Physics

2.1 Stellar structure and evolution

The common definition of a star is a ball of plasma, held in hydrostatic equilibrium by the interaction between gravity and pressure forces, radiating energy generated by thermonuclear fusion. This definition of a star covers a very broad range of bodies, from the cool brown dwarves with a mass of about one percent of that of the Sun, and a radius one tenth its size, through to the hottest O stars with a mass one hundred times that of the Sun, and one hundred-thousand times its brightness.

There are also other stellar-scale objects which do not follow the above definition but are still often associated with the stars, for instance white dwarves and neutron stars. These 'compact objects' are comparable in mass to the Sun, (0.4-2.1 $M_\odot$), but are notably smaller in radii (10 000-10 km; $2{\times}10^{-2} - 2 \times 10^{-5}\,R_\odot$).

Many of these objects are able to show pulsational variability and are under active research in the field of asteroseismology.

2.1.1 The Hertzsprung-Russell diagram

The Hertzsprung-Russell (HR) diagram, also known as the colour-magnitude diagram, is a scatter-plot of the luminosity and temperature of stars. Stars of different mass, composition and evolutionary stage form distinct patterns in this phase-space, making the diagram a useful tool for the exploration of stellar properties.

The most prominent feature of the HR diagram (Figure 2.1) is the broad swathe running from the bright, hot stars in the top left, to the dim, cool stars in the bottom right. These are the 'main-sequence' stars in which hydrogen is fused to helium in the stellar cores.

Above and to the right of the main sequence lie the giant stars. These are primarily evolved

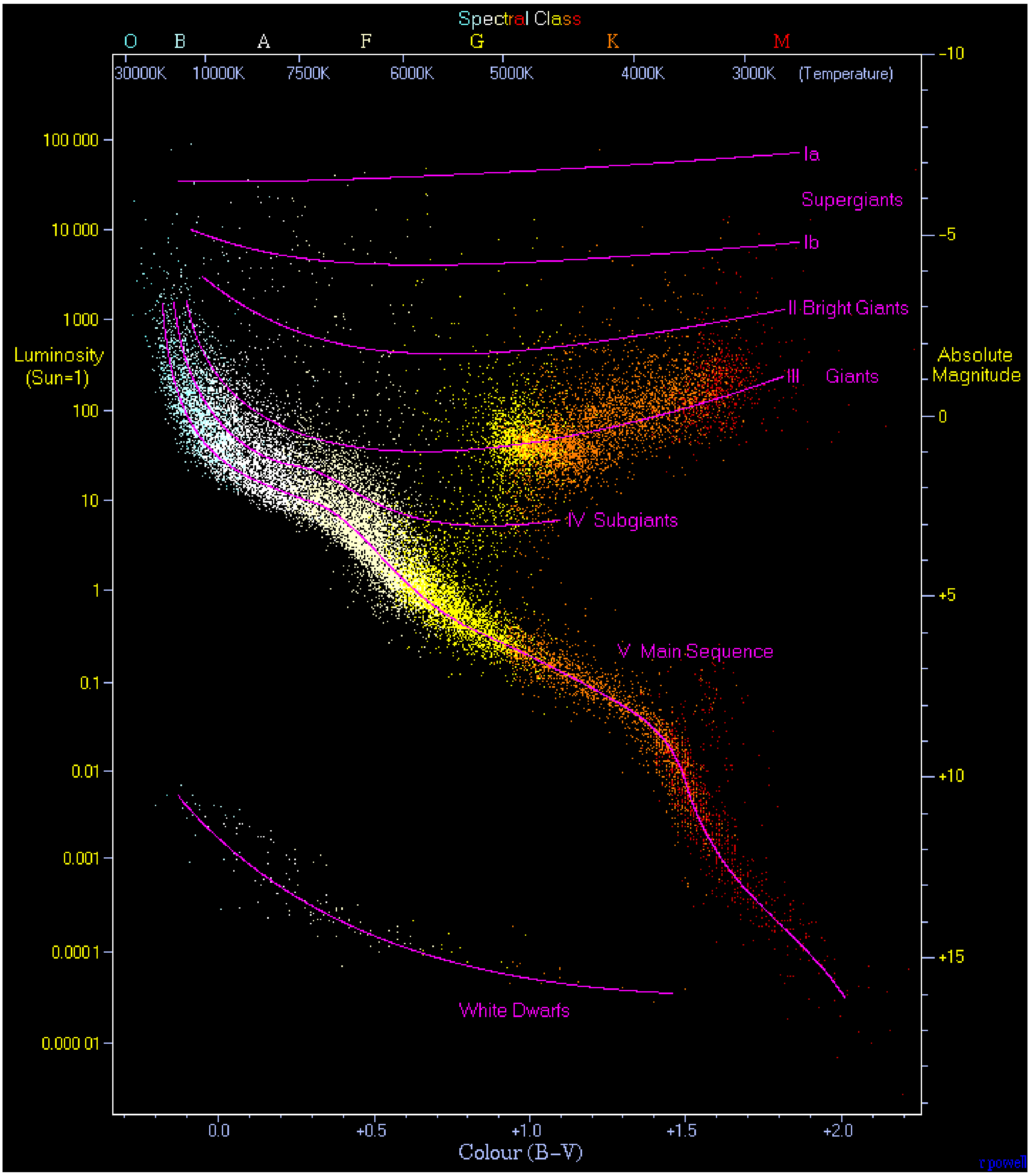

Figure 2.1: This diagram is a plot of 22000 stars from the Hipparcos Catalogue together with 1000 low-luminosity stars (red and white dwarfs) from the Gliese Catalogue of Nearby Stars. The Sun is located at a temperature of approximately 5777 K, and luminosity of 1 $L_{\odot}$. Taken from Powell (2009).

main-sequence stars which now burn heavy elements, or hydrogen in a shell around a core composed of heavier elements. This region of the diagram also includes the T Tauri stars, pre-main-sequence stars which are still condensing from primordial clouds of gas.

Below the main sequence lie the compact objects; white dwarves and neutron stars. It is here that stars end their lives once their nuclear fuel has been used up, with any remaining radiation of the body coming from gravitational collapse and residual heat. Another form of compact object, black holes, radiate no light of their own, and so cannot be placed on the diagram in any meaningful sense.

Figure 2.1 is largely composed of stars from the Hipparcos catalogue, a catalogue which consists of stars brighter than magnitude 11, and is only complete (showing all stars) to magnitude 7.3. This means that the figure is prejudiced towards the brighter stars, and shows the upper-main sequence and giants as being more numerous than would be the case in a representative numerical sample. In reality approximately 90% of all stars are on the main sequence, and of all main-sequence stars some 90% are of lower mass (and thence lower temperature and luminosity) than the Sun.

2.1.2 The Sun and Sun-like main-sequence stars

The internal structure of stars can be complicated and will vary across the HR diagram. Here the Sun is taken as an example of a typical main-sequence star, to which other bodies will later be compared.

The Sun is a slightly oblate spheroid (a flattening of $\approx 10^{-5}$), consisting primarily of a plasma of hydrogen (74% by mass), with smaller amounts of helium (24%), and heavier elements (1.77%) (metals in the language of astronomy). It has a mean equatorial radius of 6.955×10^8 m, a mass of 1.9891×10^{30} kg, and a mean density of 1.408×10^3 kg/m^3 (only a little greater than that of water).

The central regions of the Sun consist of a core, in which energy is generated by the fusion of hydrogen into helium via the p-p (proton-proton) chain reaction. The density of the core reaches approximately 150 000 kg/m^3, and a temperature approaching 13.6 million Kelvin. The core extends outwards from the very centre of the Sun to about 0.2-0.25 solar radii.

Outside of the core the rate of energy generation is negligible, and the dynamics of energy transfer come to dominate the internal structure. Throughout the core and surrounding layers radiative energy transfer is dominant, and so the region outside of the core is called the radiative zone. Here material is stratified by a combination of temperature, pressure and density (Section 2.4). The radiative zone extends from the core at around 0.2-0.25 to about 0.7 solar radii. Across this region the temperature falls from approximately 7 to 2 million Kelvin, and the density drops from around 20 000 kg/m^3 to only 200 kg/m^3.

It is thought that the inner layers of the Sun undergo solid-body rotation (all latitudes rotating at a single angular velocity) although rotation rates derived from helioseismology are uncertain for radii of $R < 0.25\mathrm{R}_\odot$. This is in contrast to the outer layers which show differential rotation, with the equatorial regions rotating significantly faster than the polar regions. The transition between solid-body and differential rotation, known as the tachocline, is located in the radiative region at, at most $R = 0.7\ \mathrm{R}_\odot$. Here a rapid change in rotational velocity occurs over a small radius. It is believed that the great shear at this level contributes to the generation of the toroidal solar magnetic field.

In the outer layers of the Sun the primary means of energy transportation changes to be by thermal convection, as material becomes unstable to vertical motions. The thermal convection cells become visible on the solar surface as a pattern of ‘granules’, and are directly responsible for the phenomenon of solar granulation and super-granulation (Section 2.7). The process of convection ensures that material is well mixed, and the composition of the convection zone is largely homogenous. It is acoustic radiation from convection which excites solar-like modes.

The visible surface of the Sun occurs where the atmosphere becomes transparent to visible light. Above this level visible light is free to propagate into space, and the energy is rapidly radiated away. At the visible surface of the Sun the temperature has fallen to approximately 5 777 Kelvin, and a density of only 2×10^{-4} kg/m^3.

It is anticipated that the Sun will spend around ten billion (10^{10}) years as a main-sequence star before expanding into a red-giant star, eventually contracting into a white-dwarf star.

2.1.3 Red-dwarf stars

In main-sequence stars of lower-mass than the Sun the convective region increases in size until in low mass red-dwarf stars (those with masses of lower than approximately 0.5 $\mathrm{M}_\odot$) it encompasses the entirety of the star. This has the effect of increasing the main-sequence life-time as fresh hydrogen is brought into the core from outer layers, such that a 0.1 $M_\odot$ star may continue burning hydrogen on the main sequence for 10 trillion (10^{13}) years.

Due to the limited age of the Universe no red-dwarf stars have reached the end of the main-sequence life-spans. However, it is expected that the end of these stars occurs *not with a bang but a whimper*. The internal temperature will never reach that required to achieve helium fusion, and at the end of its life, with the hydrogen all burnt, the star will contract into a degenerate white dwarf, composed chiefly of helium-4 nuclei.

2.1.4 High-mass main-sequence stars

While nuclear fusion through the pp-chain continues in high mass stars, the CNO (carbon-nitrogen-oxygen) cycle will dominate energy production in stars of greater mass than approximately 1.5 $M_\odot$. In this process the elements carbon, nitrogen and oxygen act in a manner similar to a chemical catalyst in the conversion of hydrogen into helium 4. The CNO cycle has a higher-temperature dependence than the pp-chain, and so the rate of nuclear fusion increases rapidly with mass in these stars.

Due to the stronger temperature sensitivity of the CNO cycle the temperature gradient within the cores of higher mass main-sequence will become convective, bringing fresh material into the core. In higher mass main-sequence stars the size of the outer convection zone will also shrink, with the envelope becoming entirely radiative at around 2.5 $M_\odot$. As the convection zone becomes thinner, it can act to retard the flow of radiation from the interior, and excite stellar oscillations. This is thought to be the reason for γ Doradus class oscillations (Section 2.8.2).

The main-sequence life span of stars scales as approximately $M^{-2.5}$. At the end of their main-sequence life span stars of lower mass than 10 $M_\odot$ evolve into red giants, while those of greater mass evolve into super- and hyper-giant stars.

2.1.5 Post-hydrogen burning stars

Once the hydrogen in the core is exhausted stars move off the main sequence. In this stage of their evolution stellar behaviour is once again dependent on the mass of the star, with a series of relatively sharp transition for lower mass stars to the giant regions, and a more gradual transition for higher mass stars.

The energy generating cores of intermediate mass main sequence stars are not convective, and so the helium products of fusion accumulate. Over time this helium settles to form a core of near pure helium, causing energy production to move outwards. As the size of the helium core increases, and energy production moves outwards thermal pressure alone is no longer able to support the core, and the material will start to collapse inwards. Eventually the core is compressed to such an extent that the electrons become degenerate, and degeneracy pressure retards further compression.

Hydrogen in the shell of material surrounding the core will be compressed by the strong gravitation forces of the dense core to a much greater density than it had been during hydrogen core burning. The high density causes it to fuse faster, increasing the rate of energy production. The increased temperature and luminosity causes the outer layers of the star to expand massively, and for the star to become a giant on the ‘red-giant branch’ of the HR diagram.

As further helium is added to the degenerate core, the negative mass-radius relationship of electron degenerate matter causes it to compress further, and the rate of hydrogen fusion increases still further, increasing the temperature of the interior. Eventually the core reaches a sufficient temperature and pressure to trigger helium fusion. This occurs rapidly in a so called ‘helium flash’, in which energy is very rapidly released. The flash causes the core to expand, and slows the hydrogen shell fusion so that energy generation decreases, the star contracts and increases in surface temperature, migrating to the ‘horizontal branch’ on the HR diagram.

During this time of helium burning the products of fusion accumulate, and form a hot core of degenerate carbon and oxygen. Thus helium is compressed in the same manner as hydrogen was by the degenerate helium core, and helium shell burning causes a further migration to the ‘Asymptotic Giant Branch’ of the HR diagram, mirroring the earlier evolution to the red-giant branch.

Each of the evolutionary stages – hydrogen core-burning, hydrogen shell-burning, helium core-burning and helium shell-burning last for progressively shorter timespans. This means that the time spent as a giant star is significantly less than that spent on the main sequence. Helium burning reactions are very sensitive to temperature changes, and fluctuations in the rate of energy generation eventually leads to the star throwing off its outer layers and the remaining core contracting down to a carbon-oxygen white dwarf.

As the lowest mass main-sequence stars have such extended lifetime, no such stars have as yet ceased hydrogen fusion. Their post-hydrogen behaviour is therefore based upon computer modelling. If the helium products of hydrogen fusion settle into the core, then hydrogen shell burning will occur and the evolution will continue to a red giant, stopping before helium core burning occurs, eventually becoming a helium white dwarf. However if the star remains fully convective then one can anticipate the rate of energy production slowing over time, and the star turning directly into a white dwarf.

The evolutionary history of the highest mass stars differs. In these stars the helium core is of sufficient size that it will commence burning prior to electron degeneracy pressure becoming dominate. This results in a smoother transition to the next stage of evolution, as helium burning occurs in parrallel with hydrogen burning. These stars are known as supergiants.

Supergiants can be broadly characterized as red or blue. Red supergiant stars are surrounded by a distended envelope, while blue supergiant stars are broadly comparable, but due to vigorous winds, or the presence of a companion body, have thrown off this outer envelope exposing the brighter internal layers.

The cores of super-giants reach temperatures sufficient to fuse elements heavier than helium. In the lowest mass supergiants fusion of carbon, but not heavier elements, will take place and the pulse of energy this provides will throw off the outer-layers of the star, leaving the core to cool to a oxygen-nitrogen-magnesium white dwarf. In the case of higher mass supergiants successive shells of fusion will occur as one goes deeper towards the core in an onion-like structure, in which progressively heavier elements are fused. When the fuel in these stars is exhausted the outer-layers collapse into the core, before being blasted off in a spectacular super-nova explosion, and a neutron star or black hole is generated from the stellar remnant.

2.1.6 Compact objects

At the end of their lives the thermal pressure of stars is no longer sufficient to support the outer layers against collapse. This is expected to happen gradually in the case of lower-mass stars, as the energy generated by hydrogen fusion decreases with time and they do *go gently into that good night*. In the case of higher-mass stars, the core temperature and pressure rise sufficiently to trigger the fusion of helium and heavier elements, the instability of which eventually leads to the outer layers of the stars being thrown off, and the remaining core contracting to dwarf size.

The contraction of these remnant bodies will continue until the degeneracy pressure of electrons is sufficient to prevent further collapse. This will occur where the density of the object reaches upwards of a million times that of the Sun, resulting in a highly compact object. Such objects have a residual heat from their time as fusing stars which is now radiated, and by the Stefan-Boltzmann law, $L \propto R^2T^4$, such a small radius means that the surface temperature is initially high, and the objects appear as white as the hottest O, A and B stars. These objects are known as ‘white dwarfs’.

For stars more massive than the ‘Chandrasekhar limit’ of 1.44 $\mathrm{M}_\odot$, electron degeneracy pressure is insufficient to prevent further collapse, and the electrons are forced into combination with protons to form neutrons. The resulting object will continue to contract until degeneracy of the neutrons (also fermions) comes into play and creates a neutron degeneracy force which prevents further collapse.

In the case of stars more massive than the neutron star limit of between 2 to 3 $\mathrm{M}_\odot$ there is a possibility that other forms of degeneracy pressure - between quarks, the posited sub-quark particles known as preons, or even more exotic unknown sub-sub-atomic particles - may allow for other types of compact objects; namely posited ‘quark stars’ and ‘preon stars’. If a neutron star can be considered to be analogous to a giant atomic nucleus, a quark star would be analogous to a giant nucleon, and a preon star to a giant quark.

However, once the radius of a star has reduced to beyond the point at which the escape velocity of the body becomes greater than the speed of light, i.e., smaller than the Schwartzschild radius, it will be hidden from view within an ‘event horizon’, and the exact details of the composition become unimportant as they can never be known. Such an object is known as a ‘black hole’.

2.2 Equations of stellar structure

The internal structure of a star cannot be directly observed by means of electromagnetic radiation, however by applying the basic physical principles regarding the conservation of mass, momentum and energy equations may be derived which allow some insights into stellar interiors.

These equations may be used to construct radial profiles for density, temperature, pressure and luminosity (i.e., energy flux).

The following definitions will apply in all subsequent sections:

- $\rho(r)$ – The density of material at a radius, r.
- $T(r)$ – The temperature at a radius, r.
- $P(r)$ – The pressure at a radius, r.
- $M(r)$ – The mass contained within a radius of r; $M(R_*)$, will be the total mass of the star.

Continuity of mass

Within a shell of material with radius dr, we will add an amount, dM, to the mass of the star. Considering a time-independent solution (i.e., that matter does not flow in to or out from the shell), dM will superficially be the density of the shell multiplied by the volume of the shell, V - i.e.

$$\begin{aligned} \mathrm{d}M(r) &= \rho(r)V = 4\pi r^2\rho(r)\mathrm{d}r, & (2.1)\\ \Rightarrow \frac{\mathrm{d}M(r)}{\mathrm{d}r} &= 4\pi r^2\rho(r). & (2.2)\end{aligned}$$

Conservation of momentum

Consider a shell of material. There will be a gravitation attraction of the shell towards the centre of the star, balanced by a pressure gradient pushing radially outwards. Again assuming time-independence (i.e., the shell is not subject to an acceleration) these forces will be in exact equilibrium.

The exact nature of the underlying force causing this pressure is not important, and it varies between different astronomical bodies. In lower mass main-sequence stars the pressure force arises primarily from thermal gas pressure, while in higher mass main-sequence stars the force is primarily from radiation pressure. For compact objects it is both electron and neutron degeneracy pressure that primarily provides the balancing pressure force.

However, pressure forces act in all directions. If there is a pressure force radially outwards at a point, there will be an equal and opposite pressure force acting radially inwards. In order to balance the gravity in crossing the shell there must a gradient in the pressure equal to the gravitational acceleration of the shell.

$$\begin{aligned}
P_{\text{outwards}} - P_{\text{inwards}} &= \frac{\partial P(r)}{\partial r}\,\mathrm{d}r, && (2.3)\\
4\pi r^2 \left(\frac{\partial P(r)}{\partial r}\right)\mathrm{d}r &= -\frac{\mathrm{G}M(r)\rho(r)V}{r^2}, && (2.4)\\
4\pi r^2 \left(\frac{\partial P(r)}{\partial r}\right)\mathrm{d}r &= -\frac{\mathrm{G}M(r)4\pi\rho(r)r^2}{r^2}\,\mathrm{d}r, && (2.5)\\
\frac{\partial P(r)}{\partial r} &= -\frac{\mathrm{G}M(r)\rho(r)}{r^2}. && (2.6)
\end{aligned}$$

2.3 Quantum degeneracy, and degeneracy pressure

In the conditions of high density an additional pressure force in to the thermal pressure arises as a consequence the Pauli exclusion principle acting on fermions (electrons, neutrons and quarks) in the matter of the body. This ‘degeneracy pressure’ prevents the gravitational collapse of the cores of high-mass main-sequence and evolved stars, and supports the entirety of the compact bodies.

The Pauli exclusion principle prevents two indistinguishable fermions from occupying identical quantum states, where a state is a statistical description of the properties of a quantum system. An example of a quantum state is the wave-function of an electron around an atomic nucleus; this wave function describes statistically the position, momentum and energy of an electron at any time. Another electron may only share the same state - i.e., the same distribution of position, momentum and energy - if it can be differentiated from this first electron. In a single atom this can only be the case if the electron adopts a spin directed in the opposite direction.

However, these consideration only apply for a single potential well. Two electrons may have the same wave function while in ‘orbit’ of different nuclei, i.e., within the potential well of a different nucleus. Where electrons are compressed within a small space the potential wells of individual nuclei merge together, and the electrons are compelled to occupy the energy levels of the space as a whole, rather than those of individual nuclei.

These circumstances are analogous to the standard quantum problem of the particle-in-a-box. In these circumstances the energy levels of the system are inversely proportional to the size of the box. Any attempt to reduce the size of the space in which electrons are trapped will increase the energy of the trapped particles, and provide a force that acts to resist further contraction. This force is known as electron-degeneracy pressure.

A similar process occurs with neutrons at higher densities. Here it is the neutrons that are forced to enter higher momentum levels with compression, to produce the force resisting compression which is known as neutron degeneracy pressure.

Degenerate matter is unusual in that it has a negative mass-radius relationship - increasing the mass of an object made from degenerate matter will cause the object to shrink.

2.4 Stability against convection

As has been noted, there are regions of stellar interiors in which energy transportation is dominated primarily by radiation or convection. The form of transfer that dominates is dependent primarily upon the temperature and density gradient, notably whether the temperature lapse rate is above or below the adiabatic lapse rate.

Consider a parcel of an ideal gas of pressure P_0, temperature, T_0 and density ρ_0, in a medium of homogenous composition. This parcel is displaced vertically upwards, to a level of pressure P_1, temperature, T_1 and density, ρ_1. If this displacement is adiabatic - i.e., no energy is gained or lost by the parcel, the parcel and its surroundings will come to be equal in pressure, and the parcel will alter to temperature, T_0' and density ρ_0'.

Hence we can identify two circumstances, where ρ_0' is greater than ρ_1 the parcel will be more dense than the surrounding media and will fall, returning to equilibrium at the the level at which the parcel was previously located. In contrast, where ρ_0' is less than ρ_1 the parcel will now be less dense that the surrounding media, and the parcel will continue to rise. This means that the atmosphere is unstable to vertical motions, and the transport of heat by convection will act to restore equilibrium by moving warmer material upwards.

2.5 Equations of state

An equation of state is formally defined as a relationship between thermodynamic state variables, i.e., parameters describing the nature of a system independent of the history of the system. These include temperature, pressure, density, internal energy, entropy and composition.

As an example a piece of iron may be heated and cooled repeatedly, but no evidence of this history will be found in the temperature and density of the iron at the end of this process (so long as the iron remains solid). In contrast the magnetization state of the iron will show a hysteresis - gaining an internal magnetic field at low temperature and losing it if the temperature is raised.

Examples of an equation of state include:

- Classical, Ideal gas, thermal pressure: $P \propto \rho T$
- Radiation pressure: $P \propto T^4$
- Classical electron degenerate matter: $P \propto \rho^{5/3}$
- Relativistic electron degenerate matter: $P \propto \rho^{4/3}$

The equation of state of neutron stars is not yet well known, with a number of competing models. This is due to the high pressure and gravitational fields in these objects, which require a complicated analysis involving general relativity.

2.6 Opacity

The opacity, κ, gives the rate of absorption of light by a medium with distance. Formally it is fraction of the intensity, I, which is absorbed or scattered per unit distance;

$$\frac{\partial I}{\partial x} = -I\kappa \tag{2.7}$$

for a given medium the constant κ may range between zero and infinity, and will in general depend upon the frequency of the light, as well as the density, temperature and composition of the medium.

For most materials the opacity will decrease as the temperature increases. This tendency is useful as it will act to damp out perturbations in the transmission of energy. For instance if the temperature of a shell of gas is raised, the opacity of the shell will diminish, less energy will be deposited by radiation in this shell, and the temperature will fall once again. However, in certain regions this tendency can be reversed. For instance, the ionization rate of a particular species will be positively correlated with temperature. In the region in which the temperature is sufficient to ionize this element, increasing the temperature will increase the rate of ionization and therefore that of energy deposition, enhancing further the rate of ionization.

2.7 Stellar granulation and active regions

The outer-layers of lower-mass stars ($M \lesssim 2.5\mathrm{M}_\odot$) show convective transportation of energy. Convection currents become visible at the photosphere as a pattern of 'granules', leading to the name of the phenomenon of 'granulation'.

A granule consists of a bright centre in which hot material from deeper inside the star is being brought to the surface, surrounded by a darker edge, where cooler material is descending back again. A single granule in the Sun will typically have a diameter in the range of 150 km to 2500 km ($\approx 1/1000\ \mathrm{R}_\odot$), and will last between 8 to 20 minutes before dissipating.

Coherency can be observed over longer length scales on the Solar surface in Doppler velocity measurements. Coherence over scales of 5-10 000 km, has been labelled meso-granulation, and of over 30,000 km, labelled super-granulation. The origins of these phenomena are not well known, however it has historically been speculated that these reflect the signature of deeper convection cells with larger horizontal scales. Alternate explanations for super-granulation have concentrated upon the influences of the Solar magnetic fields.

The pattern of granulation, meso-granulation and super-granulation can also be detected in stellar timeseries. There is coherence in the photometric output over time-scales shorter than the life-span of a granule, while at greater time-spans the output will be de-correlated, and for all practical purposes can be regarded as white noise.

A further source of aperiodic variability, comparable to granulation, occurs in the creation and destruction of active regions on the solar surface. Active regions are areas of the solar surface which show an unusually intense amount of magnetic activity which inhibits solar convection, forming regions of reduced surface temperature.

The power-spectrum of granulation is often simulated by the 'Harvey model' (Harvey 1985);

$$P(\nu) = \frac{4\sigma^2\tau}{1 + (2\pi\nu\tau)^2}, \tag{2.8}$$

in which σ is the power of the process, and τ is the life-span of the granules. A series of Harvey power-laws is used to encompass the behaviour over all length and time-scales; i.e., granulation, meso- and supergranulation, and Active Regions.

Typical time-scales and amplitudes , as given by Harvey (1985), are shown in Table 2.1.

Table 2.1: The power and time-scale for stellar granulation and active regions.

Process	Timescale (s)	Amplitude (m/s)
Granulation	400	0.7
Mesogranulation	10^4	0.3
Supergranulation	10^5	1.9
Active Regions	10^6	3.0

Recently, evidence has been presented that a better fit to Solar data can be produced if the Harvey model is altered to allow the slope of the power-law to vary from 2 (e.g. Aigrain et al. 2004). The modified Harvey model thence becomes:

$$P(\nu) = \frac{4\sigma^2\tau}{1 + (2\pi\nu\tau)^n}, \tag{2.9}$$

in which n is a free parameter.

2.8 Stellar variability and asteroseismology

Stars across many regions of the HR diagram show variability of some form. This can vary from the Mira class variables showing changes in luminosity of more than eight magnitudes over periods of many hundreds of days, through main-sequence stars of similar mass to the sun that show oscillations of a few parts-per-million (a few micro-magnitudes), to predictions (and some speculative observations) of modes in neutron stars with periods of less than 0.1 ms.

2.8.1 Forms of variability

If a star is noticed to be variable, then a number of questions may be asked regarding the nature of this variability. For instance, if it is a property of the star itself (intrinsic variability) or influenced by the position or nature of observations (extrinsic variability)? Whether the variability is associated with periodic changes in the nature of the star (pulsational variability), or with single or rare disruptive events that change this nature (eruptive variability)? Finally it

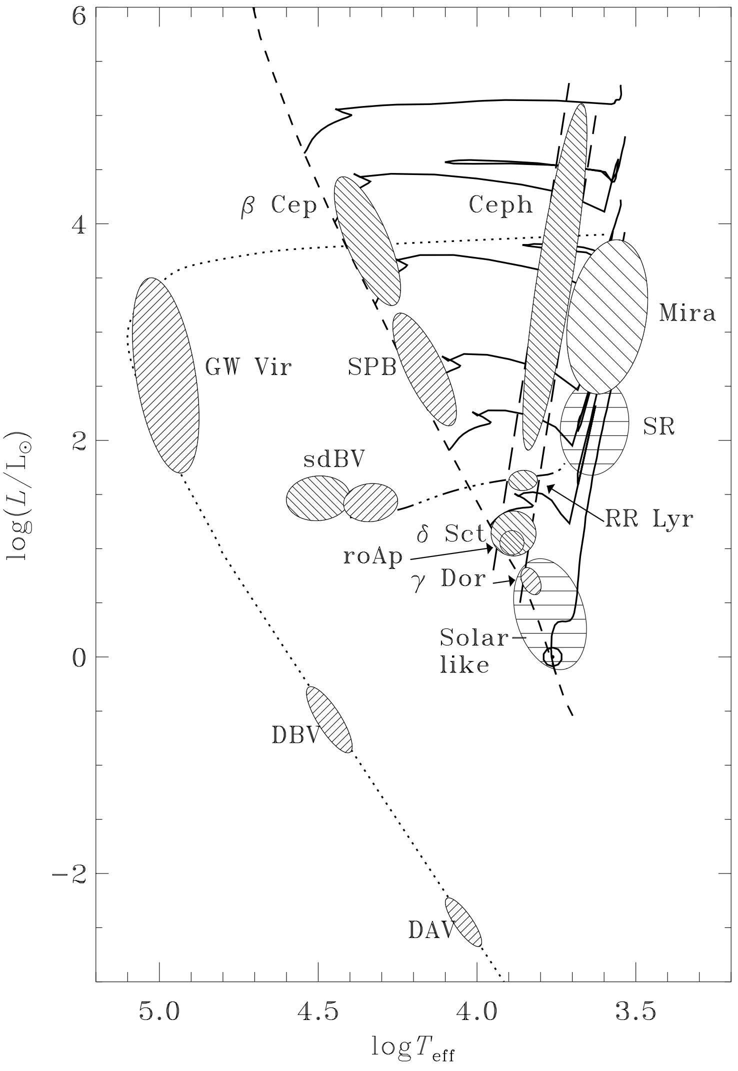

Figure 2.2: The locations of oscillating stars in the Hertzsprung-Russell diagram. The dashed line shows the zero age main sequence, the continuous curves are evolutionary tracks at masses 1, 2, 3, 4, 5, 12, and 20 solar masses. The dot-dot-dot-dashed line is the horizontal branch, the long-dashed line the classical instability strip, and the dotted curve is the white dwarf cooling curve. The hatching indicates the type of modes and excitation mechanism; up-left for opacity driven acoustic (p) modes, up-right for opacity driven internal gravity (g) modes and horizontal for stochastically excited (solar-like) modes (taken from Christensen-Dalsgaard 2003, p. 30).

may be asked: what drives this star to be variable, and in the case of a periodic variation, what causes a return to the previous state?

Intrinsic and Extrinsic variability

Variable stars showing intrinsic variability are those in which the luminosity of the star shows a change with time. This change will, by the Stefan-Boltzmann law, necessarily correspond to a periodic change in radius or surface temperature (or indeed it may be anticipated that both are somewhat variable).

Intrinsic variables make interesting targets as the cause of the variability must be associated with processes occurring within the star, and the study of the variability can therefore reveal details of processes which are hidden from casual view on the stellar surfaces.

Extrinsic variability occurs in stars in which the amount of light that can reach Earth is affected by something external to the star itself, for instance due to an orbiting companion that impinges upon our line of sight. This is another star in the case of eclipsing binaries, or a planet in the case of stars with transiting exoplanets. Extrinsic variability is also observed in the class of rotational variable stars. In these stars rotation reveals deviations from sphericity, or surface features such as a hot-spot or a region containing a concentration of star-spots.

The study of an extrinsic variable can reveal much about the local conditions of the star, for instance the presence of companions (and the ratio of sizes and mass in the system), and in the case of the rotational variables, characteristics of the rotation and features of the stellar surface.

Pulsational, Eruptive and Cataclysmic variability

Pulsational variability refers to stars which change in brightness due to changes in radius or surface temperature by the excitation of modes of oscillation in the star. This results in variability in a regular periodic or semi-regular, quasi-periodic manner. These oscillation modes represent eigenfunctions of the three-dimensional wave-equation within the star.

Knowledge of the interior structure of a star should allow one to predict to high-precision the frequency of these eigenmodes, by means of solving the wave-equation under the requisite internal conditions (i.e., the profile of density and composition with depth). Conversely, by knowledge of the frequencies of particular modes one can reconstruct models for the interior of the star which would be consistent with these frequencies. This process is known as an 'inversion'.

Eruptive variables show aperiodic changes in brightness. These changes tends to be associated with the gain or loss of mass from a star. Eruptive variables are therefore commonly those at the extrema of the class of stars - those at the beginning and ends of their lives, and those of highest and lowest mass and radii. It is typically for a proto-star to exhibit irregular changes in brightness as it evolves towards the main sequence. These changes are associated with interactions between the accreting circumstellar dust and the primitive stellar body. Only a small number of main-sequence stars show eruptive variability. The high mass main-sequence Wolf-Rayet stars regularly eject material, brightening in the process. Eruptive variability is also observed in low-mass flare stars, in which changes in brightness appear to be associated with phenomena comparable to solar flares on the Sun - i.e., most likely due to magnetic reconnection. Stars of a large radius have a lower gravitational potential in the outer regions than lower radius stars, making the loss of matter comparably easier for these stars. Therefore eruptive variability is fairly common amongst giant and super-giant stars.

Cataclysmic variables are supernovae and recurrent novae. The classical example of a recurrent nova is where a white dwarf star in a binary system accretes material from a nearby companion in a dust disk. Instabilities in this disk can cause material to rain down on to the surface of the star and cause irregular increases in brightness. When the density and temperature of the material which has accumulated on the stellar surface reaches a critical point, the material undergoes nuclear fusion, rapidly fusing hydrogen into helium. Should the mass exceed the Chandrasekhar limit, then the entire body of the white dwarf may undergo fusion from helium into carbon, triggering a type I-a supernova.

Excitation Mechanisms

Stochastic excitation Convection cells exist in layers from about $0.7R_{\odot}$, extending close to the visible surface of the Sun. As material reaches the top of the convection zone the temperature gradient becomes super-adiabatic and consequently the material moves very rapidly upwards, emerging at the solar surface in a random manner, exciting acoustic waves over a wide continuous range of frequencies. Due to destructive interference, only those excited waves that can become standing waves within the cavity (i.e., the modes) will show sufficient amplitudes to be observed on the solar surface.

Convective excitation is expected to happen in main-sequence stars with masses of less than about 2.0 $M_\odot$ (Samadi et al. 2007), as larger stars have a radiative outer layers. The presence of convection cells, and therefore convective excitation, may be expected in all giant stars cooler than the instability strip.

As convective excitation of oscillations is a stochastic process, it can be identified by the random nature of the excitation. Whereas modes of constant amplitude and frequency manifest as a single spike in a power spectrum, stochastically excited modes may be identified by showing a width in the power spectrum, i.e. a resonant mode profile which, in the case of a high-quality mode, may be approximated as a Lorentzian function. Stochastic excitation can also be observed in the time domain by examining the time-evolution of mode amplitudes and phases. A stochastic mode will vary in amplitude when considered over periods comparable to or shorter than the lifetime, and the phase will de-correlate over a comparable period.

κ mechanism excitation The opacity or κ mechanism occurs where a shell of material in a star cyclically experiences a change in ionization state, altering the opacity of the shell and retarding the flow of energy from the interior.

The process will occur as follows; a perturbation will cause a shell of material, for instance Helium(I), to move out of equilibrium position, to a region of increased pressure. Here the material will be compressed and ionize into Helium(II). This increases the local opacity, and will trap the energy flowing from the core within this layer for an extended period, leading to local heating. The warmed shell of material will expand and cool, allowing for the recombination of ions and electrons, lowering the local opacity back to the original value. This in turn causes trapped radiation to be released and will act to further cool the shell, thus leading to contraction and compression of the Helium(I), restarting and enhancing the process.

Stars within the instability strip, including Cepheid variable stars, have oscillations which are excited by the opacity mechanism. In the case of Cepheids it is the Helium II shell. The mechanism also occurs in δ Scuti and β Cephei variables in which shells of various different metals provide the required changes in opacity.

Exotic means While the majority of intrinsic pulsational variables are excited by stochastic excitation, or the κ mechanism, other processes have been suggested or observed to explain excitation in certain stars.

The energy or ϵ mechanism was first proposed as a possible excitation mechanism for variable stars, particularly Cepheids, by Eddington (1926). It occurs due to cyclical enhancement and diminution of nuclear reactions in the stellar core due to the strong temperature dependence of the rate of nuclear reactions, particularly the CNO cycle, which becomes important in stars of a few solar masses.

The ϵ process occurs as follows: heating of the core region leads to an increase in the rate of nuclear reactions, and therefore the rate of energy production. This will lead to further heating and an expansion of the material in and surrounding the core. As the material expands it will cool slowing the rate of energy production. The lower rate of energy production will lead to further cooling, resulting in contraction of the material of the core, causing it to warm and therefore the process to begin once again.

While the ϵ mechanism does not in fact provide the primary source of energy for oscillations in Cepheid variables, it may excite g mode oscillations in δ Scuti variables, (Lenain et al. 2006) and Wolf-Rayet stars (Blecha et al. 1992).

The excitation of γ Doradus (see Section 2.8.2) type variable stars is believed to be driven by a process known as 'convective blocking'. This process was first proposed for White Dwarf stars by Pesnell (1987), and extended to γ Doradus by Guzik et al. (2000).

'Convective blocking' in γ Doradus stars occurs at the base of the convection zone. Here the rate of energy transfer by convection is slow to adapt to changing conditions in the stellar interior. In the event of a pulsation causing a perturbation in the rate of energy transportation at the transition region, convection will not be able to immediately transport this additional luminosity, and pulsations are driven.

Due to the somewhat unique conditions under which convective blocking operates, the process occurs only in a small range of stars - those which have a relatively narrow convection zone close to the stellar surface. A narrow convection zone will occur in late-A and early-F type stars.

Restoration Mechanisms

Pressure (p modes) Acoustic modes, also known as p (pressure) modes, are standing density waves of compression and rarefaction. The restoring force in this case is simply down to the induced pressure forces causing motions of material from regions of high to low density.

In order for standing acoustic waves to occur a cavity is required, at the boundaries of which waves are reflected. The boundaries of the cavity in which the standing pressure modes are maintained differs between the top and bottom. At the top of the convection zone there is a sharp decrease in density, and the acoustic cut-off frequency becomes very high. Therefore almost all modes are reflected back into the interior. The depth of the bottom of the cavity varies between modes. A sound wave launched at an angle to the surface will be slowly bent by refraction on account of the increasing temperature (e.g. see Chaplin 2006, p. 69). In the Sun, modes of $l \lesssim 20$ will penetrate the radiative interior, while for modes of higher l the cavity will be entirely contained within the convective zone.

The dynamics of a p mode will be determined by the local speed of sound, and therefore depend upon the local temperature and density. The different penetration of p modes of different angular degree (figure 2.3) makes these modes useful for performing helioseismological inversions, with modes of medium and high l values returning detailed information on outer layers, and the low l modes probing the core.

Gravity (g modes) Internal gravity modes, known as g modes, have gravity (and buoyancy) as the force acting to restore equilibrium. These modes occur where a parcel of fluid vertically displaced from a level in which it is in equilibrium with the surrounding media will show a density differential, and so will exhibit positive or negative buoyancy in a manner that acts to return the fluid to equilibrium. This will occur in regions in which the primary form of energy transportation is by radiative means. In convective regions a displaced parcel of gas will continue to rise or fall, so standing gravity waves are not able to propagate, and become evanescent within these regions.

In lower mass main-sequence stars, like the Sun, a radiative central region is surrounded by a convective envelope. The g modes are therefore confined inside the stellar interior and have only a low residual amplitude at the surface. Nevertheless continued attempts to observe g modes in the Sun are a major endeavour of helioseismologists, as these modes have higher residual amplitudes at the core than the p modes, and are able to give detailed information about the

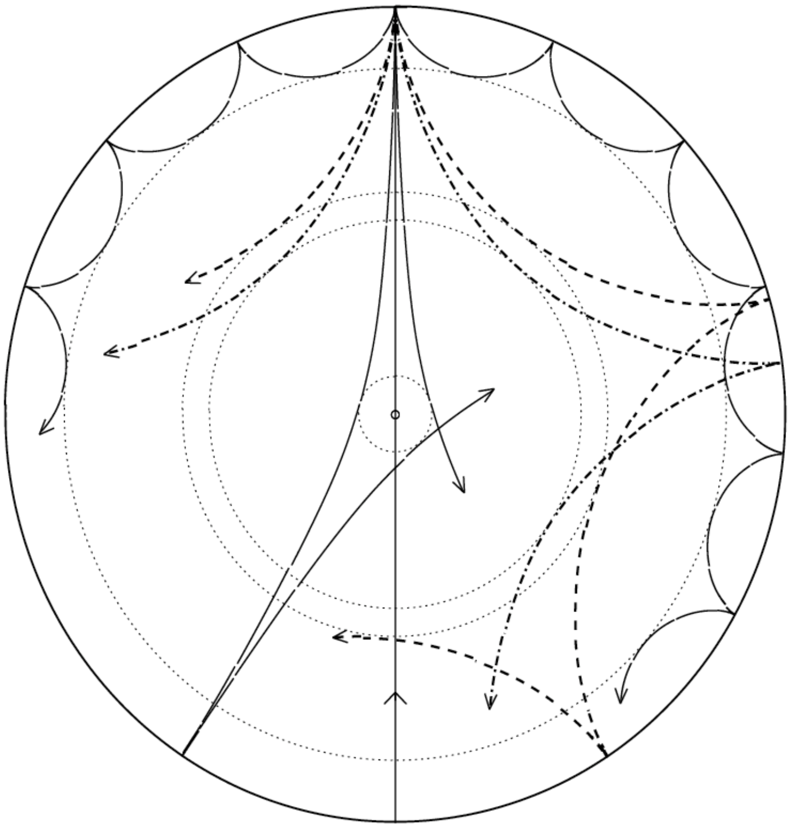

Figure 2.3: P-modes of different angular degree penetrate to different depths within the solar or stellar interior, with modes of the lowest angular degree (solid and very long dashed lines passing close to the centre) reaching all the way to the core, while modes of higher angular degree (dotted, dot-dashed and outer, long dashed line) only probe the outer regions (From Christensen-Dalsgaard 2003).

conditions of this region.

Under some circumstances, especially in evolved stars where the frequencies of g and p modes overlap, g modes may interact with p modes of the similar frequencies to form ‘mixed modes’ (see below).

The Brunt-Väisälä frequency (see Section 3.5.2) gives an upper limit on the frequency of g modes. There is also a selection effect in angular degree, l, (see Section 3.1) which means that solely non-radial modes ($l \geq 1$) are observed.

Surface gravity (f modes) Surface gravity waves, or f modes, are waves which occur solely on the surface of a medium, without any radial nodes. They are therefore analogous to many everyday observations of waves, for instance ripples on the surface of a pond, and waves in the deep ocean.

Mechanically f modes are created by a similar process to gravity waves, with both gravity/buoyancy as the restoring force. They are distinct as they occur in the region of transition between convective and radiative regimes close to the surface, where the temperature gradient falls below the adiabatic lapse rate and the waves can propagate.

The observation of f modes in the Sun was important as it allowed a calibration of the radial overtone number, n, of p modes. As f modes oscillate without a radial component, they could be considered to have $n = 0$, the next lowest frequency modes at a given l would have $n = 1$, etc (see Chaplin 2006, p. 135).

2.8.2 Variability of specific star-types

As has been seen, variability is common across the HR diagram. Here I discuss in detail the nature of a number of types of variability which will be further referenced in later sections of the thesis. As the varieties of oscillation are manifold, no attempt is made to be comprehensive.

Main sequence, Sun-like stars

In the Sun many modes of oscillation are seen simultaneously, with periods in the range of 3–15 minutes (frequencies extending between approximately 1100–5500 μHz). These oscillations are p modes, stochastically excited by convective noise. Mode amplitudes vary with frequency, peaking at around 3050 μHz with an amplitude of a few parts per million in photometry, and a few tens of centimetres per second (a RMS amplitude of 16 cm/s) in Doppler velocity.

G modes are also anticipated to occur within the inner radiative regions of the Sun. As such modes are evanescent, and thence decay exponentially, within the outer convective regions residual mode amplitudes at the solar surface are tiny in comparison to the p modes. There have been numerous claimed detections of individual modes at low amplitude (Garcia et al. 2007), however the Phoebus group, having reviewed the evidence, conclude that they could not confirm these findings, and put an upper limit of g-modes amplitudes of 3 mm/s (Appourchaux 2008).

It is anticipated that all stars having an outer convection zone will show similar oscillations. This includes all stars on the main sequence with a mass lower than approximately 2.0 $M_{\odot}$. In this thesis the term *solar-like* will refer to p modes stochastically excited by convective noise.

Cool-giant stars

Cool-giant stars show a variety of forms of variability, encompassing both κ and stochastically excited oscillations. The study of cool giant stars presents a model of what may be the destiny of our own Sun and similar local stars such as α Centauri A and B when they enter the red-giant stage of evolution.

Cool-giant stars can be broadly characterized by the energy generation processes occurring in the core. A star will enter the red-giant era of its lifespan where core-hydrogen is exhausted, however a shell of hydrogen may continue to fuse around the core (now composed of degenerate helium). Such stars cluster on the HR diagram in a region known as the red-giant branch. When the helium core itself reaches sufficient temperature it will itself fuse and the star will come to lie on either the horizontal branch in the case of metal poor, or red clump in the case of metal rich stars. Once again the core Helium may come to be exhausted, and stars may continue to burn Helium in a shell around the degenerate carbon core. Such stars are located on the asymptotic-giant branch.

All stars cooler than the classical instability strip are expected to have convective outer layers and thence may be expected to show some form of solar-like oscillation. Mode amplitudes in these giant stars are predicted to be large in comparison to stars on the main sequence, of the order of parts-per-thousand in comparison to parts-per-million in the Sun. Due to the lower density of the giant stars the oscillations are of much longer duration - for instance a 1 $M_\odot$, 25 $R_\odot$, 4500 K star is expected to show maximum oscillation power at a period of approximately 2.1 days.

The OGLE II survey of stars in the Large Magellanic clouds observed more than 23 000 red-giant stars. A number of period-luminosity relationships were identified for asymptotic-giant branch stars, corresponding to oscillation in low-order radial modes. Kiss and Bedding (2003) identify a further two sequences below the tip of the red-giant branch, consisting of almost 10 000 short period ($15 < P < 50$d), low amplitude ($A < 0.04$) mag red variable stars. They propose that a significant fraction of these are likely to be on the red-giant branch and show radial pulsations in the second and third overtone modes.

Time series arising from the CoRoT mission, and Kepler long-cadence data (see Section 3.6.2) should allow a comprehensive mapping of the locations in the HR diagram of where each of these forms of variability are manifest by stars.

β Cephei Stars

β Cephei stars are bright, hot, B stars, primarily on the main sequence, but encompassing a few sub-giants and giant stars. The stars undergo periodic pulsations of the order of 0.1 - 0.6 days with an amplitude of 0.01 - 0.3 magnitudes, and are at their brightest during minimum contraction. Many stars of this kind exhibit multiple pulsation periods. The pulsations are driven by a κ mechanism process associated with the ionization of iron.

As variables at the upper end of the main-sequence, β Cephei stars provide an important window into the behaviour of the most massive stars. Such stars have a large inner convective core and may provide important insights into the phenomenon of convective overshooting (in which material set in motion by convection penetrates - ‘overshoots’ - into non-convective regions). β Cephei stars were amongst the first stars in which rotational splittings were observed (Jerzykiewicz 1980).

Recently observations by CoRoT (Belkacem et al. 2009) have demonstrated the presence of solar-like oscillations in the β Cephei pulsator, V1449 Aql. Intriguingly these seem to occur, in part, in the same frequency range as κ mechanism driven modes, while in other stellar types showing multiple forms of variability (e.g. the combined γ Doradus and δ Scuti variables) the two regimes are well separated in frequency.

γ Doradus Stars

γ Doradus stars are typically intermediate mass early F-type main-sequence (V) or sub-dwarf (IV) stars. They are variable with typical periods in the range 0.5 to 3.0 days, and amplitude of a few hundredths of magnitude ($\approx$10 ppt). There is some overlap between the regions of the HR diagram occupied by γ Doradus and δ Scuti stars, and some stars show both forms of variability (Handler 2009).

Although variability has been known in γ Doradus since the 1960's, it was only in the 1990's that variability in γ Doradus and similar stars was confirmed as a novel form of variability. Approximately 50 such stars are known, with dedicated studies over the past decade adding most to this number.

Oscillations in γ Doradus-class stars are gravitationally restored (g mode) pulsations. The pulsational mechanism for gamma-Doradus-class oscillations is thought to be a flux modulation induced by the rapid transition in temperature, density and composition between the radiative interior and the upper convective layer (for instance, see Dupret et al. (2006a), Section 2.8.1), however, the exact details of this process are still in need of clarification.

As γ Doradus class stars are g mode pulsators, a great number of modes of oscillation are possible. However, due to the periods lasting about one day, obtaining good data from the ground is challenging, and currently only a few frequencies have been observed in any single star (Uytterhoeven et al. 2008).

In addition, the pulsation periods are comparable in size to the expected rotational periods, making it difficult to detect and identify the individual pulsation modes (Handler 2005). Long-period datasets, such as the 150-day observations of CoRoT (Bouabid et al. 2008, Mathias et al. 2009), and potentially longer timeseries of Kepler (see Section 3.6.2) promise to enhance our knowledge of these stars.

γ Doradus class stars are of particular interest for asteroseismology, as g modes are sensitive probes of stellar cores. In Section 7.1 we report on observations of variability in the prototype star of this class, γ Doradus.

δ Scuti Stars

δ Scuti stars are main-sequence variable stars on the classical instability strip, with masses of between 1.5-2.5 $M_{\odot}$. They are closely related to, and may for a group with the AI Velorem variable stars. The term *Dwarf Cepheids* seems to be used interchangeably between these two classes, dependent on author. As oscillators on the classical instability strip δ Scuti variables show kappa mechanism oscillations, excited by the Helium II ionization shell.

δ Scuti stars undergo oscillations with periods of half-an-hour to a few-hours, and amplitudes of between a few parts-per-thousand and a magnitude. The prototype of the class, δ Scuti, exhibits brightness fluctuations between magnitudes 4.60 and 4.79, with a period of 4.65 hours.

The oscillations in δ Scuti stars are in low overtones ($n \leq 6$), and it appears that both p and g modes are present (e.g Kurtz 1996). δ Scuti stars are interesting targets for asteroseismology as they show a great number (over 20 in pre-CoRoT data) large amplitude non-radial modes. CoRoT data have revealed stars in which many hundreds of oscillation frequencies are present (Poretti et al. 2009). The stars also show period and amplitude changes over timescales many times faster than those expected from stellar evolution (Breger 2009).

Chapter 3

Helio- and Asteroseismology

The previous chapter has described the many causes of variability which arise in stars. Asteroseismology refers specifically to the study of stars showing pulsational variability, primarily with the intention to derive the internal structure by interpretation of the frequency spectra of the star. Helioseismology is the comparable study involving the Sun.

One of the particular differences between the disciplines lies in the ability to resolve an image of the Sun. This is in contrast to stars in which only a single value for the flux may be obtained at any one time which is an integration of the pattern of flux across the visible face. The ability to resolve the surface permits the observation of a very large number of modes of high-angular degree by means of measuring the differential motions between points of the solar surface, while integrated data measurements permit only the observation of modes of low angular degree.

Helioseismology may be divided into global and local sub-disciplines. Global helioseismology consists of measuring the frequencies of standing waves trapped within the solar interior which show a coherent signal across the entire surface, and then searching for a seismic solar model whose oscillation frequencies match those observed in the Sun. Local helioseismology by contrast examines the evolution of individual excited waves in both time and space to examine conditions over a much smaller scale - for instance the perturbations of the solar medium in the region surrounding a sunspot.

3.1 The nature of oscillatory modes

We make the assumption that a large majority of stars are sufficiently spherical that they can be well approximated by a sphere. This will be the case in a vast majority of stars with the exception of certain ‘rapid rotators’. These are stars which have such a great rotational velocity that the magnitude of gravitational and centrifugal forces at the surface become comparable, and a significant degree of rotational flattening is seen. An example is the star ‘Achernar’ which is the least spherical star studied to date, and has an equatorial diameter that is more than 50% greater than its polar diameter (Domiciano de Souza et al. 2003).

Oscillatory modes are solutions to the spherical wave-equation;

$$\nabla^2\psi = \frac{1}{c^2}\frac{\mathrm{d}^2\psi}{\mathrm{d}t^2}, \tag{3.1}$$

where c is the speed of the wave. In spherical coördinates form this can be written as:

$$\frac{1}{c^2}\frac{\mathrm{d}^2\psi}{\mathrm{d}t^2} = \frac{1}{r^2}\frac{\mathrm{d}}{\mathrm{d}r}\left(r^2\frac{\mathrm{d}\psi}{\mathrm{d}r}\right) + \frac{1}{r^2\sin^2\phi}\frac{\mathrm{d}^2\psi}{\mathrm{d}\theta^2} + \frac{1}{r^2\sin\phi}\frac{\mathrm{d}}{\mathrm{d}\phi}\left(\sin\phi\frac{\mathrm{d}\psi}{\mathrm{d}\phi}\right), \tag{3.2}$$

which is separable into independent radial and angular solutions. The solutions can be characterised by three numbers, one describing the radial solution and two describing the angular component - i.e the pattern of waves at the surface. These are the eigen-numbers of each term of the above equation. These are known as the radial order, n - the number of nodes seen from the origin to surface radially; the angular degree, l, and the azimuthal order, m.

An example would be the $l = 1$ mode. Here one half of the star will be in motion in one radial direction while the other hemisphere is travelling in the opposite radial direction, i.e., one hemisphere will expand outwards while the other contracts inwards. When $m = 0$ it is the northern and southern hemispheres which oscillate in anti-phase, while when $m = 1$, it is the eastern and western hemispheres which are oscillation in anti-phase. Examples of other, more complicated modes are shown in figure 3.1.

In general the frequency of a mode will be determined by the characteristic numbers, n and l, for instance by the asymptotic equation given in the following section. In a non-rotating homogeneous sphere modes of different m will have the same frequency, however rotation of the body breaks the degeneracy, and a splitting between different values of the azimuthal order is seen.

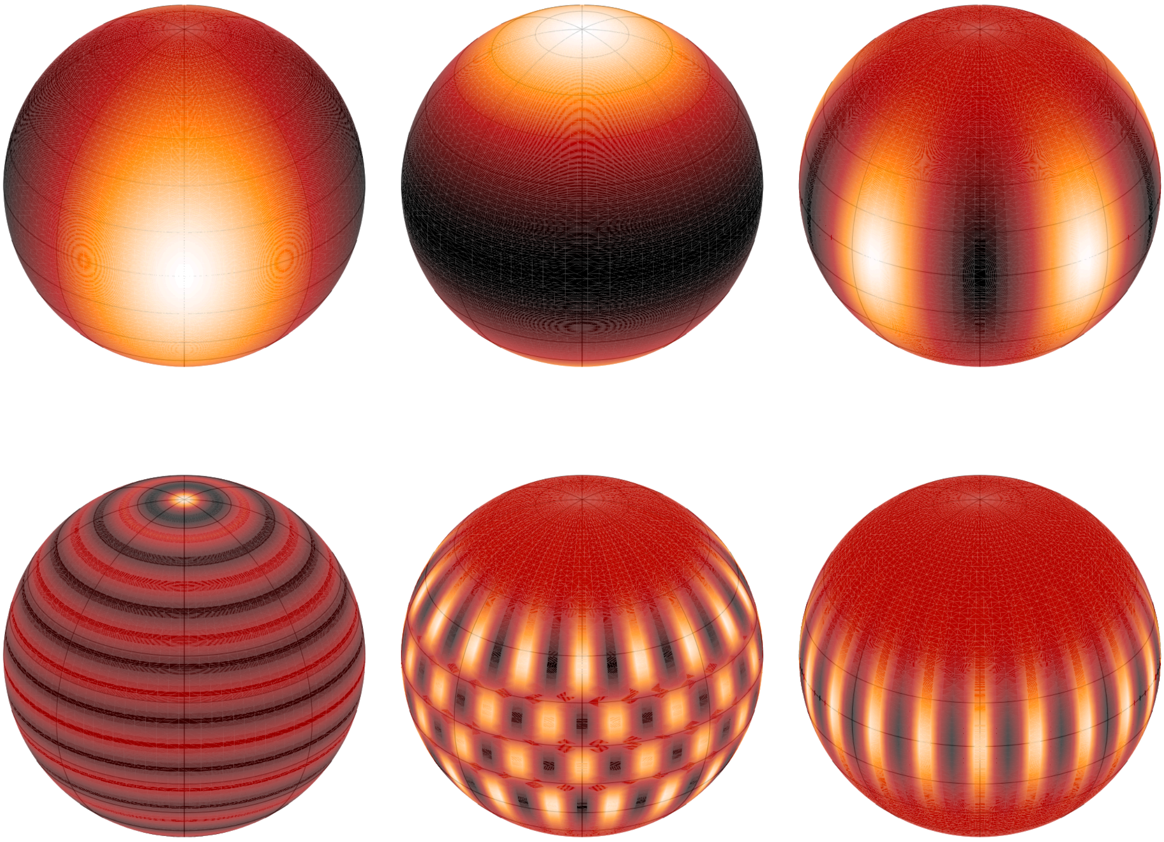

Figure 3.1: Examples of surface displacements (i.e., the angular components) for a number of modes with different values of m and l. Spheres are oriented to show the north polar region.

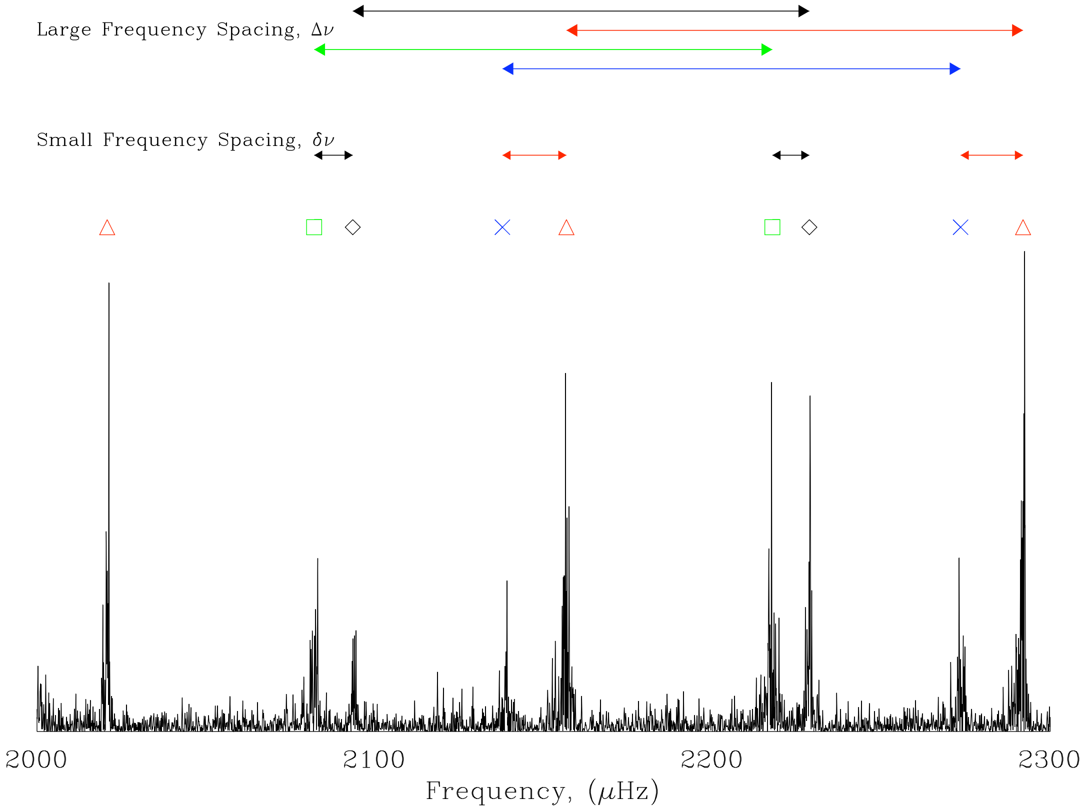

Figure 3.2: A small section of the Solar spectrum, taken from a sixty day BiSON dataset. In this diagram the location of $l = 0$ modes are marked by black diamonds, $l = 1$ modes by red triangles, $l = 2$ modes by green squares, and $l = 3$ modes by blue crosses.

3.1.1 Terminology

Frequencies, spacings and splittings.

Figure 3.2 shows a small section of the solar spectrum. The locations of $l = 0, 1, 2$ and 3 modes are marked by symbols. It can be seen that the modes of even and odd angular degree each form clusters, separated by approximately half the spacing between modes of adjacent radial order.

The frequencies of low-degree p-mode oscillations in main-sequence stars are well approximated when $n \gg l$ by a regular series of peaks with frequencies given by the asymptotic relation (Tassoul 1980):

$$\nu_{n,l} = \Delta\nu \left(n + \frac{l}{2} + \epsilon \right) - l(l+1)D_0. \tag{3.3}$$

In this expression n, and l are the radial order and angular degree. The factors, ϵ, $\Delta\nu$ and D_0, are all characteristics of the star itself, and related to the structure of the body. Therefore, by specifying two parameters, the spacing between adjacent radial orders and the spacing between modes of different angular degree (which will be related to D_0), the entire pattern of modes can be specified within an additive constant, to a good approximation.

The spacing between adjacent radial orders of the same angular degree is termed the large frequency spacing, $\Delta\nu_{n,l}$. It is conventionally defined as:

$$\Delta\nu_{n,l} = \nu_{n,l} - \nu_{n-1,l}. \tag{3.4}$$

The large frequency spacing is drawn atop Figure 3.2 for modes of different angular degree. The large frequency spacing for the Sun varies with both n and l, but is in general around 135 μHz.

The small frequency spacing, $\delta\nu_{n,l}$ is that between the pairs of even and odd modes. it is defined as:

$$\delta_{n,l} = \nu_{n,l} - \nu_{n-1,l+2}. \tag{3.5}$$

The small frequency spacing for pairs of adjacent modes is marked in Figure 3.2 for both the odd, and even sets of modes. Over the range of modes shown in Figure 3.3 on page 41 the mean small spacing for $l = 0, 2$ modes is 7.928 μHz (0.0586$\Delta\nu$), and for the $l = 1, 3$ modes is 15.511 μHz (0.1146$\Delta\nu$).

A final splitting, which is not visible in Figure 3.2, is that between modes of different azimuthal order, m. This value is know as the rotational splitting.

‘Cadence’

The term *cadence* has been appropriated from musical terminology, where it is defined at ‘The measure or beat of music, dancing, or any rhythmical movement’. The scientific definition of the word is used to reflect the rhythm of data collection. However, as the term is not in common English usage, it has unfortunately acquired two conflicting definitions within the field.

- ‘Due to the 30-minute observing cadence, asteroseismology...’ (Christensen-Dalsgaard et al. 2008). Here cadence is being used as a unit of interval, with the dimensions of time.

- '... are read out of the CCD at a cadence of 10 Hz' (Bruntt 2007). Here cadence is being used as a unit of frequency, with the dimensions of time^{-1}.

While the first usage appears to be the more common, the second definition is common where the terms 'high' and 'low cadence' are used. For instance Kepler data is typically divided into two sets, data collected at 'high cadence', with a one-minute interval, and at 'low cadence', with a thirty-minute interval.

Different terminology between helio- and asteroseismology

Although the disciplines of helio- and asteroseismology now interact very closely, it is important to remember that research groups have often entered the field from different backgrounds, and use different conventions regarding the preferred units and presentation of results.

The tendency is for helioseismologists to look at periodograms in the power domain - power-spectra or power-density-spectra. The amplitude of modes as determined through intensity measurements are expressed as fractional intensities in units of parts-per-thousand, or million (as appropriate). Frequencies are most often written using the second as the base unit - i.e., expressed in milli- or microHertz.

Asteroseismologists have traditionally preferred to look at amplitude spectra, and will express the amplitude of modes seen in photometry in terms of an amplitude in astronomical magnitudes. They are also more ready to switch between describing an oscillation in terms of periods and frequencies, expressing both in days or cycles-per-day.

3.2 The use of seismology

While knowledge of the frequencies of oscillations in the Sun and stars is intrinsically interesting, it is the use of these frequencies in determining the internal structure of these bodies that seismology really shows its power.

In helioseismology, detailed determinations may be made through the process of the helioseismic inversion (Section 3.2.1). This relies upon knowing the frequencies of a huge number of modes, and as such can only be performed for the Sun using data from those modes which are viewed in resolved data across the surface.

When dealing with data from asteroseismology, and the comparable Sun-as-a-star data, one is restricted to observing only the small number of modes with l of less than 3 (see Section 3.4 on page 45). However, even with these restrictions, a number of determinations may be made regarding the internal structure of the star under observation.

3.2.1 The helioseismic inversion

An inversion is where one attempts to determine parameters describing a model from empirical data. Within the field of helioseismology the forward problem would be to calculate the frequencies of a known solar model. The inverse problem is, knowing the frequencies, to calculate the parameters describing the model.

The trouble with many inverse problems is that they are ill-posed. When given a wire of known length and stiffness it is a ‘well-posed’ problem to calculate the natural resonant frequencies of the wire. The problem is called well-posed as we know a solution exists, that it is unique (i.e., there is only a single set of frequencies for any wire) and the frequencies depend continuously on the parameters, i.e., the frequency is a continuous function of length and stiffness.

The inverse problem to this, calculating the length and stiffness of a wire given the frequencies is ill-posed. We may be unsure that a solution exists - if the frequencies are those of a two-dimensional surface it is likely that a 1D model will offer a fit to them. The solution will not be unique, e.g. a short, flaccid string will have the same frequencies as a long, stiff string, and an additional source of data will be required to differentiate between these solutions.

The comparable two-dimensional problem, of hearing the shape of a drum, also suffers from the problem of uniqueness. It is not possible in general to determine the shape of a drum given the eigen-frequencies (Gordon et al. 1992). We run in to similar problems in the 3D case - it is not possible in general to uniquely determine the internal composition of a spherical body solely from the eigen-frequencies. However, one is fortunate as there are additional constraints which can be laid upon a solution, i.e., that it obeys the equations of stellar structure (Section 2.2 on page 13), and the structure must, in general, be smooth with, for instance, no sharp changes in temperature.[1]

---

[1] However, note that the assumption of smoothness is not always appropriate, for instance there is a sharp change in properties between the convective and radiative regions, and at the locations of ionization shells.

In a full helioseismic inversion the frequencies observed in the Sun are compared to those obtained from a standard solar model. A standard solar model is created by taking a one solar mass stellar model of zero age and evolving this to the age of the Sun. The zero-age model has a homogenous distribution of chemical elements, and nuclear reactions are just starting to generate a majority of the energy. All structural changes from that date are due to the nuclear reactions in the core[2]. This model is tuned to have the same radius and luminosity (and therefore temperature) at the surface as the solar radius and luminosity. Only two free-parameters occur in the model - the helium abundance, and the mixing length (a parameter which describes length scales in convective regions).

Differences between the frequencies of the model and those seen in the Sun can reveal the presence of processes which are unaccounted for in the standard solar model, for instance the phenomenon of 'convective overshooting' in which undifferentiated material from the convective regions penetrates into the largely differentiated material of the radiative regions.

3.2.2 Proxy determinations

While the full helioseismic inversion can provide a wonderfully detailed description of the properties of the solar interior, it is not appropriate to use on other stars. To construct a model akin to the standard solar model we would need a detailed idea of metallicity, age, radius and temperature/luminosity of the star, and for a number of stars under asteroseismic research this detail is simply not available. In addition a true inversion makes use of the data from the resolved Sun, and this is obviously unavailable for a star.

Instead we must look at only the modes of low angular degree, and use these in combination to find a proxy for the information we wish to extract from a star - the mass, radius, luminosity and age etc. Fortunately two measures we have already met, the small and large frequency spacings, both provide a useful proxy measure.

The large-frequency spacing is proportion to the frequency of the fundamental radial mode of the star. The frequency of the fundamental radial mode is in turn proportional to the mean density of the star. Therefore, by using the the large frequency separation in combination

---

[2] However, in the real Sun and stars there are additional processes of settling, diffusion and mixing which cause further structural changes As there is no preferred way to model these processes, inclusion results in a 'non-standard' solar model.

with other astronomical observations, such as the surface gravity $g = \mathrm{G}M/R^2$, one is able to determine the radius and mass of the star.

Consider two modes whose separation defines a small-frequency spacing, i.e., two modes of angular degree 0 and 2, or degree 1 and 3. These will have radial profiles which show similar amplitudes in the outer-layers of the star, however the mode of lower angular degree will have a greater amplitude in the deep stellar interior. Comparing the frequencies of these two modes will cancel out to some extent the influences of the outer layers of the star, and show variations of the sound speed within the central part of the star. The small-frequency separation therefore provide a probe of the energy generating core.

Figure 3.3 shows an 'Echelle' diagram of modes in the Sun. This takes the full solar spectrum, and folds it with the large frequency spacing to illustrate the pattern of modes. It can be seen that modes of a given angular degree form ridges in this diagram.

From the Echelle diagram it can be seen that the large and small frequency spacings are not constant across the whole range of frequencies. As modes of different radial order show different profiles of amplitude with depth these variations can be used to infer variations in the internal structure, for instance the extent of the degenerate helium core in a sub-giant star.

Taken together, the large and small frequency separations produce what is known as the 'asteroseismic HR diagram' (Christensen-Dalsgaard 1993), also known as the Christensen-Dalsgaard diagram, is seen in Figure 3.4 on page 42. The Christensen-Dalsgaard diagram may be used to determine the age and mass of a star.

Further combinations of the frequencies can give additional information on stellar composition, for instance the second differences can be used to reveal variations in the first adiabatic exponent, γ, which should be dependent upon the influence of the ionization of helium on frequencies.

3.3 Observing stellar modes

There are three main methods by which oscillations can be observed - Doppler velocity shifts of spectral lines, fluctuations in the surface intensity and spectrophotometry, the observations of and comparison between intensity at differing points in a spectrum.

As each technique has different responses across the solar disk, each will have different

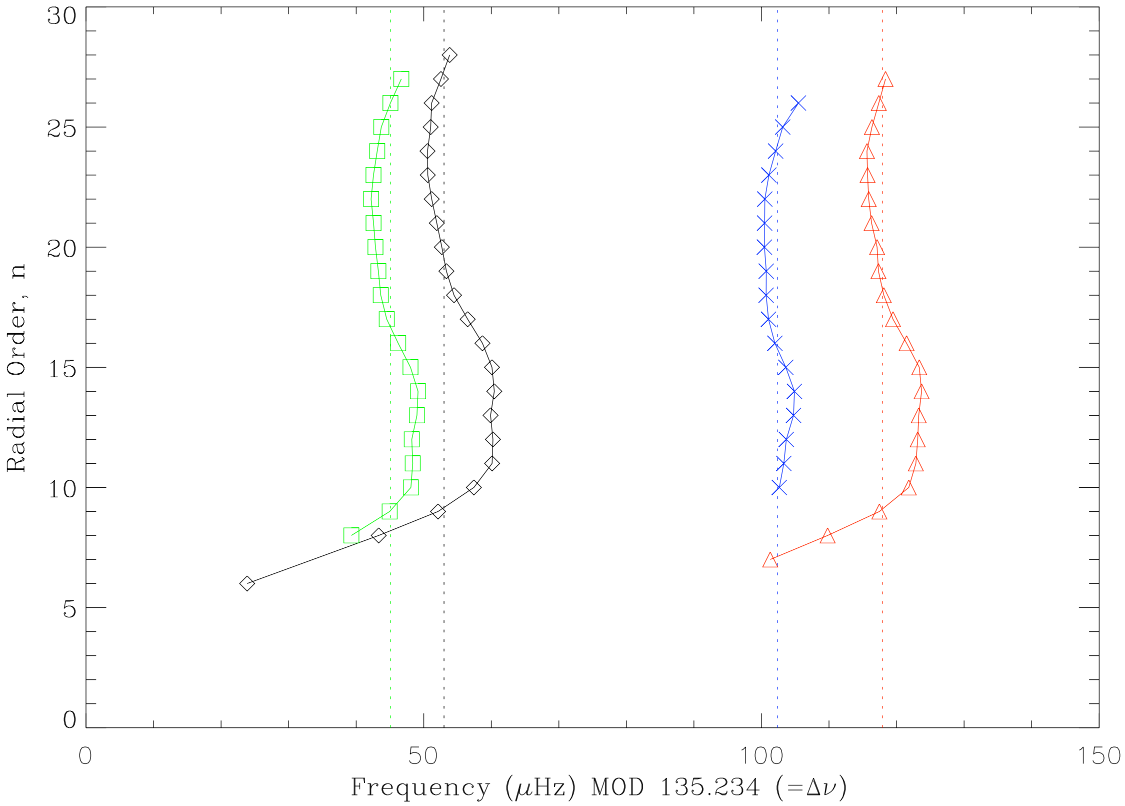

Figure 3.3: Echelle diagram of the Sun. Here the location of modes in frequency are folded by the large-frequency spacing, with every section of folded spectra offset vertically. In this diagram the location of $l = 0$ modes are marked by black diamonds, $l = 1$ modes by red triangles, $l = 2$ modes by green squares, and $l = 3$ modes by blue crosses. Data taken from Chaplin et al. (1999), with additional frequencies from Broomhall et al. (2009a).

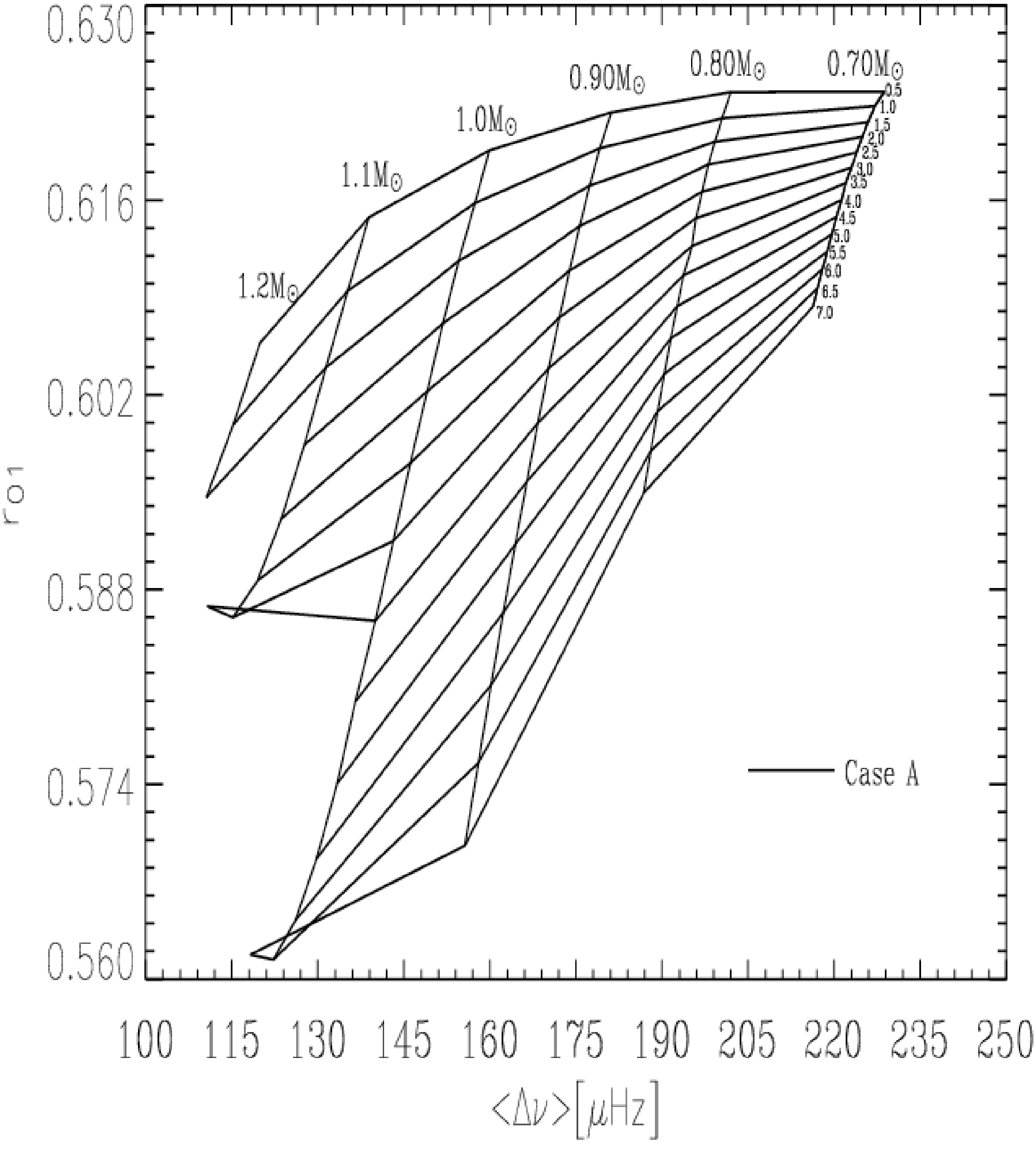

Figure 3.4: Asteroseismic HR diagram for $Y = 0.28$. Vertical lines mark evolutionary tracks for stars of a given mass (labelled at the top). Horizontal lines mark points of constant age, labelled to the right with ages from 0.5 to 7.0 Ga. Here the vertical axis is scaled as r_{01}, which is the ratio of the average small separations between $l = 0, 2$, and $l = 1, 3$. Taken from Tang et al. (2008).

sensitivities to modes of a given angular degree, as seen for Doppler and Intensity measurements in figure 3.5 on page 48, with, in general, velocity and equivalent-width measures more sensitive to modes of higher l. Different sensitivities between the methods can be useful and aid in the process of mode identification (Bedding et al. 1996).

Intensity and spectrophotometric measurements are more sensitive to the granulation background (section 2.7 on page 18) of stars as they detect the temperature changes which are associated with granulation cells. Velocity measurements have the disadvantage of degraded precision due to broadening from stellar rotation, however only in a limited numbers of stars will this effect be significant. Currently velocity measurements remain the method of choice for ground-based studies, despite the requirements for extremely high-precision instruments, with intensity measurements favoured in most space-based missions.

3.3.1 Velocity measurements

As oscillations result in gross motions of material in the stars outer layers, this motion can be observed through the Doppler shift of spectral lines.

The level at which a particular spectral line is generated will depend upon the local conditions of temperature and pressure. These factors will come together to determine the depth within the stellar atmosphere at which the modes are observed. Observing at a different depth will influence the amplitude of observed modes. The fact that the same five-minute oscillations may be observed in all spectral lines supports the observation that the modes are global in nature.

The current helioseismological networks observe the Sun using Doppler methods. As the amplitudes in Sun-like stars are extremely small, positive detections of p-mode oscillations have been difficult, however interest in the field has been growing as a result of programs to detect longer terms variations caused by extra-solar planets. The average root-mean-square amplitude of Doppler shifts observed for individual radial modes in the Sun by BiSON is around 0.16 m s^{-1}.

3.3.2 Intensity measurements

As flux from a given region is strongly related to the temperature by the Stefan-Boltzmann law, $F \propto T^4$, which in turn is related to the relative compression, $\delta T/T \propto \delta\rho/\rho$ of the atmosphere assuming adiabatic conditions, (see also section 3.5.1 on page 50) there will be a direct relationship between oscillations and changes in the luminosity of a region.

Intensity measurements offer an advantage over Doppler methods as they can in principle be made using radiation of all emitted frequencies, including those regions of the spectrum barren of spectral lines. In addition a large number of stars can be observed using the relatively simple equipment of a calibrated CCD.

Unfortunately scintillation from the Earth's atmosphere limits the precision of ground-based photometry measurements, however these problems are diminished close to the pole and proposals have been (repeatedly) made for an asteroseismological observatory on the Antarctic plateau (Linsky 1989, Heasley et al. 1996, Schmider et al. 2002, Kurtz 2007).

It is in space that some of the most interesting intensity measurements have been made, both by dedicated asteroseismology missions such as MOST (Section 3.6.2 on page 58) and the recently launched CoRoT (Section 3.6.2 on page 59), and using other resources such as the fine guidance sensors on the Hubble Space Telescope (Zwintz and Weiss 2000) and the star-tracker aboard the failed WIRE satellite (Buzasi 2000 2002, Bruntt and Buzasi 2006, Fletcher et al. 2006).

3.3.3 Spectrophotometry

Spectrophotometry refers to any of a number of techniques which contrast photometric measures at different wavelengths. One such method is to monitor changes in spectral lines whose equivalent widths are temperature sensitive, notably the hydrogen Balmer lines, which have detected a spectrum of p modes in η Boo (Kjeldsen et al. 1995).

The method used in the Kjeldsen paper works as follows; given that the Balmer line series arises from transitions from the second to higher excited states, the line-width will be dependent on the number of hydrogen atoms in the excited state. This number shows a strong temperature dependence (approximately $n^*_{\mathrm{H}} \propto T^6$ in F and G type stars), and therefore the changes in relative compression caused by modes which result in relative temperature variations (as above) will cause alterations in the equivalent width. Heasley et al. (1996) also suggests the possibility of examining the colour changes of an individual star as a function of time, anticipating that the variation in a broad-band colour index (for example the V-I magnitude) would be comparable in size to intensity fluctuations - of the order of a few parts per million.

Spectrophotometric techniques are useful for ground-based observations as comparisons are made simultaneously between radiation which will have passed through the same pattern of atmospheric disturbances, therefore compensating for scintillation.

3.4 Mode visibility

For a mode to be observed it is required that the mode is present at an appreciable amplitude - i.e., that a particular mode has been excited in the star. A star will have a theoretically infinite number of possible oscillatory modes, of which only a limited number will be excited under the conditions of the stellar interior.

The observing conditions must also permit a particular mode to be observed. This means that the amplitude of the mode when integrated across the visible surface of the body needs to be non-zero. This will depend on both spatial harmonic of the mode itself, inclination of the star, and the nature of the instrument (i.e., whether it observes in intensity or Doppler velocity), and the limb-darkening profile.

3.4.1 Intrinsic selection

There are a theoretically infinite number of eigen-modes possible in a star, however only a fraction of these are available to be excited. For both p and g modes there are limits on the frequency of modes imposed by the physics of the oscillations.

For p modes a lower-limit on frequency comes from the fundamental radial mode. This is the mode in which a single oscillation occurs between core and surface, and as such is the simplest form of oscillation and at the lowest possible frequency for a pressure-restored mode. An upper limit on the frequency of p modes is the acoustic cut-off frequency. For modes at above this frequency, the oscillations will not be trapped in a cavity within the star, but will propagate as travelling waves through the chromosphere.

An upper limit to the frequency of g modes is given by the Brunt Väsälä (see Section 3.5.2

on page 55) frequency. At higher frequencies than this, the motion of material is sufficiently fast in comparison to the restoring force, so as to smooth out any density differentials. Internal gravity modes (g modes) can only be excited for angular degrees of greater than $l = 1$. This is as a gravity mode must feature the motion of material about the centre of gravity.

A mode may be characterised by the inertia of the mode - this is a measure of the energy required to excite and damp an oscillation. This is akin to a fat child versus a thin child sitting on a swing. The fat child requires a greater exertion of force to start in motion than the thin child, but will also require a greater force to stop swinging once in motion. The inertia of a mode will depend upon both the characteristic numbers of the mode (n, l and m), and the internal structure of the star.

Dupret et al. (2009) discuss mode inertia in red-giant stars, and find that for these stars the inertia of $l = 1$ and 2 modes is typically much greater that that of $l = 0$ modes. This is due to mode-mixing between p and g modes, which leads to a much greater energy being required to excite the non-radial modes. One therefore expects to see only those small number of oscillations in which the inertia of the mode is low enough to allow the mode to become excited to an observable amplitude; resulting in a spectrum resembling that of the Sun with well separated $l = 0$, 1 and 2 modes, despite the near continuum of $l = 1$ and 2 oscillations arising from the g modes.

3.4.2 Extrinsic selection

Angular-degree selection

For a slow rotator, the intensity of an observed mode at a given point on the surface of a body is given by the product of the spatial harmonic ($Y_{l,m}$) and oscillation in time (equation 3.6).

$$\begin{aligned} I(\theta, \phi\, t) &= \sqrt{4\pi}\Re\left\{I_0 Y_l^m(\theta,\phi)\exp\left[-i(\omega_0 t - \delta_0)\right]\right\}, && (3.6) \\ &= I_0\sqrt{4\pi}(-1)^m c_{lm} P_l^m(\cos\theta)\cos(m\phi - \omega_0 t + \delta_0), && (3.7) \end{aligned}$$

where $\Re(z)$ is the real part of z, and P_l^m is the Legendre polynomial.

The observed oscillation intensity in Sun-as-a-star and stellar observations (I') will be the average of this expression integrated across the area of the visible disk, A;

$$I'(t) = \frac{1}{A}\int_A I(\theta,\phi,t)\,\mathrm{d}A. \tag{3.8}$$

Since, as yet, the expression is co-ordinate independent, it is convenient for the integration to choose an orientation of axes in which we are observing along the polar axis. Considered qualitatively this means that only modes with no longitudinal nodes (i.e., $m = 0$), in which the entire hemisphere will oscillate in phase, will be observed and so intensity can be represented in the form:

$$\begin{aligned}
I'(t) &= S_l^{(I)} I_0 \cos(\omega_0 t - \delta_0), && (3.9)\\
\text{Where:} \quad S_l^{(I)} &= \frac{1}{\pi}\int_0^{2\pi}\mathrm{d}\phi\int_0^{\frac{\pi}{2}}\sqrt{2l+1}P_l(\cos\theta)\cos\theta\sin\theta\mathrm{d}\theta, && (3.10)\\
&= 2\sqrt{2l+1}\int_0^{\frac{\pi}{2}}P_l(\cos\theta)\cos\theta\sin\theta\mathrm{d}\theta. && (3.11)
\end{aligned}$$

However there is a further subtlety as this does not yet account for the effect of limb darkening. This will act to lower the intensity at large θ when observing along the polar axis, and will in general cause modes of high l to be enhanced in amplitude, while those of low l are suppressed. One can account for limb darkening by adding a limb-darkening function, $W(\theta)$ into our intensity equations.

$$S_l^{(I)} = 2\sqrt{2l+1}\int_0^{\frac{\pi}{2}}W(\theta)P_l(\cos\theta)\cos\theta\sin\theta\mathrm{d}\theta \tag{3.12}$$

The above analysis has been performed for intensity observations, however a similar expression applies for velocity observations, with a modification of an extra factor of $\cos\theta$ due to the projection of motion along the line of sight, resulting in:

$$S_l^{(V)} = 2\sqrt{2l+1}\int_0^{\frac{\pi}{2}}W(\theta)P_l(\cos\theta)\cos^2\theta\sin\theta\mathrm{d}\theta. \tag{3.13}$$

A plot of these response functions for low values of l is seen in figure 3.5. It should be noted that the values are negligible for $l > 4$. Where the S_l value falls below zero this should be interpreted to mean that the signal is in antiphase to that at the reference longitude - i.e. while

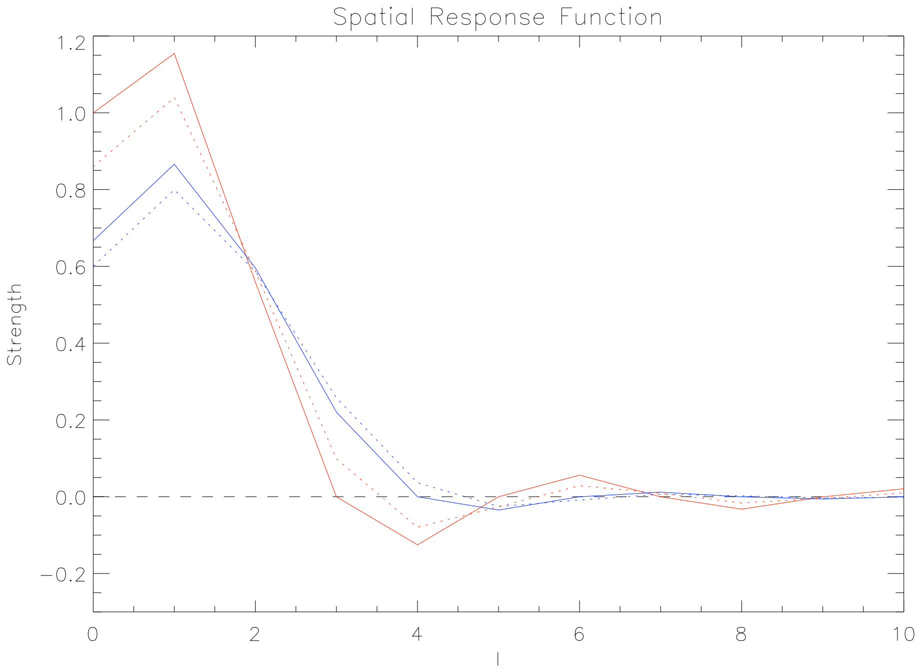

Figure 3.5: Spatial response functions, $S_l^{(I)}$ (red) and $S_l^{(V)}$ (blue) for observation of whole disk integrated intensity and velocity measurements. The dotted lines show the responses where a limb darkening function has been included. This was chosen to be of the form: $W(\theta) = 1 - a_0(1 - \cos(\theta)) - a_1(1 - \cos^2(\theta))$ with $a_0 = 0.75$ and $a_1 = -0.22$, which is quoted for the BiSON network in Christensen-Dalsgaard and Gough (1982).

the reference point is experiencing a maxima, the integrated signal shows a minima.

Inclination selection

To generalise the above result to other inclinations we transform the co-ordinate system of our integral and find that the response can be written as;

$$S'_{lm} = \Gamma_{lm} S_l, \tag{3.14}$$

where Γ_{lm} is the components of the co-ordinate rotation matrix for the relevant mode, given by Gizon and Solanki (2003). This leads to the geometric formula for power $\epsilon_{l,m}(i)$ in a mode being given by the expression:

$$\epsilon_{l,m}(i) = \frac{(l - |m|)!}{(l + |m|)!} \left[P_l^{|m|}(\cos i) \right]^2 . \tag{3.15}$$

The results of Equation 3.15 for all inclination angles is shown in Figure 3.6. In the case of the Sun, in which one observes along the stellar equator ($i = 90°$), this gives a simple formulation

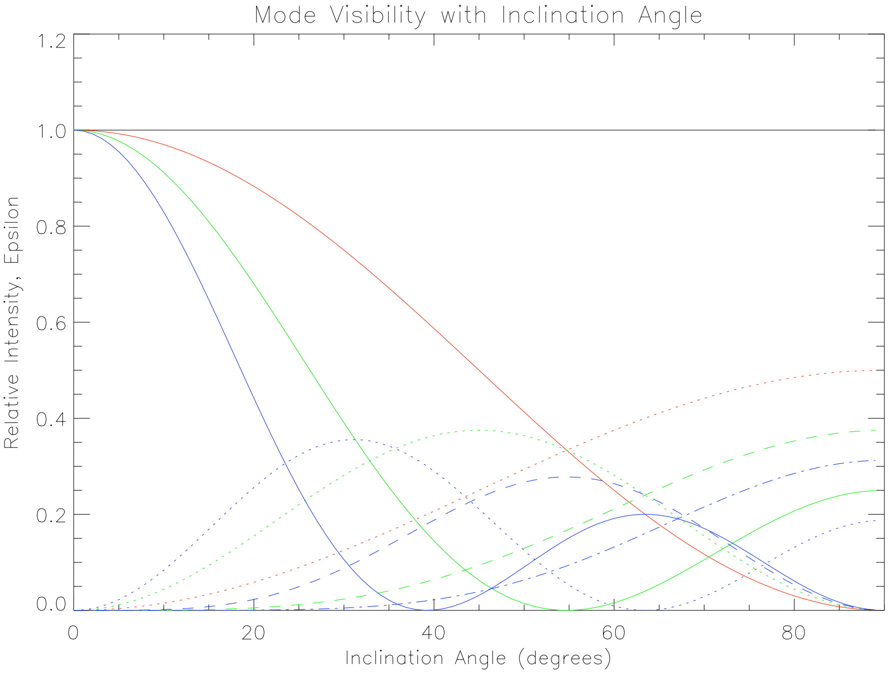

Figure 3.6: Visibility of modes from $l = 0$ to $l = 3$ with inclination angle; colours signify values of l: black - 0, red - 1, green - 2, blue - 3; line styles signify value of m: solid - 0, dotted - 1, dashed - 2, dot-dashed - 3

for which modes are visible; those in which the sum of l and m is even.

Gizon and Solanki propose using the differences in response function to determine the inclination of stars in which modes are observed. To date, no sufficiently high-quality data on the modes of stars have been produced, as to be able to determine the inclination where this is not already known.

3.5 Scaling laws

When attempting to observe modes in other stars it is often useful to have some idea about what values are taken by the parameters describing these modes. For instance it is not useful to attempt to observe oscillations in a main-sequence star with data on a 100 minute cadence, as the periods of around five minutes in these stars will be above the Nyquist frequency. Similarly to look for solar-like oscillations in data with a one-per cent white noise background is unlikely to provide positive results as such modes are anticipated to have amplitudes of only a few parts-per-million.

Using basic physical principles it is possible to scale from the known frequencies and amplitudes in the Sun to other stars. Expressions for amplitudes are based upon the assumption that modes are excited by similar processes to those which excite solar modes, which will not be the case in κ mechanism excited oscillations, however the expressions for frequency should be common to all p-mode oscillations.

3.5.1 Amplitudes

Let $\delta L/L$ be the fractional variation in the luminosity of the star due pulsation. In Sun-like oscillations the change in radius will be negligible, thence this will almost wholly be down to changes in temperature, $\delta T/T$. Assuming that oscillations are adiabatic, changes in temperature will scale with relative compression (the most compressed regions being the warmest), $\delta\rho/\rho$.

$$\frac{\delta L}{L} \propto \frac{\delta T}{T} \propto \frac{\delta \rho}{\rho}. \tag{3.16}$$

The density compression for an adiabatic sound wave in a medium with a sound speed c_s is given by $\delta\rho/\rho = v/c_s$, where v is the velocity of the gas. When considering oscillations in Doppler velocity this determines the amplitude that we observe, $v_{obs} \propto v$.

The adiabatic sound speed can be estimated using the equation:

$$c_s^2 = \left[\frac{\partial \ln P}{\partial \ln \rho}\right]_{\text{adiabatic}} \frac{P}{\rho}. \tag{3.17}$$

For a fully ionised gas the adiabatic gradient, $[\partial \ln P/\partial \ln \rho]_{\text{adiabatic}}$ takes a constant value of 5/3. The assumption of a constant value holds for the outer parts of cool stars, fortuitously the region in which most observed solar-like modes have greatest amplitudes. Thence from the ideal gas law, $P \propto \rho T$ one can determine a relation between oscillations amplitude in intensity and velocity:

$$\left(\frac{\delta L}{L}\right) \propto \frac{v_{\text{osc}}}{T_{\text{eff}}^{1/2}}. \tag{3.18}$$

Kjeldsen and Bedding (1995) test the above expression with 90 oscillating stars, including β Cephei, δ Scuti, δ Cephei and RR Lyrae stars, they determine that a better fit to the data is found where the exponent of the effective temperature (-1/2 above) is -1. They suggest that this is due to the simplistic adiabatic description of the stellar atmosphere not accounting fully for temperature variations. A further possibility is the influence of radius variations which will not be negligible for the classical pulsators used for calibration. This modification results in the following expression, calibrated from the Sun, relating velocity and luminosity intensities;

$$\left(\frac{\delta L}{L}\right) = \frac{v_{\rm osc}(\text{in ms}^{-1}\ )}{T_{\rm eff}/5777\ \text{K}} 17.7\ \text{ppm}. \tag{3.19}$$

As a final calibration, the velocity amplitude predicted from models of solar-like oscillations, taken from Christensen-Dalsgaard and Frandsen (1983), are fitted by Kjeldsen and Bedding (1995) resulting in a relationship of $v_{\rm osc} \propto L/M$, which, once again calibrating from the Sun, results in:

$$v_{\rm osc} = \frac{L/L_\odot}{M/M_\odot}(0.23 \pm 0.014)\ \text{cm s}^{-1}, \tag{3.20}$$

$$\Rightarrow \quad (\delta L/L) = \frac{(L/L_\odot)}{(M/M_\odot)\,(T_{\rm eff}/5777\ \text{K})}\ 4.1 \pm 0.3\ \text{ppm}. \tag{3.21}$$

Samadi et al. (2005) comment that an exponent of 0.7 provides a better fit to contemporary amplitudes of solar-like oscillations. In this case the above expression would become:

$$(\delta L/L) = \left(\frac{L/L_\odot}{M/M_\odot}\right)^{0.7} (T_{\rm eff}/5777\ \text{K})^{-1}\ 4.1 \pm 0.3\ \text{ppm}. \tag{3.22}$$

3.5.2 Frequencies

Oscillations in the Sun occur over a broad range of frequencies, with the profile of mode amplitudes being described by a broad envelope of roughly Gaussian or Lorentzian form.

The locations of modes in frequency are characterised by a number of parameters;

- The range of frequencies in which modes may theoretically be observed. For p modes this has both an upper limit in the acoustic cut-off, and a lower limit in the frequency of the fundamental radial mode. For g modes this has an upper limit in the BruntVäisälä frequency.

- The frequency at which the highest amplitude modes are observed. In the case of solar-like p modes it is known as $\nu_{\rm max}$ and related to the acoustic cut-off frequency.

- The spacings between modes of different radial order, angular degree, and rotational order (the ‘large’ and ‘small’ frequency spacings, and ‘rotational splittings’; see Section 3.1.1 on page 35).

Acoustic cut-off frequency and $\nu_{\max}$

A sound wave is fundamentally a periodic pattern of compression and rarefaction occurring in a medium. These waves travel at the local sound speed. Where the medium is able to flow, it will naturally readjust in order to smooth out this pattern. Should the time-scale over which this readjustment occurs be shorter than the period of the wave, then the compression will be smoothed out prior to passage, and the wave will be unable to propagate.

The multiplicative inverse of the timescale for this adjustment is expressed as a parameter known as the acoustic cut-off frequency, and as well as acting as an upper limit on p-mode frequencies, it also acts to determine the limits of the cavity in which the waves propagate.

$$v_{\mathrm{ac}} = c_s/H_P, \tag{3.23}$$

where c_s is the sound speed, and H_p is the pressure scale height of the atmosphere. We may expect that $H_P \propto T/g$ where composition is constant, and $c_s^2 \propto T$ where the material is a fully ionized ideal gas. Assuming an isothermal atmosphere at $T = T_{\mathrm{eff}}$, which will be the case as modes are observed near the surface, we have:

$$v_{\mathrm{ac}} = g/\sqrt{T_{\mathrm{eff}}} \tag{3.24}$$

As the acoustic cut-off frequency also defines a typical timescale for the atmosphere, it has been argued that the frequency of maximum power in the oscillations (hereafter referred to as $\nu_{\max}$) should scale in other stars with ν_{ac}; i.e., $\nu_{\max}/\nu_{ac} = \nu_{\max,\odot}/\nu_{ac,\odot}$. Therefore, one should be able to scale from the Sun ($\nu_{\max} \approx 3050$ μHz) to predict the frequency of maximum power for an arbitrary star:

$$\nu_{\max} = \frac{M/M_{\odot}}{(R/R_{\odot})^2\sqrt{T_{\mathrm{eff}}/5777K}}\, 3050\mu\mathrm{Hz}. \tag{3.25}$$

Using our expression for the spacing between adjacent radial modes, the large frequency spacing (see below), we can use this expression to predict the radial overtone of the mode of maximum power:

$$n_{\max} \approx \left(\frac{M/M_{\odot}}{(T_{\rm eff}/5777K)(R/R_{\odot})}\right)^{0.5} \times \frac{3050\ \mu\text{Hz}}{134.9\ \mu\text{Hz}}, \tag{3.26}$$

Here we have assumed that the asymptotic relationship between mode spacings applies across all radial order. We know that this relationship can break down for modes of low radial order where the spacings between modes can be greater than the asymptotic large frequency spacing, and indeed for the Sun this equation yields a value of 22.6 when the maximum power is in fact seen for $n \approx 21$ Assuming that a simple factor can be subtracted from the equation to correct for this effect, we can correct the above expression to the form:

$$n_{\max} \approx \left(\frac{M/M_{\odot}}{(T_{\rm eff}/5777K)(R/R_{\odot}}\right)^{0.5} \times 22.6 - 1.6. \tag{3.27}$$

Dynamical time scale and the fundamental radial mode

The dynamical time-scale is the length of time required for a change in the structure to be communicated across the body. A change in stellar structure may only be conveyed by means of an acoustic wave travelling at the speed of sound within the stellar medium, so the dynamical time-scale may be given by:

$$t_{\rm dyn} = \int\limits_{r=0}^{R} \frac{\mathrm{d}r}{c_s}. \tag{3.28}$$

The dynamical time scale will be approximately equal to the period of the fundamental radial mode of the star, i.e the oscillation with only a single radial node (in which all radii are moving in phase). The frequency of the fundamental radial mode is proportional to the spacing between adjacent radial modes, so ultimately large frequency spacing will be proportional to the the dynamical time scale.

The dynamical time-scale may be derived by a number of different methods; the method presented here formally calculates the free-fall time-scale. This is the time a particle would take to fall through a gas cloud of the same size and density of the body in the absence of internal pressure forces. This will differ from other determinations only in terms of a numerical constants.

Consider a particle of mass m sitting at a radius of r within the body of a star. If all internal pressure forces were absent, this will experience an acceleration solely due to gravitational attraction of:

$$m\frac{\mathrm{d}^2r}{\mathrm{d}t^2} = -\frac{m\mathrm{G}M(r)}{r^2}; \tag{3.29}$$

where $M(r)$ is the mass contained within a radius r, which may be approximated by assuming the density is constant at the mean density, $\langle\rho\rangle$;

$$M(r) = \int\limits_0^r \rho(r)\mathrm{d}r \sim \frac{4\pi\langle\rho\rangle r^3}{3} \tag{3.30}$$

and all other symbols have their usual meanings. Simplifying Equation 3.29, and substituting for $M(r)$ gives:

$$\frac{\mathrm{d}^2r}{\mathrm{d}t^2} = -\frac{4\pi\langle\rho\rangle\mathrm{G}}{3}r. \tag{3.31}$$

We can recognise the above as the equation for simple-harmonic-motion, with a frequency of:

$$\omega^2 = \frac{8\pi\langle\rho\rangle\mathrm{G}}{3}, \tag{3.32}$$

and a period of,

$$P = \sqrt{\frac{3\pi}{2\langle\rho\rangle\mathrm{G}}}. \tag{3.33}$$

The time taken for a particle to fall from the surface to the centre of the star, i.e., the free fall time, will be one quarter of this, giving us:

$$t_{\mathrm{freefall}} = \frac{1}{4}\sqrt{\frac{3\pi}{2\langle\rho\rangle\mathrm{G}}}, \tag{3.34}$$

and that therefore:

$$t_{\mathrm{dyn}} \propto \langle\rho\rangle^{-1/2}. \tag{3.35}$$

As we have stated, the spacing between adjacent radial modes - the large-frequency spacing - will be proportional to the dynamical timescale. We can derive an expression for the spacing by scaling from the Sun ($\Delta\nu = 134.9\ \mu$Hz), using the $t_{\mathrm{dyn}} \propto 1/\sqrt{\rho}$ relation;

$$\begin{aligned}
\Delta\nu &\propto \sqrt{\rho}, && (3.36)\\
\Delta\nu &\propto \left(\frac{M}{R^3}\right)^{\frac{1}{2}}, && (3.37)\\
\Delta\nu &= \frac{(M/\mathrm{M}_\odot)^{(1/2)}}{(R/\mathrm{R}_\odot)^{(3/2)}}\ 134.9\mu\mathrm{Hz}. && (3.38)
\end{aligned}$$

Brunt-Väisälä frequency The Brunt-Väisälä, or buoyancy frequency (N) is the frequency at which a vertically displaced parcel of gas will oscillate within an atmosphere which is stable against vertical motions. It acts as an upper limit on the frequency of g modes.

Consider a parcel of gas displaced from the level of its equilibrium density, ρ_0, to a new vertical level at ρ_1. Two forces will be acting upon this parcel, gravity $F_{\mathrm{grav}} = -g(r)\rho_0 V$ and buoyancy $F_{\mathrm{buoy}} = g(r)\rho_1 V$. For a parcel of gas, or given size V:

$$\begin{aligned}
F(r) = F_{\mathrm{grav}}(r) + F_{\mathrm{buoy}}(r) &= -g(r)(\rho_0(r) - \rho_1(r)), && (3.39)\\
\text{but: } \rho_1(r) &= \rho_0 + \delta\rho(r), && (3.40)\\
\text{and: } \delta\rho(r) &= \frac{\mathrm{d}\rho}{\mathrm{d}r}.\delta r, && (3.41)\\
\text{so: } F(r) = \rho_0\ddot{\delta r} &= g(r)\delta\rho(r) = g(r)\frac{\mathrm{d}\rho}{\mathrm{d}r}.\delta r && (3.42)\\
\text{thence: } \ddot{\delta r} &= \frac{g(r)}{\rho_0}\frac{\mathrm{d}\rho}{\mathrm{d}r}\cdot\delta r. && (3.43)
\end{aligned}$$

Which we can identify as the equation for simple-harmonic motion, $\ddot{x} = -\omega^2 x$, with a frequency of:

$$\omega = \sqrt{\frac{g(r)}{\rho_0}\frac{\mathrm{d}\rho}{\mathrm{d}r}}, \tag{3.44}$$

$$\Rightarrow \nu_{\mathrm{BV}} = \frac{1}{2\pi}\sqrt{\frac{g(r)}{\rho_0}\frac{\mathrm{d}\rho}{\mathrm{d}r}}. \tag{3.45}$$

3.5.3 Other parameters

Rotational period

Rotation can be a cause of variability in certain classes of stars (see Section 2.8.1 on page 21), but even where rotation is not suspected to be the mechanism behind variability, the rotational splittings, ν_m (between components of a mode of a single angular degree, l, but different rotational order, m) are inversely proportional to the rotational period.

Although we may often choose to think of the rotational period as a single value, the Sun shows a period of rotation which varies with both latitude and depth.

For low mass ($M < 1.3\mathrm{M}_{\odot}$) stars on the main sequence, Cardini and Cassatella (2007) give relationships between rotational period, P_{rot} and mass for three open clusters which span a reasonably wide range of ages. For the Hyades they find that P_{rot} can be linearly correlated with stellar mass ($P_{\mathrm{rot}} = 26.9 - 19.2(M/\mathrm{M}_{\odot})$), while for the Pleiades and IC 2602 similar linear relationships define an approximate upper limit to the rotational period.

Considering giant stars, we may attempt to make the approximation that both mass and angular momentum are conserved in the evolution from main-sequence to giant stars. From the expression for angular momentum, $L \propto MR^2/P$, we can then scale from the Sun to give:

$$P_{\mathrm{rot}} = P_{\mathrm{rot},\odot}\left(\frac{R}{\mathrm{R}_{\odot}}\right)^2 \text{ (Giant stars)} \tag{3.46}$$

However this gives rotational periods of the order of many thousands of days, which is not in agreement with observational determinations of rotational periods, which are typically of the order of a few hundred days.

This anomaly may be explained by noting that the core of a giant star is much more dense than the surface, and will contain a majority of the stellar mass. Our assumption of a giant star as being a solid body of homogenous radius is therefore not justifiable. A better approximation can be obtained by assuming that the surface layers of a giant star will rotate at the same velocity as those of a star on the main sequence of the same mass. The rotational period may then be obtained by scaling up to the radius of the giant star. This will not violate the conservation of angular momentum due to the inhomogenous structure noted above.

$$P_{\mathrm{rot,M.S.}}(M) = \mathrm{P}_{\mathrm{rot},\odot}\left(\frac{M}{\mathrm{M}_\odot}\right) \text{ (main-sequence stars)}, \tag{3.47}$$

$$\Rightarrow P_{\mathrm{rot,Giant}}(M) = \mathrm{P}_{\mathrm{rot,M.S.}}\left(\frac{R}{\mathrm{R}_\odot}\right) \text{ (Giant Stars)}, \tag{3.48}$$

For Arcturus ($M \approx 0.8M_\odot$, $R \approx 25R_\odot$) this predicts a rotational period of the order of 500 days, in closer agreement than Equation 3.46 with studies which suggest the period to be of the order of 2 years (Gray and Brown 2006)

3.6 Helio- and asteroseismic observatories

3.6.1 Ground-based observatories

Ground-based observations have been extensively used throughout the history of helio and asteroseismology, despite the difficulty of keeping an object under continual observation due to the rotation of the Earth. The lower costs and ability to easily maintain and upgrade instruments make ground-based observatories attractive even today.

Due to atmospheric scintillation ground-based observatories will typically detect oscillations through Doppler-velocity measurements. Doppler velocity also has a substantially lower signal-to-noise in most cases than comparable photometric data.

BiSON network

The BiSON Network (Chaplin et al. 1996) has been in operation since 1975 and consists of six stations located around the world so-as to be able to achieve near continuous monitoring of the Sun. Each instrument consists of a resonant-scattering spectrometer viewing a Potassium spectral line.

BiSON data are collected at 4-second cadence, and integrated into 40-second datapoints.

Over the long-term fill has averaged around 80% (Chaplin 1997).

SONG network

The SONG (Stellar Oscillations Network Group) (Grundahl et al. 2006) is a proposed global network of one-meter robotic telescopes, intended to be constructed over the next decade for the purposed of asteroseismology and studies of extrasolar planets. The planned instrument is a high-resolution spectrograph, with a facility to include further instrumentation.

It is hoped that the SONG network will enable objects to be observed with a high-duty cycle over long (months) periods of time. It is planned that for objects within 30 degrees of the celestial equator 85% fill is achievable, with data collected at a cadence which may be varied dependent on the object under observation.

3.6.2 Space-based observatories

Space-based missions have the advantage of often being able to keep an object under observation for longer periods than a ground-based observatory, and also to avoid atmospheric scintillation.

Due to the relatively low cost, and ability to monitor a large number of objects simultaneously, photometry measurements from CCDs are typically used in space-based observatories.

MOST

The MOST (Microvariability and Oscillations of Stars) (Walker et al. 2003) space telescope was launched in June 2003. It consists of a 15 cm collecting mirror, projecting onto a 1024×1024 CCD camera, with a single broadband filter which transmits light in the range 350-700 nm.

MOST has been used extensively for the study of variability across the HR diagram. Probably the more interesting and controversial of MOST results was the initial null-detection of asteroseismic variability in the slightly-evolved main-sequence star Procyon (α CMi, HIP 37279, HD 61421) (Matthews et al. 2004). As oscillations of Procyon in Doppler velocity were later detected by Arentoft et al. (2008), this prompted re-evaluation of the scaling between Doppler and photometric amplitudes. These discussions have largely been resolved by a lowering of the noise level in MOST, who in their latest data can see a power-excess in the appropriate region, but still no individual modes of oscillation (Guenther et al. 2008).

CoRoT

The CoRoT (Convection, Rotation and planetary Transits) (Baglin et al. 2006) is a joint CNES and ESA mission is a space mission intended to detect extrasolar planets by means of the transit method, and for asteroseismology.

CoRoT observes two circular regions of roughly 12 degrees radius the sky (the 'eyes of CoRoT'), located at approximately 6 and 18 hours right-ascension, where the galactic plane intersects the celestial equator. The CoRoT instrument consists of four CCDs, two extrasolar planet fields, and two asteroseismology fields. In the seismology fields up to 10 stars of between magnitude 6 and 9.5 are monitored, and in the exoplanet fields up to 12 000 stars of between magnitude 11 and 16 are monitored. Seismology field observations are made at 1 second cadence, integrated onboard into 32 second observations. Exoplanet field observations are made at a cadence of either 32 seconds (for a limited number of stars) or 512 seconds.

As of June 2008, the CoRoT mission had observed 50 objects in the seismology field, including solar-like pulsators, F and K giant stars, eclipsing binaries and β Cephei and γ Doradus variables. Stars in the field have also been subject to a period-search, in an endeavour to find for new variable stars (Michel et al. 2008). In addition the exoplanet field has been used to detect oscillation in red-giant stars (Hekker et al. 2009), and to automatically identify many oscillating stars (Debosscher et al. 2007 2009).

Kepler

The JPL-NASA space mission Kepler is primarily intended to detect telluric ('Earth-like') extrasolar planets by means of the transit method (Borucki et al. 2007). Access to these data for the purposes of asteroseismology has been negotiated by a group known as the Kepler Asteroseismic Science Consortium (Christensen-Dalsgaard et al. 2009).

The Kepler spacecraft was launched on March 7, 2009. Kepler will constantly monitor a region of approximately 12 degrees square, just above the galactic equator in Cygnus (Figure 3.7). Around 400 000 stars will initially be monitored for fluctuations in brightness, dropping down to 100 000 stars by the end of the nominal mission duration of 3.5 years. The first data was released to the KASC on Thursday 27 August, 2009[3].

---

[3] Due to data policies of the KASC, no illustrative data may be included in this thesis

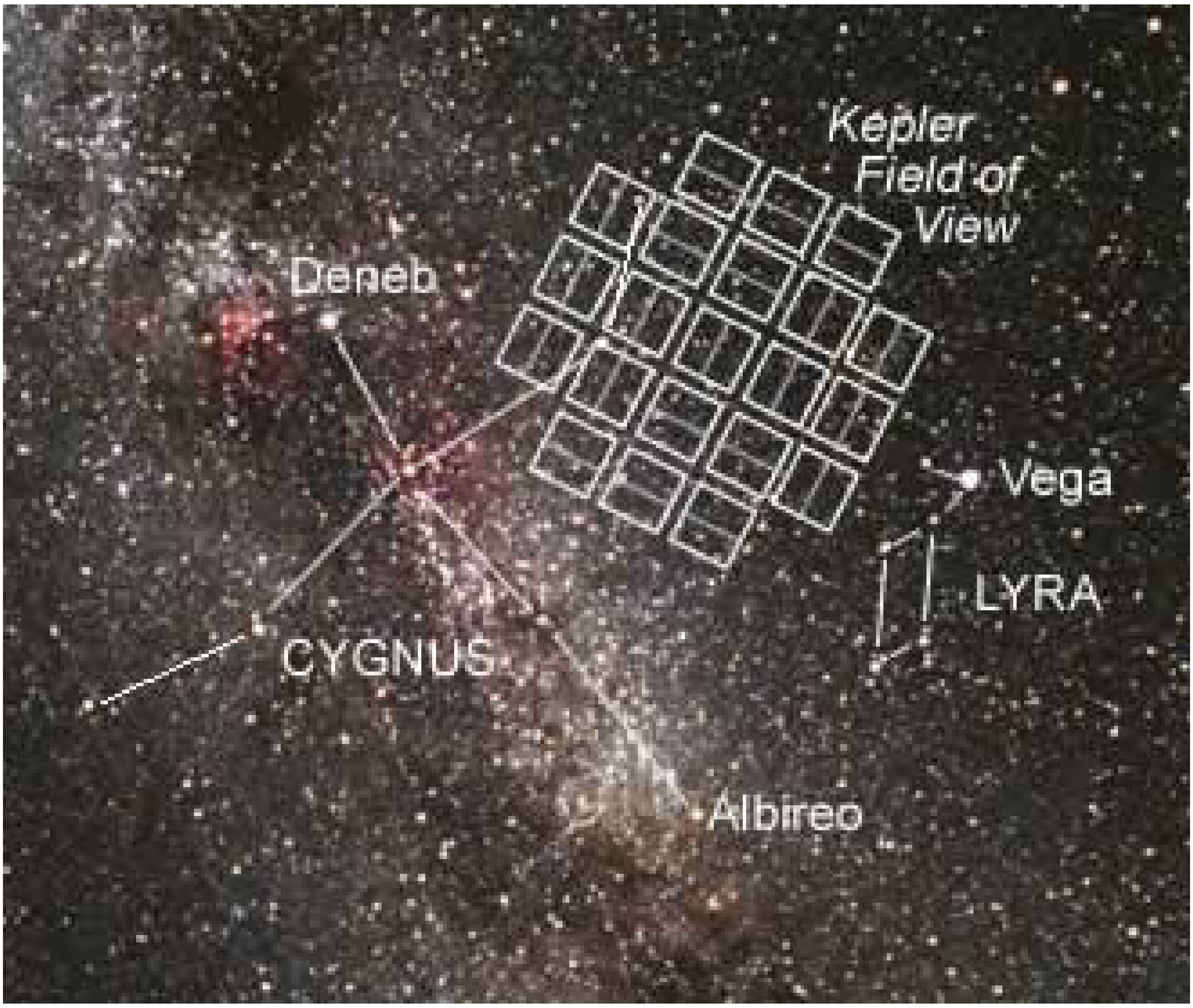

Figure 3.7: The Kepler field of view, showing the relative location of each of the 42 individual CCD images (Koch and Gould 2007).

Data will be collected on all stars at a cadence of 30 minutes, with certain target stars being selected for observation at 1-minute cadence. The asteroseismology targets of Kepler cover almost all regions of the colour-magnitude diagram. It is expected that Kepler will increase by an order-of-magnitude the number of main-sequence stars for which a large number of solar p modes have been observed.

Chapter 4

SMEI

The primary data used in this thesis are photometric timeseries from the Solar Mass Ejection Imager (SMEI) instrument.

Sections 4.1 through 4.2 on page 65 describe the instrument and primary stages of the initial science frame processing pipeline. These sections consist mainly of work done by other individuals, in particular Steve Spreckley who developed the initial frame processing pipeline.

Section 4.3 on page 67 describes the steps which have been taken to verify the quality of the data, and to identify any anomalies which occur within SMEI timeseries data.

Section 4.4 on page 84 describe studies of stellar variability and asteroseismology which have been done by others to date with SMEI, both using the pipeline referenced in this chapter, and using a pipeline developed independently.

Asteroseismology results from SMEI will be reported on in subsequent chapters.

4.1 The instrument

The Solar Mass Ejection Imager (SMEI) is an all sky photometer carried aboard the Coriolis satellite. The primary science goal of the instrument was to observe coronal mass ejections (CMEs) and other eruptive events; more specifically to image through means of Compton-scattered light Earthbound events that traditional coronographs are largely unable to observe. Results from these observations may be used for predictions of potentially damaging space-weather events a few days prior to such an event reaching the Earth, and the primary goal of the SMEI mission has been to evaluate the usefulness of remote sensing of the heliosphere as a tool in making such forecasts.

SMEI was designed and built by members of the University of California, San Diego (UCSD), the University of Birmingham, the Rutherford Appleton Laboratories (RAL), and the United

States Air Force Research Laboratory (AFRL). Continued operations have been co-ordinated in a weekly teleconference between members of the SMEI team located at AFRL, UCSD, the University of Birmingham, RAL and Boston College.

Eyles et al. (2003) may be consulted for further details and technical specifications regarding the SMEI instrument. For specifics regarding the use of SMEI in stellar photometry, Spreckley (2008) provides a comprehensive description of the data extraction and processing undertaken.

4.1.1 Coriolis and WindSat

The Coriolis satellite was launched on 2003, January 6 from Vandenberg Air Force Base in Santa Barbara County, California, entering regular science operation mode one month later. The satellite is in an 800 km, circular, sun-synchronous polar orbit with an orbital period of 101 minutes.

In addition to the SMEI instrument, Coriolis also provides a platform for the AFRL/NRL (Naval Research Laboratory) 'WindSat' experiment. This is a demonstration project intended to measure ocean and surface wind speed and direction by means of a polarimetric radiometer.

4.1.2 Camera construction

The optical component of the SMEI instrument is composed of three near identical camera systems, each with a $60^\circ \times 3^\circ$ field of view. The cameras are aligned such that the instantaneous total field of view approximates a strip of sky of size $170^\circ \times 3^\circ$. This strip will co-rotate with the satellite, and by using data from the three cameras a near complete image of the sky is obtained once per orbit, with an exception being the region directly towards the Sun, and a small region in the anti-solar direction.

The faint nature of CMEs required SMEI to provide 0.1% relative photometry over a $1^\circ \times 1^\circ$ field at 90° elongation from the Sun. This required a reduction in the stray light from the Sun, Earth and Moon by a factor of 10^{15} relative to the brightness of the solar disc. The reduction was achieved by a baffle in front of the SMEI optics chamber, and suitable placement of the components within the optics chamber, resulting in a stray light signal of less than 1 Analogue to Digital Unit (ADU). The precise design of the instrument was a key factor in being able to achieve high-quality stellar photometry, and to ensure that milli-magnitude point-to-point

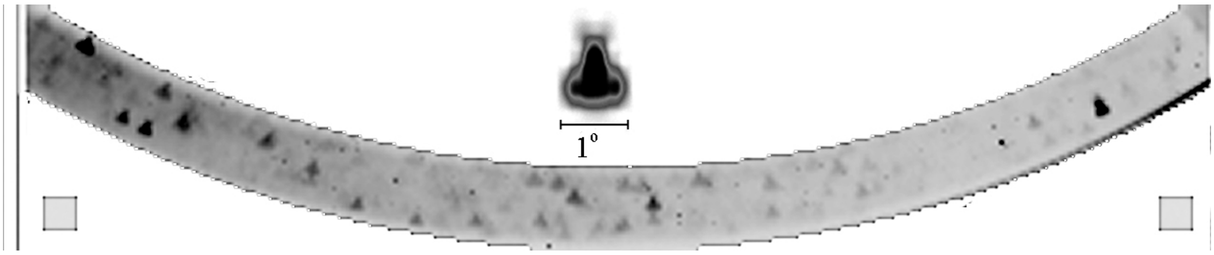

Figure 4.1: A single science frame from SMEI. The PSF is illustrated above the image. The image here is a photographic negative, hence stars appearing dark and the background light.

precision was achievable for the brightest stars ($M < 2$).

After launch it was discovered that there was a stray light path into the optics box which allowed for a significant level of light to reach the CCD. A correction to the data is applied in the frame processing pipeline in order to remove this contribution.

The CCDs used in the SMEI cameras each have an image area of 1242 pixels, with one partially covered pixel at the end of each image row, plus 20 columns of underscan pixels, and 8 columns of overscan pixels at the other, giving a total of 1272 columns of pixels. The optical system is unfiltered, and therefore the bandpass is dictated by the spectral response of the CCD. This shows a peak in quantum efficiency of 45% at 700 nm, and has a roughly triangular form, falling to 10% at approximately 460 nm and 990 nm.

The SMEI image is projected onto the CCD in an arc shape with a radius of around 1200 pixels and a width of 92 pixels, meaning that images only cover roughly one sixth of the total pixels. Columns at the edge of each image are used to store dark-current only, and allow for the variable dark current signal to be calibrated and subtracted from the image.

Due to telemetry constraints it is not possible for full-resolution images from the SMEI cameras to be downloaded. Therefore images from Camera # 1 and #2 are usually binned by a factor 4×4 such that the final images are 318×64 image bins with a bin size of $\approx 0.2° \times 0.2°$. Camera # 3 bins are only binned by a factor of 2×2, however this camera has not been used for stellar photometry due to hot pixels and a higher background level. These binned images will be henceforth referred to as 'science frames'. A single SMEI science frame is shown in Figure 4.1.

Point spread function

A consequence of the unique optical design of the SMEI cameras is the unusual shape of the point-spread-function (PSF), which has been likened to a fish, nose, or angel (see Figure 4.1, 4.2).

Figure 4.2: A high resolution of the usual SMEI PSF. The image of an unresolved point object is smeared over around 250 pixels. This image is a 50 × 50 pixel cut from an engineering mode frame in which the image is unbinned. Images are typically binned by a factor of 4 × 4 to generate science frames.

For a point-source the PSF covers about 25 bins in a science image for a bright star. The shape of the PSF also varies as a function of position in the field of view, rotating such that the axis of symmetry is always approximately perpendicular to the arc of the field of view at the position of the star. As well as the rotation, the PSF shrinks as it moves through the field of view in the narrower dimension, and varies slightly in width as it crosses the wide axis of the field of view.

As each pixel corresponds to a 0.05° × 0.05° region of the sky, a bright star covers a sky area of approximately 1 square degree. This leads to confusion noise in regions which have a high density of stars, such as the Galactic plane, and for any stars within clusters such as the Pleiades.

4.1.3 Post launch events

In the week of 2005, April 25 parts of the instruments aboard Coriolis were reaching critical temperature limits after diagnostic tests were performed in an attempt to resolve a technical issue with the WindSat instrument. As a consequence the vehicle was commanded to enter a Sun-pointing mode of operation rather than the normal reference-point mode. This change of pointing modes successfully brought the WindSat temperatures back within safe limits.

The SMEI instrument failed during the month of April 2006, the failure lasting for over a

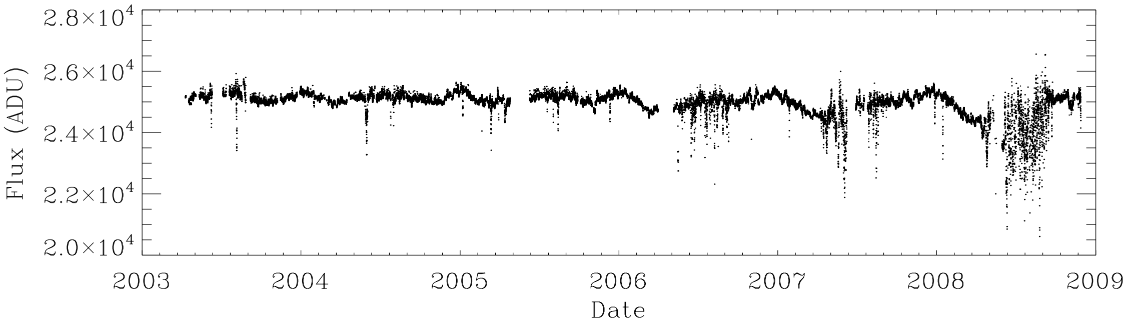

Figure 4.3: Data on β UMi, a K4III, magnitude 2 star. A significantly greater scatter can be seen in the middle months of the year following April 2006, following several issues with the instrument. An annual periodicity can be easily observed in the data, see Section 4.3.4 on page 74 for more details. The asteroseismology of β UMi is reported on in section 6.2 on page 134.

month. A gap is therefore present in all datasets at this time.

These failures have significantly impacted on the quality of data that have been returned from the SMEI instrument. The timeseries of β UMi (HIP72607) is shown in Figure 4.3. A significantly greater scatter can be seen in the data in the middle months of 2006-2008, relative to the same time in 2003-2005.

In October 2008, it was decided that new SMEI data would no longer be archived after December 2008 at Birmingham. Therefore the longest duration timeseries used in this thesis will run to approximately 5 years and 9 months (2 100 days).

4.2 Data reduction pipeline

The data reduction pipeline for SMEI stellar photometry used to generate the data in this thesis was developed during the PhD of Spreckley (2008). The main steps of the pipeline are: the recognition of bad frames; the selection of frames containing the target star (conventionally known as astrometry); image preparation; photometry, and post-processing correction. The final light-curves contain a source of noise whose origin has not been identified, and is removed in post-processing.

The first stage in data processing is to remove those frames in which no data were collected: i.e., those in which the camera shutter was not open or the internal LED (used to check the flat-field of the CCD) was switched off; and to confirm that the image was in “science format” (that is to say, the 4 × 4 binning had been applied).

Next, poor quality frames are identified. Those in which CCD temperature was outside of the range of −60° to −24° are excluded to avoid using frames with high dark current. The SMEI instrument continues to operate during passage though the South Atlantic Anomaly (SAA), and Auroral regions, meaning that certain frames suffer from an excess of cosmic rays. The test for cosmic rays is performed by simply noting those frames in which there are an excess of spikes at greater than 6σ.

In order to produce a photometric timeseries, it is necessary to determine which stars are in the field of view of a given SMEI frame, or conversely in which frames a given star will appear. Due to the complicated nature of the SMEI optics (which produce an arc shaped image), and the fact that each frame will be centred at a different point in both right-ascension and declination, this process is not straightforward.

An initial rough location of each frame is determined by taking sixteen positions at a regular spacing along the image. The sky co-ordinate of each of these positions is determined by using two sets of quaternions, the first describing the attitude of the satellite in three dimensional space, and the second describing the orientation of the camera with respect to the satellite.

This method yields star centroids to an accuracy of roughly 0.2 bins in the science image. This accuracy is limited by the pointing knowledge of the Coriolis satellite, which corresponds to roughly 0.1 bins, smearing of the PSF by small offsets in position introduced by motions of certain satellite components and a small offset which may be introduced by the on board re-binning of the data. For this reason an additional centroiding step is carried out before photometry is performed. A number of different methods of centroiding are used, with the one that yields the lowest scatter on the data being chosen for the final light-curve.

Data obtained from three distinct revisions of the pipeline have been used in this thesis;

Revision one of the pipeline dates from mid 2006, and has only been used to generate some of the Arcturus data highlighted later.

Revision two of the pipeline dates from May 2007 and three-year datasets on a large number of stars are available from this pipeline. This revision of the pipeline was used for a majority of initial studies of stars, and has been used in Section 4.3 to verify the quality of the data. Between revision one and two extensive changes were made to the pipeline, primarily involving the centroiding and pointing accuracy of the instrument. These have resulted in a significantly lower point-to-point scatter in this, and later revisions.

Revision three of the pipeline dates from December 2008 and in general is only used to generate the five year datasets where interesting results have been noted in a three-year dataset. Between revisions two and three changes were made to the dark-current subtraction, as well as some other minor tweaks to the pipeline.

4.3 Data Quality and verification

The aims of this section will be to answer the questions:

- What quality (point-to-point scatter) can we expect to get for a given star in the SMEI data?
- Do the data follow the statistics we expect?
- Can we trust signals seen in the data - does the instrument or processing pipeline introduce any periodic noise?
- What is the best way to represent the instrumental background?

In order to facilitate verification a selection of photometric-reference stars, that is stars which are not known or suspected to show variability, was obtained from Budding and Demircan (2007, p.207). Of the fourteen stars listed, nine had SMEI data readily available. In forthcoming sections these stars will be referred to as the ‘photometric-reference stars’, and used where a constant luminosity source is required.

4.3.1 Point-to-point scatter

It is common to express the quality of a timeseries as a point-to-point scatter. This is the scatter remaining on data when any underlying trend - be it stellar or long-term instrumental effects - has been removed from the timeseries. A point in this context is a single datum, i.e., a single collection of data taken once per orbit. The point-to-point scatter measures the statistical error which may be associated with a data-point, i.e excluding any systematic errors that cause a constant offset in the value recorded.

Table 4.1: The 'photometric-reference stars' sample. Taken from Budding and Demircan (2007, p.207). Data on Vmag, RA and Dec were taken from the SIMBAD catalogue. The 'Lump' refers to the anomalous feature noted in Section 4.3.6 on page 78.

Hip Num	Vmag	RA (ICRS)	Dec (ICRS)	Lump observed?
74605	5.10	15 14 38.3	+67 20 48.2	No
83947	5.075	17 09 33.2	+40 46 37.3	No
89246	6.256	18 12 42.6	+41 08 48.6	No
89348	5.03	18 13 53.8	+64 23 50.2	No
90052	5.981	18 22 35.3	+12 01 45.8	Yes
90844	5.947	18 31 57.0	-01 00 10.7	Yes
91499	6.384	18 39 36.9	+05 15 51.4	Yes
93138	6.217	18 58 23.7	+06 14 23.7	Yes
94916	6.316	19 18 52.8	+09 37 05.1	No

A lower-limit to the point-to-point scatter comes from the photon shot noise - the variability associated with the discrete nature of the light being received by the instrument, i.e., consisting of single photons. These will follow Poisson statistics, such that the scatter on N received photons will be $\sqrt{N}$. One ADU corresponds to 4.7 electrons (Eyles et al. 2003), and each photon will liberate a single electron in the CCD, so $P_{\mathrm{ADU}} = 4.7N_{\mathrm{photons}}$, thence $\sigma_{\mathrm{ADU}} = \sqrt{P_{\mathrm{ADU}}/4.7}$. The Poisson-noise will therefore be $\sigma_{\mathrm{Poisson,PTP}} = P/\sigma_{\mathrm{ADU}} = 1/\sqrt{4.7P_{\mathrm{ADU}}}$

One method to calculate the point-to-point scatter is to remove a smoothed profile from the timeseries, for instance to calculate a moving box-car mean over a small number of points, subtract the resulting profile from the timeseries, and determine the standard deviation of the remaining data-points. This method can break down where there is a strong signal at high-frequencies, which will not be removed by this moving-mean, and therefore can not be differentiated from the true scatter.

A method which may be used to avoid this error is to estimate the white-noise (point-to-point scatter) by means of determining the power-in-white noise in the frequency domain. By Parsevals' theorem the white-noise power in the frequency domain will equal the white-noise power in the time domain (i.e., the point-to-point scatter). At high-frequencies the power-in-white-noise associated with the point-to-point scatter will dominate over frequency dependent instrumental and stellar-noise effects, thence an estimate of the point-to-point scatter can be found by integrating the high-frequency noise over the entire frequency range.

Figure 4.4 shows the point-to-point scatter for a sample of 10066 SMEI stars, calculated by

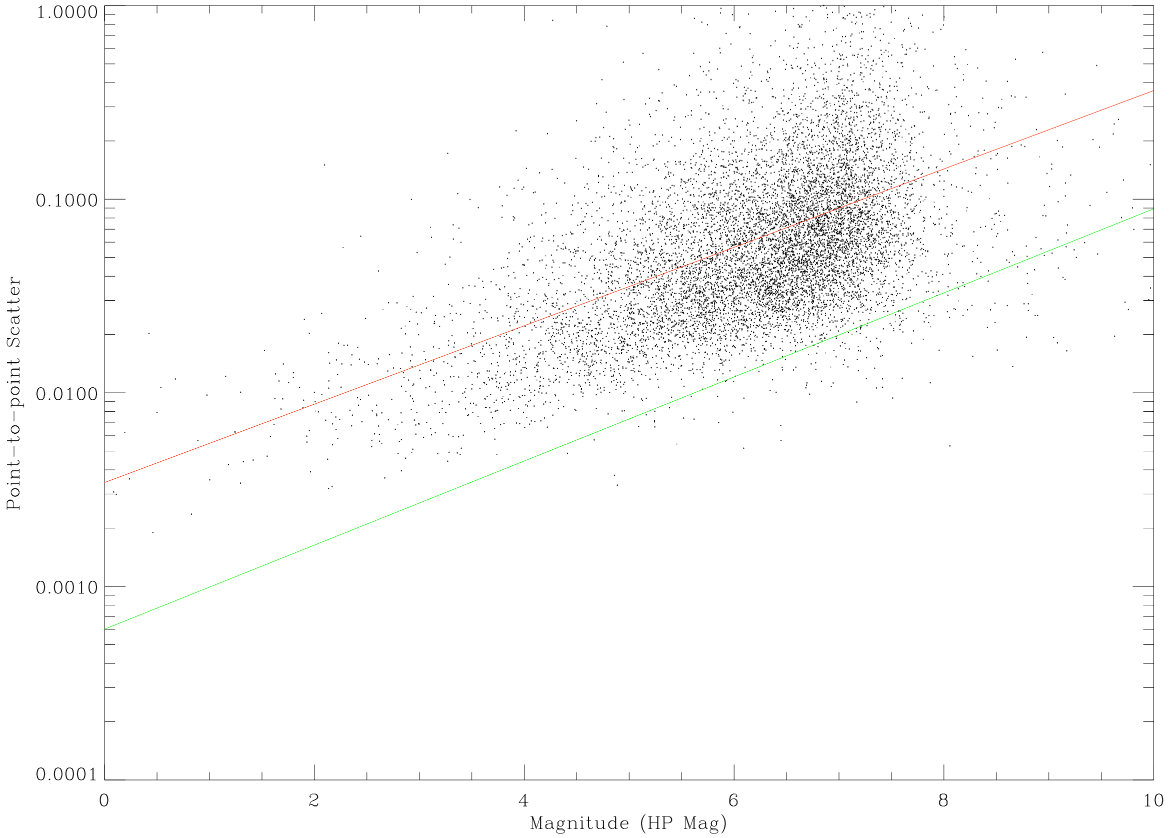

Figure 4.4: Scatter on data from a sample of 10068 stars taken with the SMEI Camera 2. The red line shows a linear fitting to the scatter, while the green line shows the predicted Poisson noise limit. The x-axis is expressed in Hipparcos Magnitudes, the native brightness units of the Hipparcos mission.

second method above, more specifically taking the mean power between 1.1 and 1.9 cycles per-day in timeseries rebinned to a regular 0.25 day cadence, and integrating across the frequency range from zero frequency to the Nyquist frequency in order to return the scatter in the original timeseries. The red line shows a linear fit between $\log(\sigma)$ and the magnitude, and the green line the expected Poisson noise limit. The few points at below the Poisson noise limit are probably due to the leakage of additional light from nearby sources into the aperture, causing a higher flux and therefore smaller than expected scatter.

The red line shows that we should on average expect a 1 % (10 ppt) scatter at magnitude 2.3, and a 2 % (20 ppt) scatter at magnitude 3.8.

4.3.2 Statistical properties

In testing the significance of features noted in a power spectrum we use our knowledge of the underlying statistics of the distribution to find the false alarm probability, i.e., the chance a given feature is observed as a result of the noise-background. Where this chance is lower than a certain threshold (typically 5, 1 or 0.1 %), the feature is noted as significant.

However, it is possible that the statistical assumptions underlying our model of the background are erroneous. Mathematically a timeseries consisting only of Gaussian distributed noise with a fixed variance, can be shown to follow a distribution with χ^2 with two degrees-of-freedom statistics in a Fourier power spectrum when sampled at the critical frequencies (see Section 5.7 on page 110 for more details). Where one sums together n multiple bins this causes an increase in the number of degrees of freedom to $2n$ - i.e., summing across 9 bins will result in a spectrum showing χ^2 with 18 degrees of freedom statistics.

Any signal in the data will corrupt this distribution - for instance adding a sinusoid to a white-noise background will add a single frequency at much higher power than the background, while adding a broad peak will cause a range of bins to be at higher power.

To confirm that the SMEI data followed the expected χ^2 with two-degrees of freedom statistics, testing of the timeseries was performed. A power-law model of the form $a + b\nu^{-c}$ was fitted to the power spectrum of a sample of stars, and a histogram taken of the resulting whitened power spectra. This procedure was repeated for power spectra which had been smoothed by 9, 29 and 99 bins. In order to prevent the corruption by the one-day signal which is consistently

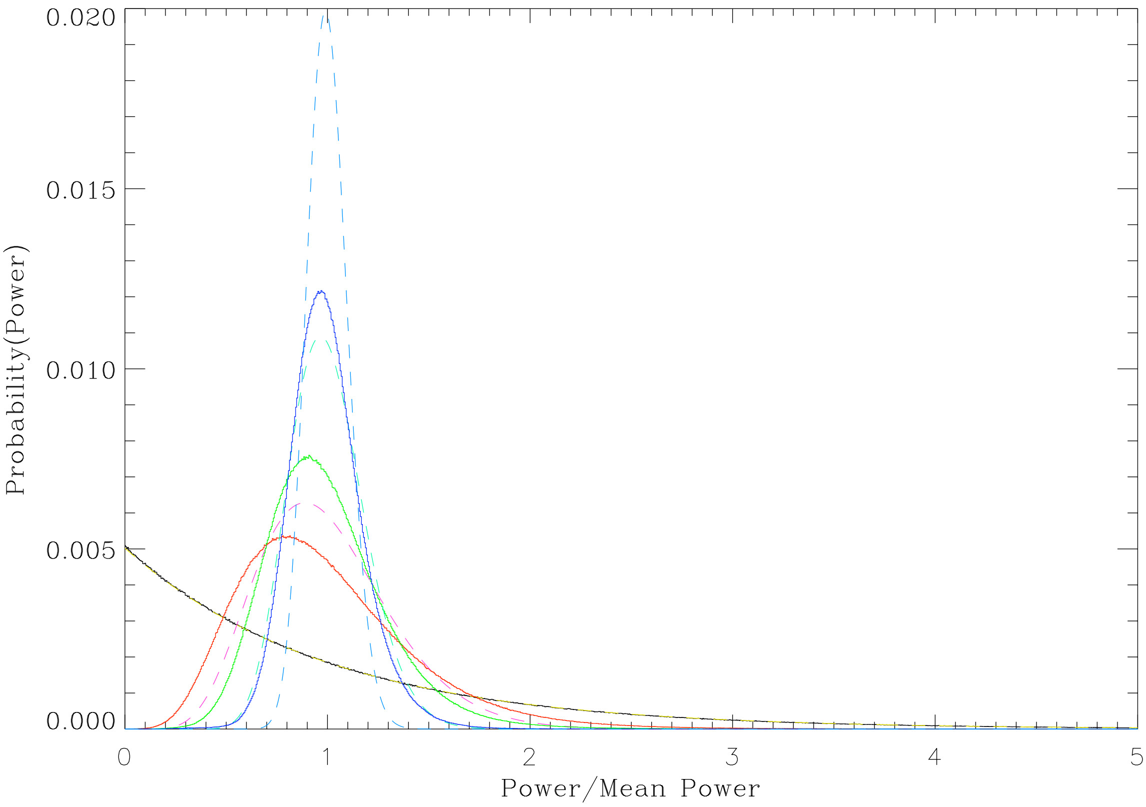

Figure 4.5: Statistics of the SMEI power spectra at a range of smoothings. Average histograms of power-series with 1 bin (black), 9 bin (red), 29 bin (green) and 99 bin (blue) smoothing are shown by solid lines. The dotted lines show the statistics which would be expected, were the curves to show χ^2 with $2n$ degrees of freedom statistics (for the 1 bin smoothing the yellow dotted line lies over the black, so close as to be indistinguishable).

present across all stars (see Section 4.3.5 on page 76), a 0.1 cycles-per-day region surrounding each daily harmonic (including where $\nu = 0$) has been removed from the power spectra.

Figure 4.5 shows the results of this test. It can be seen that while for single bins the distribution of power closely follows that of the χ^2 distribution, for the three smoothed spectra there is a significant deviation.

It seems likely that the additional width is due to the background not being adequately represented by the power law. Non-noise features can be noted in the background (see subsequent sections), which, as noted will influence the statistical distribution. These deviations from a flat background may have altered the shape of the histogram for the smoothed power spectra, while for the single-bin statistics it seems likely that the additional scatter has been swamped by the width of the statistical distribution, resulting in a very close fit between the observed and expected distributions.

In summary; these results imply that for single bin tests the SMEI data follow the expected distribution, and the results can be largely trusted. When looking for concentrations of power by means of integrating across a range of bins the distribution of power observed in SMEI data does not follow the expected distribution, and caution should be taken.

4.3.3 Background features

Figure 4.6 shows a 7-bin ($\approx$0.008 μHz) smoothed version of data gathered from 10,000 Hipparcos stars observed with Camera #2 of SMEI. The data from multiple stars were normalised such that the mean power in those bins between 1.1 and 1.9 d^{-1} was 1.0 (termed the 'characteristic power' on the scale). This range was chosen as it excluded any diurnal cycles, and, as data had been re-binned onto a 0.25 day cadence, was the highest range over which a baseline could be calculated.

In a normal star one of three sets of six apertures is considered, with the set chosen dependent upon the brightness of the star. For the brightest stars of magnitude less than 3.0, apertures ranging from 1.8 to 2.8 times the FWHM of the PSF are considered, while for the stars of magnitude greater than 4.5, the apertures range from 1.2 to 2.2 times the FWHM. From this set the aperture with the lowest point-to-point scatter is selected. In revisions two and three of the pipeline the timeseries from the selected aperture, along with the apertures one greater and smaller, is presented as an IDL save-file. These three apertures are shown in red, green and blue in Figure 4.6.

This smoothed background should be largely independent of any oscillations seen in the individual stars, therefore any features observed in the mean power spectrum should represent an average of the stellar and instrumental background, along with any features which have been introduced by the instrument and processing pipeline.

One may expect the mean background to be composed of noise arising from three sources, each of which shows a different profile in frequency:

Instrumental background: A frequency-dependent noise background is seen in almost all electronic devices, known as flicker noise. This comes from a number of sources, for instance fluctuations in resistance or base current noise in transistors (Horowitz and Winfield 1989). Flicker noise has a profile characteristic of $P(\nu) \propto \nu^{-1}$.

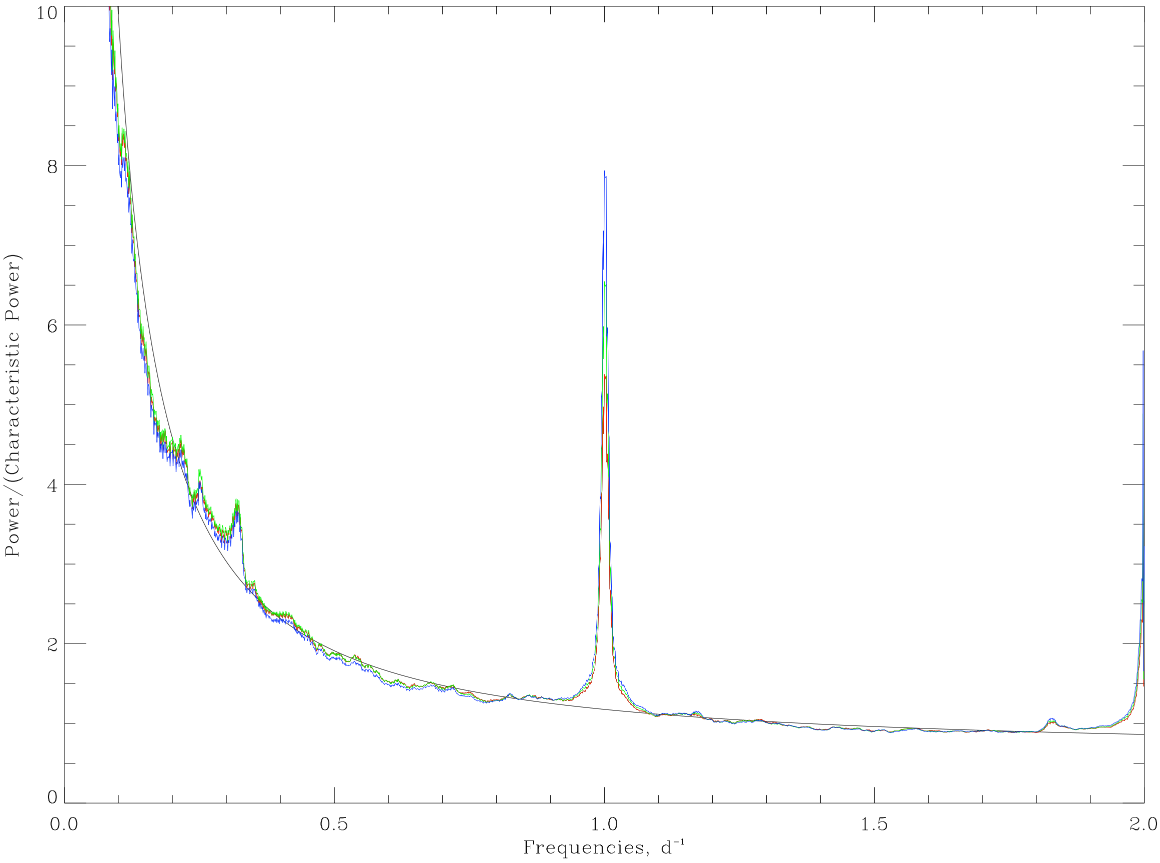

Figure 4.6: Smoothed representation of the mean power spectrum representation of 10,000 Hipparcos catalogue stars observed with SMEI. Here the red, green and blue lines represent three apertures progressively increasing in size. The thicker, yellow line is a power-law fitting to the background of the middle sized aperture (the green data). Data have been normalised as described in the main text.

Non-oscillatory variability of the star: This is the signature of granulation and active regions on the stellar surface (see Section 2.7 on page 18 for more details). Stellar noise can be anticipated to show a profile characteristic of noise with a memory, also known as a brown noise source, showing $P(\nu) \propto \nu^{-2}$.

Photon shot noise: Light will arrive at a CCD in a finite number of discrete packets (photons). Where the number of photons is small, this can give rise to detectable statistical fluctuations in a measurement (the noise being roughly proportional to $\sqrt{N}$, where N is the number of photons received.) Photon shot noise will vary independently between individual measurements, and therefore show a white-noise profile in frequency, $P(\nu) = c$.

The individual anomalies which are seen in Figures 4.6 over this background will be discussed in the sections which follow.

4.3.4 Annual noise

A substantial fraction of stars observed with SMEI show long-term variability which appears at a period of ≈ 1 year. Time series from three of the photometric-reference stars are shown in Figure 4.7. In these timeseries which have been phase-folded with period 365.25 days the annual pattern is striking. Figure 4.8 on page 76 shows the lowest frequencies of the mean SMEI power spectrum, with the annual frequency and harmonics highlighted.

The source of the annual signal can be traced to a variety of phenomena. A star in Camera #2 will track across a CCD throughout an observation season, being observed first by CCD pixels close to one edge of the frame, then by pixels in the centre of the frame, and finally by pixels at the opposite edge of the frame. In the next observing season, roughly six months later, the star will track in the alternate direction across the CCD.

If there is any systematic alteration in the response of the pixels across the CCD, for instance an increasing sensitivity, this will manifest as an increasing intensity observed through one season, and a decreasing intensity through the next season (as the CCD is crossed in the opposite direction). While the response of the pixels should be corrected by the processing pipeline, if the correction is not perfect power at one cycle per annum and multiples thereof will be observed.

In addition Coriolis and the SMEI instrument itself vary in temperature across the year, as the positions of the craft, Earth and Sun vary with respect to each other. Periodic temperature

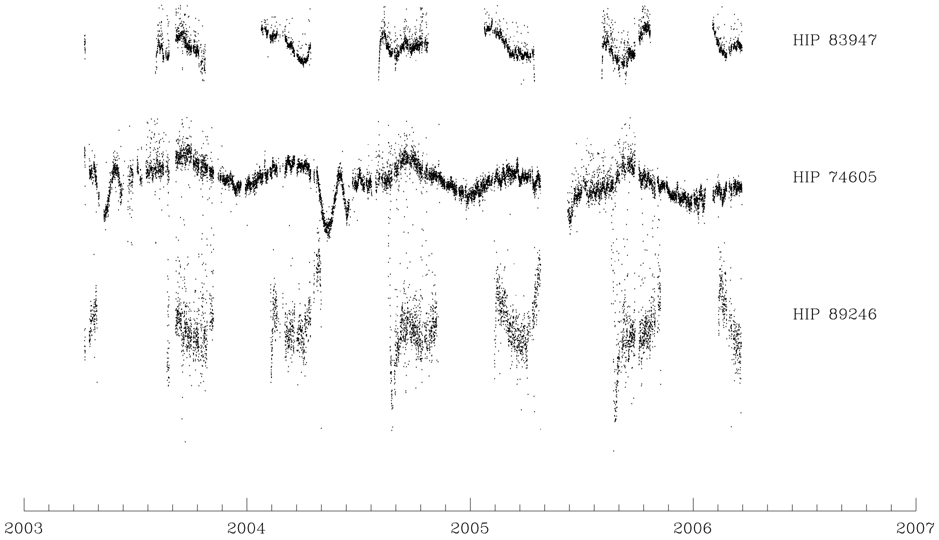

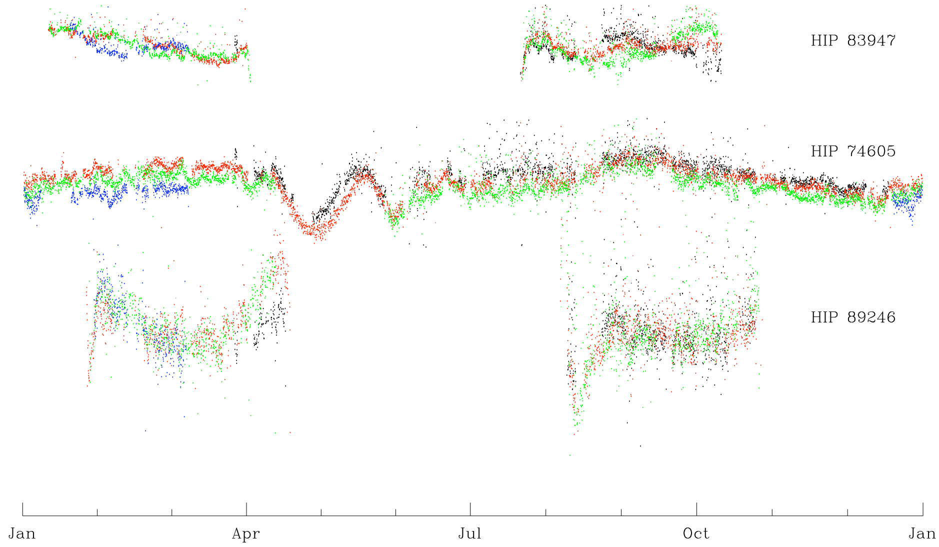

Figure 4.7: Data from three of the photometric-reference stars. In the top figure a three-year timeseries from pipeline revision two can be seen, and strong periodicities in the data can be easily observed. In the bottom figure the timeseries have been phase-folded with a period of 365.25 days. Observations taken in 2003 are shown in black, 2004 in red, 2005 in green and 2006 in blue.

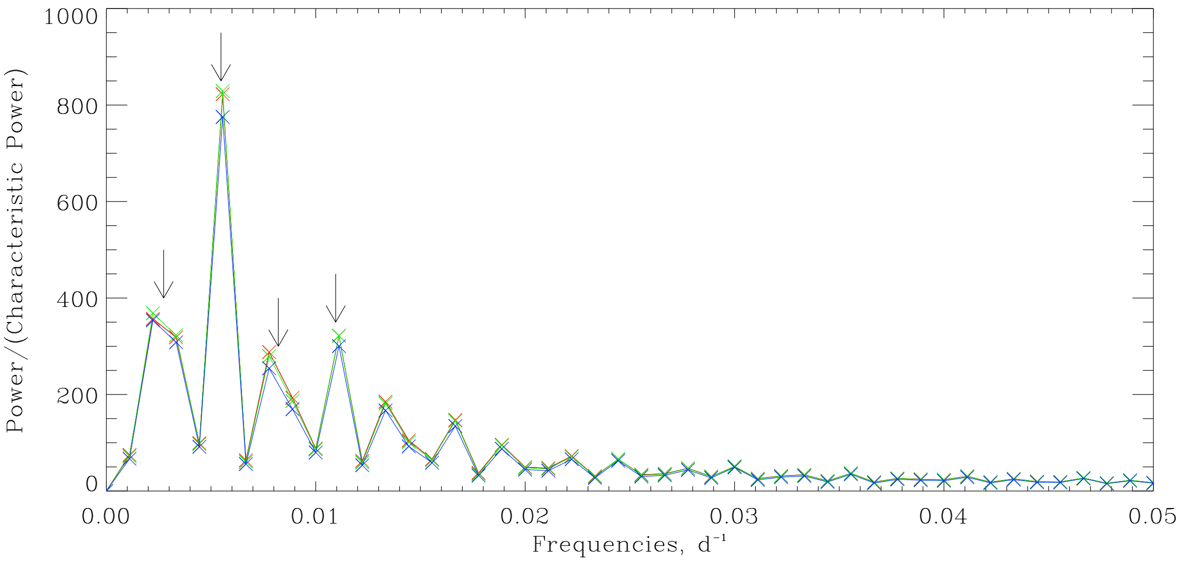

Figure 4.8: Low frequencies of the mean power spectrum, as seen in Figure 4.6 on page 73. Arrows showing frequencies of 1 to 4 year^{-1} have been added to guide the eye. It should be noted that we anticipate substantial redistribution of power by the window within this frequency range, so actual amplitudes may be lower than at first appearance.

oscillations in the SMEI instrument have been noted to be comparable in structure to long term variations observed in some stars, and so it is suspected that an imperfect cancellation of the temperature dependent dark-current is also responsible in part for the presence of annual cycles.

4.3.5 Diurnal noise

A strong peak can be seen in Figure 4.6 on page 73 at 1.0 d^{-1}, and a second at 2.0 d^{-1}, i.e., with periods of 1.0 and 0.5 days. Comparable diurnal noise has been noted in all versions of the pipeline. The size of these peaks appear to be aperture-dependent, with a lower-power seen in data of a smaller aperture.

It is likely that a major contributory factor to the diurnal noise is the passage of the Coriolis satellite over the the South Atlantic Anomaly (SAA). This is a large, roughly oval region extending across much of South America and the South Atlantic, where the Van Allen radiation belts make their closest approach to the Earth. An orbiting body passing through the SAA will experience a strong radiation flux from the Sun and cosmic rays.

It is common practice for an orbiting observatory not to make any observations, or even to switch instruments into standby while passing through the SAA. However, SMEI continues to

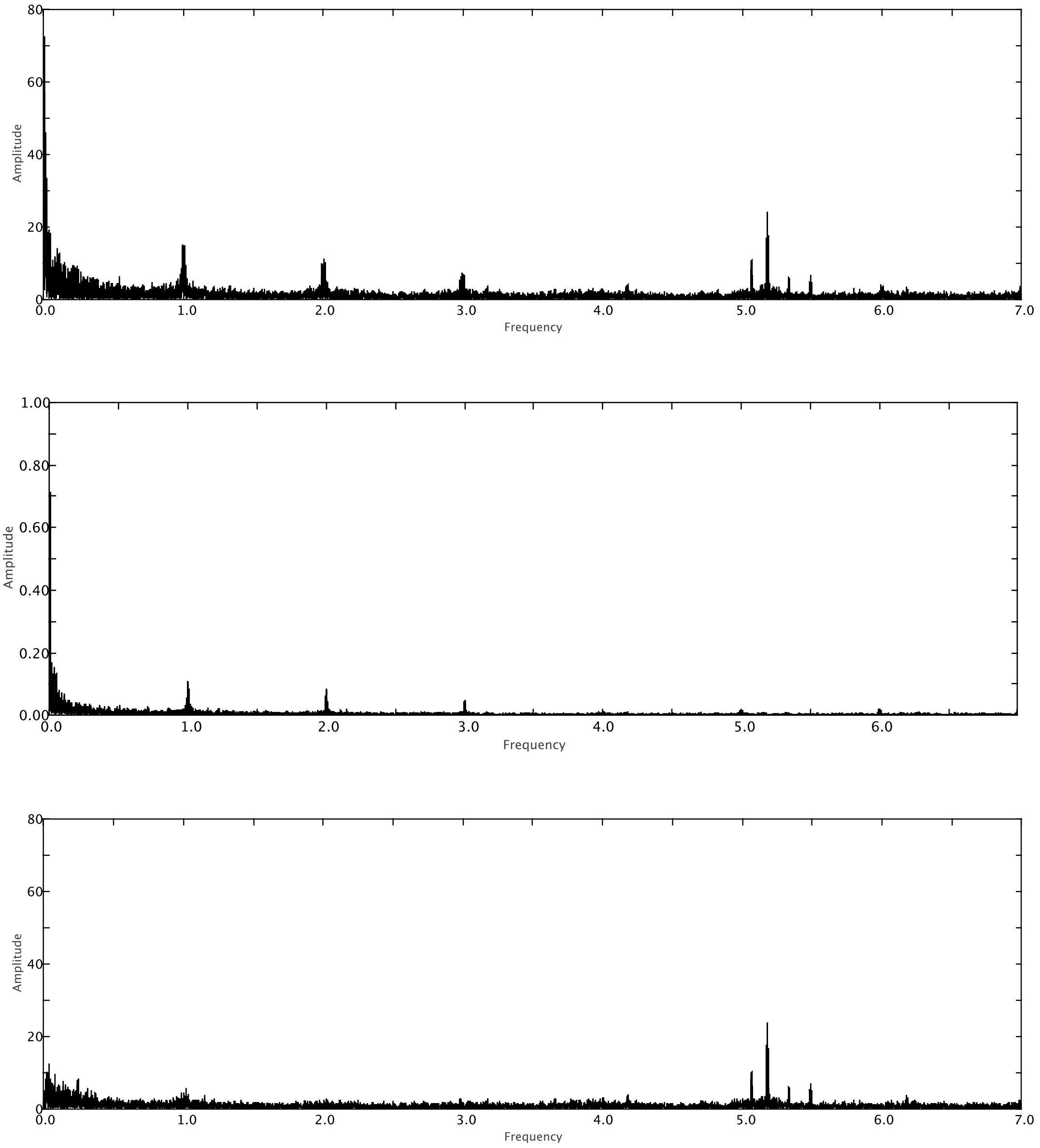

Figure 4.9: Data on the Beta-Cephei star DD Lac (HIP 112031). In the top, uncleaned spectrum, feature at 1.0 cycles-per-day and higher harmonics are prominent. The middle spectrum shows the spectral window of the data. In the lower, cleaned spectrum five frequencies at approximately 1, 2, 3, 3.5 and 4 cycles-per-annum have been removed from the spectrum, a small diurnal signal can still be observed at 1.0 d^{-1}.

operate in this region. A plot of those images rejected from processing in the pipeline shows a strong correlation with the location of the SAA. SMEI will pass through this region at a time at which it would make an observation roughly once a day, and this will cause a periodic gap in data collection which would be visible in the spectral window of the resulting timeseries.

Figure 4.9 shows diurnal cycles in the β Cephei star DD Lac (HIP 112031) (top). The origin of the diurnal features in the power spectrum can be largely traced to the spectral window (middle), as when five low frequencies corresponding to roughly 1 2, 3, 3.5 and 4 cycles-per-annum have been cleaned from the power spectrum (bottom) the diurnal signal has been largely removed, however a small residual remains indicating that this is not the only origin of a diurnal signal.

4.3.6 Anomalous features

A notable deviation from the power-law background common to all stars can be seen in Figure 4.6 on page 73 at $\approx 0.3\ \mathrm{d}^{-1}$ where a significant broad excess of power occurs. The origins of this feature are not obvious, as the period of the oscillation is approximately 3.1 days, and no processes in either the satellite or the processing pipeline occur on such a schedule.

A criterion for identifying which stars show this leakage of power has been adopted, those for which the integrated power in the range of 0.3 to 0.35 cycles-per-day exceeds twice that in the range 0.35 to 0.4 cycles-per-day:

$$\int\limits_{\nu=0.3\,\mathrm{d}^{-1}}^{\nu=0.35\,\mathrm{d}^{-1}} P(\nu) > 2 \int\limits_{\nu=0.35\,\mathrm{d}^{-1}}^{\nu=0.4\,\mathrm{d}^{-1}} P(\nu). \tag{4.1}$$

The locations of stars which pass this criterion is shown in figure 4.10, plotted in the celestial cöordinate system. It can be seen that stars passing the criterion form a broad band located roughly along the celestial equator and extending between roughly 25°North and South in declination. A histogram comparing the locations in declination of those stars which pass and fail the criterion is shown in Figure 4.11 on page 80.

Within the -25°to +25°band approximately 21.6% of stars pass the criterion, while outside it only around 2.7% of stars pass it. For any star there is a probability that the criterion will be passed, even in the absence of any anomalous process that adds power in the requisite range;

Table 4.2: The distribution of stars which pass and fail the criterion in Equation 4.1.

	Passing the criterion	Failing the criterion	Total
Within 25°declination	1002 (9.8%)	3718 (36.3%)	4720 (46.0%)
Outside of 25°declination	149 (1.5%)	5382 (52.5%)	5531 (54.0%)
Total	1151 (11.2%)	9100 (88.8%)	10251

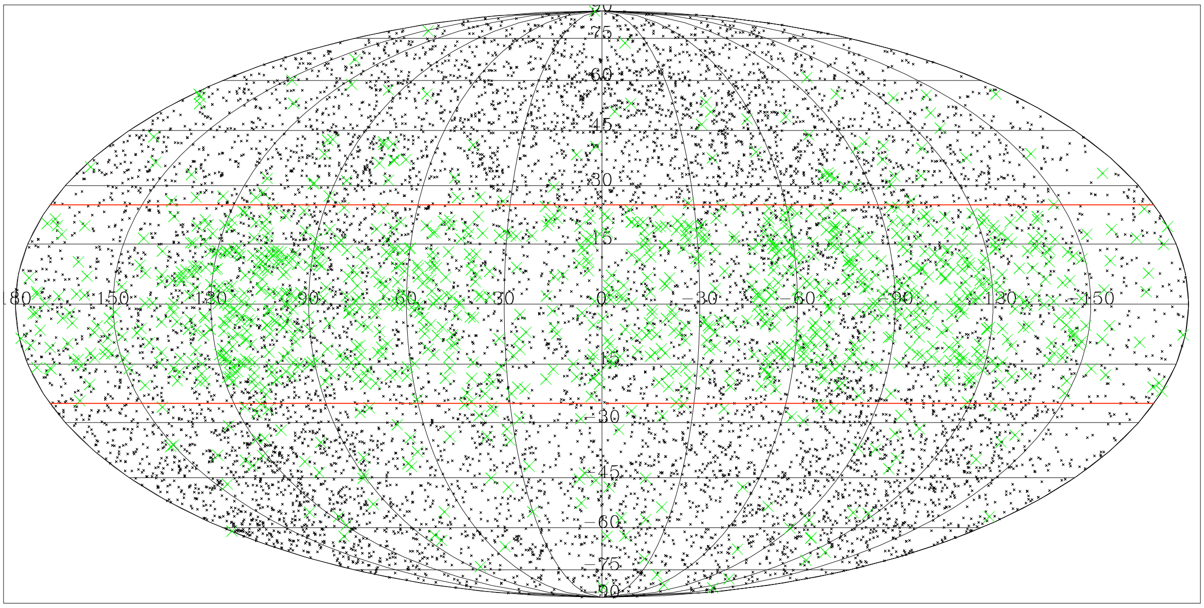

Figure 4.10: Locations of stars in the sample. Stars which pass the criterion are shown as large, green crosses, and those which fail as small, black crosses. The red lines mark the limits at +/- 25°. The chart is shown in a Mollweide projection, with locations specified the ICRS coödinates system.

for instance a star may actually show an oscillation with a period of around 3 days, or it may be a strong spike of noise randomly occurs in this region. It may therefore be argued that the presence of the anomalous feature is restricted to only those stars within 25 degrees of the equator, with the other stars passing the criterion for other reasons.

One may question whether the anomalous concentration of power is as a result of an additive or multiplicative process. That is to say whether a signal of the requisite period has been added to the stellar signal, or the anomaly represents a modulation of the reported amplitude with the requisite period.

If the process that generates the signal is additive then we may expect the amplitude of the signal to be independent of the magnitude of the star, and therefore to be more prominent in less bright stars, i.e., those of a higher magnitude. Figure 4.12 on page 81 shows a histogram of the magnitudes of those stars passing and failing the criterion. It can be noted that the distribution in magnitude of passing and failing stars does not appear to differ in any significant regard.

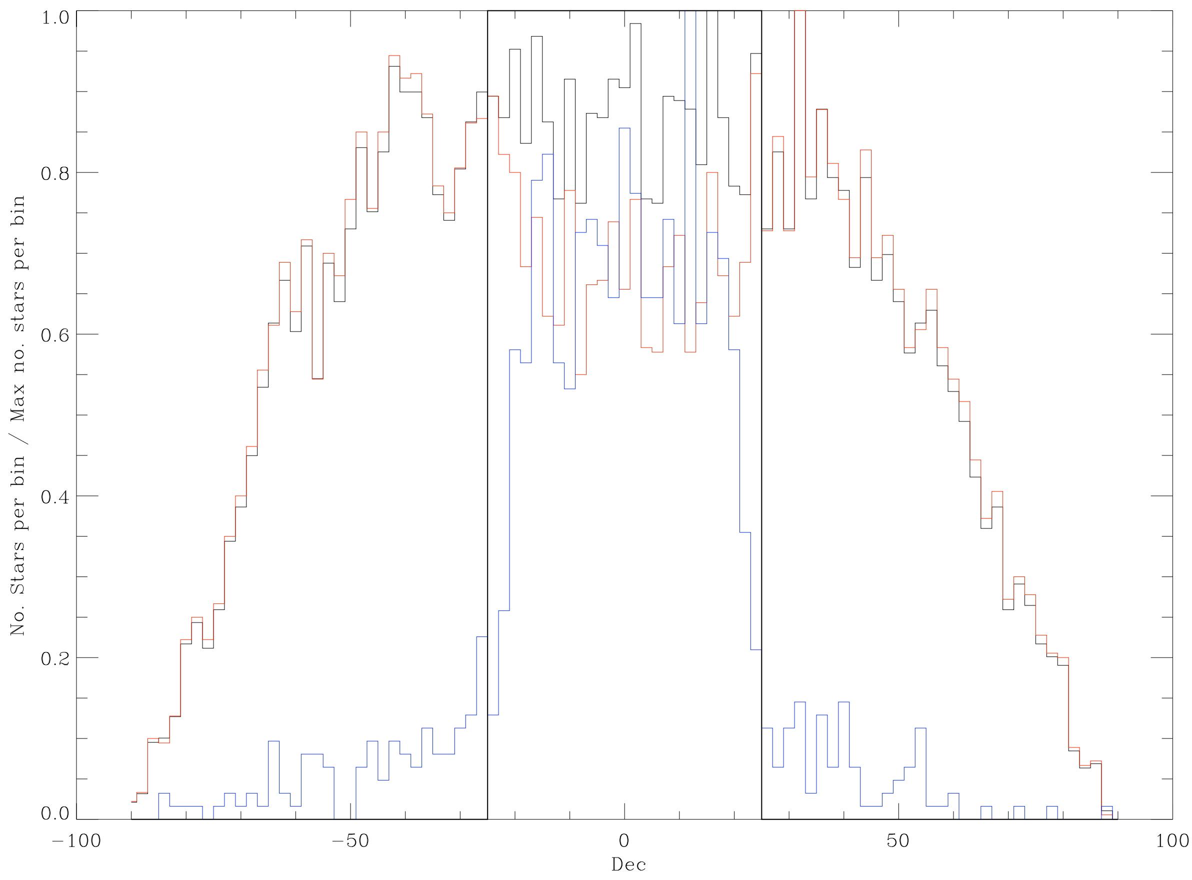

Figure 4.11: Histograms showing the locations of stars in declination. The histogram of all stars is shown in black, of those stars passing the criterion in blue, and of those stars failing the criterion in red. In order to make the histograms comparable, each has been scaled such that the bin with the greatest number of stars has a value of 1.0.

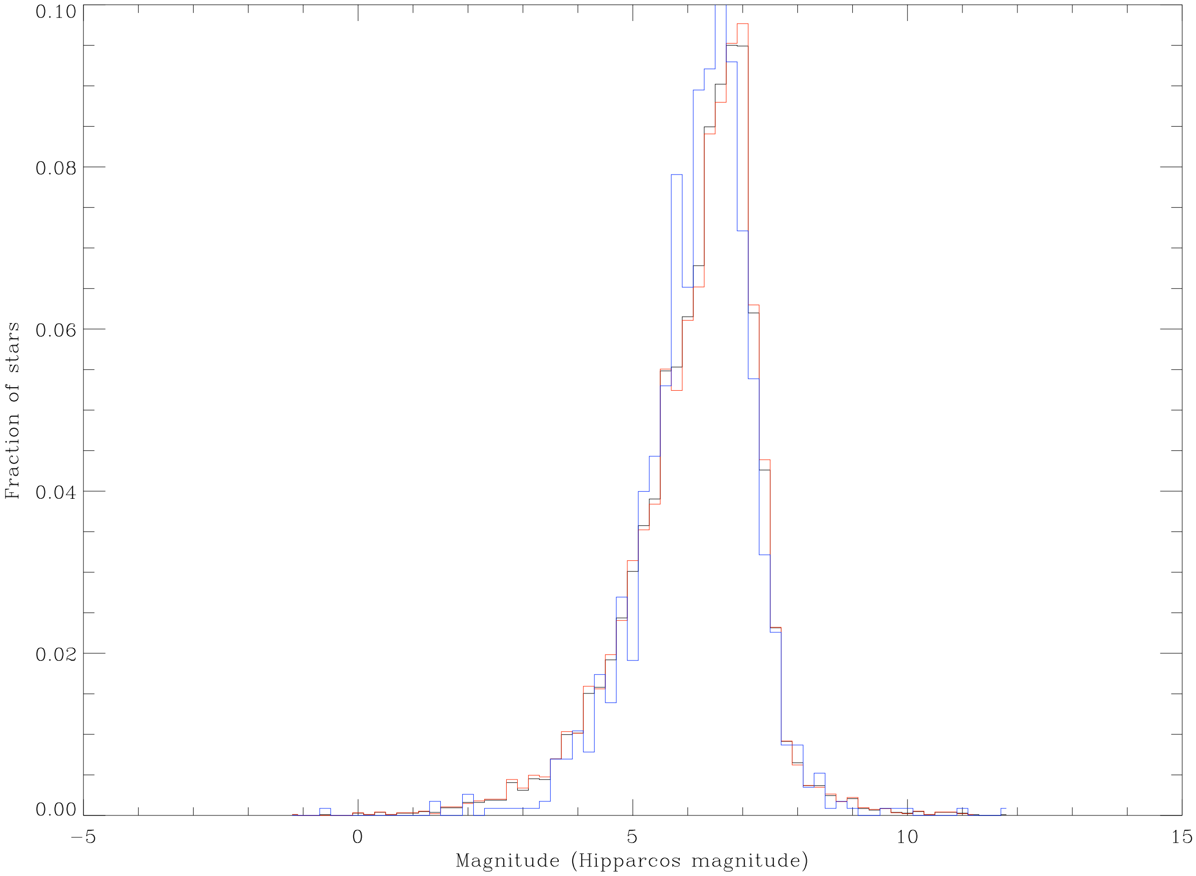

Figure 4.12: Histograms showing the magnitude of stars in the sample. The histogram of all stars is shown in black, of those stars passing the criterion in blue, and of those stars failing the criterion in red.

A multiplicative modulation will scale to the magnitude of the star, and may be expected to affect stars of all magnitudes equally. This does indeed appear to be the case in Figure 4.12.

A further affect of a multiplicative modulation is that it will not directly add power at that frequency to the power spectrum. As a multiplication in the time-domain, it is equivalent to a convolution in the power-domain, so we should expect to see the signal convolved with a transform of the modulation.

Consider a multiplicative modulation with a profile of $A + B\sin(2\pi\omega t)$, i.e., a constant term and a sine wave with a frequency of ω. If this is applied to a timeseries showing a single oscillation with a frequency of ν, the resulting power spectrum will show three peaks, located at ν, $\nu - \omega$, and $\nu + \omega$, with the amplitude of the second being roughly B/A times that of the first. It is modulation of the zero-frequency component which results in the presence of a signal at the frequency of the modulation, i.e., ω in the example above.

If it is the case the modulation is multiplicative we should expect to see similar aliases at $\pm 0.3\,\mathrm{d}^{-1}$ of the frequencies of known stellar oscillations, for instance in the strong peaks of a β Cephei star. In the β Cephei stars which have been studied with SMEI no such aliases have been noted, despite a possible observation of the anomaly in ν Eri (Section 7.2 on page 161). However, it may be that the size of the modulation is sufficiently small that it is only for the highest amplitude, low frequency bins that the aliases of notable size. i.e. If the size of the modulation is only 2% of the mean flux, then any aliases will only be 2% of the amplitude of the actual frequency. Any aliases introduced should also be removed by the CLEAN algorithm (see Section 5.2 on page 100).

Finally we may question whether the anomaly is limited in time to a brief period of the SMEI data, or whether it is continuous across all times. The fact that it is observed in stars of all longitudes given that these stars will be observed in different months of the year implies that the phenomenon is not only limited to a single season, or occurred across a length of time shorter than a year.

Figure 4.13 shows the periodogram of all the observation seasons for HIP 93138, one of the photometric-reference stars. A feature at approximately 0.32 cycles -per-day can be seen in five of the seven seasons, with the exceptions being the first (black), and last (yellow), where the number of data-points is less than one fifth of the number in the remaining seasons.

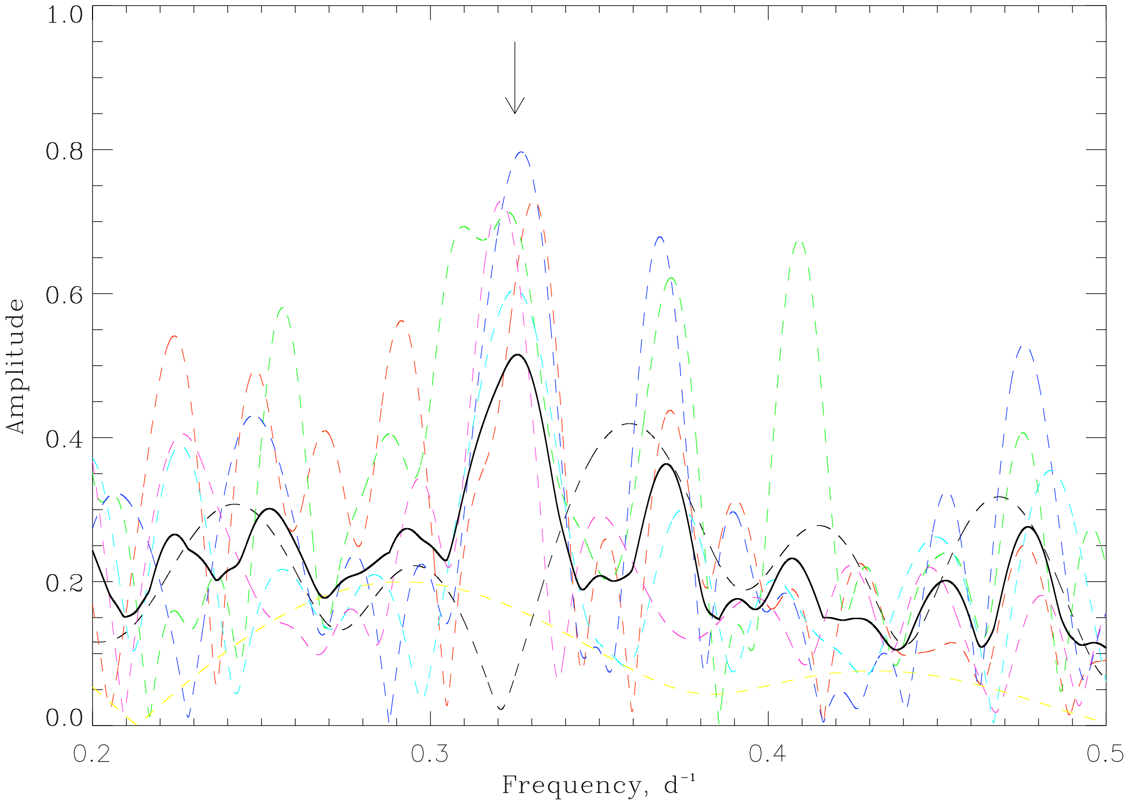

Figure 4.13: Time evolution of the anomalous signal. Seven observation seasons of the photometric-reference star HIP 93138 are shown here by the dotted lines, with each season indicated by differing colours. A mean of all seasons is show by the solid black line, with the location of the anomaly indicated by an arrow.

In conclusion; the origin of the anomalous feature at 0.3 cycles-per-day remains a mystery. However it appears to be an anomaly affecting the timeseries of certain stars between -25 and +25°in latitude, in a multiplicative manner. The phenomenon does not appear to be limited in time, occurring across the whole duration of three year timeseries of photometric-reference stars.

4.4 Studies of stars with SMEI

In addition to the work reported later in this thesis, SMEI has been used to study the low-amplitude Cepheid variable star Polaris. This star has historically shown changes in the amplitude and period of oscillations, with a trend of decreasing amplitude observed in the 1960's. Two papers have been released on the photometric variable of Polaris as observed with SMEI. Spreckley and Stevens (2008) observed an increase in the amplitude of oscillation at a rate of 1.39 ± 0.12 mmag a year using the pipeline previously described in this section. Bruntt et al. (2008) analysed the same star using an independent pipeline, and found an increase in the amplitude of oscillations of 30% over a comparable timescale, consistent with the Spreckley pipeline results. George et al. (2009) have also used SMEI data to report on the null-observation of variability in the K0 III star Schedar (α Cassiopeiae) .

SMEI data are now also being requested by members of other research groups. Pribulla et al. of the Astrophysikalishes Institut, Jena, Germany, are using SMEI data from the Birmingham pipeline in the study of the eclipsing binary star δ Velorum, and Hans Bruntt of the Observetoire de Paris intends to use SMEI data in analysis of ψ Centauri , both an eclipsing binary and pulsating variable of unknown type, ζ Ophiuchi , a Be Star, and λ Scorpii, a β Cephei variable star.

Chapter 5

Analysis procedures and techniques

5.1 Periodogram analysis

A periodogram is a deconstruction of a timeseries into periodic components. For a timeseries with data-point, x_i, a periodogram, $Pg(\omega)$ will return a value for a given frequency, ω, of:

$$Pg(\omega) = f\left(k\sum_{i=0}^{N} x_i \cdot e^{i\omega}\right), \tag{5.1}$$

in which k is an normalization constant which will be dependent upon the scaling of the periodogram, and $f(...)$ is a function which takes the complex sum and returns a real value, i.e., $\sqrt{\Re(...)^2 + \Im(...)^2}$ for an amplitude spectrum, and $\Re(...)^2 + \Im(...)^2$ for a power spectrum.

The value, $Pg(\omega)$, expresses the quality of fitting between the data and an oscillation of the frequency, ω. It will thence show which frequencies are present most strongly within a timeseries, which can be linked with various time-dependent phenomena, for instance oscillations, binarity, and stellar granulation. Periodogram analysis is therefore an invaluable tool in the study of complex periodic phenomena.

5.1.1 Frequencies and independence

For a timeseries sampled at discrete intervals, there is a unique set of frequencies which may be used to reconstruct the original data. These will be at a comb of frequencies from 0 to $1/2\tau$ at a spacing of $1/T$, where T is the duration of the timeseries and τ is the cadence (sampling interval) of the dataset. As each frequency can be assigned an amplitude and phase this results in $2 \cdot (1/2\tau)/(1/T) = T/\tau$ points, sufficient to reconstruct the T/τ data points of the original timeseries.

The power observed at each of these frequencies is statistically independent, and will show χ^2 with two-degrees of freedom statistics.

The value $1/2\tau$ is an upper limit to the frequency which can be unambiguously determined for data sets with a regular cadence. This is known as the Nyquist critical-sampling frequency, often abbreviated to the Nyquist frequency. Oscillations at a frequency greater than the Nyquist will be folded to a lower-frequency (see the Section 5.1.2).

5.1.2 Sampling of data

Imagine we are examining a phenomenon which shows a 24 hour periodicity, and taking a brief sample ($\delta t << \tau$, in which δt is the length of time over which each data point is collected) of the value of the phenomenon every 25 hours. If we define our initial, 'zeroth' sample as being at a phase of zero, then at the time of our first sample one-and-one-twenty-forth cycles will have occurred, i.e., we will sample the oscillation at a phase of one-twenty-forth. Thence, over the course of 24 days, we will sample a complete oscillation with an apparent period of 24 days, and an amplitude equal to that of the original, 24 hour oscillation.

This 'aliasing' is a well known phenomenon, and means that there is an inherent ambiguity between oscillations at a frequency of ν and $2n\nu_{\rm Nyq} \pm \nu$, in which n is an integer, and $\nu_{\rm Nyq}$ is the Nyquist frequency. For instance an oscillation at a frequency of $\nu = 0.5\nu_{\rm Nyq}$ is indistinguishable from one at $\nu = 1.5\nu_{\rm Nyq}$, $2.5\nu_{\rm Nyq}$, etc.

The phenomenon of aliasing may be reduced, if integrated data ($\delta t \approx \tau$) is used. Consider if we collect data across the 25 hours of our sampling and average this to a single data point. Of this time, 24 from the 25 hours will cover a single cycle, the integral of which equals zero, with only the final hour contributing to the value of the returned data-point. Therefore the returned amplitude, as an average over the whole period, will only be approximately one twenty-fifth of that where we took a brief sample.

Mathematically, the power seen in an integrated spectrum is expected to show a distribution of:

$$P'(\nu) = \mathrm{sinc}^2(\pi\nu\delta t)P(\nu), \tag{5.2}$$

in which δt is the time over which the integration is carried out - i.e., if we integrate for some fraction, f, of the cadence, τ, the $\delta t = f\tau$ (R. New, Private Communication). Therefore at the Nyquist frequency, $\nu_{\mathrm{Nyq}} = 1/2\tau$, we expect the power to be $\mathrm{sinc}^2(\pi \cdot 1/2\tau \cdot f\tau) = \mathrm{sinc}^2(\pi f/2)$, which in the case of integration across the whole period, $f = 1$, will give a power of $4/\pi^2 = 0.405$ times the original power.

In order to avoid over-saturation of the CCD, measurements tend to be taken over a brief period of a few seconds. However the effect of integration over a length of time can be seen as equivalent to taking a number of measurements and averaging. This technique is commonly used to reduce the point-to-point scatter (averaging over n points will lower the error on each point from σ, to $\sigma/\sqrt{n}$), and can reduce the processing overhead.

It is important in this case to note that Δt must be continuous. For instance the BiSON network integrates for two-seconds on a four-second cadence, however the two seconds are spread throughout the whole of the four second period. Under these circumstances a value for f of 100% is appropriate as we are sampling though out the whole of the cadence.

Figure 5.1 shows the effects on integration upon a comb of sine-waves of constant amplitude. Here a timeseries has been over-sampled at 1/16th of the cadence, and then summed across 16 points, resulting in what is effectively an integrated timeseries with 100% fill. The red-line traces the expected modulation of the amplitude by the sinc function.

In the case of SMEI data is only collected for around 40 seconds on a cadence of 100 minutes, i.e., an f of 0.67 %. Therefore the effects of integration may safely be ignored.

5.1.3 Dealing with irregular gridding

A major problem with using the FFT (see below) is that data are required to be presented on a regular grid in time. While this may not be a problem for observation of Earth-bound phenomena, the finite light-transit time between a body under observation requires a consideration of the distance between the object and detector, and a correction where this distance alters significantly - typically moving from the local Julian Date to the Heliocentric Julian Date.

For example at perihelion, the point of closest approach between the Earth and Sun, light will take approximately 491 seconds in transit between the two, while at aphelion, the point of greatest distance between the two bodies, the light transit time rises to 507 seconds, a difference of 16 seconds. For an instrument observing an equatorial star with an instrument on, or in orbit

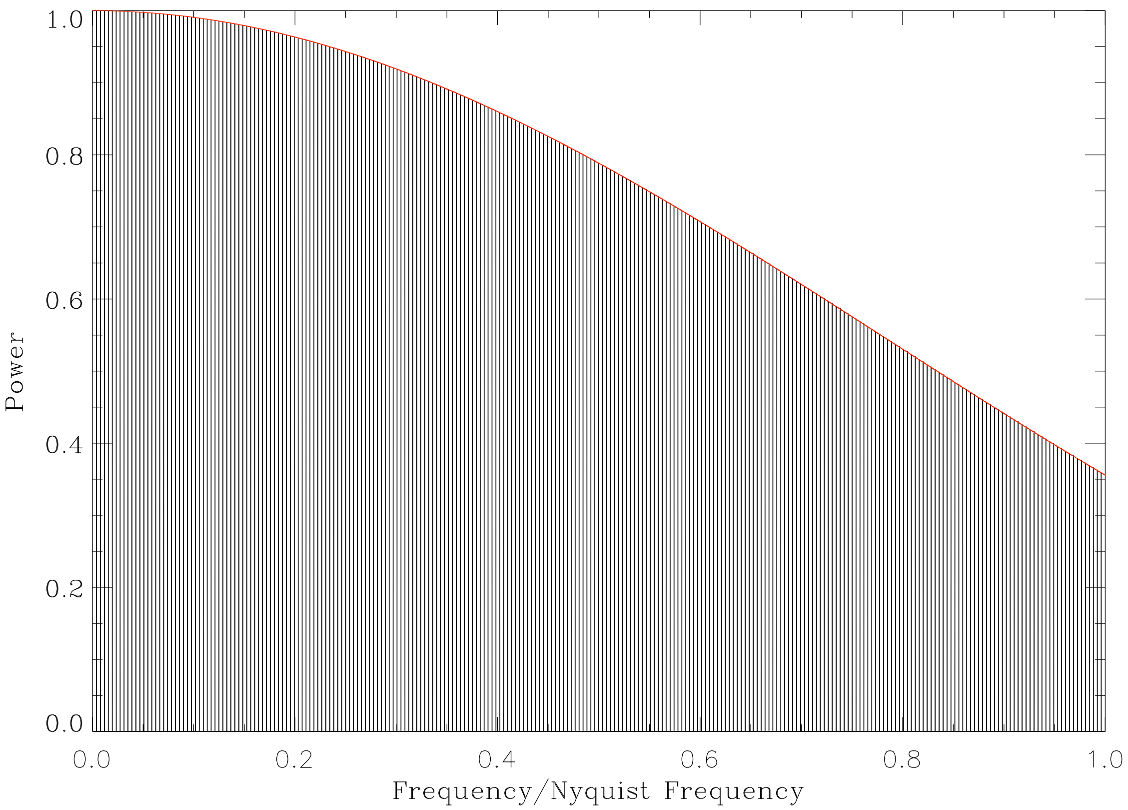

Figure 5.1: The effects of integration upon a timeseries. Here a comb of sine-waves at a constant amplitude of 1.0 has been modulated by integration with 100% fill, resulting in the above comb. The red line traces the expected effect upon the amplitude.

around, the Earth the difference in light transit time between when the Earth is located closest to the star, and when it most distant, can amount to approximately 1000 seconds.

However, the absolute value of this difference is not important, but the proportional difference this causes to the cadence, i.e., the differential of the time-stamps. Parametrising the amplitude of the time-difference as A (e.g. 1000 seconds above), the period of the cycle of varying cadence as P (e.g. 1 year above), and the mean cadence as τ, we find that the amplitude of the cadence variation will be $A_\tau = 2\tau A\pi/P$. For the two cadences of Kepler data, this will correspond to an amplitude of 950 microseconds for the 1-minute data, and 28.5 milliseconds for the 30-minute data.

A number of approaches may be naïvely taken to solve the problem of irregular gridding of a dataset: one may ignore it and treat all data as it were on a regular grid; one may re-grid the data by taking a time average over a number of data-points (for instance re-gridding data with a mean cadence of $\approx$ sixty seconds, onto a regular grid of data points every ten minutes); one may use some form of interpolation to estimate the value the timeseries would take, were it to be regularly sampled; or one may calculate the full discrete Fourier transform.

Figure 5.2 shows the consequences of using these four different processes upon a simulated oscillation. A simulated timeseries was created with a mean cadence of one unit, and an oscillation with a frequency of 0.025 units. A perturbation to the cadence was chosen to vary in the functional form of a sine wave centred on one unit, and with an amplitude of 0.05 units. This perturbation meant that at the mid-point of the perturbation the oscillation would be sampled with a phase difference of 0.5 - i.e., if a point which would have been anticipated to be a maxima under regular spacing, would be a minima in the perturbed timeseries.

As Figure 5.2 shows, the results of each technique produce a spectrum which looks approximately the same, showing an oscillation centred at the correct frequency of 0.025 units. However, the returned amplitude differs significantly between the methods. By ignoring the effects of the irregular gridding (the black line) the power of the oscillation is spread over a considerable range of bins, and the maximum amplitude of the mode never reaches more than about 2% of the known amplitude. This is corrected by the re-binned data (red), which rises to an amplitude of just over 0.3 units, however the noise level is raised in comparison to the Lomb Scargle Periodogram and full Fourier transform.

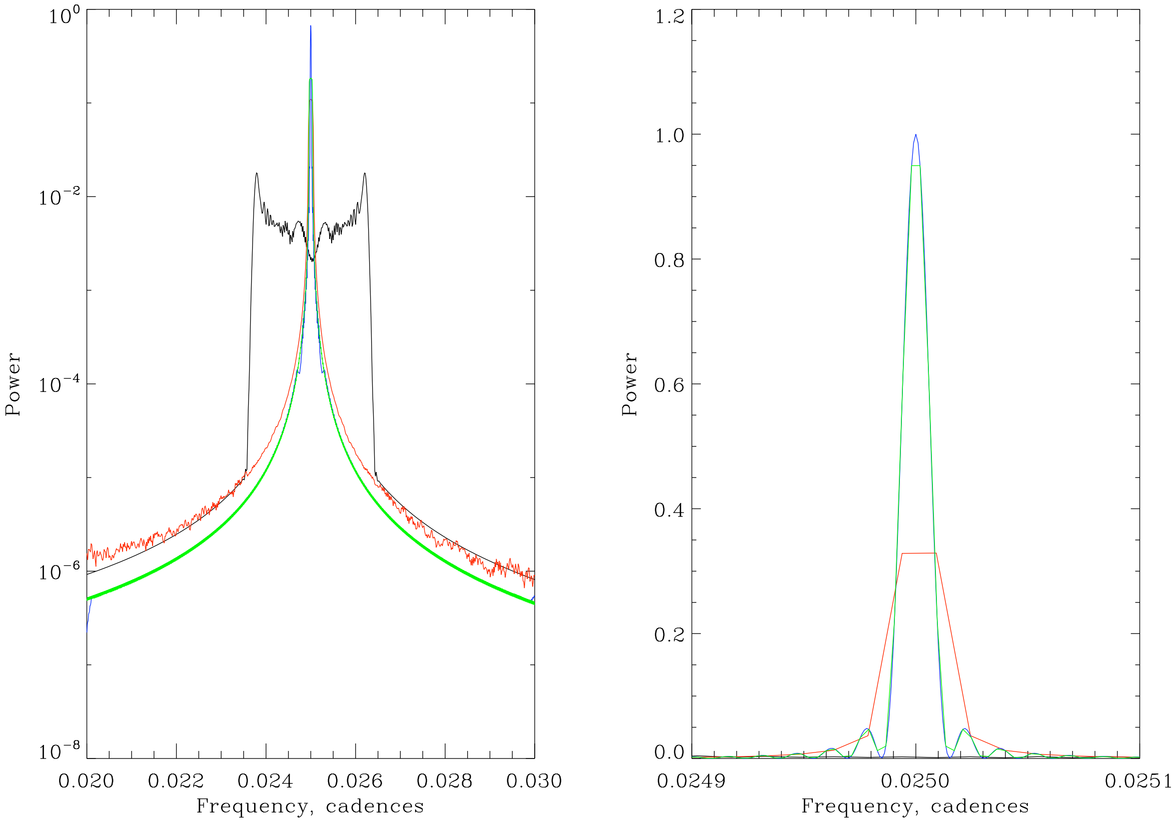

Figure 5.2: A comparison between different methods of periodogram analysis for an irregularly gridded timeseries. Here the black ignores the perturbations to the times and performs a FFT on the dataset, the red re-bins the data onto a regularly grid of ten times the mean-cadence and performs a FFT on the resulting timeseries, the green performs a Lomb Scargle periodogram (see Section 5.1.6), and the blue a full discrete Fourier transform. It should be noted that the figures on the left and right are on different horizontal and vertical scales.

The best results come from use of the Lomb Scargle periodogram (green), and full Fourier transform (blue). These produce results which closely follow each other across all frequencies, with the only deviation being at the peak of the oscillation, where the lower-resolution of the LSP doesn't capture the peak of the distribution. However the resolution of the LSP may be increased, and the faster processing speed should make it, in general, the technique of choice for irregularly gridded data.

5.1.4 Statistics on an irregular grid

Another major problem with data on an irregular grid is that we are no longer sampling at the 'natural frequencies' of the timeseries. To envision what these mean we can consider the information contained within the timeseries. For data taken at a regular cadence with 100% fill the natural frequencies will be a comb with a spacing of $1/T$. The amplitude and phase at each of these frequencies will be statistically independent, and sufficient to precisely reconstruct the timeseries. Information is conserved - we transform N data-points in the time-domain into $N/2$ values for the amplitude, and $N/2$ values for the phase, i.e., a total of N values, and conservation of information.

However, were we to gather data on an irregular grid it would be harder to determine these frequencies. If we naively consider taking samples as in the regular grid, i.e at $N/2$ frequencies to $N/2T$ then there will be some times at which sampling is greater than the average, and using only frequencies of lower than $N/2T$ will not be able to capture this behaviour. For instance if data were to be gathered every hour for a ten day period, once per year then the average spacing of data-points would be once every three days. In this case our naïve approach would only sample frequencies of up to $1/3\ \mathrm{d}^{-1}$, so any variability over short time scales would not be adequately represented.

If instead we make a regular timeseries extending out to higher frequencies, we will gain more than N pieces of information given N pieces as an input. By the conservation of information - as we have not added any more data into the timeseries - it is therefore not possible for each value to be independent.

The Window Function

Most data is intended to be gathered on a regular gird, with only small corrections needed to account for time-travel affects. However the problem of irregular gridding is not merely academic. Even where gridding is regular we should expect the occasional data drop-out or gap - for instance a point may be lost due to weather events, cosmic rays, instrument maintenance, pointing errors, etc. Additionally an object may only be in a position to be observed during a limited season, for instance the Sun will typically only be observable from a single site for 8 hours a day, and a star may only be visible for a few months of the year.

These gaps in the data are known as the 'window function'. Mathematically this can be represented for discrete data as a series of 1's and 0's, where 1 indicates that an observation has been made, and 0 where no observations were taken. The 'spectral window' is the transform of the window function. Any periodic signal will be seen in the time-domain as a multiple of the window function with the signal itself. This will manifest in the frequency domain as a convolution of the spectral window with the transform of the signal. This will add a correlation between bins.

For instance in Figure 5.3, the top chart shows a window where a signal is kept under observation for a period, followed by a period of equal duration in which no observations are taken, repeated four times. A proportion of the power at zero-frequency has been redistributed to 4, 12, 20, 28, and in general to bins $8n + 4$ away from the zero-frequency component (where one bin corresponds to $1/T$) - i.e the Fourier components of a square wave with period $1/4$ that of the observation duration.

In general, power will be re-distributed over whatever cycles occur in the window function - for instance in the second chart of Figure 5.3 the prominent spectral window peaks occur at 8 bins and multiples thereof. In the third power both cycles of length one forth and one eight of the observation duration are present; in the duration of the observation window, and in the period between windows; and both can be seen in the spectral window.

Where the observation window is random, power will be redistributed across all frequencies, as shown in the bottom chart of Figure 5.3. This dataset has a 50% fill, with a Poisson distributed random duration of observation intervals and gaps.

As the spectral window acts to 'link' bins, the power observed in these bins will be correlated.

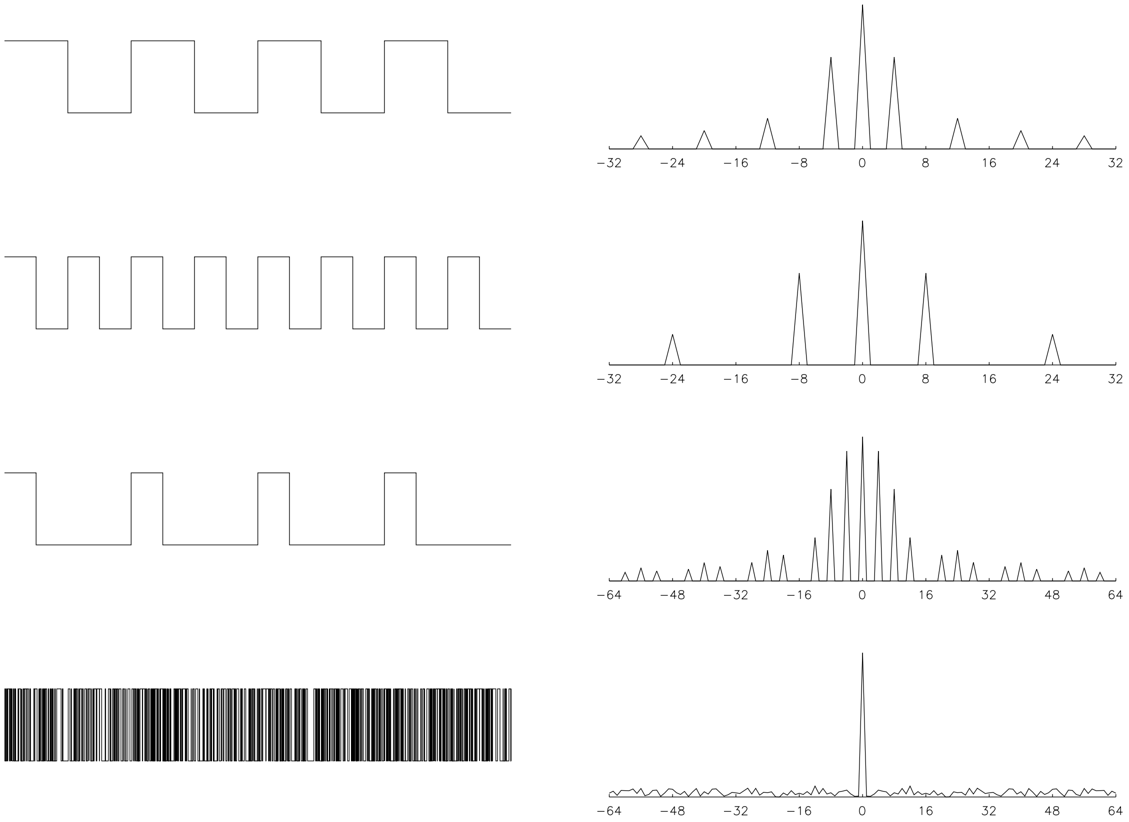

Figure 5.3: Window functions are shown upon the left of the image, where high should be interpreted as the object being under observation, and low as not be observed. Spectral windows are shown upon the right of the image, in which the horizontal scale is calibrated in multiples of the lowest frequency observed - i.e., $1/T$.
From top to bottom the functions are respectively: a dataset with half-on, half-off, and four observation seasons; dataset with half-on, half-off with eight observation seasons, a dataset with observations taken for one quarter of the time, with four observation seasons; a dataset with observations taken in continuous intervals of random length, such that observations are taken for roughly half the time.

We may anticipate this changing the underlying statistics of the distribution.

Figure 5.4 shows the effect of the window upon an exemplum timeseries. This has been generated from a model of brown noise: $F(t_{i+1}) = F(t) + R_i$, in which R_i is a random impulse with a mean of zero, and a standard deviation of 1 unit. This will result in a power spectrum with a power-law background. A power-law model has been fitted to these data (left plot in second row, data in black, model in green) and the statistics of the resulting whitened power spectrum show χ^2 with two degrees of freedom statistics (bottom plot; data in black, χ^2 distribution in yellow).

Where a window function has been applied to the raw timeseries, resulting in the dataset highlighted in red, the power-series is corrupted (centre plot in second row, data in red, fitted model in green) by a large number of aliases of the low-frequency noise. This results in the whitened power spectrum deviating from the χ^2 statistics (bottom plot; data in red).

The effects of the window function upon the timeseries can be partially compensated by suppression of the low-frequency noise (top figure, blue data). Here a 4096-bin smoothed profile (the length of the observation windows) has been subtracted from the raw timeseries. This returns the statistics of the resulting distribution to resemble those of a χ^2 distribution with two degrees of freedom.

[Note: the timeseries shown in Figure 5.4 has been chosen to show significant low-frequency noise so as to amplify the effect of the window upon the statistics. In other examples, generated by the same procedure, the effect was less pronounced, thence Figure 5.4 should be considered to be something of a worst case scenario].

5.1.5 Fast Fourier Transform

The Fast Fourier Transform (FFT) is an implementation of a discrete Fourier transform (DFT) which is efficient in terms of processing power (and therefore time taken). In formal terms, calculating the Fourier transform of N points from the definition of the transform will require some number proportional to N^2 operations - labelled $O(N^2)$ in the notation of computer science. Implementations of the FFT algorithm exist which for all numbers are able to reduce the number of operations to $O(N \log N)$. Practically this means that for a dataset of one-million points a full DFT would require $O(1 \times 10^9)$ operations, while the FFT would only require $O(6 \times 10^6)$ -

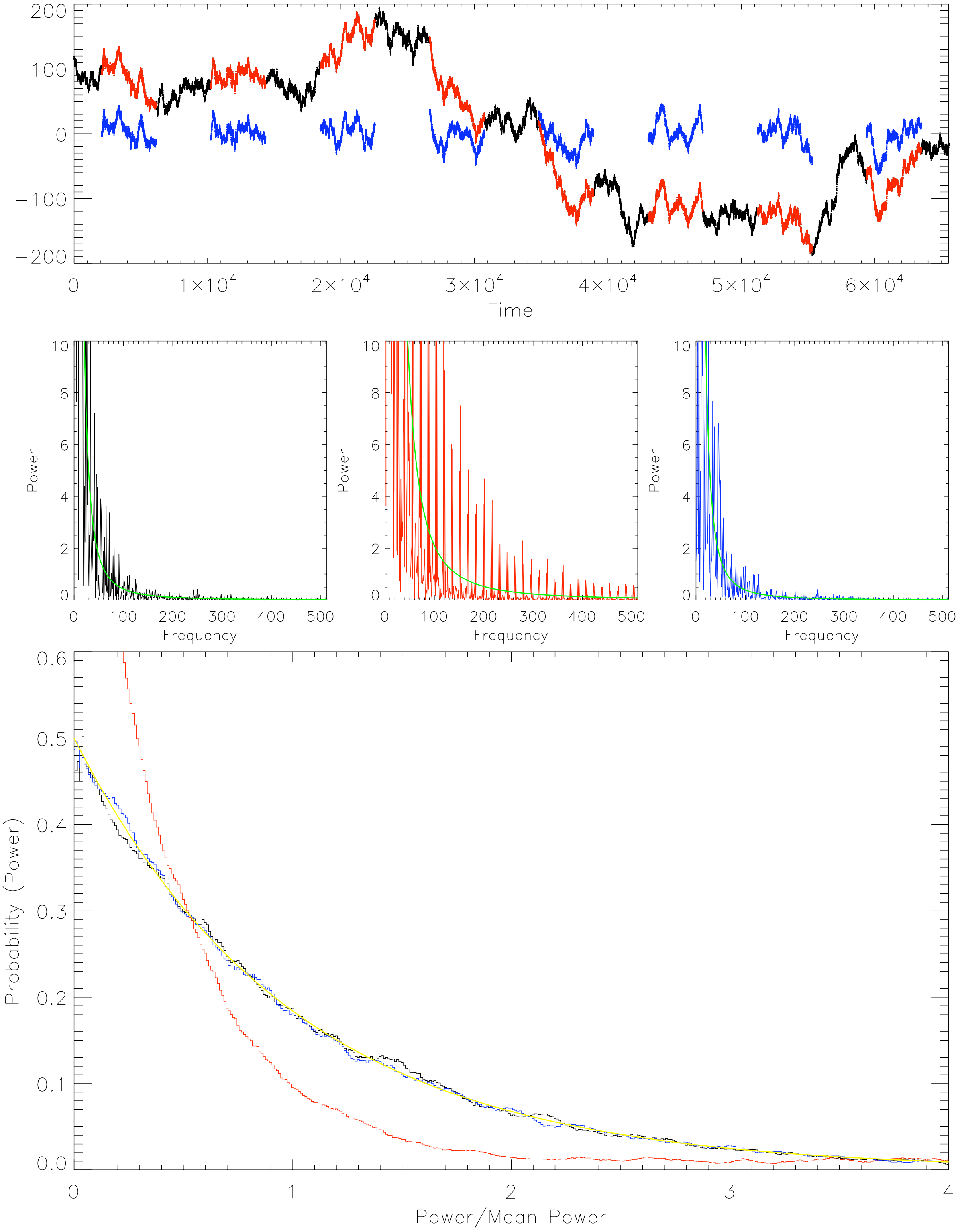

Figure 5.4: The effects of a window function upon the statistics of a noise-distribution. The top plot shows data in the time domain, original data in black, data with the window in red, and data with each window normalised to the same mean in blue. The second row of images shows the power spectra of each of these timeseries, with a fitted power-law in green. The bottom plot shows histograms of the whitened power-spectra of each dataset, following the colour convention of above.

a speed improvement of some hundred-times.

A problem with the FFT is that, while it is possible to find procedures which will calculate the DFT for any number of datapoints, it is not practical to include such special cases in a practical computer procedure. The most well known implementations of the FFT depend upon the factorisation of a dataset into a number of smaller-subsets, and running a rapid procedure on each of these subsets. The speed at which the transform can run is approximately proportional to the number of subsets of equal size which can be created, with a greater-number of sets preferable.

As an exemplum, the IDL FFT routine has a run time which can be expressed in the form:

$$T_{\mathrm{FFT}}(N) = T_0 + N(T_1 + 2K_2T_2 + T_3(3K_3 + 5K_5 + ...)), \tag{5.3}$$

where K_2, K_3, K_5, ... are the number of times N may be factorised by 2,3,5, ..., i.e., $N = 2^{K_2}3^{K_3}5^{K_5}...$, and $T_{0,1,2,3}$ are constant times associated with each procedure. The running time of this procedure can therefore differ significantly for only a small change in the number of points - e.g. 65536 ($= 2^{16}$, i.e., with 16 prime factors, each of 2) will be expected to have a run time approximately 4000 times lower than that of 65537 ($= 2^{16} + 1$, a prime number). In the case of a prime-number for N most implementations of the FFT will perform no better than the DFT.

5.1.6 Lomb Scargle Periodogram

The Lomb Scargle Periodogram (LSP) was first described by Lomb (1976). Unlike the FFT it is able to deal with data which is not on a regular grid. Suppose there are N data points, $h_i = h(t_i)$, $i = 1, ..., N$. Defining the mean and variance of the data by the usual formulae;

$$\overline{h} \equiv \frac{1}{N}\sum_1^N h_i, \tag{5.4}$$

$$\sigma^2 \equiv \frac{1}{N-1}\sum_1^N (h_i - \overline{h})^2. \tag{5.5}$$

The LSP for $\nu > 0$ is defined by:

$$P(\nu) \equiv C_N \frac{[\sum_i (h_i - \overline{h}) \cos 2\pi\nu(t_i - \tau)]^2}{\sum_i \cos^2 2\pi\nu(t_i - \tau)} + \frac{[\sum_i (h_i - \overline{h}) \sin 2\pi\nu(t_i - \tau)]^2}{\sum_i \sin^2 2\pi\nu(t_i - \tau)}, \tag{5.6}$$

where τ is an offset that makes $P(\nu)$ independent of the effect of a linear offset in the values of t, defined by the relation:

$$\tau = \frac{\sum_i \sin 4\pi\nu t_i}{\sum_i \cos 4\pi\nu t_i}, \tag{5.7}$$

and C_N is a normalisation constant, which will alter the vertical scaling of the periodogram. $C_N = 1/2\sigma^2$ gives a normalisation such that the mean power-in-white-noise will be 1.0 in the frequency domain - i.e., the data will be pre-whitened. $C_N = 1/N$ will give a scaling in power-per-bin (therefore transforming the Lomb periodogram into those units as will be given by a raw Fourier transform), and $C_N = \Delta t$, where Δt is the cadence will give a scaling in power-per-hertz (transforming the Lomb periodogram into a power-density spectrum).

The LSP is computationally more intense than the fast Fourier transform, requiring four calls to trigonometric functions for each frequency. Where one is sampling on a regular grid one can achieve a factor of 4 speed up by replacing these trigonometric calls by recurrences, however this will still have $O(N^2)$ operations (Press et al. 2007).

However, a fast implementation of the LSP has been created by using *extirpolation*. This is a process analogous to interpolation, however while a formal definition of interpolation is to take data on a regular grid and determine the value of a function between the grid points, extirpolation will take data on an irregular grid and determine the value at regular points. This regular gridded data can then be evaluated by a FFT. This results in an implementation which will return an approximation to the LSP evaluated in $O(N \log N)$ time. Due to additional processing associated with the extirpolation the algorithm will however always perform less efficiently than the pure FFT.

An advantage of the Lomb periodogram is that where data shows a sufficiently random sampling, the LSP is able to extract frequencies at greater than the Nyquist critical sampling frequency. In a regularly gridded dataset an ambiguity is created between frequencies at ν and $(2n-1)\nu_{\mathrm{Nyq}} \pm \nu$, where ν_{Nyq} is the Nyquist critical sampling frequency, and n is an integer.

For example sampling a 24 hour period ($\nu = 1$ d^{-1}) with a cadence of 18 hours ($\Rightarrow \nu_{Nyq} =$ 0.667 d^{-1}) would produce an identical dataset to a 72 hour period ($\nu' = 0.334$ d^{-1}). However where the sampling intervals have some randomness, this ambiguity is broken and only the 24 hour period provides an appropriate fit to the data. This is illustrated in Figure 5.5, in which

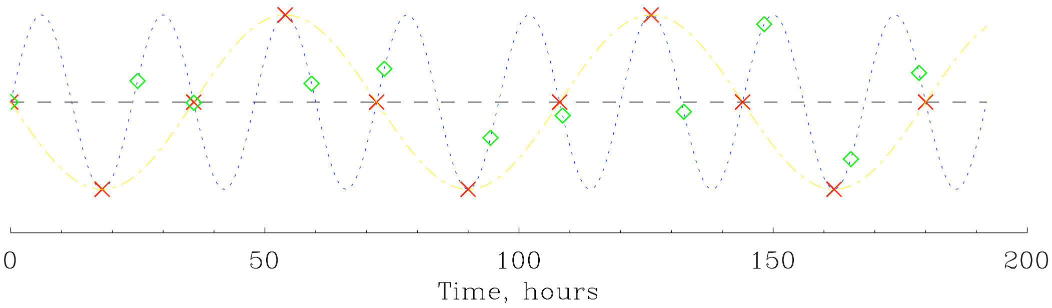

Figure 5.5: Sampling at a regular cadence of 18 hours (red crosses) cannot distinguish between an oscillation of period 24 hours (blue), and one of period 72 hours (yellow). However, a sampling with some random scatter on the cadence (green squares) is able to unambiguously show that only the 24 hour period provides an appropriate fit.

the red data is regularly gridded at 18 hour cadence, and the green data has a mean cadence of 18 hours, with a standard deviation of 3.6 hours.

5.1.7 Synthesis method (least-squares spectrum)

The *Synthesis Method* (Elsworth, private communication), or *Least-squares Spectrum* is a version of a discrete Fourier transform, differing from the DFT only in the normalisation of the returned power. Formally it is an implementation of a least-squares fitting, defined such than a commensurate oscillation (i.e., one in which an integer number of periods are seen) with an amplitude of 1 in the time domain has a peak with an amplitude of 1 in the amplitude spectrum, and a power of 1 in the power-density spectrum. The method shown here is taken from Karoff (2008).

Considering a single sine wave, we can set up a model for this oscillation:

$$x_i = \alpha \cos(2\pi\nu t_i) + \beta \sin(2\pi\nu t_i), \tag{5.8}$$

this is equivalent to a single sine wave with a phase offset, $x_i = A\sin(2\pi\nu t_i + \delta)$, where we have $A = \sqrt{(\alpha^2 + \beta^2)}$, and $\delta = \tan^{-1}(\alpha/\beta)$.

The parameters α and β are calculated by performing a least-squares fit, i.e., by minimisation of the following equation:

$$S(\nu) = \sum_i (x_i - f_i)^2 = \sum_i (x_i - [\alpha \cos(2\pi\nu t_i) + \beta \sin(2\pi\nu t_i)])^2, \tag{5.9}$$

as α and β are the only free parameters in the above equation, the minimum may be found where:

$$\frac{\partial S}{\partial \alpha} = \frac{\partial S}{\partial \beta} = 0. \tag{5.10}$$

This leads to two simultaneous equations, expressible in terms of various sums of sines, cosines, and the data points. Defining the following identities for convenience:

$$\begin{aligned}
XC &= \sum_i x_i \cos(2\pi\nu t_i), && (5.11)\\
XS &= \sum_i x_i \sin(2\pi\nu t_i), && (5.12)\\
SS &= \sum_i \sin^2(2\pi\nu t_i), && (5.13)\\
CC &= \sum_i \cos^2(2\pi\nu t_i), && (5.14)\\
CS &= \sum_i \cos(2\pi\nu t_i) \sin(2\pi\nu t_i). && (5.15)
\end{aligned}$$

we find that α and β may be expressed as follows:

$$\begin{aligned}
\alpha(\nu) &= \frac{SS \cdot XC - CS \cdot XS}{CC \cdot SS - CS^2} && (5.16)\\
\beta(\nu) &= \frac{CC \cdot XS - CS \cdot XC}{CC \cdot SS - CS^2} && (5.17)
\end{aligned}$$

The least-squares power spectrum can then be obtained as:

$$P(\nu) = \alpha(\nu)^2 + \beta(\nu)^2. \tag{5.18}$$

As noted a major advantage of the synthesis method is that it will natively deal with unevenly sampled data - no attempt is made to interpolate or re-grid the original observations. One can also choose the frequencies at which to sample the data, for instance choosing to consider a region of the spectrum in which an interesting feature is noted at a higher-resolution. However, the effects of aliasing by the window will still be present due to the time-structuring of the data, and a single oscillation may still produce multiple peaks in a power spectrum.

If data points have a different associated statistical error - for instance having been gathered at different sites, or by different instruments - this can be easily included in the above equation, for instance by pre-multiplying XC and XS by normalised errors. Errors may even be used to optimise data for alternative purposes, for instance Arentoft et al. (2009) ‘tune’ the errors on the stars α Cen A, α Cen B and β Hyi in order to minimise side-lobes caused by the window.

5.2 The CLEAN algorithm

The CLEAN algorithm as described below is based upon the initial description by Högbom (1974). This has been modified into a one dimensional form for use in timeseries analysis of oscillations.

A periodogram analysis of a periodic signal is performed to identify the strongest oscillation present within a chosen frequency range, i.e., that which shows the greatest amplitude. A sine-wave of the amplitude and phase of the strongest oscillations identified is subtracted from each data-point in the time-domain.

$$x'(t_i) = x(t_i) - A\sin(2\pi\nu + \phi) \tag{5.19}$$

where $x'(t_i)$ is the modified timeseries, $x(t_i)$ is the original timeseries, and A, ν and ϕ are the amplitude, frequency and phase of the removed oscillation. By this method the power at a given frequency will be removed from a dataset. This has the complementary effect of removing the alias peaks in the power-domain that arise as an consequence of the window.

As an example of the progressive use of the CLEAN algorithm as implemented by PERIOD04 is shown in Figures 5.6 and 5.7. The top part of figure 5.7 shows the amplitude spectrum of the β Cephei star ν Eri between 5.5 and 6.0 cycles per day. Four modes exist in this region, a prominent single spike at a location of approximately 5.76 d^{-1}, and a triplet of modes at 5.62, 5.63 and 5.66 d^{-1}.

Looking at the timeseries both prior to, and after CLEANing of the prominent frequencies

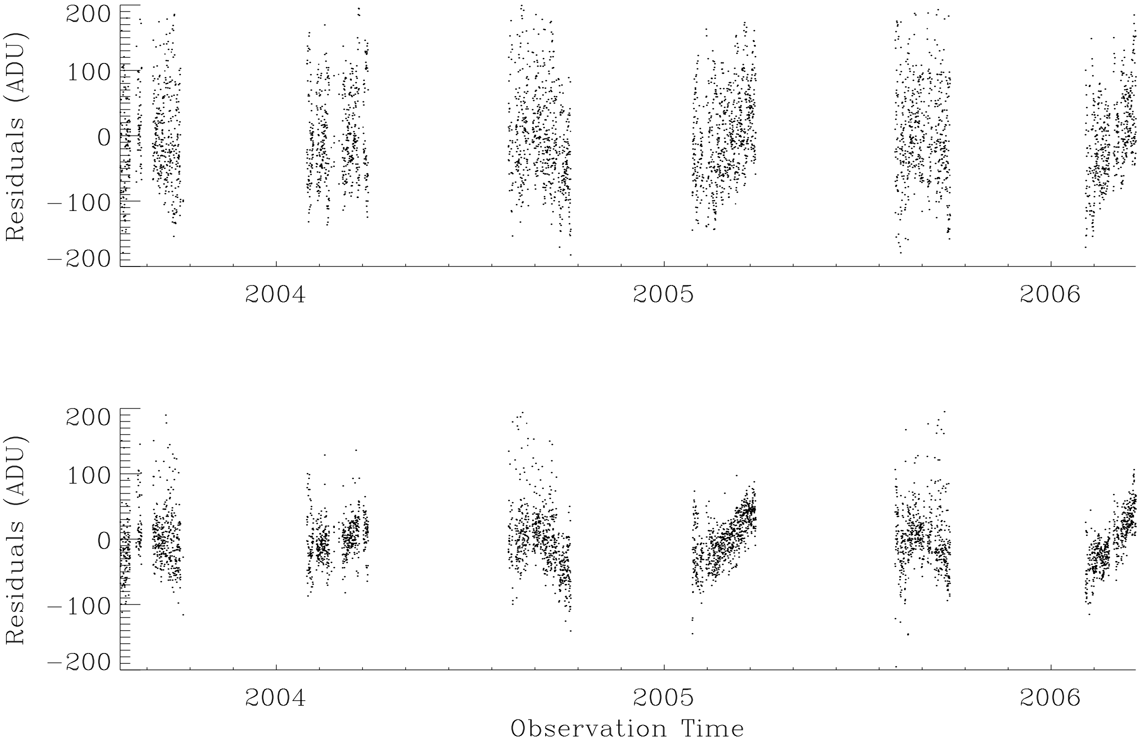

Figure 5.6: Time series of the β Cephei star ν Eri. Data prior to cleaning are shown in the topmost plot, and data post cleaning are shown in the lower plot. The scatter on the data can be noted to be much diminished between the two after having removed the four oscillations noted in the text.

identified above, as shown in Figure 5.6, one can note the scatter on the data has been greatly reduced by the CLEAN processing. As only these four frequencies have been removed, the strong annual harmonics present in the SMEI data of some stars can be easily observed.

It can be seen that the single spike at 5.76 d^{-1} is considerably altered by convolution with the spectral window (which is shown in the bottom of Figure 5.7, and is on the same horizontal scale as the plots above it in the Figure), presenting a series of five spikes with a spacing of approximately 0.055 d^{-1}, i.e., reflecting the time distribution of the data with one observation season every six-months. Further scatter occurs in the spectral window as a result of aperiodic gaps in the timeseries, leading to the random background.

5.3 Whitening in the power-domain

The CLEAN algorithm is an excellent means of whitening when an oscillation may be well described by a coherent sine wave. However, where an oscillation shows a lifetime, and therefore has a width in frequency space, a single sine wave cannot adequately represent an oscillation.

Where there is a background to data (instrumental or stellar in origin) we can no longer assume χ^2 with two-degrees of freedom statistics in the power-domain. Instead the data will show noise with χ^2 with two-degrees of freedom statistics around a limit spectrum, where the limit spectrum is the background. It is therefore possible to ‘pre-whiten’ a series in the power-domain by dividing throughout by a model of the background. This will result in a whitened spectrum, with a mean power of 1.0, that shows χ^2 with two degrees of freedom statistics.

An exemplum of this process is seen in Figure 5.4. Here a model of noise-with-a-memory, i.e., a brown noise model (topmost plot of the Figure), which shows a power-law background has had a power-model fitted to the data (second row of plots in the figure). The resulting statistics, seen at the bottom of the figure, show that this process has resulted in a whitened timeseries showing χ^2 with two-degrees of freedom statistics.

5.4 Fitting Procedure

When fitting a background model one needs to be aware of the statistics underlying the distribution of noise. If the noise is distributed normally (i.e., the signal seen at a single point is

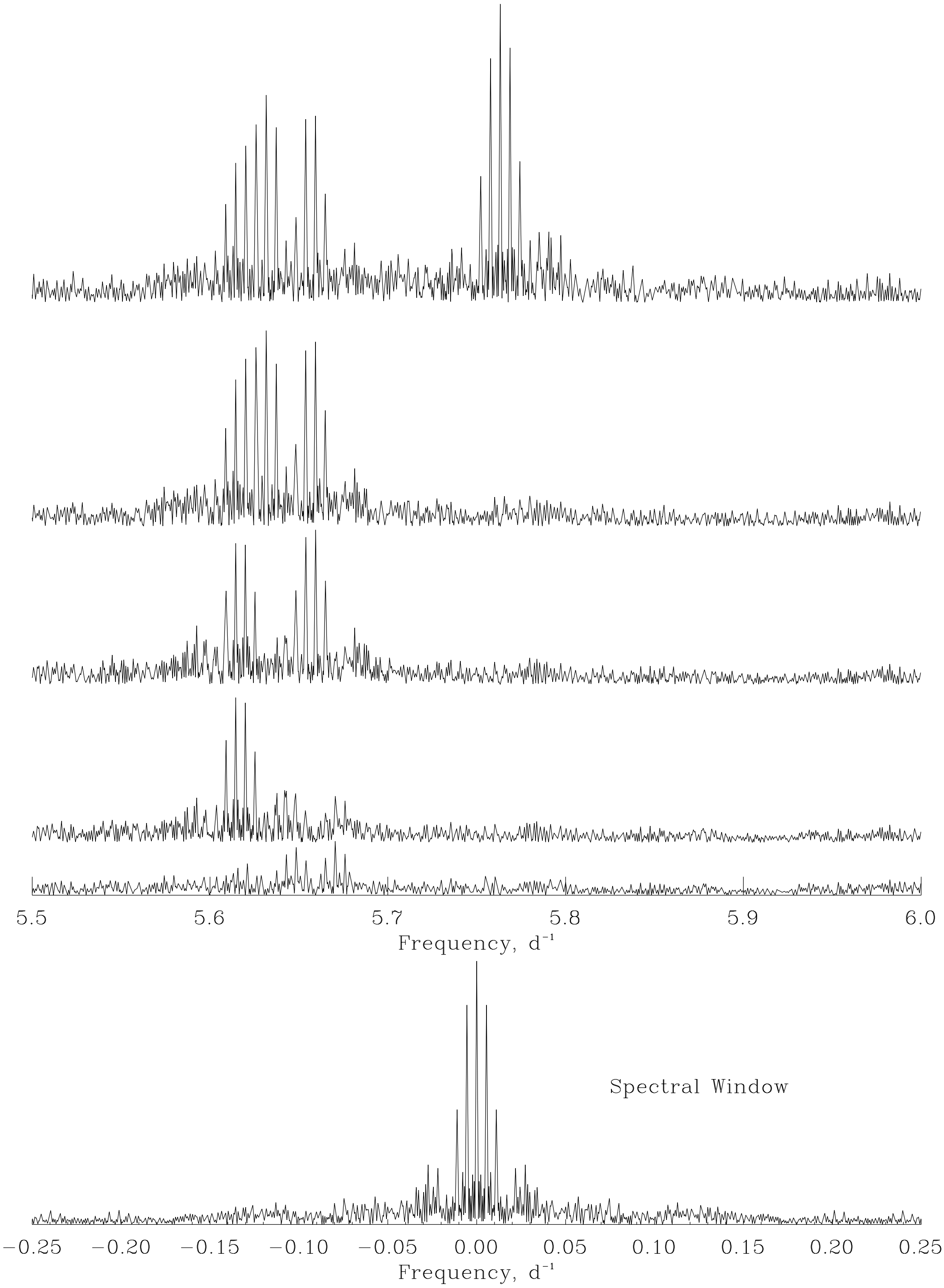

Figure 5.7: Data on the β Cephei star ν Eri, showing the effects of the CLEAN algorithm in the power domain. The top-most plot is the raw data from which oscillations has been progressively removed in lower power-spectra.

governed by a Gaussian distribution), then the probability of a particular value matching the predicted result is given by:

$$P(x_i) = \frac{1}{\sigma_i\sqrt{2\pi}} \exp\left(\frac{-(x_i - M(\mathbf{a})_i)^2}{2\sigma_i^2}\right), \tag{5.20}$$

in which x_i is the observed data, $M(\mathbf{a})_i$ is the model describing the data at a given point, i, described by parameters $\mathbf{a}$, and σ_i is the error on the datapoint.

In order to obtain the best fit between the observed data and the model, the values of a which maximise the probability in Equation 5.20, taken as a product over all data, must be maximised;

$$L = \prod_i P(x_i), \tag{5.21}$$

where L is the likelihood function.

In practice it is easier to maximise the sum of the logarithm of the probability;

$$\ln(L) = -\frac{1}{2}\sum_i \left[\frac{(x_i - M(\mathbf{a})_i)}{\sigma_i}\right]^2 - \sum_i \ln(\sigma_i\sqrt{2\pi}), \tag{5.22}$$

hence, in order to maximise the likelihood, one must minimise the quantity:

$$\sum_i \left[\frac{(x_i - M(\mathbf{a})_i)}{\sigma_i}\right]^2. \tag{5.23}$$

This is simply the weighted sum of the squared differences. Thence the method of ‘least squares’ fitting can be shown to produce a maximum likelihood estimation where errors are normally distributed.

However, a whitened power spectrum will show a noise-distribution consistent with χ^2 with two degrees of freedom statistics. This means that the probability of a particular value matching the predicted result is given by:

$$P(x_i) = \frac{1}{M(\mathbf{a})_i} \exp\left(\frac{-x_i}{M(\mathbf{a})_i}\right), \tag{5.24}$$

and the maximum likelihood estimator is given by:

$$-\ln(L) = \sum_i \left(\ln[M(\mathbf{a})_i] + \frac{x_i}{M(\mathbf{a})_i} \right) = S. \tag{5.25}$$

Maximising the likelihood, L, as defined here is equivalent to minimising the parameter S.

Mode width and height are typically strongly anti-correlated, as a reasonable value for the likelihood coefficient may be found by a model showing a tall, thin, feature fitting to the strongest spike within a broad mode, or a broad, flat feature which fits to the background power (with a corresponding reduction in the apparent background).

The problems with a fitting failing are often reduced by restricting the range of the fitting to a smaller number of bins, centred on the mode frequency. For instance by fixing the model used for the background, and performing the summation in Equation 5.25 over only those bins within one large-frequency-spacing of the frequency of a mode. Further improvements to the quality of a fitting can be achieved by ensuring that the parameters are fit in the best parameter space (for instance it is better to fit some parameters as their logarithms). Finally one may alter the direction of the fitting vectors - for instance requiring that if the mode height is increased, then the width will show a decrease - maintaining the power of the mode.

In order to produce the best fitting to the data, close to the location of maximum likelihood the parameter space of the model should show a simple peak, i.e. a Gaussian-like profile. However, as noted in Section 5.7, the statistics regarding the level of power found in a bin are not governed by Gaussian errors, and it is not surprising that the parameters linked to power, for instance the mode amplitude and background-power, do not have a Gaussian profile in parameter space.

Duvall and Harvey (1986) report that under the conditions of a sufficiently small change in the parameters and a long-timeseries, then the parameter space will be Gaussian if the width, amplitude and background power are seen in logarithmic space. Therefore it is accepted practice that these parameters are fitted as their logarithms.

5.5 Error and uncertainties

The helio- and asteroseismic parameters returned by a fitting are directly used to infer properties of the internal structure of the body under study. However, the reliability of the properties we infer will be dependent upon the accuracy and precision of the parameters determined. Therefore determining a reliable estimate of the uncertainty associated with the parameters is both useful and important to the field.

5.5.1 The Hessian matrix

A Hessian matrix consists of elements given by:

$$h_{k,l} \equiv \frac{\partial^2 S}{\partial a_k \partial a_l}, \tag{5.26}$$

where $S = -\ln(L)$, the likelihood function, the vector $\mathbf{a}$ is the model parameters, and k and l give the corresponding matrix elements. The inverse of this matrix is then taken to give an estimate of the uncertainties on the fitted parameters. Substituting our expression for the likelihood function of the χ^2 distribution, Equation 5.25, gives the following:

$$h_{k,l} = \sum_i \frac{M(\nu_i) - P(\nu_i)}{M(\nu_i)^2} \frac{\partial^2 M}{\partial a_k \partial a_l} + \frac{2P(\nu_i) - M(\nu_i)}{M(\nu_i)^3} \frac{\partial M}{\partial a_k} \frac{\partial M}{\partial a_l}. \tag{5.27}$$

This expression may be evaluated numerically when performing a fitting.

When evaluating the parameters of the Hessian matrix numerically we must choose a value for the change applied to the parameter, i.e., Δa_k. Where a problem is well stated then, given a small enough change in a model parameter, the derivative calculated numerically will tend asymptotically to the true derivative, i.e., $\Delta M/\Delta a_k$ will tend to $\partial M/\partial a_k$.

It has been found that for the giant stars studied in this thesis the errors returned by a Hessian matrix are not consistent when a different change in the parameter, i.e., if a different value for Δa_k, is taken, a different error will be returned. This may indicate that the problem is not mathematically well-stated, and the errors returned from the Hessian are not a reliable estimate of the errors. Therefore an alternate approach has been taken to generate errors, based upon numerical simulations with a Monte Carlo method.

5.5.2 Monte Carlo simulation

When performing a Monte Carlo simulation to derive errors on fitted parameters, one assumes that the model which has been fitted to the data is correct, and then explores how the returned parameters would vary for different realisations of noise.

For instance, if one is fitting a model, $M(\mathbf{a})$, described by a vector of values $\mathbf{a}$, to a set of data-points, x_i, and one wishes to determine the errors on the values, $\mathbf{a}$, then one creates a new simulated set of data points, x'_i, given by:

$$x'_i = F(M(\mathbf{a})_i, R_i)), \tag{5.28}$$

in which R_i is a random variable, and $F(M, R)$ is a function described by the probability distribution of errors. In the case of Gaussian distributed errors, with a point-wise standard deviation of σ_i, the equation for x'_i is given by:

$$x'_i = M(\mathbf{a})_i + \sigma_i R_i, \tag{5.29}$$

in which R_i is a Gaussian distributed random variable, with a mean of zero, and a standard deviation of 1; i.e., in this case our simulated data will be the sum of the model and a Gaussian distributed error. In the case of a timeseries showing χ^2 with two degrees of freedom statistics, x'_i is given by:

$$x'_i = -M(\mathbf{a})_i \cdot \ln(R_i), \tag{5.30}$$

in which R_i is a uniformly distributed random variable between zero and one. The natural logarithm function will transform this into a variable between zero and infinity that shows the required negative exponential distribution.

Thus a Monte Carlo simulation allows one to implicitly explore the parameter space of the model by considering what would happen to each parameter if fitted to a simulated dataset that shows similar noise characteristics to the original dataset. It will also test the efficacy of the fitting procedure. There may exist realisations of noise for which the fitting technique will not produce an appropriate representation of the power spectrum. If this is the case it is likely that at least one such realisation will occur within a simulated dataset. This may indicate that the model we are fitting is not appropriate - i.e. that it does not reflect the underlying structure of the power spectrum.

Monte Carlo simulations suffer from problems where the fitting fails to produce an adequate representation of the power spectrum. For instance as noted above it is not unusual for a fitting to latch onto a single, sharp peak or to fit to the background rather than the feature we have identified as an oscillation. In this case it is arguable that the individual simulation in question is not fitting to the feature, and if such fittings are included within those used to determine the error upon a parameter, then the errors returned will be an overestimate.

5.5.3 Multiple determinations

Perhaps the most reliable estimate of the errors associated with a fitted parameter is to calculate multiple independent determinations of the fitting. For instance, often for a star with SMEI we have data gathered by both camera #1 and #2, and for other datasets one may choose to subdivide the timeseries. An estimate of the errors can then be determined by considering the spread of values returned by these estimates.

However, the frequencies and amplitudes of modes may alter over time as an effect of stellar cycles (e.g Broomhall et al. 2009b). This may result in an over-estimate of the error associated with a frequency and amplitude, but more importantly if one is ignorant of this effect, one may miss interesting science associated with the presence of these changes.

5.6 Identifying stochastically excited oscillations

The turbulent motions in convection zones stochastically excite modes in solar-like oscillators. The same process will also act to suppress, or damp the oscillations.

It is possible to model such a system using a damped harmonic oscillator;

$$\frac{\mathrm{d}^2}{\mathrm{d}t^2}x(t) + 2\eta\frac{\mathrm{d}}{\mathrm{d}t} + (2\pi\nu_0)^2x(t) = f(t) \tag{5.31}$$

in which $x(t)$ is the displacement; ν_0 is the natural frequency of the undamped oscillator; η is a constant describing the damping; and $f(t)$ is a random forcing function (i.e., the effect of the convection). For a single mode $f(t)$ can either be assumed to be a delta function, when considering a single excitation, or else may be assumed to be nearly white, as the solar granulation background will not vary much over the range in which we are interested - i.e., a few times the width of a mode.

Applying a Fourier transform yields the power-frequency response of an oscillator:

$$X(\omega) = \frac{F(\omega)}{\omega_0^2 - \omega^2 + 2i\eta\omega}, \tag{5.32}$$

where $X(\omega)$ and $F(\omega)$ are the transforms of $x(t)$ and $f(t)$ respectively. In the case of $f(t)$ being a delta function, $F(\omega)$ will be a constant value, and where $f(t)$ is a white-noise source the limit spectrum will be a constant value. As observations are only taken over a finite time, this function should be modulated by the transform of a 'top-hat' function, i.e., a sinc squared function (see Section 5.7, Figure 5.10 on page 115), however this factor will be ignored in the forthcoming analysis as it will only become significant where the lifetime is comparable to the length of the observations.

Taking the power spectrum, $P(\omega) = |X(\omega)|^2$, we find that:

$$P(\omega) = \frac{H}{(\omega_0^2 - \omega^2)^2 + 4\eta^2\omega^2}; \tag{5.33}$$

in which H is a parameter describing the amplitude of the mode. In the limit that the damping time-scale is long in comparison with the frequency of the oscillation, i.e., $|\eta| << \omega$, that the oscillations are of high quality (i.e. the mode lifetime is long in comparison with the period), and observations are taken for longer than the mode lifetime. This will simplify Equation 5.33 to a Lorentzian profile:

$$P(\omega) = \frac{H}{(\omega - \omega_0)^2 + \eta^2}, \tag{5.34}$$

where H is once again a parameter describing the amplitude of the mode, distinct from the H defined for the full resonant profile.

When examining stellar data, stochastically excited oscillations may be determined by examination of their properties in both the frequency and time domain.

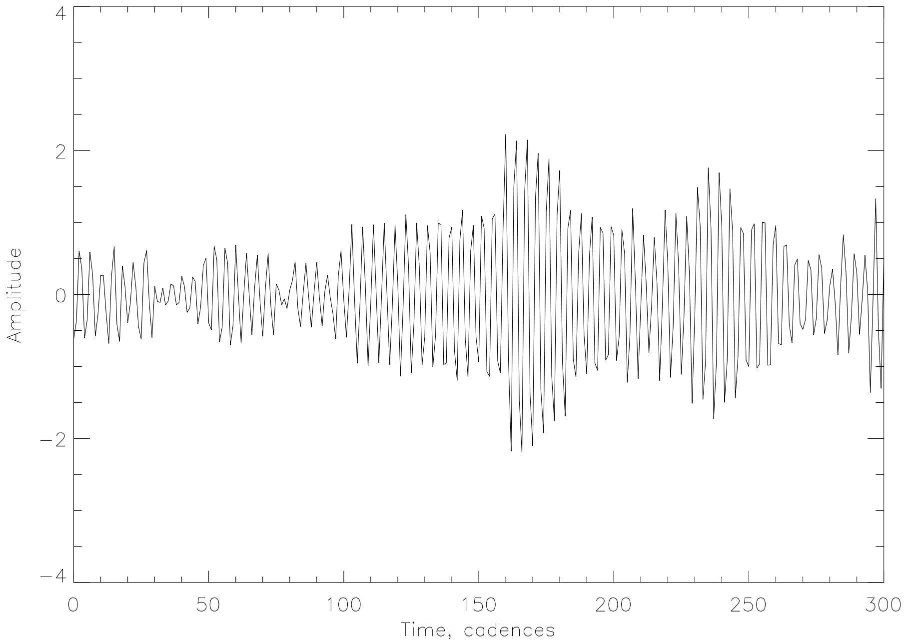

Figure 5.8: A stochastic oscillation, seen in the time domain. The amplitude of the oscillation can be observed to vary in amplitude, and phase over a time-scale of roughly 100 cadences.

In the time domain a stochastically excited oscillation, as seen in Figure 5.8, can be observed to vary in amplitude and phase between periods. This is due to the random nature of the forcing function, which will cause the amplitude of the oscillation to periodically rise and fall. The lifetime over which the forcing remains in phase with the oscillation is inversely proportional to the value of η, i.e., the damping.

In the frequency domain a stochastically excited oscillation, as seen in Figure 5.9, will show a width in frequency, i.e., the power of the oscillation will be spread over more than a single bin.

5.7 Statistical testing

Consider the form of a discrete Fourier transform;

$$X_k = \sum_{n=0}^{N-1} x_n e^{-\frac{2\pi i}{N}kn}, \tag{5.35}$$

in which all symbols have their standard meanings. The only noise source here will be in x_n, as $e^{-\frac{2\pi i}{N}kn}$ is exact. Assuming that each datapoint is statistically independent, we can calculate the error on X_k using techniques of error propagation. However, $e^{-\frac{2\pi i}{N}kn}$ will consist of both

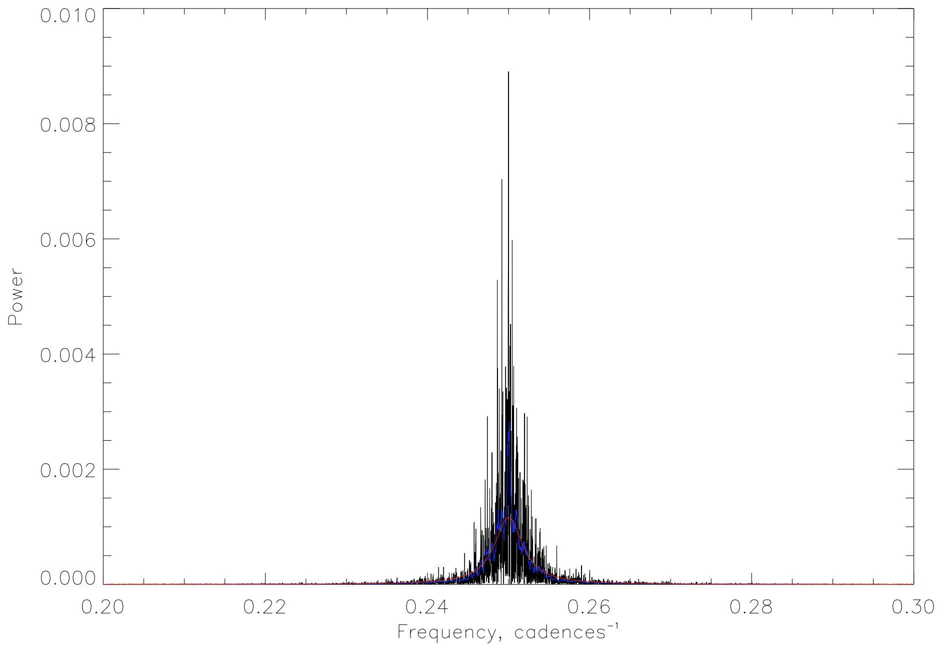

Figure 5.9: A stochastic oscillation observed in the frequency domain. Here the black shows the raw data, the blue shows the raw data smoothed over 21 bins, and the red shows a fitted Lorentzian

real and imaginary parts which must be treated separately.

If the errors on each data point, $\sigma(x_n)$, are Gaussian distributed, then both the real and imaginary parts of the error of the transform, $\sigma(X_k)$, will also be Gaussian distributed (the sum of two Gaussian distributions being a Gaussian distribution). Thence, the power spectrum, $\Re(X_k)^2 + \Im(X_k)^2$, will show the statistics of the sum of two squared-Gaussians, that is χ^2 with two degrees of freedom statistics.

The general form of the χ^2 distribution is as follows:

$$P(x) = \frac{(1/2)^{k/2}}{\Gamma(k/2)} x^{k/2-1} e^{-x/2}, \tag{5.36}$$

in which k is the number of degrees of freedom, $\Gamma(k/2)$ is the Gamma function, and x is the power seen at a given frequency. However this form will have a mean value of k, and in general one will work with normalised spectra with a mean value of 1, thence we can modify the expression as follows:

$$P(x) = \frac{(1/2)^{k/2}}{\Gamma(k/2)} \left(\frac{x}{k}\right)^{k/2-1} e^{-x/2k}, \tag{5.37}$$

where the number of degrees of freedom of our χ^2 distribution is equal to 2, this expression simplifies to the negative exponential distribution;

$$P(x) = \exp\left(\frac{-x}{\langle x\rangle}\right). \tag{5.38}$$

The probability of observing in a given bin a power equal to, or greater than a given value, y will thence be:

$$P(\geq y) = 1 - \int_{x=0}^{x=y} P(x)\mathrm{d}x = \exp(-y). \tag{5.39}$$

To determine the probability of observing at least r such bins across a range of N bins in the spectrum one makes use of a cumulative binomial (Bernoulli) distribution.

$$P(r; p(y); N) = \sum_{r=r}^{N} p(y)^r [1 - p(y)]^{N-r} \frac{N!}{r!(N-r)!}. \tag{5.40}$$

Where $r = 1$, and $p(y)$ is sufficiently small, this can be approximated by the expression $P(1; p(y); N) \approx Np(y)$.

As discussed in Section 5.3, data which do not show Gaussian white-noise can be whitened in the power-domain by means of dividing throughout by a model of the background fitted to the data. Therefore tests based upon the assumption of χ^2 with two degrees of freedom statistics can be applied even if it is known that noise is non-white.

A number of statistical tests may be applied to a whitened power spectrum, to detect whether any notable deviations from the noise background occur:

- Within a single bin (a ‘spike’);
- Within a small number of adjacent bins (adjacent spikes);
- Within a number of bins within a range of bins (spikes-in-a-range);
- Summed across a wide number of bins (a ‘lump’).

The statistical test is what is called a ‘false-alarm’ probability, i.e., the chance of observing a given feature as a result of a white-noise background, not the chance the a given feature arising as the result of an oscillation.

The conceptually most simple test is to observe where the power within a single bin rises above a given probability threshold, $p_{\rm thr}$ to form a spike in the power spectrum. Working backwards from the approximate form of Equation 5.40, and Equation 5.39 we can find that:

$$P(\text{Spike}) \leq p_{\rm thr} = Np(y) = N\exp(-y), \tag{5.41}$$

thence, for a spike to be significant at $p_{\rm thr}$, we need it to rise to above y times the mean power, where y is given by:

$$y = \ln N - \ln p_{\rm thr}. \tag{5.42}$$

So, for a spectrum of 100 bins ($N = 100$), a spike is required to rise about 6.91, 7.60 and 9.21 times the mean power for respectively a probability of 10, 5 and 1%, while for a spectrum of 1000 bins the thresholds are 9.21, 9.90 and 11.51 times the mean power.

The second test observes where the power in two or more adjacent bins rises above a given probability threshold, $p_{\rm thr}$. As we are working under the assumption that the power in the two bins is statistically independent, the chances of two bins each rising above a value, y, will be:

$$p(\text{2 adjacent bins above y}) = \exp(-y)\cdot\exp(-y) = \exp(-y)^2 = \exp(-2y), \tag{5.43}$$

and in general, for k adjacent bins rising above y,

$$p(\text{k adjacent bins above y}) = \exp(-ky). \tag{5.44}$$

One again, working backwards from Equation 5.40, we find that the threshold value of y is given by:

$$y = \frac{\ln N - \ln p_{\rm thr}}{k}, \tag{5.45}$$

i.e., a simple linear scaling with k compared to the single bin case.

5.7.1 The value of N

In all statistical tests described above the value of N, the number of independent frequencies, plays a prominent rôle in determining the changes of a feature being observed. For a series with 100% fill and regular spacing, the value N simply consists of half the number of datapoints in the timeseries. However, due to the correlations between bins, the value of N in timeseries with gaps, or equivalently a timeseries taken on an irregular grid, is not intuitively obvious.

Overpadding a timeseries refers to extending a timeseries by the addition of zeros. When taking the transform of the resultant timeseries this has the effect of sampling at intermediate frequencies, i.e., of oversampling the transform. An overpadding factor of p will refer to multiplying the length a timeseries by p, i.e., the addition of $p-1$ times the original length of the timeseries in zeros.

Figure 5.10 shows how over-sampling can affect the structure of a power spectrum, showing a single oscillation. If a pure-sine wave oscillation is present in a timeseries, in the Fourier domain this will show a delta function at the frequency of the oscillation. As practically observations will be taken over a finite period, this delta function will be convolved with the transform of the observation window, a 'top hat' function, and the oscillation will therefore show a sinc squared function of width 1/T. At the critical frequencies (i.e., integer multiples of $1/T$), this will have an amplitude of 0.0, and so shows that the power observed at the critical frequencies is independent.

Where there is more than a single oscillation present in data over-padding can cause the tallest peak to appear higher than any seen in the critically sampled periodogram. Figure 5.11 reveals the interaction of two adjacent critical frequencies. In this figure, one should envision a power spectrum in which the bins at ±0.5 units have a power of 1.0, and all other bins have a power of 0.0. At frequencies between the critical frequencies the form of the power spectrum will be dependent on the relative phase of the two bins at ±0.5 units. The coloured lines show the effect of the phase on the power spectrum. The darkest blue line shows where the power in the two bins is in-phase; while the vivid red line shows where the power in the bins is in anti-phase.

It can be seen that under these circumstances the power at intermediate frequencies between two bins can rise to just over 1.6 times the power of each bin, or fall to nothing. Thus if one were to over-sample a power spectrum it likely that one would see features which pass the threshold for significance due to constructive interference between the power in adjacent bins.

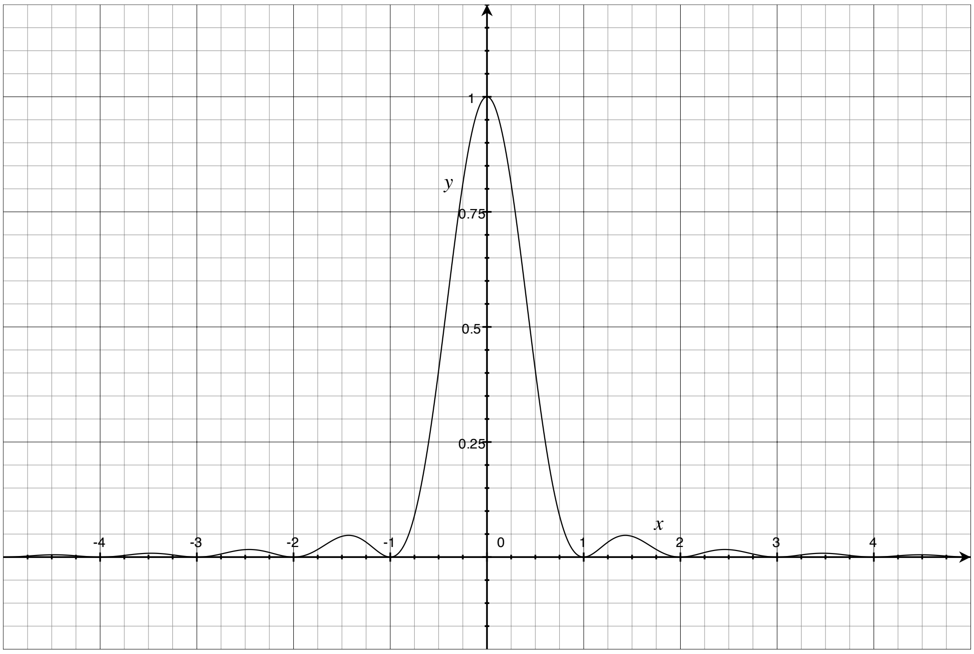

Figure 5.10: Oversampling a single peak. It can be seen that the functional form is that of a sinc^2 (sinc(x) = sin(x)/x) function. A FFT would sample this curve at the critical frequencies, x=±1,2,3...; at which the amplitude of the sinc^2 function is zero, demonstrating that critical frequencies are indeed independent of each other.

The situation will become still worse when more than a pair of bins is under consideration. By summing a sufficient number of bins with an appropriate phase relationship it is possible to create a peak of arbitrary size.

In an over-sampled power spectrum we must therefore re-evaluate the statistics of the distribution, and the number of independent frequencies, N, of the spectrum. Figure 5.12 compares the histograms of a critically sampled (black), and 16 times over sampled (red) power spectrum with the expected χ^2 with two degrees of freedom statistics (blue). Here 256 simulations have been performed, each consisting of 2^{20} (just over 1 million) points, histograms made of each, and each histogram summed to produce the histogram shown in the Figure. It can be seen that the two histograms are both identical with each other, and with the expected χ^2 with two degrees of freedom statistics.

These results show that the distribution of power in single bins in unaffected by oversampling. A power spectrum which has been oversampled by 16 times will have 16 times as many bins passing a given criterion as the critically sampled power series.

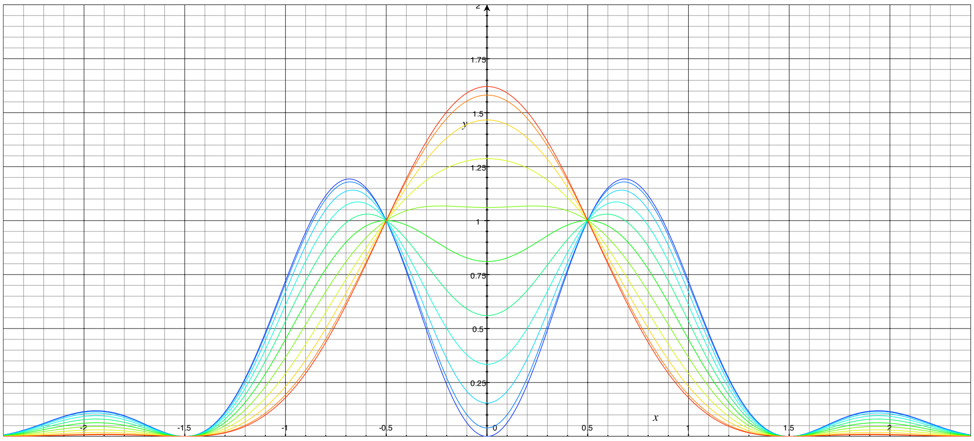

Figure 5.11: Where multiple peaks are present in a power spectrum the tallest peak can rise above that in the critically sampled power spectrum. Here two Fourier bins would be located at ±0.5 units along the x axis. It can be seen that the amplitude of two can sum together to reach a significantly greater power than the amplitude of either bin.

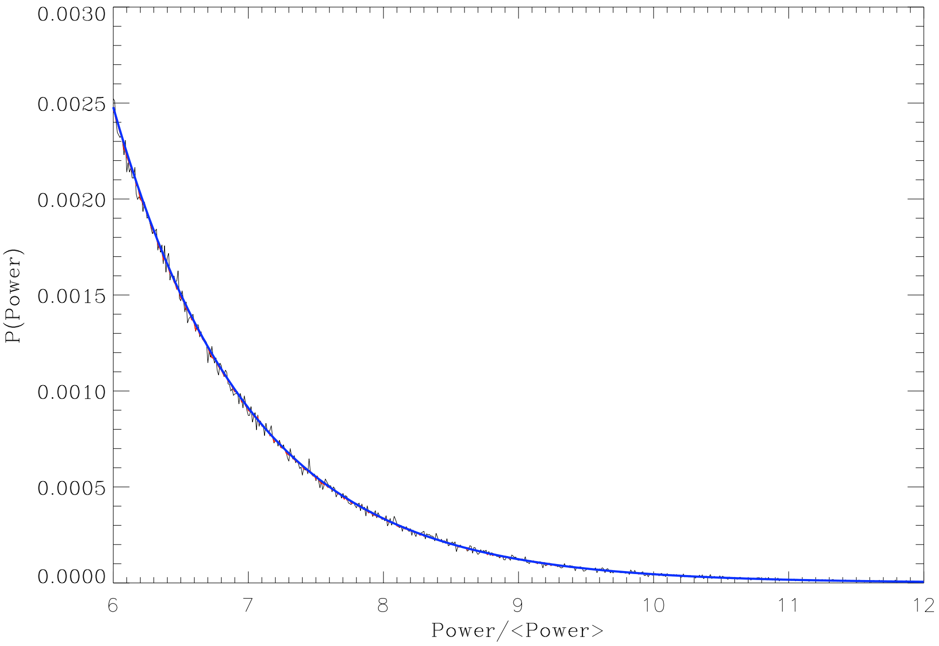

Figure 5.12: The statistics of an over-sampled timeseries. Here, shown in black is a histogram of a timeseries of white noise with 100% fill, red is the same data, having been over sampled by 16 times ($p = 16$), and blue the theoretical prediction ($P(\text{Power}) = \exp(-P/\langle P \rangle)$)

Table 5.1: Values for the padding factor as given by Gabriel et al. (2002) .

Padding Factor, n	p Factor
1	1.0
3	2.4
5	2.8
6	2.9
7	2.9

5.7.2 Overpadding and features

In general we are not interested in the number of bins passing a threshold, but rather the number of 'events' or 'features' which are significant. If we see a peak like that shown in figure 5.11, we would identify this as being the signature of a single oscillation, that at maximum rose above 1.5 in the units of the y-axis, and would not be interested that there were, say, 4 oversampled-bins above this level.

Gabriel et al. (2002) consider the chances of at least a single bin rising above a threshold power, m. Here the probability, $P(m)$ will follow the χ^2 with two degrees of freedom statistics; $P(m) = e^{-m}$; thence the probability of a bin being lower than m ($Q(m)$) is given by $Q(m) = 1 - P(m) = 1 - e^{-m}$. Assuming that each bin is independent the probability of no bin in a range of N bins showing power at a level greater than m will be:

$$Q_N(m) = Q(m)^N = (1 - e^{-m})^N, \tag{5.46}$$

and in the event of oversampling the probability of at least one peak having a power greater than m will be given by the modified expression:

$$P_N(m) = 1 - (1 - e^{-m})^{pN}. \tag{5.47}$$

in which p is a padding factor.

In this case we find that the padding factor does not simply equal the amount by which the spectrum has been oversampled. Gabriel et al. (2002) give values for the padding factor as shown in Table 5.1.

In order to test and confirm these results independent tests were carried out with varying degrees of oversampling, and observing the number of power spectra in which at least one event

Table 5.2: Values determined for the oversampling factor. Values at powers of 2.0 were determined through simulations, while other values, highlighted in italics, have been interpolated to allow a direct comparison between this, and Table 5.1

Padding Factor, n	p Factor
1	1.000
2	1.875
3	*2.475*
4	2.940
5	*3.172*
6	*3.344*
7	*3.411*
8	3.458
16	3.611

surpassed a number of given threshold in comparison to the number which would be expected by Equation 5.47. In each of 2^{20} (approximately one million) simulations, a time-series consisting of 2^{14} (approximately 16,000) points showing a white noise distribution of power was constructed. Given these numbers we may anticipate that small-number effects are insignificant for all but the highest thresholds.

Figure 5.13 shows how the ratio of the number of spectra in which a bin surpassed the threshold in an oversampled timeseries versus the number in the same critically sampled time-series. As it can be seen the ratio tends asymptotically to a fixed value at high power-levels. However, the pattern appears to differ slightly from that expected by Equation 5.47, shown by the dot-dashed lines in Figure 5.13.

Table 5.2 shows the values of the over-padding factor determined from these simulations. It can be noted that these differ significantly from the values given Gabriel et al. (2002). This suggests that the asymptotic values may be dependent on the number of points within the spectrum, and should perhaps be calculated on a case-by-case basis.

5.7.3 The 4.0 signal-to-noise test

In asteroseismology it is common to use a signal-to-noise of 4.0 in amplitude as the critical threshold for significance (a criterion established by Breger et al. (1993)). This criterion takes no account of the number of datapoints under consideration. As the amplitude spectrum will be the square-root of the power spectrum it will follow a different statistical distribution, the χ

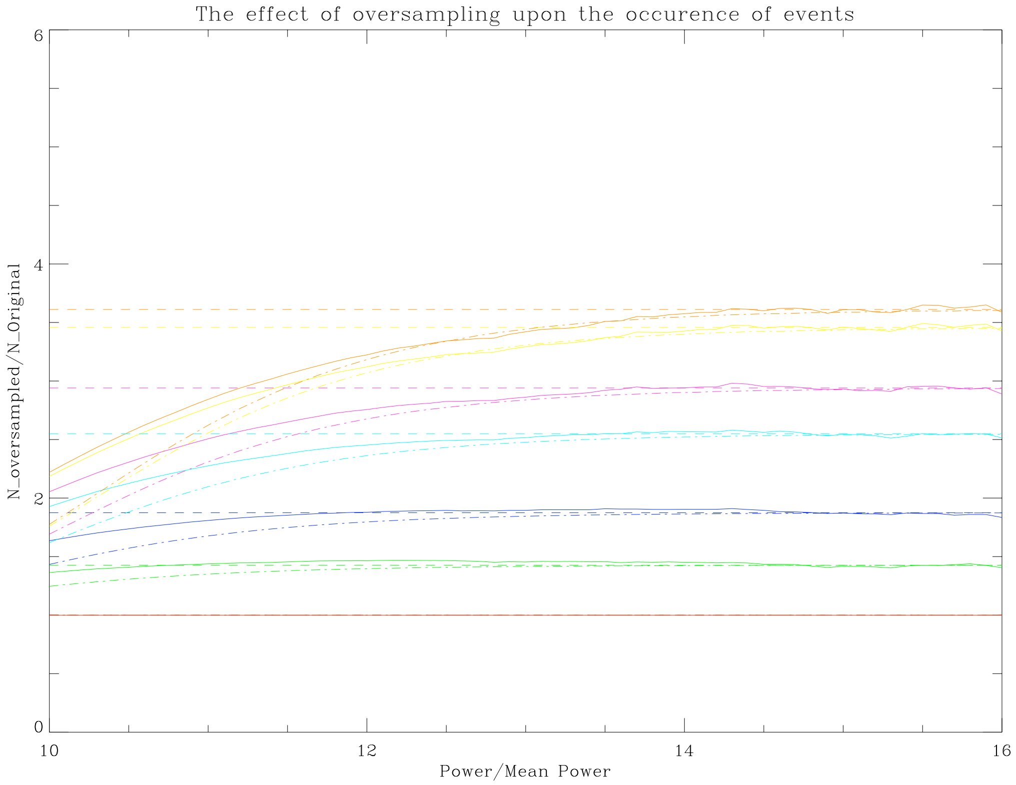

Figure 5.13: The effects of oversampling upon the number of oscillations observed to be above a given threshold. Degrees of oversampling are indicated by the colour used: 16 - orange, 8 - yellow, 4 - magenta, 3 - cyan, 2 - blue, 1.5 - green.

distribution. This has a cumulative distribution function of:

$$P(\geq x, k) = \frac{\gamma(k/2, x^2/2)}{\Gamma(k/2)}, \tag{5.48}$$

in which $\gamma(k/2, x^2/2)$ is the 'lower incomplete gamma function', $\gamma(s, x) = \int\limits_0^x t^{s-1}e^{-t}\mathrm{d}t$. In the case of the χ distribution with two-degrees of freedom this simplifies to:

$$P(\geq x) = 1 - e^{\frac{x^2}{2}} \tag{5.49}$$

When we determine the value of signal-to-noise, this is relative to the local mean power. In units of the dummy variable, x in the above distribution the mean value of the χ distribution is given by;

$$\mu = \sqrt{2}\frac{\Gamma((k+1)/2)}{\Gamma(k/2)}, \tag{5.50}$$

therefore a bin with a signal to noise of 4.0 in a two-degrees of freedom amplitude spectrum will have a value of the dummy variable of $x = 4.0 \times \sqrt{2}\Gamma(1.5)/\Gamma(1.0) = \sqrt{8\pi} \approx 5.01$. Substituting this into the cumulative probability distribution, and one find that, $P(S/N \geq 4.0)$ is 3.48763×10^{-6}.

Using the cumulative binomial distribution (Equation 5.40 on page 112) we can estimate numbers of points at which this will correspond to certain probability thresholds. It turns out that if it is required that a spike is significant at a 1% criterion, then fewer than 2 280 bins must be present; for a 5% criterion fewer than around 14 700 bins must be present, and for a 10% criterion fewer than around 30 000 bins must be present.

This bodes well for the 4.0 S/N test - to date few asteroseismic datasets have exceeded a few thousand bins. However, as the subject comes of age with datasets of long duration it may become appropriate to reconsider whether a single observation at such a signal to noise is sufficient to determine the presence of a mode. For instance a 3.5 year, long-cadence Kepler dataset may be anticipated to have of the order of 60 000 individual observations.

However, the results of Section 5.7.2 should be considered in the case of an oversampled timeseries. In this case it may be appropriate to adopt a more stringent test for significance due to the padding factor of the over-sampling, ideally simulating the spectrum with Monte Carlo simulations to determine an appropriate value for a significance threshold.

Chapter 6

Results: Pulsations in Giant Stars

Oscillations have been observed in a number of G and K-class red-giant stars (see Bedding and Kjeldsen 2006, and references therein). The oscillations appear to be Sun-like in nature (Frandsen et al. 2002, De Ridder et al. 2006, Barban et al. 2007), meaning they are stochastically excited by convection.

As the frequency of modes will scale in inverse proportion to the radius squared (Equation 3.25 on page 52), giant stars will in general have modes with periods that are significantly longer than those observed in main-sequence stars, of the order of hours or days. The long periods of these modes make the asteroseismology of giants accessible to the relatively low cadence observations of SMEI and similar instruments.

The observation of individual modes of oscillation may be a non-trivial problem for red giants. The spacings in frequency between radial overtones are anticipated to scale as the square root of the mean density (Equation 3.38 on page 55) of the star, and can therefore can be expected to be small. Therefore, observations taken over a lengthy period, of the order of months to years, are required in order to clearly separate the modes in frequency. As the SMEI instrument has timeseries of over five years in length, it is well placed to study giant stars.

Recently there has been discussion regarding whether mode-damping is strong in giant stars (e.g. Stello et al. 2006). If this is the case, the damping may be strong enough to cause neighbouring modes to overlap significantly in frequency, complicating the analysis. However, more recent observations, such as those taken at higher signal-to-noise with CoRoT (De Ridder et al. 2009) have shown that at least some giant stars have modes with long lifetimes.

It had been thought that only the radial acoustic (p) modes would be present in the oscillation spectra (Dziembowski et al. 2001) of giant stars. However a number of recent observations (e.g.

Hekker et al. 2006, De Ridder et al. 2009), along with theoretical calculations (Dupret et al. 2009), imply that non-radial modes are to be expected in giants. If the lifetimes are brief in comparison with the spacings, the presence of these non-radial modes would add to the difficulties in resolving individual modes in the spectrum of a giant star.

6.1 Arcturus

Arcturus, α Boo, is a bright K1.5III giant star with an age of approximately 4.5 billion years. The star has been the subject of a number of observing campaigns that have studied its variability: observations of Arcturus made from the ground in Doppler velocity (e.g. Innis et al. 1988, Belmonte et al. 1990, Hatzes and Cochran 1994, Merline 1995), and from space in photometric intensity (e.g. Retter et al. 2003). These campaigns have uncovered evidence for variability with periodicity of the order of a few days, and amplitude of $\approx$100 ms^{-1} in velocity, or a few parts-per-thousand in brightness. These periods correspond to frequencies of a few micro-Hertz, and are close to predictions for acoustic modes based on estimates of the mass, radius and effective temperature of Arcturus (see Table 6.1).

Studies by Hatzes and Cochran (1993), Brown et al. (2008) have also suggest the presence of long-term periodic changes in the Doppler velocity of Arcturus, such as that which might be associated with the expected rotational period of the star of a few hundred days, a result which has been confirmed by ongoing observations at Lick Observatory, University of California (Hekker, private communication).

While Arcturus is, indisputably, a variable star, no studies to date have presented convincing evidence for the identification of *individual* modes of oscillation. It was our intention to use the SMEI data in an attempt to determine whether such modes could indeed be resolved.

6.1.1 Data

The initial dataset for Arcturus was composed of a three-year timeseries covering the time span from April 2003 to March 2006. Figure 6.1 on page 126 shows the data for the two Cameras, # 1 and # 2. The point-to-point scatter in the data were computed from the high-frequency noise, and estimated to be approximated 1.5 ppt, consistent with independent estimates made by Steven Spreckley who developed the pipeline (Spreckley, private communication).

Table 6.1: Stellar parameters for Arcturus. Here the luminosity has been calculated based on the effective temperature and interferometric radius, and the asteroseismology predictions are based upon the scaling laws of Kjeldsen and Bedding (see also Section 3.5 on page 49).

Parameter	Value
Astronomical observables:	
Parallax [1]	$88.82 \pm 0.53\,\mathrm{mas}$
$\mathrm{V}_{\mathrm{mag}}$ [2]	-0.05 (no error given)
B-V [1]	1.239 ± 0.006
Angular Diameter [3]	$21.0 \pm 0.2\,\mathrm{mas}$
[Fe/H] [5]	-0.55 ± 0.03
Stellar Values:	
Distance	$11.26 \pm 0.07\,\mathrm{pc}$
Effective Temperature [4]	$4290 \pm 30\,\mathrm{K}$
Radius (interferometric)	$25.4 \pm 0.3\,\mathrm{R}_{\odot}$
Luminosity	$196 \pm 10\,\mathrm{L}_{\odot}$
Param 1.0[6] Values:	
Age	$9.1 \pm 2.0\,\mathrm{Ga}$
Mass	$0.984 \pm 0.065\,\mathrm{M}_{\odot}$
Radius	$22.9 \pm 0.8\,\mathrm{R}_{\odot}$
Asteroseismology predictions:	
Frequency of maximum power, ν_{max}	$6.1 \pm 1.8\ \mu\mathrm{Hz}$
Overtone of maximum power, n_{max}	4 ± 1
Large frequency spacing, $\Delta\nu$	$1.15 \pm 0.3\ \mu\mathrm{Hz}$
Maximum predicted RMS amplitude in SMEI; $\delta L/L$ (700 nm)	$1300 \pm 600\,\mathrm{ppm}$

[1] from the revised Hipparcos catalogue (van Leeuwen 2007b)

[2] from the Hipparcos catalogue (Perryman et al. 1997)

[3] from Quirrenbach et al. (1996)

[4] from Griffin and Lynas-Gray (1999)

[5] from an average of Cenarro et al. (2007), Soubiran et al. (2008) [6] see da Silva et al. (2006)

Due to Arcturus being reasonably close to the ecliptic (+19° 10′ 57″), Arcturus was visible with Camera # 1 for approximately 120 consecutive days each year, followed by a gap of approximately 240 days until it next entered the camera, i.e., an annual cycle. Within each of the observing seasons around 60 % of the datapoints were usable, with the remaining points having been rejected in the processing pipeline due to instrument failures or having excessive noise. Over the full 812.2 day length of the dataset, (i.e., including the gaps) the fill was 25.6 %.

Arcturus was visible in Camera # 2 for periods of approximately 60 consecutive days twice annually, with approximately 120 days gaps between each period of observation. Within each of the periods in which Arcturus was observed by Camera # 2, typically 70 % of the data were usable, and the fill was 23.1 % over the 975.7 day full-length of the dataset.

There appear to be some long-term variations in brightness observed in our Arcturus dataset (Figure 6.1), continuing between cameras. However as annual cycles have been noted in SMEI data (Section 4.3 on page 67) it may be that these variations correspond to a local, and not stellar effect.

6.1.2 Initial analysis

An initial analysis of variability in Arcturus was carried out using data gathered with revision one of the SMEI data processing pipeline.

Figure 6.2 on page 127 shows power-density spectra for the two cameras of SMEI. The two SMEI cameras view the stars during distinct time periods, and therefore can be used as quasi-independent observations of the periodic behaviour of the star. In common with a number of SMEI stars, Camera # 1 shows a prominent spike of power at a period of 11.57 μHz, corresponding to a period of 1 cycle per day. Both cameras also have a spike of smaller height at 23.14 μHz (2 cycles per day).

The window spectra are inset into each of these figures, showing that these are heavily dominated by the box-car nature of the observation windows - i.e the 60 or 120 days of observation, followed by a 120 or 240 day break, in a cycle of 180 or 360 days in length. This results in strong aliases at 0.03 μHz ($=[360\ \text{days}]^{-1}$) in the case of Camera # 1, and 0.06 μHz ($=[180\ \text{days}]^{-1}$) in the case of Camera # 2.

Taking a preliminary look at the data in Figure 6.2 on page 127 one can note a broad

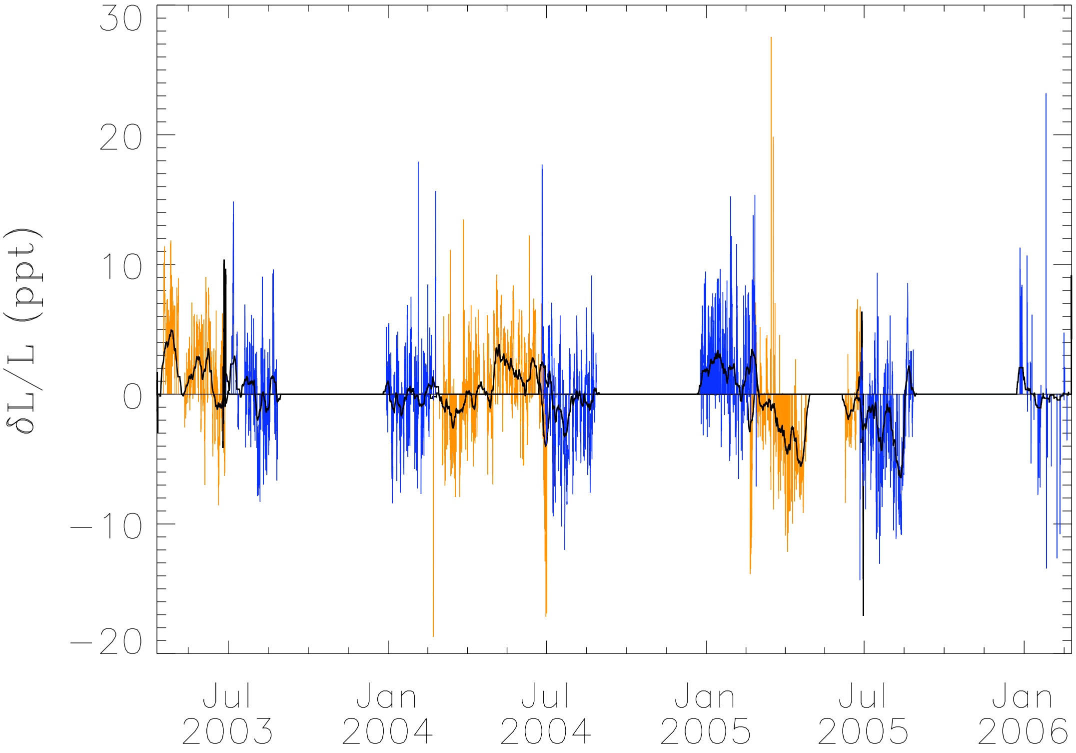

Figure 6.1: The SMEI light curve of Arcturus generated using data from Camera # 1 (orange) and # 2 (blue). The black line illustrates a box-car smoothed representation of the timeseries with a smoothing width of approximately 7 days.

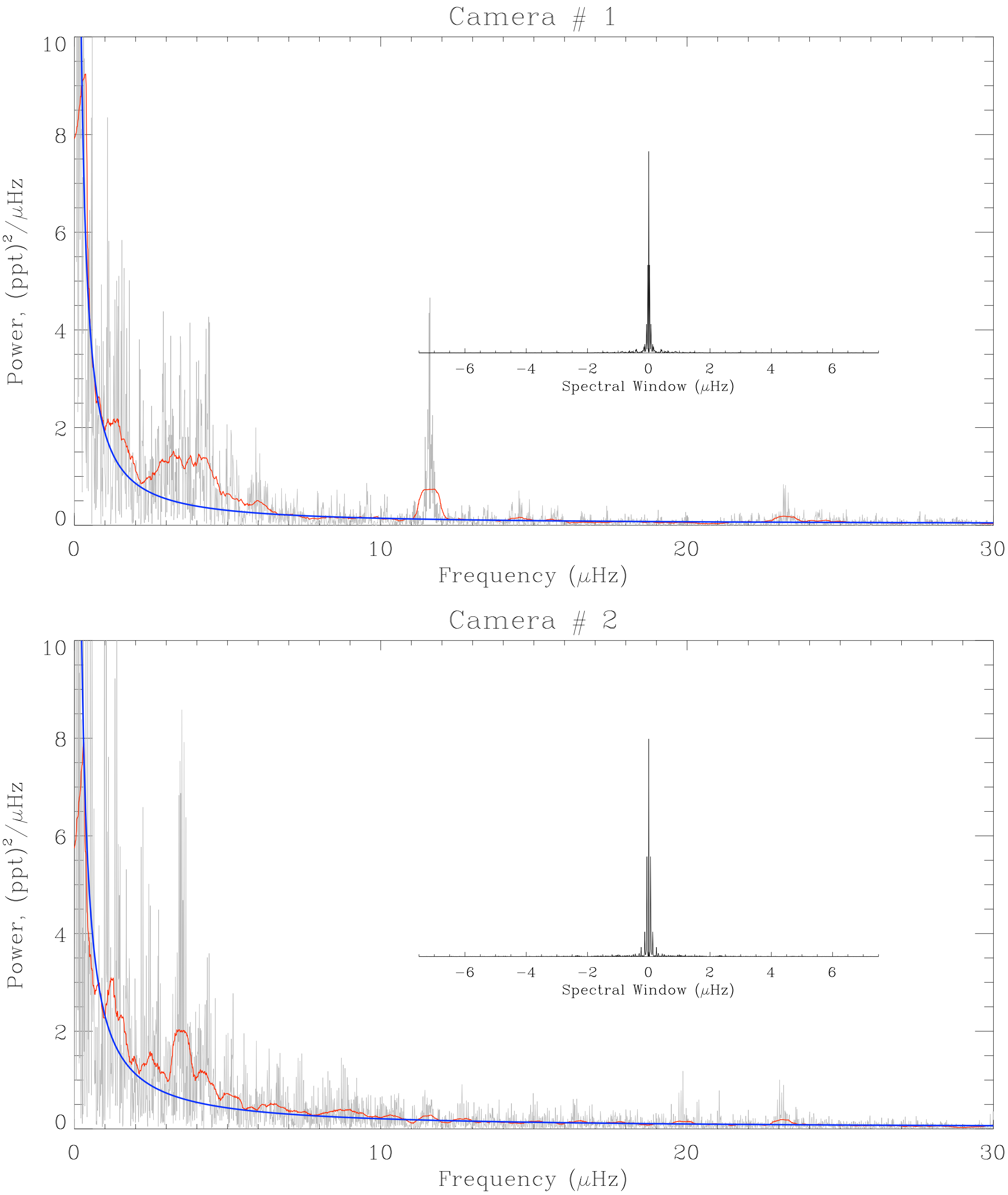

Figure 6.2: The power density spectra of the two cameras from SMEI. Here the raw spectrum is shown in grey, a smoothed representation of the spectrum in red, and a power-law model fitted to the background is shown in blue.

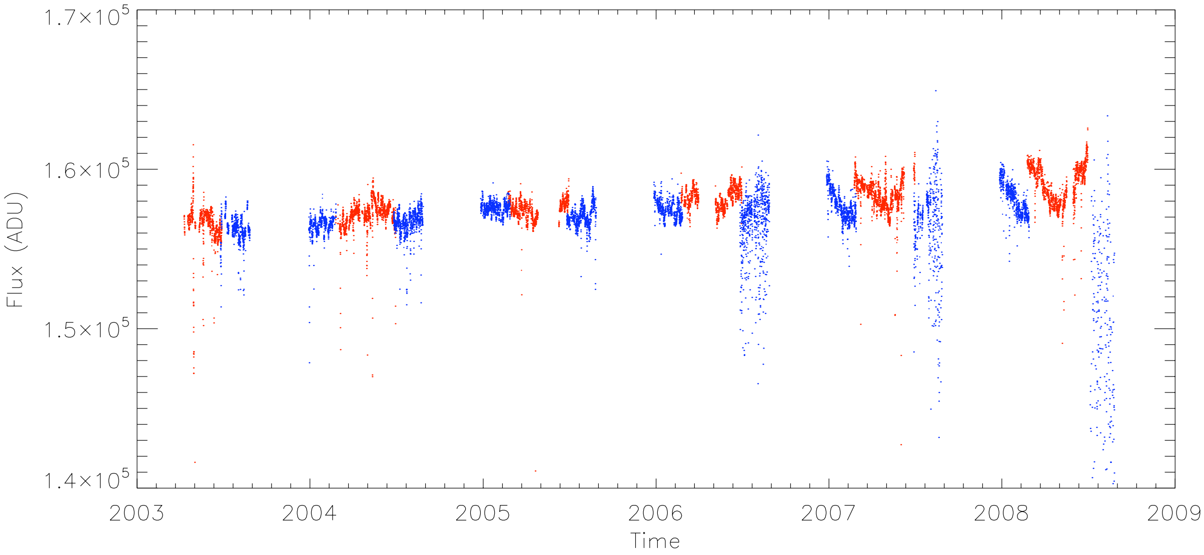

Figure 6.3: The SMEI light curve of Arcturus for the revised timeseries. Data collected with Camera #1 is shown in red, and data collected with Camera #2 is show in blue.

concentration of power above the background located between roughly 2 and 6.5 μHz, which is present in data gathered with both cameras.

Results, based upon this initial analysis, were published in Tarrant et al. (2007) (attached as Appendix B.1 on page 174), reporting the discovery of a single mode of oscillation in Arcturus, with a frequency of $\nu = 3.51 \pm 0.03$ μHz and a lifetime of $\tau = 24 \pm 1$ day.

6.1.3 Re-analysis

After the publication of Tarrant et al. (2007) the pipeline was refined and extended by Steve Spreckley (Pipeline # 1 and # 3). A new version of the timeseries was generated which consisted of five years of data, taken between Julian dates 2452816.28 (2003 June 25) and 2454705.06 (2008 August 26). A timeseries of the revised data is show in Figure 6.3. Increased scatter during the later periods of observations can be observed in camera # 2 (see Chapter 4 on page 61 for further details on the reasons behind this).

Figure 6.4 shows data from a single observation season for Camera # 2 which have been processed with both the old and revised pipeline . It can be seen that the broad periodic trends in the data-points appear to roughly correspond between the two datasets - i.e., where the first set shows a rising flux in the smoothed timeseries, the smoothed second set will also show a rising flux. The scatter around the underlying trend on the data from the revised version of the

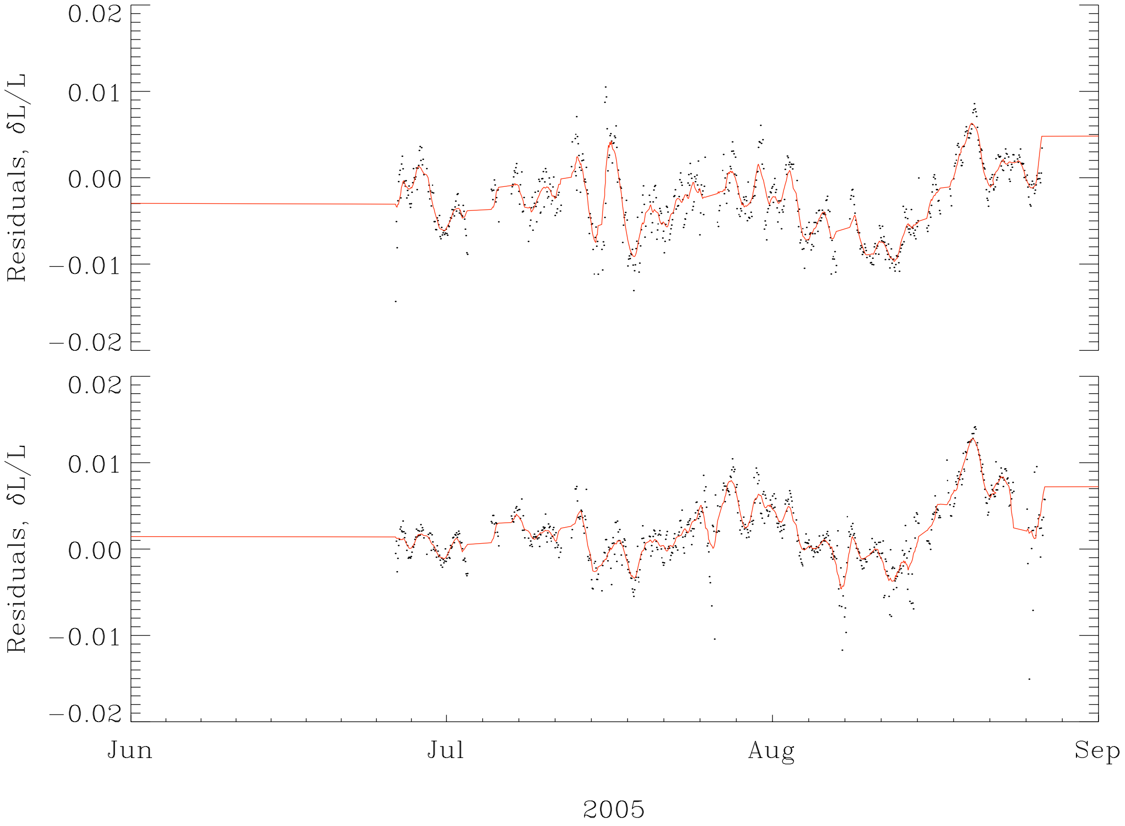

Figure 6.4: Simultaneous periods of observation of Arcturus taken with the old (top) and new (bottom) versions of the pipeline.

pipeline is lower than that on the earlier revision.

However, when considering the respective power spectra of the old and new data, when taken over comparable time periods (i.e., disregarding the additional two years of data in the revised timeseries) a distinct change was noted in the region of interest in Camera # 2, where the posited mode had been observed. Power spectra of the data processed with the former (top) and revised (bottom) pipelines can be seen in Figure 6.5.

One immediately notices that the feature at approximately 3.5 μHz which was strongly visible in the Camera # 2 dataset generated with Pipeline # 1 is no longer present in the Pipeline # 3 data. As this feature had been labelled an oscillatory mode, the absence in the revised data immediately causes alarm. Can any features noted in SMEI data be trusted to be stellar in origin? The following section will discuss this feature, it s origins and the issues it raises regarding SMEI data.

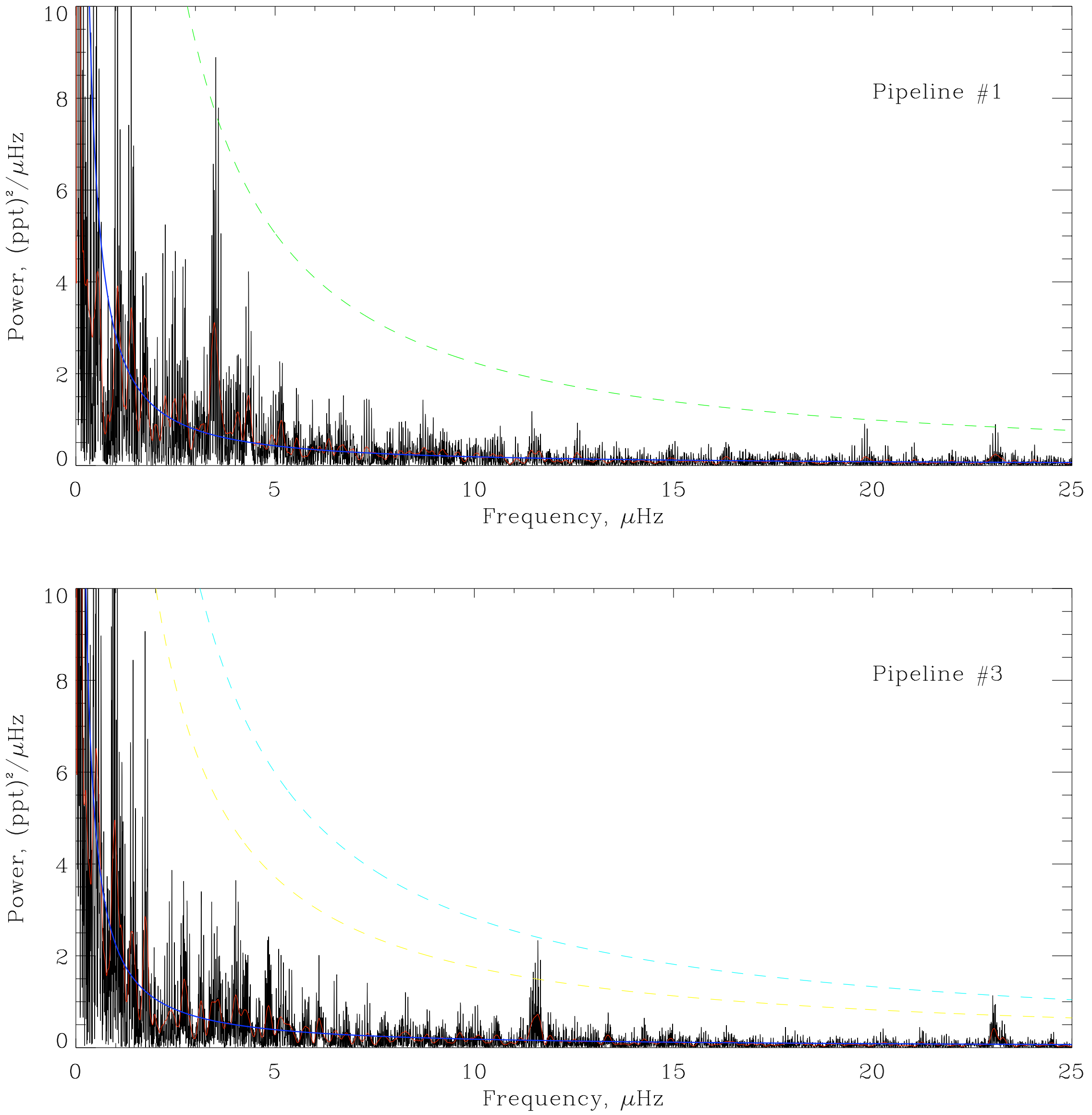

Figure 6.5: Comparison of the SMEI Arcturus data generated with the former (top), and revised (bottom) pipeline. The prominent concentration of power noted at approximately 3.5 μHz in the former, Pipeline # 1 data can be seen to rise above the probability threshold for a single spike (dotted green line, top plot), however in the revised, Pipeline # 3 data the concentration of power can be seen to be no longer present. Assuming the revised data to be accurate, we can set a threshold on the level of variability present in Arcturus - the orange dotted line showing this threshold if noise is incoherent with the signal, and the cyan dotted line if noise is coherent with the signal.

The origin of Arcturus power-spectra changes

A number of origins may be speculated to cause the changes in the power spectrum noted above:

- A change in the star itself has caused the mode to no longer be visible.
- A different object is being observed in the two timeseries; for instance in the first one may be observing Arcturus, while the second observes another star in Boötis.
- An unknown change in the pipeline has caused power to be added, or removed in this frequency range.

Of these we can reject the first immediately. Data from Pipelines # 1 and # 3 cover the same time period and were generated from the same SMEI science frame images. The second hypothesis, that a different object is being observed also seems unlikely because broad trends in the timeseries are common across the two datasets. We are therefore led to conclude that it must be a change in the pipeline which has caused these changes in the power-spectra.

As the older Arcturus timeseries came from an early revision of the Spreckley pipeline, which has subsequently been lost in a series of computer failures, it is unfortunately not possible to fully analyse which change in the code has led the the loss of the signal. Nor were any datasets other than that of Arcturus maintained from this early revision to which the Arcturus data may be compared to, to determine if other stars showed the same anomaly. It therefore seems likely that it is impossible to unambiguously determine what phenomenon added power at 3.5 μHz in the earlier data, or which acts to suppress the power specifically at that frequency in the later data.

A major source of revisions to the pipeline was in the determining the position of the locations of the star in a science frame (i.e., the location in terms of the coördinates of the CCD image). As the pointing accuracy of the image is only about 0.2 bins, an additional centroiding step is taken in order to determine the location to a greater accuracy. Due to the complicated nature of the SMEI point-spread function this is not a superficial process, and a number of different centroiding methods were used over the development of the pipeline. One can imagine that if the determined centroid is not correctly aligned relative the position of the star this may introduce apparent flux changes, as respectively more or less of the flux is included within the aperture.

As the feature is broad in frequency, we can speculate that it is not a strictly periodic process which has introduced the power. A pure periodic process may have been caused by rounding errors on time stamps, or a regular influence such as changing the dark-current maps which are generated daily. A quasi-periodic process will in contrast arise where there is a process which does not repeat with a precise period. A problem with the centroiding may however show only a quasi-periodicity, as the star passes across different regions of the CCD, with subtle differences in the PSF, or sensitivity.

It should be noted that Arcturus lies within the latitude range (± 25°) for which the broad anomalous feature was identified at around 0.32 d^{-1} ($\approx 3.7\ \mu$Hz) [see Section 4.3.6 on page 78], so it may be that the feature in Arcturus shares a common origin with the anomalous feature. Arguing against this surmise is the fact that the feature in Arcturus is at a somewhat lower frequency than the anomalous feature, and that is no longer present in revised data, while the 0.32 d^{-1} anomaly remains. As we believe that the 0.32 d^{-1} anomaly is most likely introduced by the pipeline, it may be that changes to the pipeline over time have caused the frequency at which power was introduced to alter, as well as no longer introducing the power into the Arcturus timeseries.

Determining a null-detection

Given that we no longer see a single prominent mode in Arcturus, the question arises: can we say anything about the variability of Arcturus? A null-detection of variability in SMEI would enable us to set an upper limit on the height of any single mode of oscillation, and therefore set a target sensitivity for future observation programmes.

Ideally one would wish to invert the statistical tests in Section 5.7 on page 110, adopting as the H0 hypothesis that a given signal arises as a consequence of an oscillation, and as the H1 hypothesis that a given signal arises solely as a consequence of noise.

The difficulty with adopting this approach is that due to the exponential nature of the χ^2 distribution there is a significant chance that a mode will be observed at a much lower-power than the limit spectrum power. For instance there is an approximately 9.5% chance ($= 1 - \exp(-0.1)$) of a single bin being observed to show less than 10% of the limit-spectrum power. Therefore to exclude the presence of oscillations higher than a given threshold at 90% confidence would require a threshold approximately 10 times higher than the feature showing the maximum power, an unrealistically high threshold which does not provide a useful limit.

However, a sinusoidal oscillation can be expected to show a peak with constant height in the frequency domain, and therefore enables us to easily set a limit on the amplitude of any sinusoidal oscillation, by observing the maximum signal-to-noise ratio which occurs within a range of bins. In the case of a signal at an amplitude, A, with a noise level of B, the expected power, P, will be dependent upon the noise is coherent across the length of observations - i.e. periodic in the time-domain, for instance a signal caused by the day-night cycle, or incoherent, for instance photon-shot noise. In the first case the amplitudes of the noise and signal will sum, while in the second case the power of the noise and signal will sum.

$$\text{For incoherent noise:} \quad P = \quad A^2 \pm B^2, \tag{6.1}$$

$$\text{For coherent noise:} \quad P = \quad (A \pm B)^2. \tag{6.2}$$

Assuming that data from the revised pipeline is trustworthy, we can then set a threshold power based upon the spike in the power spectrum of highest signal-to-noise, which in the case of the revised Arcturus spectrum is 8.48 times the local mean noise (an amplitude of 2.91 times the mean noise amplitude). Therefore we can state that we see no evidence for a sinusoidal oscillation with a power of greater than 9.48 ($= 2.91^2 + 1^2$) times the mean power-in-noise in the case of an oscillation with incoherent noise, or 15.28 ($= (2.91 + 1)^2$) times the mean power-in-noise in the case of an oscillation with coherent noise.

Therefore, having fitted a model of the background power to the data, one can determine a limit to the height which would be shown by a sinusoidal signal. This will be frequency dependent, due to the background rising at low frequencies. These two thresholds as a function of frequency are shown in Figure 6.5 on page 130, in orange for that of incoherent noise, and cyan for that of coherent noise. As one would expect at no frequencies, apart from at the diurnal cycles, does the power rise above the threshold.

All of these values are well below the predicted amplitude for Arcturus given in 6.1. However, it should be noted that these amplitudes have been determined only for a sinusoidal oscillation, and the predicted amplitude is that of a stochastic oscillation. A stochastically excited modes shows an amplitude and phase which vary in time. As has been seem earlier this results in the

Table 6.2: Null detection thresholds for the amplitude of a sinusoidal oscillation showing the width of a single bin in the revised Arcturus dataset.

Frequency range	Limiting amplitude (incoherent noise) (ppt) [mmag]	Limiting amplitude, (coherent noise) (ppt) [mmag]
≥ 2 μHz	0.346 [0.375]	0.438 [0.476]
≥ 4 μHz	0.238 [0.258]	0.301 [0.327]
≥ 8 μHz	0.163 [0.177]	0.207 [0.224]
≥ 12 μHz	0.131 [0.142]	0.166 [0.180]

mode showing a Lorentzian profile in frequency space, with power spread across multiple bins. The amplitude associated with a stochastic mode is thus given as a function of the product of the mode width and height in the power spectrum, $\sqrt{\pi/2\Delta H}$ (in which Δ is the FWHM, and H is the height in the power-density spectra). A broad mode (i.e. one with a relatively brief lifetime) may be of high amplitude, while no single bin shows a large amplitude. It may therefore be possible for stochastic modes of an amplitude comparable to predictions to be present in the time series, if they exhibit a broad mode profile.

6.2 β UMi

β UMi, also known as Kochab, is a K4III giant on the cool side of the instability strip. Therefore we expect that β UMi will show solar-like oscillations. The star is a suspected variable, as noted by its entry in the New Catalogue of Suspected Variable Stars (NSV 6846; Kukarkin et al. 1981), however, the period and amplitude of variability have not yet been presented in the literature. Stellar parameters on β UMi, taken from the revised Hipparcos catalogue (van Leeuwen 2007a), Mozurkewich et al. (2003), and Decin et al. (2003), are shown in Table 6.3.

Using the scaling laws to make predictions for solar-like oscillations of the star, the maximum power of the modes is expected to be in the range of 3.3 to 4.7 μHz (Equation 3.25 on page 52), with a significant RMS amplitude of 1.1 to 2.1 parts per thousand (ppt) (Equation 3.21 on page 51). The large frequency spacing is expected to be between 0.6 to 0.8 μHz, small in comparison to main-sequence and other stars (Equation 3.38 on page 55).

As β UMi is at high declination (+74°), it is only observed by Camera # 2 of SMEI (that which points perpendicular to the Earth-Sun direction). The coverage by this camera was very good, with a fill of approximately 70%. The time series under consideration here was gathered

Table 6.3: Physical properties of β UMi.

Parameter	Value
Literature Values:	
Parallax [1]	24.91 ± 0.12 mas
V_{mag} [1]	2.2044 ± 0.0008
B-V [1]	1.465 ± 0.005
Mass (from evolutionary tracks) [2]	2.2 ± 0.3 $M_\odot$
Mass (from $\log g$) [2]	2.5 ± 0.9 $M_\odot$
Angular Diameter [3]	10.3 ± 0.1 mas
Derived Values:	
Distance	40.1 ± 0.2 pc
Effective Temperature[4]	4040 ± 100 K
Luminosity	475 ± 30 $L_\odot$
Radius (photometric)	43.5 ± 0.5 $R_\odot$
Radius (interferometric)	44.4 ± 0.7 $R_\odot$
Predictions:	
Frequency of maximum power, ν_{max}	4.0 ± 0.7 μHz
Large frequency spacing, $\Delta\nu$	0.7 ± 0.1 μHz
Maximum predicted RMS amplitude in SMEI, $\delta L/L$ (700 nm)	1.6 ± 0.5 ppt

[1] from the revised Hipparcos catalogue (van Leeuwen 2007a)

[2] from two determinations in Decin et al. (2003)

[3] from Mozurkewich et al. (2003) [4] from the B-V value by the tables given in Flower (1996)

between April 2003 and March 2006, with a total duration of 1056 days.

Figure 6.6 (top) shows the residual light curve of the timeseries in units of parts per thousand. The annual periodicities are pronounced in this dataset, as can be seen in a phase-folded plot (Fig. 6.6, middle) with a period of 1 year. Fits were performed up to the eighth harmonic of a year ($n = 8$) and were removed from the data by subtraction in the time domain, leading to a reduction in the RMS amplitude of the timeseries from ≈6 to ≈4 ppt.

Zooming in on a three-month section of the data between Dec 2003 and Mar 2004 (Fig. 6.6, bottom) an oscillation with a period of ≈4.6 days and an amplitude of a few ppt is clearly seen.

A power density spectrum of the timeseries is shown in Figure 6.7 on page 138. A prominent spike and concentration of power can be seen at a frequency of ≈2.5 μHz, in agreement with the strong oscillation of 4.6 days visible in the timeseries. Further spikes and concentrations of power can be seen within the range 2 to 4 μHz; in particular, the eye is drawn to three prominent features, located between approximately 2.2 to 2.6 μHz (including the above noted spike), 2.7 to 3.1 μHz, and 3.2 to 3.4 μHz. In the smoothed spectrum (red), the features at 2.2 to 2.6 μHz and 2.7 to 3.1 μHz could be construed as being composed of two or more distinct concentrations of power, dependent on the width of the smoothing.

Missing data in a timeseries can result in power being redistributed between frequencies (see Section 5.1.4 on page 92). This redistribution is represented in a plot of the spectral window, shown in Figure 6.7 on page 138 as an inset. Apart from the central peak, there are evidently no prominent spikes in the spectral window, which is very clean. However, outside of the range visible in the plot, peaks occur at the diurnal frequency of 11.57 μHz with a size of roughly one thousandth that of the central peak. Sub-harmonics of a day do not appear to be visible.

To ensure redistribution of power by the window function was not in any way responsible for the excess power observed between 2 to 4 μHz in the real power density spectrum, we created artificial data with a power-law background model – as described in the first paragraph of the results section below – to which the window function of the original data was applied. No such simulation gave any concentration of power in the region 2 to 4 μHz of comparable prominence to what is seen in the β UMi power density spectrum.

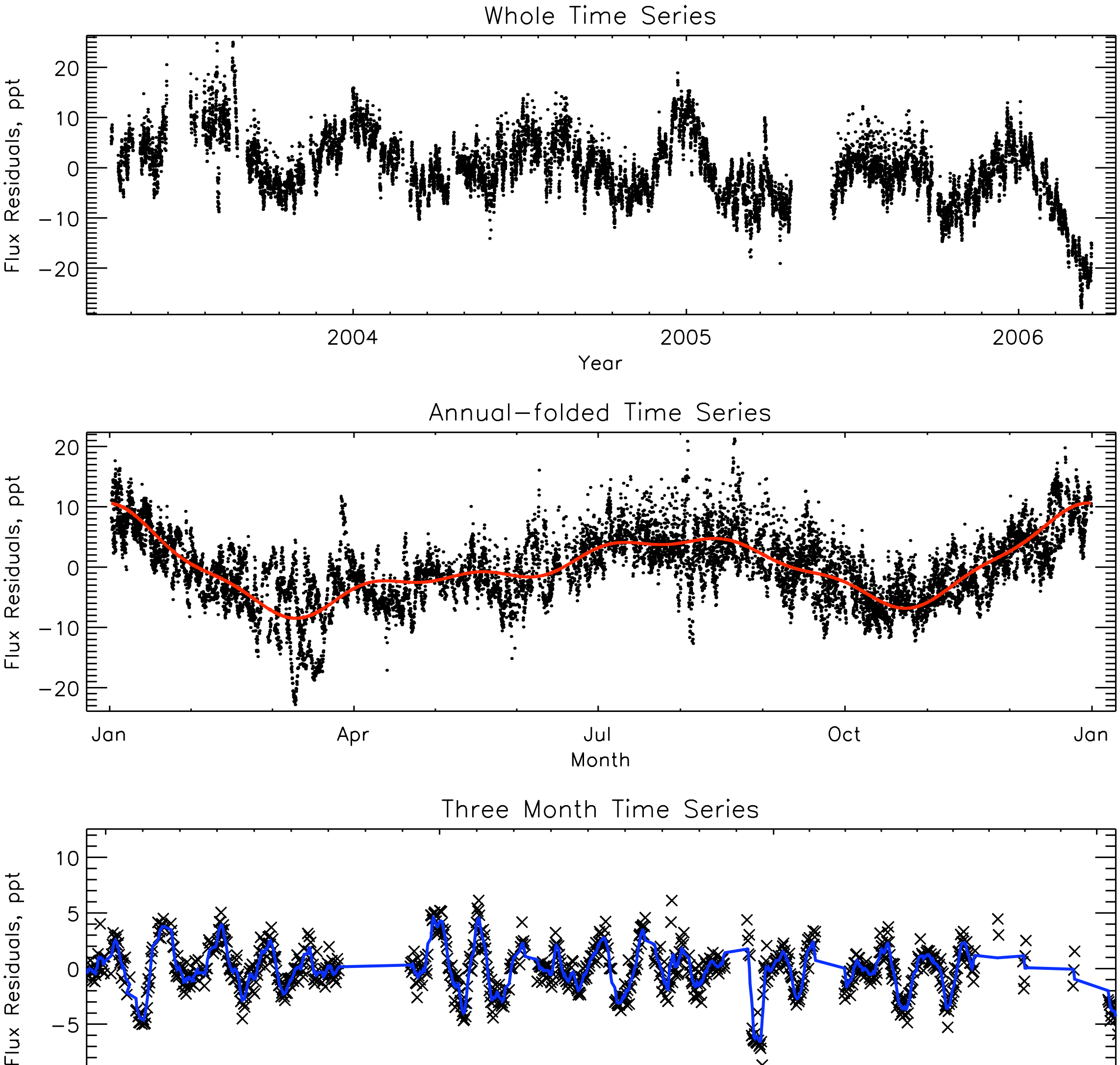

Figure 6.6: The first three years of SMEI data on β UMi. Shown are the entire timeseries (top), phase-folded over 365.26 days with the fitting to the annual cycles in red (middle), and a three month timeseries with smoothed data (blue) (bottom).

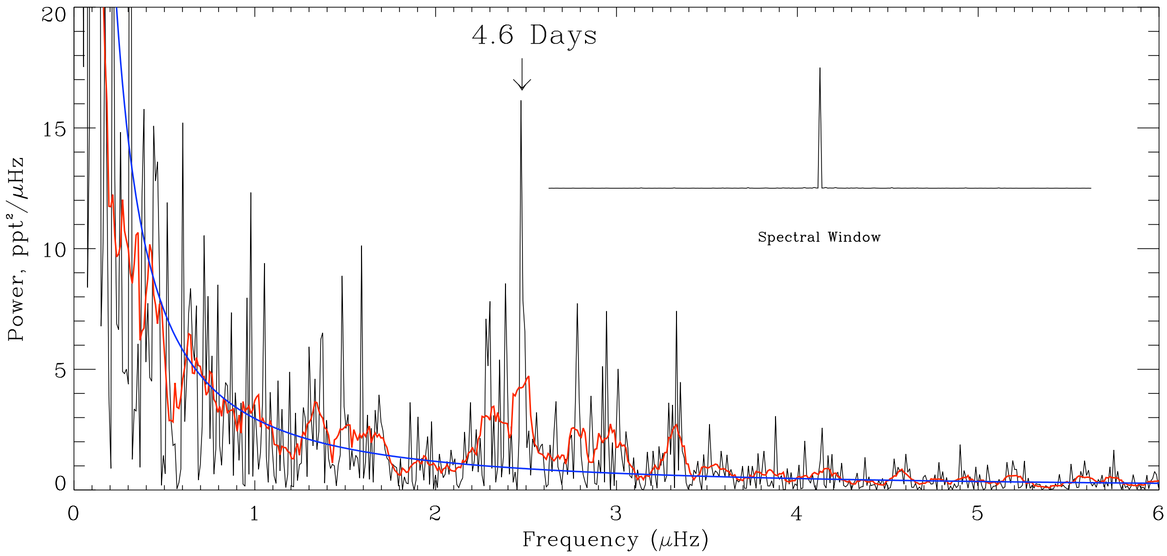

Figure 6.7: Power density spectrum with spectral window at the same frequency scale. Here the spectrum is shown in black, with a 9-bin (≈0.1 μHz), moving-mean smoothed spectrum in red, and a fitted power-law background in blue.

6.2.1 Results

Next, we applied statistical tests to determine whether the prominent features in the power density spectrum between 2 and 4 μHz could be accounted for as a product of smooth broad-band background noise. In these statistical tests the power was compared to the local background, and any significant deviations noted. In the case of β UMi, a power-law model of the form $a + b\nu^{-c}$, in which a, b, and c are parameters to be fitted, was chosen to represent the background. To account for the redistribution of power by the spectral window the background model was convolved with the spectral window, during fitting. In this way we sought to ensure that the model background gave a good representation of the actual background.

The statistical tests described in Section 5.7 on page 110, were performed upon the power density spectrum, detecting first the presence of any significant spikes over the background noise, that is, power concentrated into a single bin. This may indicate the central frequency of a sharp mode. A second test highlighted any significant concentrations of power across a narrow frequency range. This may in turn indicate a broad mode in which the power is spread over a number of adjacent bins.

Considering the spectrum as a whole and setting a probability threshold of 1% being required for significance, only one instance of a single bin with a significant excess of power was observed,

Table 6.4: Best-fitting estimates of identified modes.

Frequency (μHz)	Width **(FWHM, Δ)** (μHz)	Height [(ppt)^2/μHz]	RMS amplitude (ppt)
2.44 ± 0.04	0.2 ± 0.1	5.4 ± 2.2	1.3 ± 0.4
2.92 ± 0.05	0.2 ± 0.1	2.8 ± 1.1	0.9 ± 0.3

located at a frequency of ≈ 2.46 μHz. This bin contains 18.5 times the background power at this frequency, giving a 'false alarm' probability of lower than 0.1 %.

Considering power within ≈ 0.1 μHz ranges, three concentrations were highlighted as having less than a 1% chance of being a product of noise, by means of considering the number of bins in a range and using the χ^2 distribution with an appropriate number of degrees of freedom. These ranges were centred at approximately 2.33, 2.44, and 2.98 μHz. However, caution should be noted in the use of this test as it has been shown in Section 4.3 that for broad concentrations of power the distribution in general no longer follows the χ^2 distribution. As this phenomenon is linked to cross-correlations between bins caused by the window function, and the window function of β UMi is very clean, we should expect the anomalous phenomena to be diminished.

These results suggest that the region of excess power between 2 and 4 μHz has some structure to it. We first tested the null-hypothesis that the power between 2 and 4 μHz is represented by a single resonant peak against the hypothesis that it would be reproduced better by two peaks. This was done by fitting resonant peak profiles (by the method described below) reflecting each hypothesis, and performing a likelihood ratio test (Appourchaux et al. 1995). This revealed that fitting two resonant profiles represented a significant increase in the quality of fit over a single profile.

Next we considered each of the two broad concentrations of power, between 2.2 to 2.6 μHz and 2.7 to 3.1 μHz, respectively. We tested whether the structure of each concentration could be ascribed to the effects of noise upon a single broad mode or represent two separate narrow modes. In this case it was found that fitting two resonant profiles offered an insignificant increase in quality-of-fit over a single profile. We therefore treated each of the two concentrations of power as composed of a single broad mode.

A fitting to the features in the power density spectrum is shown in Figure 6.8 in which each of the two concentrations of power at 2.2 to 2.6 μHz and 2.7 to 3.1 μHz was fitted as a single mode by means of a maximum likelihood technique. As the mode lifetimes appear not

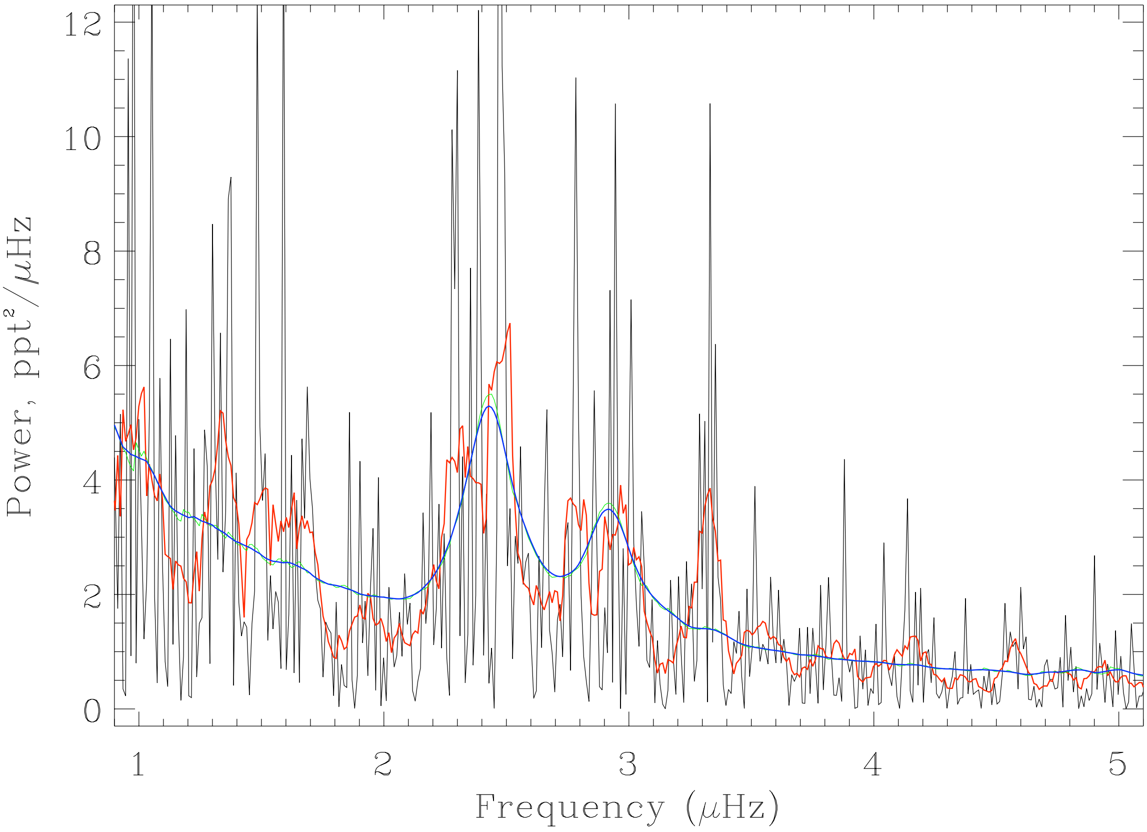

Figure 6.8: Fits to the most prominent features in the power density spectrum. Here the raw spectrum is show in black, and a 9-bin (≈0.1 μHz) moving-mean smoothed spectrum in red. The fitting is shown in green, and a representation of the fitting smoothed over 9 bins in blue.

to be significantly longer than the period of the oscillations, it was necessary in this case to use the full resonant profile describing a classically damped oscillator as the model to describe each mode, instead of the usual simplification of a Lorentzian model. In this case we have chosen to simultaneously fit a power-law model of the background and the two resonant profiles, which were constrained to have the same width. The window function can alter the parameters describing a fitted mode, so we convolved our model with the window function. By this means we hoped to better achieve a true description of the modes. The best-fitting parameters describing each mode are listed in Table 6.4.

As the signal-to-noise ratio is low, tests using the Monte-Carlo method described in Section 5.5.2 on page 107 were performed to further ensure that the fitted parameters were a robust representation of the power density spectrum. In these a model spectrum was made consisting of the background and two modes described by the parameters in Table 6.4. Artificial power density spectra, $P'(\nu_i)$, were then created point-wise in which $P'(\nu_i) = -\ln{(x_i)}P(\nu_i)$, where x_i is a uniformly distributed random variable in the range $[0, 1]$, and $P(\nu_i)$ is the model power at the frequency ν_i. Fittings to these artificial spectra were performed and the returned parameters compared to those of the input model. Each fitted parameter showed a distribution around a mean value consistent with the initial fitting. The standard deviation of each parameter was used to determine the error estimates shown in Table 6.4 on page 139.

Considering other spikes and concentrations of power in the region of the two identified modes, it is tempting to speculate that some of these may represent additional modes. However, we note the strongest feature at ≈ 3.3 μHz occurs at the same location as an alias introduced by the window function, as can be observed by the slight hump seen in the fitting in Figure 6.8. In addition, the feature at 3.3 μHz does not show the width of the identified modes at 2.44 and 2.92 μHz, and occurs at a lower frequency than would be expected for a higher harmonic respecting the same frequency spacing shown between the other two modes.

6.2.2 Discussion

Two features have been identified as unlikely to be part of the background in both probabilistic and numerical models of the data. We suggest that these features are radial modes separated by the large frequency spacing. Given the quality of the data, we feel it is not possible to say whether there might also be non-radial modes present. However, we believe that we can exclude the possibility of the separation between the features being several times the large frequency spacing, as this would require modes to be missing from the spectrum, and the lower spacing thus implied would give an unrealistic mass estimate (see below).

As we have measured two independent seismic quantities – the frequency of maximum power, $\nu_{\rm max}$, and large frequency spacing, $\Delta\nu$ – one may use Equations 3.25 on page 52 and 3.38 on page 55 to determine an estimate for the mass of the star, as follows:

$$\left(\frac{M}{\mathrm{M}_\odot}\right) = \frac{(\nu_{\rm max}/3050\ \mu\mathrm{Hz})^3 (T_{\rm eff}/5777\ \mathrm{K})^{3/2}}{(\Delta\nu/134.9\ \mu\mathrm{Hz})^4}, \tag{6.3}$$

where 3050 μHz, 134.9 μHz, and 5777 K are respectively the frequency of maximum power, large spacing, and effective temperature of the Sun (errors on these values will be insignificant when compared with errors on the β UMi values and have been ignored).

We determined the frequency of maximum power by smoothing the power spectrum by means of a boxcar (moving mean) smoothing filter of width $2\Delta\nu$ applied twice. This will result in the convolution of the power spectrum with a triangle shaped filter, producing a smooth spectrum even where the original spectrum shows sharp peaks. This will produce a single hump of excess power that is insensitive to the discrete peaks of the oscillation spectrum. The frequency of maximum power observed with this method was $\nu_{\rm max} = 2.61 \pm 0.08$ μHz, where the uncertainty comes from the scatter on results observed for the artificial spectra described in Section 3. We note that this location seems somewhat inconsistent with predictions based upon the scaling laws (Table 6.3 on page 135).

When we use the observed values of $\Delta\nu = 0.48 \pm 0.06$ μHz and $\nu_{\rm max} = 2.61 \pm 0.08$ μHz we obtain a mass estimate of 2.3 ± 1.4 $\mathrm{M}_\odot$, very close to the mass estimate from evolutionary tracks. This means of estimating the mass is highly sensitive to both $\nu_{\rm max}$ and $\Delta\nu$ (third and fourth power dependence, respectively). As both values have significant errors, this leads to a very large fractional uncertainty in the derived mass. We have therefore used two other approaches to estimate the mass, which give better constrained estimates. In the first approach (Stello et al. 2008), based upon Equation 3.25 on page 52, we use estimates of the luminosity (from use of the parallax) and effective temperature from 6.3 on page 135, in combination with the value for $\nu_{\rm max}$. This expression is -

$$\left(\frac{M}{\mathrm{M}_\odot}\right) = \frac{(\nu_{\rm max}/3050\ \mu\mathrm{Hz})(L/\mathrm{L}_\odot)}{(T_{\rm eff}/5777\ \mathrm{K})^{3.5}}. \tag{6.4}$$

For β UMi this method returns a mass estimate of 1.4 ± 0.2 $\mathrm{M}_\odot$. In the second approach, we make use of the dependence of $\Delta\nu$ on the square root of the mean density of the star. This expression, based upon Equation 3.38 on page 55, is:

$$(M/\mathrm{M}_\odot) = (\Delta\nu/134.9\ \mu\mathrm{Hz})^2(R/\mathrm{R}_\odot)^3. \tag{6.5}$$

When we use the independent interferometric determination of $R = 44.4 \pm 0.7$ $\mathrm{R}_\odot$ (Table 6.3 on page 135), we obtain a mass of 1.1 ± 0.3 $\mathrm{M}_\odot$. The mass estimates obtained from these two approaches are consistent with each other, but do differ significantly from the $\log g$, the evolutionary track mass estimates shown in Table 6.3 on page 135, and the combined $\Delta\nu$ and

$\nu_{\max}$ mass estimate determined above . Since the two approaches make use of input data that are independent, we may give a combined mass estimate of 1.3 ± 0.3 $M_\odot$.

From the fitted width, a mode lifetime $\tau = 1/(\pi\Delta)$ (where Δ is the mode width) of 18±9 days is obtained giving a low Q-factor (ν/Δ) of approximately 12. It has been suggested that Sun-like oscillations may show a trend of decreasing quality with decreasing frequency. Our results here respect this trend, when considered in the context of other results obtained for ξ Hya ($\nu_{\max} \approx 80$ μHz, $Q \approx 55$; Stello et al. 2006). However the ξ Hya results have recently been questioned by the author (private communication), and results from the CoRoT (De Ridder et al. 2009) and preliminary results from Kepler have not confirmed this trend. Thence it may be that the mode lifetimes are significantly longer, but SMEI lacks the signal-to-noise to confirm this.

We observe a maximum RMS mode amplitude ($\sqrt{\pi/2\Delta H}$) of 1.3 ± 0.4 ppt. This observed amplitude agrees with our original prediction of 1.6 ± 0.5 ppt shown in Table 6.3 on page 135. However, the Table 6.3 prediction was made from the scaling laws based upon an estimated mass of 2.2 $M_\odot$ (based on the evolutionary track mass estimate). The prediction assumes that mode amplitudes scale linearly with the luminosity-to-mass ratio (L/M). If we re-calculate the predicted amplitude using our estimated mass from above (1.3 ± 0.3 $M_\odot$), we obtain a value of 2.8 ± 0.8 ppt. While this prediction is more than double our observed amplitude, the large errors on both the prediction and observation mean the two values lie only 1.5σ apart.

6.2.3 Re-visiting β UMi

In the light of the Arcturus results having been called into question we may ask whether the features noted in the β UMi data were also introduced by the pipeline. Data from β UMi was initially obtained using pipeline # 2, after extensive changes had been introduced. However, we may speculate that problems with the introduction of signal remain in pipeline # 2, and this is responsible for the above identified signal.

Arguing against this is the fact that the signal-to-noise of the Beta-UMi results is at its best greater than that of the Arcturus result, with a single-bin located at approximately 2.46 μHz rising to over 18.5 times the fitted background power. The most prominent spike indicates a period of 4.7 days, and as such is not a simple multiple of 1 day. This indicated that it is less likely to associated with a local process. The excess of power also occurs outside of the range in which the anomalous feature has been noted in other SMEI stars. Perhaps most reassuringly the 4.7 day period is clearly visible in the time-domain in Figure 6.6 on page 137, while for Arcturus the oscillation could not be clearly observed in the time-domain.

Data on β UMi from revision # 3 of the SMEI data analysis pipeline was considered to confirm the continued presence of the oscillation. Figure 6.9 shows a comparison between data gathered prior to March 2006 (as used in the initial analysis), the full length dataset, and data gathered after March 2006. The same structure of multiple peaks in the range of 2-4 μHz is visible in all three datasets, despite the lower signal-to-noise on the later data.[The differences between the top spectrum in Figure 6.9, and Figure 6.7 on page 138 can be explained by slight differences in the pipeline, and method of data processing.]

However, in light of the better signal-to-noise ratio of the complete dataset one may call into question the interpretation of the spectrum as two broad modes, as instead suggested the presence of two sharp peaks, located at approximately 2.46 and 2.78 μHz, with suggestions of other sharp features visible in at a lower amplitude at higher frequencies.

6.3 γ Crucis

The ‘semi-regular variable stars’ (SRs), are a broad range of giant stars characterised by variability in the amplitude, period and shape of the light curve from cycle to cycle. Semi-regular variables appear to encompass both the red giant and asymptotic giant branch of the colour-magnitude diagram, where the former is characterised by hydrogen, and the latter by helium shell burning. The class blend into Mira class variables in the coolest stars.

SR stars are interesting targets for long-term monitoring as the mechanism by which pulsations are excited is still subject to debate, and may vary across the class. Mira class variables show regular, large amplitude oscillations which are self-excited by opacity variation (the κ mechanism). In contrast, oscillations in less bright and hotter SR variables have smaller amplitudes and less regular light curves. A number of SRs have been observed to show multiple periods, and this is generally interpreted in terms of multimode pulsations (Kiss et al. 1999, Percy et al. 2001).

Christensen-Dalsgaard et al. (2001) have suggested that amplitude variability seen in SR

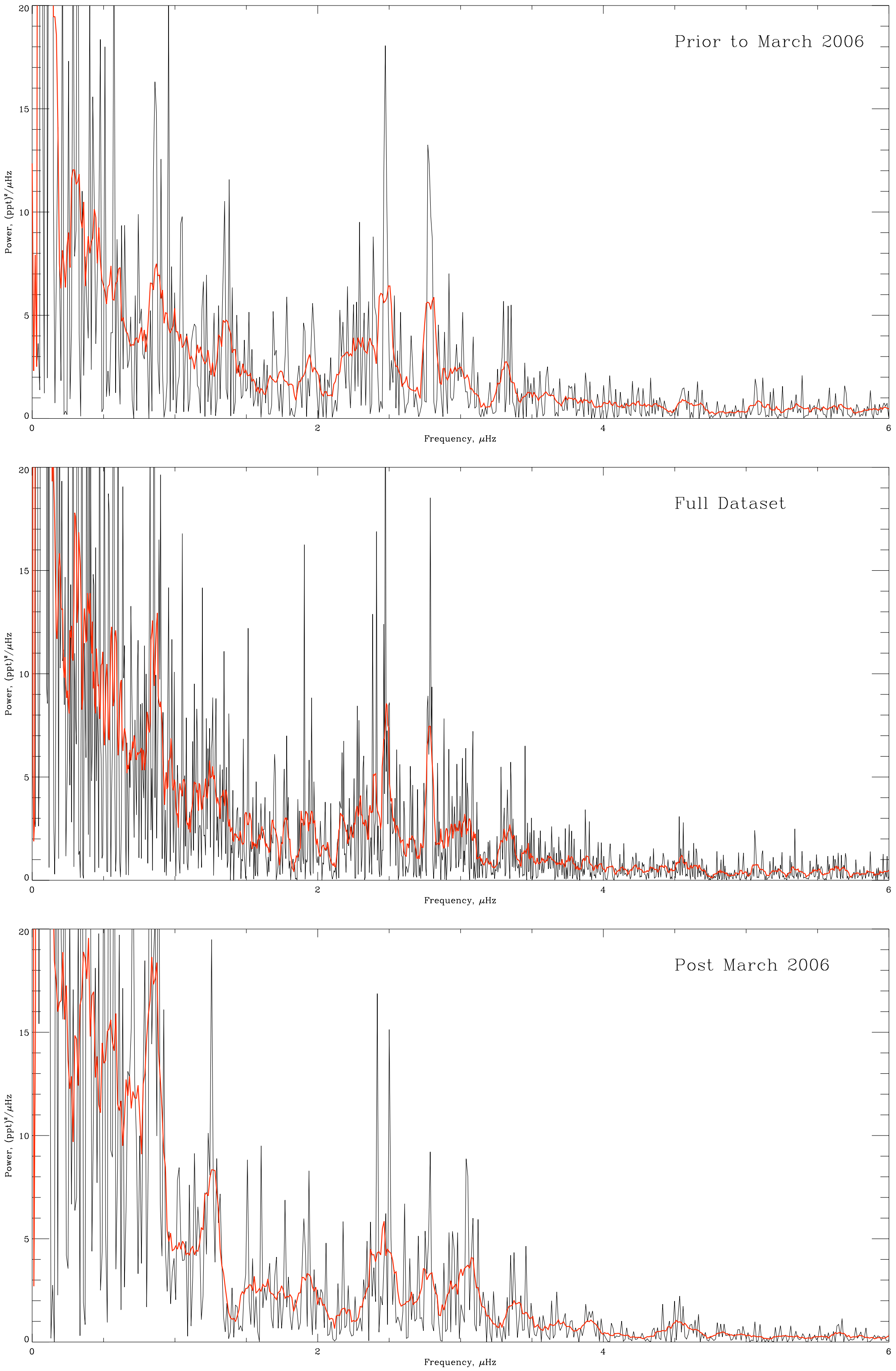

Figure 6.9: power spectrum comparison of Beta Umi data gathered prior to, and post March 2003.

Table 6.5: Physical properties of γ Crucis. Luminosity (i) calculated from the magnitude and bolometric correction, luminosity (ii) calculated from the temperature and interferometric radius. Asteroseismology predictions assume a range of masses from 0.8 to 2.0 $M_\odot$.

Parameter	Value
Catalogue Parameters:	
Spectral Type	M3.5III
V [mag]	1.600±0.008
(B-V) [mag]	1.60±0.01
Parallax, p [mas]	36.81±0.18[1]
Angular Diameter, θ [mas]	25±2[2]
Derived Parameters:	
Distance, d [pc]	27.17±0.13
M_v [mag]	-0.570±0.014
T_{eff} [K]	3770±30[3]
Radius, R [$R_\odot$]	73±6
Bolometric Correction	-1.54±0.05
L [$L_\odot$]	(i) 600± 50
	(ii) 970±200
Asteroseismology Predictions[4]:	
ν_{max}	0.04-0.1 d^{-1} (0.5-1.1μHz)
$\Delta\nu$	0.017-0.026 d^{-1} (0.19-0.31 μHz)

[1] Taken from van Leeuwen (2007a).
[2] Taken from Ireland et al. (2004).
[3] Derived from the (B-V) value using the table in Flower (1996).
[4] Derived from the scaling laws of Kjeldsen and Bedding (1995).

stars is consistent with the pulsations being solar-like in nature, i.e., stochastically excited by convection. Further to this work, Bedding et al. (2005) presented evidence that oscillations in the semi-regular variable star L_2 Puppis are indeed stochastically excited.

γ Crucis is the brightest and closest M giant (Murdoch et al. 1992, Ireland et al. 2004). The star has been previously observed to show radial velocity variability at low amplitude, and is thought to be a variable of the semi-regular class. Murdoch et al. (1992) noted three concentrations of power in the power spectrum with periods of 13, 17 and 88 days in radial velocity data, and photometric variability has also been noted (Koen and Eyer 2002).

Physical properties of γ Crucis are shown in Table 6.5. No literature value for the metallicity could be obtained. There is an inconsistency ($\approx 1.8\sigma$) between the luminosity estimated from magnitude, parallax and bolometric correction versus the luminosity estimated from effective temperature and interferometric radius. Colour–effective-temperature relations can be metallicity dependent, especially at low temperature (e.g. Kučinskas et al. 2006), and this may explain

Table 6.6: Best fitting parameters for a range of metallicities, given the V magnitude and parallax in Table 6.5. Errors on $T_{\rm eff}$ were set at ±100 K, and on [Fe/H] at 0.05.

[Fe/H]	$T_{\rm eff}$ (K)	Age (Ga)	Mass ($M_\odot$)
-0.3	3710	10.9±0.7	0.92±0.06
-0.25	3700	10.7±1.0	0.94±0.05
-0.1	3610	8.6±2.2	1.01±0.09
0.0	3590	5.8±1.9	1.14±0.12
0.1	3590	3.7±1.1	1.32±0.13
0.25	3590	2.5±0.4	1.53±0.09
0.4	3590	2.4±0.3	1.55±0.08

the discrepancy.

To estimate the mass, age, and effect of metallicity upon the effective temperature, we have used the PARAM 1.0 web interface for the Bayesian estimation of stellar parameters (da Silva et al. 2006). For each value of [Fe/H] the parallax and V magnitude were kept constant at the values in Table 6.5, while the effective temperature which most closely reproduced the known radius and (B-V) value was determined by a process of trial and improvement. The results, as shown in Table 6.6, show that an effective temperature in the range 3750 to 3600 K, and mass in the range 0.9 and 1.6 solar masses provide a best fit to the known parameters. These results are based upon [Fe/H] values in the range of -0.3 to 0.4. Values outside this range would result in an age of greater than 13 Ga, therefore providing and inappropriate model for the star.

6.3.1 Data

Due to the orbital geometry of the Coriolis satellite, γ Crucis has primarily been observed by Camera #2 of the SMEI instrument. The data under consideration in this thesis were gathered over approximately 5 years between Julian Dates 2 452 739.56 and 2 454 661.38 (2003 April 10 to 2008 July 13). Within this time the data can be broken into six annual observing seasons, descriptions of which are given in table 6.7. The fill of the data considering the entire length of observation was 42.1%.

The 2008 observing season is illustrated in Figure 6.10. It should be noted that during the latter part of the season the scatter on the data is significantly greater. This is both due to the continual degradation of the CCD unit over time, and problems which caused SMEI to temporarily shut down in late 2006.

Table 6.7: Observing seasons of γ Crucis by the SMEI Camera #2 instrument

Era	Start Time (HJD-2 450 000)	End Time (HJD-2 450 000)	Duration (days)	Fill (%)
2002-03	2739.57	2855.99	116.42	55.3
2003-04	2969.01	3221.47	252.46	61.8
2004-05	3334.62	3587.28	252.66	55.9
2005-06	3702.55	3952.73	250.18	58.8
2006-07	4065.59	4316.27	250.68	63.6
2007-08	4431.03	4661.38	230.35	62.3

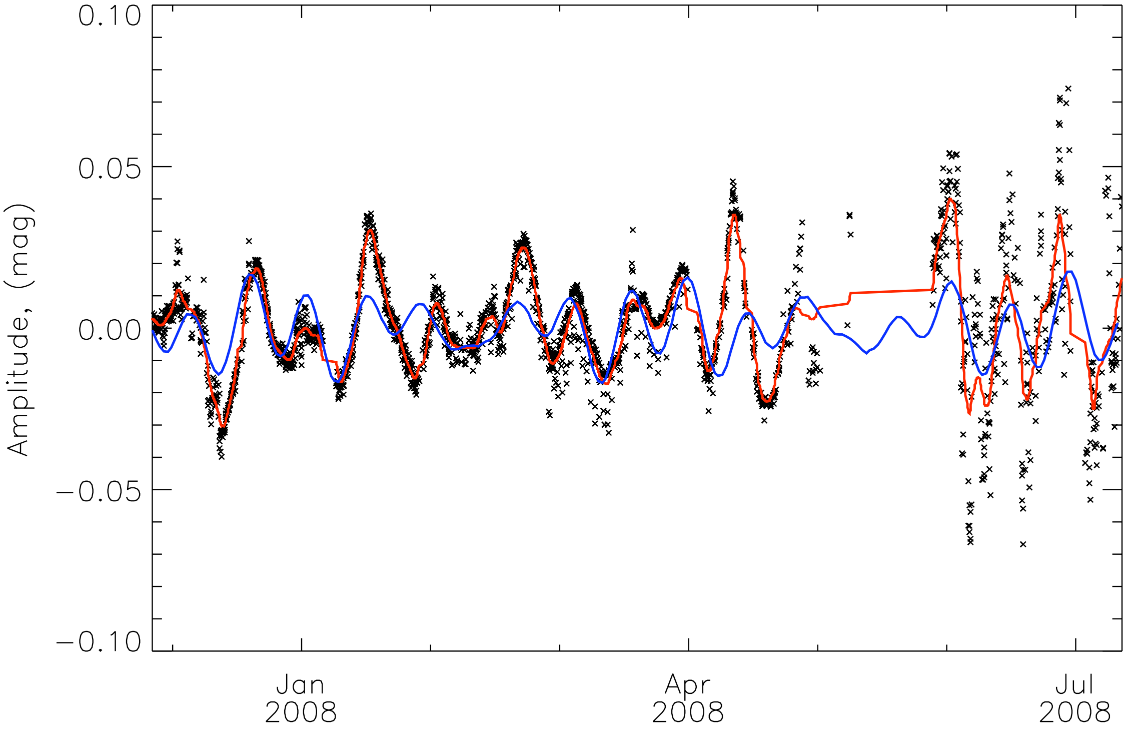

Figure 6.10: The 2008 observing season. Raw data is marked by the black crosses, a 21 bin (≈1.5 day) smoothing shown by the red line, and a three-component sine-wave with frequencies and amplitudes as in 6.9 on page 151 shown in blue.

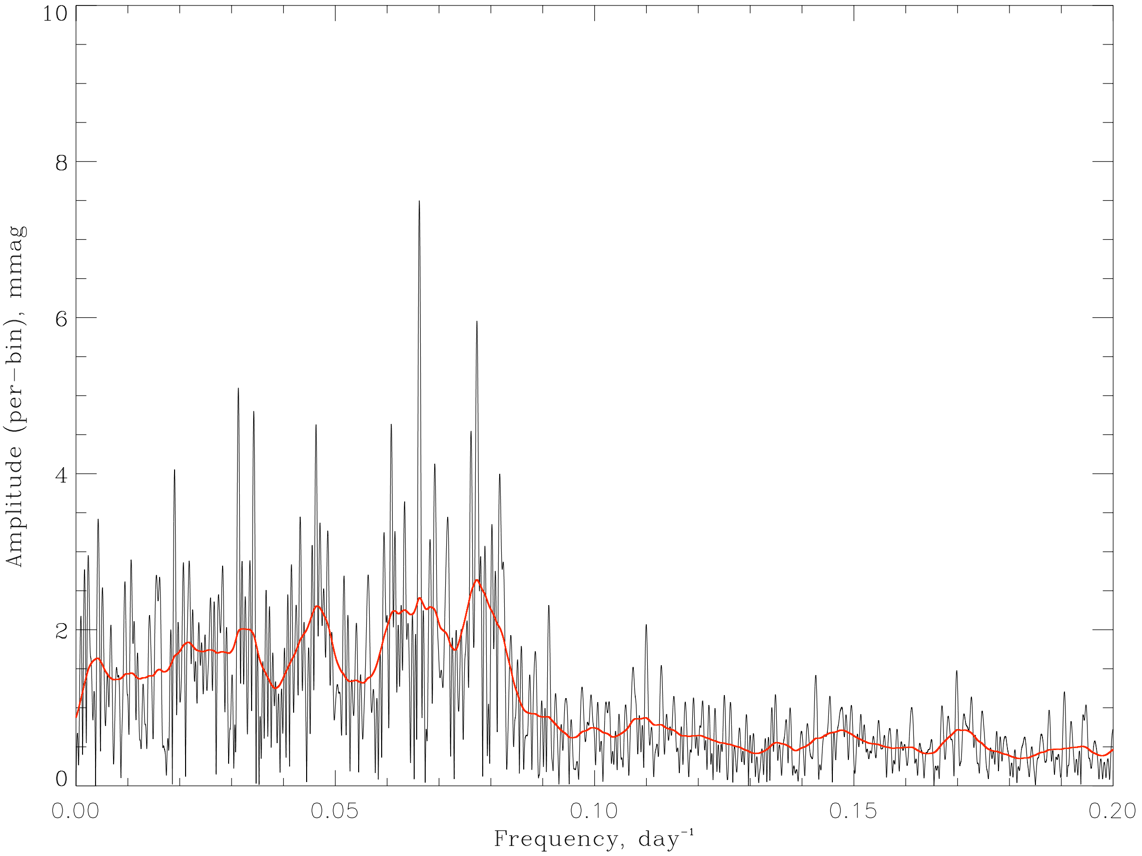

Figure 6.11: Amplitude spectrum of the γ Crucis data showing the region in which an excess of power is present. The thick line shows a spectrum twice smoothed with a 0.04 d^{-1} boxcar, and the spectral window is show in the upper right corner at the same scale as the frequency axis.

6.3.2 Mode nature and excitation

Three prominent spikes can be noted in the power spectrum, with frequencies of approximately 0.031, 0.066 and 0.077 cycles per day (periods of approximately 32, 15 and 13 days). In addition there appears to be a broad background of power at below 0.1 d^{-1}. This may arise as a result of stellar granulation, further modes of lower amplitude (see following sections), or as a result of long-term drifts in the performance of the SMEI cameras.

In order to investigate the nature of the excitation, changes in the phase of oscillations between observing seasons were considered. A pure sine-wave would expected to remain phase coherent over long time-scales, with the only scatter on the fitted phase being that associated with influences of the window function and noise-background. Due to the nature of stochastic excitation, a solar-like oscillator will show additional irregular changes in phase, independent of

Table 6.8: Modes lifetimes and linear phase scatters for simulated stochastic modes.

Lifetime (days)	Linear Phase Scatter
35	0.236
70	0.235
140	0.225
280	0.202
560	0.184
1120	0.154
2240	0.125
4500	0.0973
8800	0.0887
17500	0.0821
35000	0.0784
> 70000	< 0.0741
$\nu_1, 0.0313$ d^{-1}	0.036
$\nu_2, 0.0663$ d^{-1}	0.036
$\nu_3, 0.0774$ d^{-1}	0.093

the influences of noise and window.

Simulations of both a single sine-wave and stochastically excited oscillations (Chaplin et al. 1997) of varying lifetimes were created. The results, shown in Table 6.8, showed that the phase scatter of each of the above frequencies was inconsistent with a stochastic oscillation of lifetime shorter than twice the observation period, suggesting that a coherent sine wave is a better model for the oscillations.

From these results it can be inferred that, were the modes to be stochastically excited this would require a lifetime significantly longer than the duration of the observations. We are therefore unable to differentiate between a sinusoidal oscillation, and a stochastic oscillation of a long lifetime.

6.3.3 Results

Three sharp features have been noted in the power spectrum at a signal-to-noise in amplitude of greater than 4.0. Parameters describing these features are shown in Table 6.9. Errors on these parameters were obtained through Monte Carlo simulations using the Period04 (Lenz and Breger 2005) software package. The signal-to-noise was consider by taking a 0.005 d^{-1} range, centred on the frequency in question, and calculating the mean power-in-noise after the cleaning

Table 6.9: Parameters describing the sharp features of the power spectrum.

	Frequency (d^{-1})	Period (days)	Amplitude (mmag)	S/N
f_1	0.06623(1)	15.099(2)	7.0(2)	8.6
f_2	0.07731(1)	12.935(2)	5.8(2)	4.3
f_3	0.03129(1)	31.96(1)	5.2(2)	4.7

Table 6.10: Parameters describing the additional, lower signal-to-noise sharp features of the power spectrum.

	Frequency (d^{-1})	Period (days)	Amplitude (mmag)	S/N
f_4	0.04629(2)	21.60(1)	4.0(2)	2.7
f_5	0.08177(2)	12.230(3)	4.0(2)	3.8
f_6	0.01899(2)	52.66(6)	3.5(2)	3.0

of all three features.

The second of these frequencies is roughly in agreement with results seen by Murdoch et al. (1992), who noted variability with periods of 13, 17 and 88 days. However they note that none of their results are particularly well defined, and indeed a broad width of approximately 0.01 d^{-1} may be observed in their power spectrum. The longest period noted by Murdoch et al. (1992) of 88 d^{-1} is entering the range of significant window aliases in the SMEI data, and, if present, has been suppressed by removal of low-frequency noise in the power spectrum. The results also approximately agree with photometric observations taken by a graduate student at Sydney University (Bedding, private communication).

There are several possible interpretations of the spikes observed in the power spectrum; either each of the spikes is a single radial mode, with a large frequency spacing of approximately 0.015 d^{-1}, or the spikes at 0.031 and 0.062 d^{-1} are adjacent radial modes, with the 0.077 mode as an intermediate $l = 1$ mode.

Having cleaned these three frequencies from the power spectrum (Figure 6.12), there still appears to be an excess of power in the low frequencies, most notably at approximately 0.05 and 0.08 d^{-1}.Three further frequencies were cleaned from the power spectrum, however, none of the spikes in this frequency range managed to rise above 4.0 in signal to noise. Frequencies, amplitude and signal-to-noise are reported in Table 6.10.

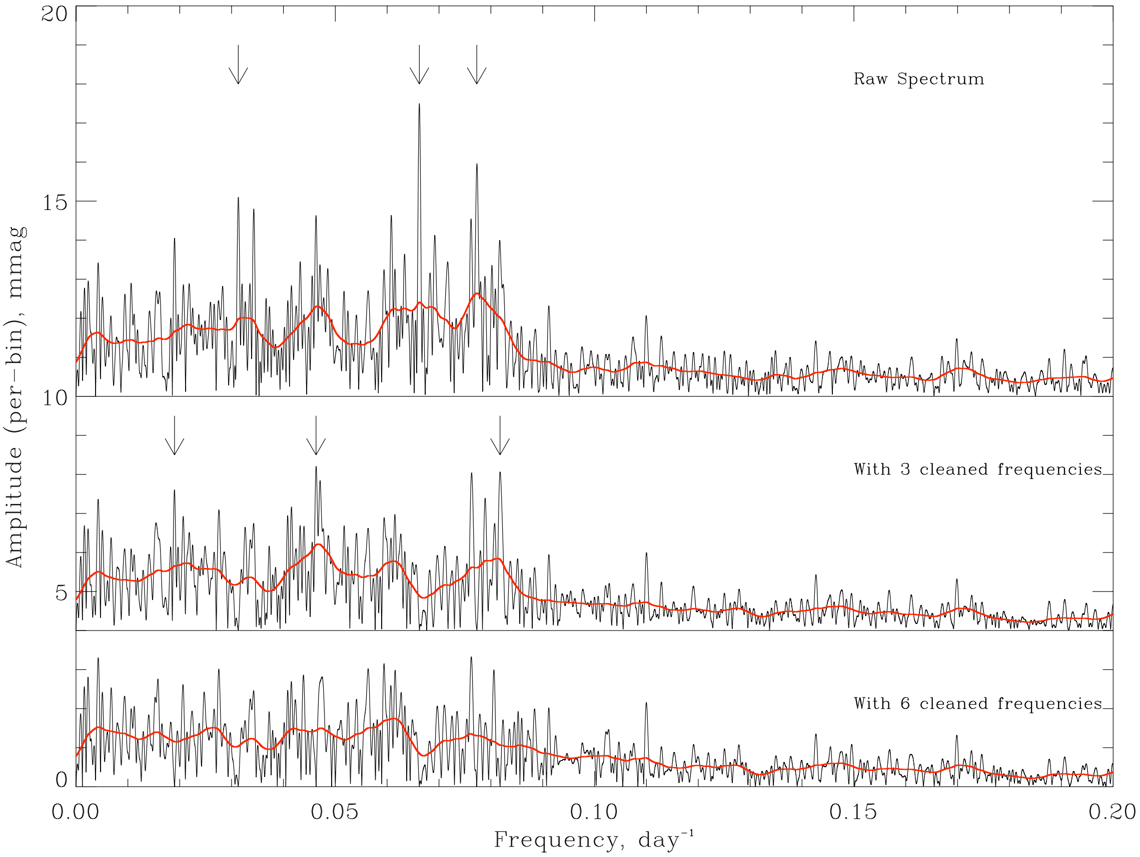

Figure 6.12: Progressive cleaning of the γ Crucis amplitude spectrum. Here the raw spectrum have been offset by 10 units vertically, and the spectrum with 3 cleaned frequencies have been offset by 4 units vertically. As before the red-line represents a profile smoothed with a 0.04 d^{-1} boxcar average.

While these features would generally be disregarded as being of insufficient signal-to-noise, the feature at 0.047 d^{-1} is approximately equidistant between the oscillations at 0.031 and 0.062 d^{-1}. Dependent upon which of the interpretations (above) is chosen, this may suggest a further radial mode, or $l = 1$ mode. It has been noted by Dupret et al. (2009) that $l = 1$ modes may have shorter lifetimes than the $l = 0$, and would therefore be broader in frequency space. It can be noted that in the amplitude spectrum the 0.077 and 0.047 d^{-1} modes each appear to be visually wider that the 0.031 and 0.062 d^{-1} modes. This width explains the relatively lower signal-to-noise for these features relative to the other modes of comparable power.

6.4 Conclusions: giants

The SMEI results for Arcturus are highly equivocal. A feature which was strong enough to reach statistical significance in one revision of the pipeline was no longer present in a later version. The feature has been ascribed to arising as a consequence of the centroiding algorithm. From data gathered with a revised edition of the SMEI pipeline, an upper threshold has been placed on mode amplitudes. This thereshold suggests that any modes present in the star would have to be at a lower ampltiude than predictions based on the scaling laws, or of a significantly shorter lifetime than the duration of observations, with power spread across multiple bins.

With the analysis of β UMI SMEI demonstrates some of its unique features. While the star has been noted as variable, no determinations of the nature of the variability had as yet been presented in literature. As SMEI covers all of the brightest stars over an extended duration there is considerable potential in the investigation of these variables of unknown type for characterisation of variability. In addition the presence of more than a single mode of oscillation has allowed an asteroseismic determination of a stellar parameter, namely the mass of the star. While the errors on the determined values are high, this demonstrates the potential for asteroseismology, not only in improving our knowledge of individual stars, but also in helping to improve evolutionary models.

γ Crucis is the first of semi-regular pulsating variable which has been studied with SMEI. The frequencies detected in the star should act as an input for modellers and theoreticians, allowing better constrained models of the stellar interior, leading to a determination of whether γ Crucis is still in the hydrogen shell-burning, or has entered the helium burning phase of its evolution.

In general hotter K-giants are not suitable targets for observation with SMEI, with oscillation frequencies at greater than the Nyquist, and mode amplitudes lower-than or comparable to the noise level. Cooler K-giants and M-giants are more suitable for observation with SMEI, as frequencies decrease and mode amplitudes increase. The sharper features in the semi-regular pulsating variables make these particular suited for the SMEI instrument.

Chapter 7

Results: main-sequence stars

Main-sequence stars, like the Sun, often also show variability. Oscillations like those seen in the Sun are inaccessible to the SMEI instrument, being above its Nyquist frequency, and at too low an amplitude to be visible. However there are several types of stars on the main sequence which show stronger forms of variability with longer periods. The SMEI instrument offers a chance to observe these oscillations over a extended duration, comparable to the best ground-based observation campaigns.

7.1 γ Doradus

γ Doradus is the prototype of the class of γ Doradus variable stars. These are usually F-type main-sequence or sub-giant stars, showing gravitationally restored (g mode) pulsations with frequencies in the range of 0.5 to 3 d^{-1} and amplitudes of a few tens of mmag.

Prior to the analysis presented below there were three known modes of oscillation in γ Doradus, at frequencies of 1.32098(2), 1.36354(2) and 1.475(1) d^{-1} (Balona et al. 1994). Through photometric methods, Dupret et al. (2006b) identified the first two of these as $l = 1$ modes.

7.1.1 SMEI data

The data under consideration in this section were gathered between Julian Dates 2452847.15 and 2453816.36 (2003 July 26 to 2006 March 21). While the SMEI data extend beyond this date, subsequent data show a higher scatter than the earlier period and are unlikely to alter or improve the precision of calculated frequencies and amplitudes.

Due to the orbital geometry of the Coriolis satellite, γ Doradus is observed by Camera #2 of SMEI for approximately two thirds of the time, seasons consisting of approximately 240 days

Table 7.1: Observation windows of γ Doradus. Times are given as the Julian date minus 2 450 000 (JD-2450000).

			Camera #1		
	Start	End	Duration (d)	No. Points	Fill (%)
1	2958.71	2986.09	27.38	182	47
2	3319.60	3349.10	29.50	195	47
3	3683.93	3717.73	33.80	280	58
			Camera #2		
	Start	End	Duration (d)	No. Points	Fill (%)
1	2847.15	3092.07	244.92	1798	52
2	3215.03	3457.68	242.65	2305	67
3	3578.45	3816.36	237.91	2200	64

of observations, followed by a 120 day gap. Data are observed concurrently by Camera #1 for approximately thirty days in each season. The timeseries analysed here consists of three sets of observations, listed in Table 7.1.

Point-to-point scatter of the Camera #1 dataset was estimated at 4.94 parts-per-thousand (ppt), and of the Camera #2 dataset at 9.27 ppt. When considering the datasets as a whole the Camera #2 fill was 46.5 per cent, and the Camera #1 fill was 6.2 per cent.

7.1.2 Analysis

The γ Dor data once again show a large annual periodicity. This will contribute broad-band noise to the spectrum due to redistribution by gaps in the window of the low-frequency power associated with this periodicity. As γ Doradus class oscillations occur only at frequency greater than about 0.33 cycles-per-day the low frequencies were not of interest, and so in order to diminish the confusion noise associated with redistribution of the annual power, a smoothed profile was subtracted from the data. This profile was obtained by a boxcar smoothing of the data, taking the median value from within each 10-day box.

Data were analysed for periodicities with the PERIOD04 package (Lenz and Breger 2005). The periodogram of the whole Camera #2 dataset is shown in Figure 7.1. Features at the three known frequencies are clearly visible, along with the daily cycle and harmonics. When considering the γ Doradus dataset, power at frequencies 1.0, 2.0, 3.0, 4.0 and 5.0 d^{-1}, along with additional peaks at 1 $\mathrm{d}^{-1} \pm (1\ \mathrm{year})^{-1}$, was removed by PERIOD04 using sine-wave fitting in the time domain, a procedure equivalent to the one-dimensional 'CLEAN' algorithm.

Canonically a signal-to-noise ratio of 4 in amplitude is taken as indicating that the amplitude

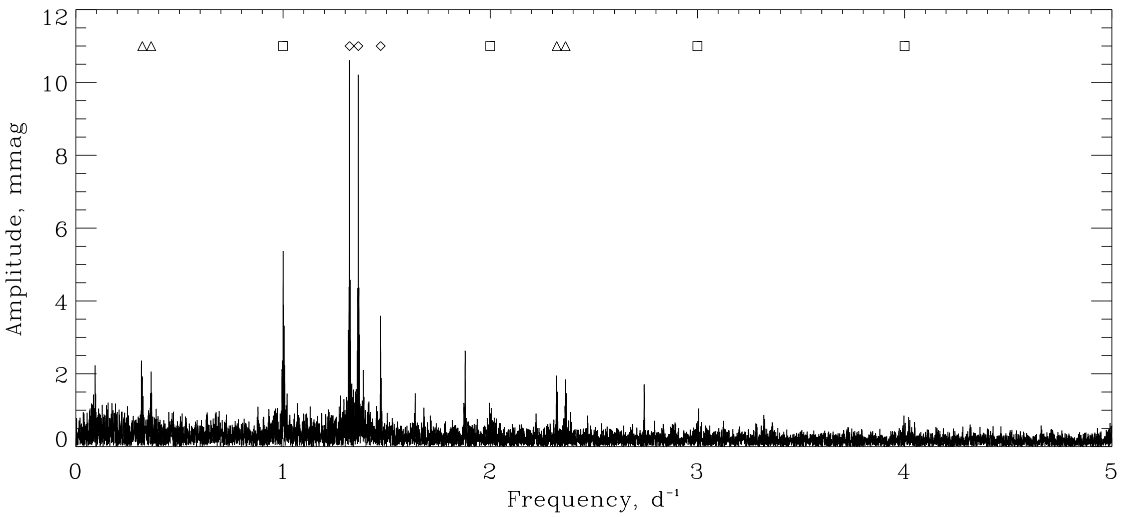

Figure 7.1: Periodogram of the entire Camera #2 timeseries. Previously identified frequencies have been marked with diamond symbols, aliases of these with triangles, and daily harmonics with squares.

seen in a single bin is significant (e.g. Breger et al. 1993). As the Camera #2 dataset is longer in duration than other available datasets, checks were performed to ensure that this threshold would be an appropriate measure of significance, testing to see whether a spike at a given signal-to-noise ratio may be reasonably explained as the product of a broadband noise background. This will in general depend upon both the length of dataset, and whether any oversampling has been used, as discussed in Section 5.7.3 on page 118 and the preceding sections. Simulations of the Camera #2 dataset showed that a spike at a S/N of 4.0 has a roughly 5% chance of occurrence. As the spike of lowest significance we choose to report in this dataset is of S/N 6.2, the chance of occurrence as a product of noise is very low.

7.1.3 Results

The periodogram of the whole Camera #2 data is seen in Figure 7.1. The three previously identified frequencies (labelled as f1, f2 and f3 in Table 7.2), marked with diamond symbols, are clearly visible. Also present are strong aliases of f1 and f2 at ± 1 d^{-1} (marked by triangles), and the stray light contributions at 1 d^{-1} and harmonics (marked by squares). After pre-whitening in the time-domain to remove the three previously identified frequencies, a further three prominent spikes (f4, f5, f6), marked by 'x' symbols in the plots, were observed in the amplitude spectrum (Figure 7.2 on page 159). These spikes do not seem to be associated with the daily harmonics,

Table 7.2: Parameters related to the observed modes. Errors are based upon the standard deviation of 100 Monte Carlo simulations of the full-length Camera #2 data. 1, 2 and 3 refer to the periods of observation shown in Table 7.1 on page 156. Notice should be taken that the Balona et al. (1994) amplitudes are in V magnitudes, whereas the SMEI response corresponds best to R magnitudes.

	Balona et al. (1994)		This Thesis		Signal-to-Noise				
	Freq. (d^{-1})	Amp. (mmag)	Freq. (d^{-1})	Amp. (mmag)	Cam #2				Cam #1
					Whole	1	2	3	
f1	1.32098(2)	11.16(50)	1.32093(2)	10.7(2)	34.3	24.6	27.1	25.1	21.6
f2	1.36354(2)	12.93(51)	1.36351(2)	10.3(3)	33.2	22.5	26.9	24.9	20.4
f3	1.475(1)	-	1.471(1)	3.8(8)	12.5	8.0	10.6	9.6	8.7
f4	-	-	1.87(3)	2.6(1.1)	8.6	5.5	7.3	7.2	5.8
f5	-	-	1.39(5)	2.0(7)	6.4	4.0	4.5	5.8	5.6
f6	-	-	2.74268(8)	1.8(3)	6.8	4.6	5.6	6.1	4.1

nor with features of the spectral window (Figure 7.3).

In order to demonstrate thoroughly the robustness of the identification of these additional frequencies, two approaches were taken; first each of the periods of observation in Camera #2 data highlighted in Table 7.1 on page 156 was considered in isolation, and second the Camera #1 data was analysed in its entirety.

In order to asses the significance of features observed in a power spectrum it is necessary to have an estimate of the local background noise. Aliasing by the window function will typically redistribute a portion of the power of an oscillation into bins close to the frequency of the oscillation. This will cause the local noise level to be higher than what it would be, were the oscillation not to be present. It is therefore a standard technique to use the CLEAN algorithm to remove spikes present in a timeseries in order to determine an unbiased estimate of the background power.

In the case of γ Doradus the signal-to-noise level was assessed relative to the noise remaining in the power spectrum after having removed the six noted frequencies, and spikes associated with daily periodicities at 1, 1+(1/year), 1-(1/year), 2, 3, 4, and 5 d^{-1}, and the three additional unidentified frequencies discussed below. A broad range centred on the frequency in question was used to determine the background noise level. In every case the signal-to-noise ratio rises above 4.0, with the exception of f5 in the first observation period of Camera #2, where the signal to noise is still greater than 3.95 (rounded to 4.0 in Table 7.2).

Considering the identification of the additional frequencies we speculate that the features at 1.38 and 1.878 d^{-1} represent additional modes of oscillation. The feature at 2.743 d^{-1} occurs

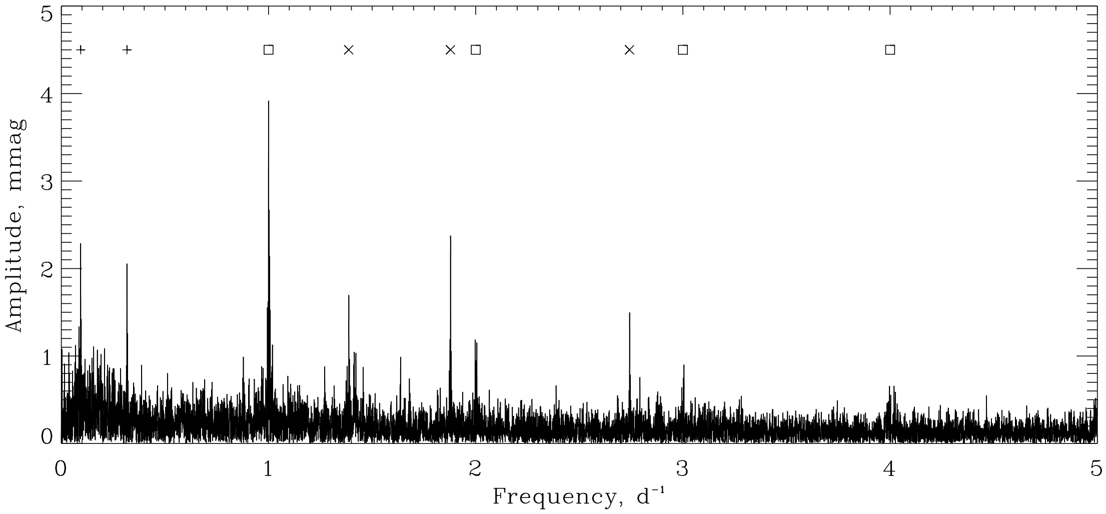

Figure 7.2: Having removed the previously identified frequencies from the Camera #2 timeseries, the additional frequencies (marked with 'x' symbols) can be distinguished from the prominent structure of overtones of 1 day, marked with squares. The low frequency spikes, suspected as being non-stellar in origin, have been marked with plus symbols.

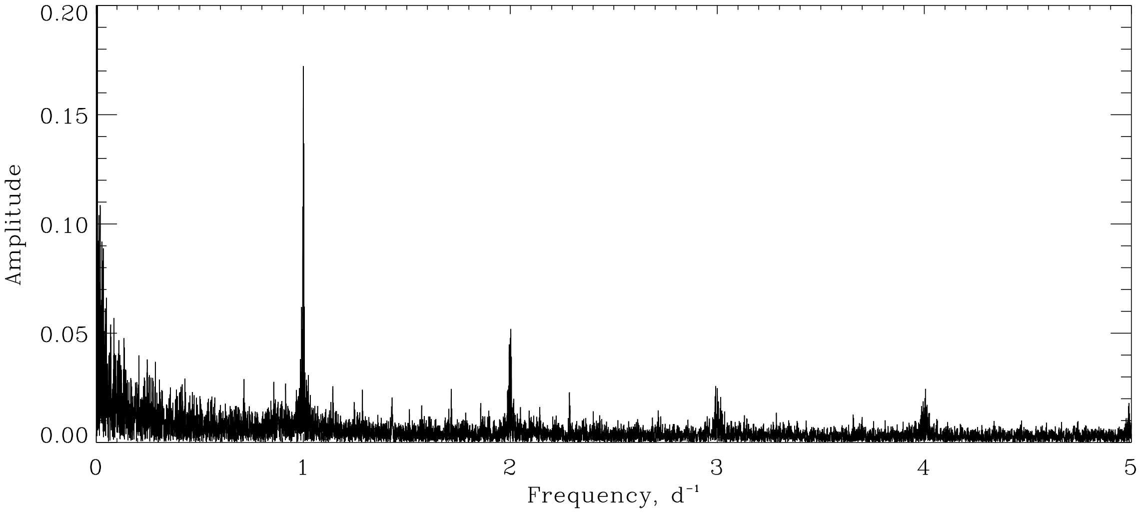

Figure 7.3: The spectral window of the entire Camera #2 timeseries; here the zero frequency component has been normalised so as to have a power of 1.0.

notably outside of the frequency range established by the other modes and is at a frequency consistent within the uncertainties with an identification as the linear combination of frequencies f2 and f5. Such combination frequencies are a common occurrence in multi-periodic stars, having been noted, for instance, in the β Cephei star ν Eri (e.g. Jerzykiewicz et al. 2005).

There are a number of additional features in the periodogram. A notable spike is located at 0.316 d^{-1}, at a high amplitude (2.37 mmag) and signal-to-noise ratio (9.5 in the Camera # 2 dataset), however the signal does not appear in the Camera #1 data. As periodicities greater than 10 days have been suppressed in our analysis, it may be that this feature is part of the rising background noise. It is possible that this frequency is associated with the anomaly noted in a number of stars at 0.32 d^{-1}. However γ Dor is outside of the range in declination for which the anomaly is typically noted (± 25°).

Another low-frequency spike occurs at 0.0932 d^{-1}, which is almost coincident in frequency with the smoothing box size, and is likely to be an artefact of the smoothing process. A further feature is observed at 1.0829 d^{-1}, however as this is equal to 1 d^{-1} + $3\times(1\ \mathrm{year})^{-1}$, and the frequency offset, $3\times(1\ \mathrm{year})^{-1}$ [$= (120\ \mathrm{d})^{-1}$] is comparable in length to the gaps between successive sets of observations, we do not feel confident in ascribing a stellar origin to this spike.

Having cleaned the six frequencies we associate with stellar oscillation, the features associated with daily harmonics, and the further features noted above, no spikes were observed at a S/N of above 4.0 in every season. However, when considering the full-length Camera #2 dataset, a number of spikes in the region of 1 to 2 d^{-1} appear at a S/N of greater than 4.0, notably at 1.637 d^{-1}, with a S/N of 4.7, leading us to speculate that further modes may be present in γ Doradus, which may require longer and higher-precision datasets to detect unambiguously.

7.1.4 The nature of mode excitation

The initial intention in studying stars of the γ Doradus class was to determine whether any evidence could be shed upon the nature of mode excitation, particularly whether the complicated convective-blocking excitation mechanism would introduce a width in frequency space observable with the unprecedented resolution available in the SMEI datasets.

No width could be observed in frequency for the modes noted, as evidenced by the fact that using the CLEAN algorithm the power at the frequency is almost completely removed (e.g.

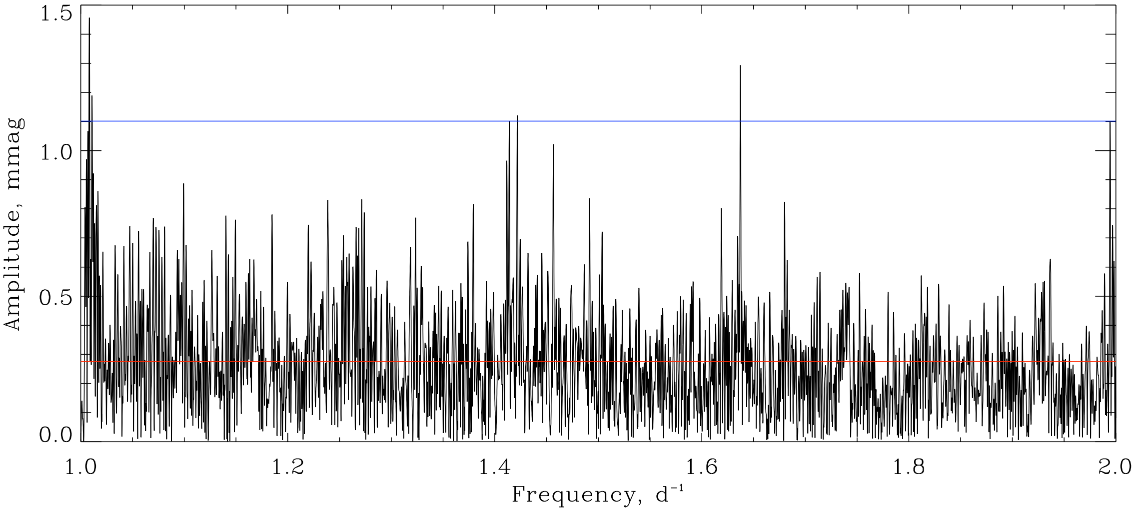

Figure 7.4: A plot of the region between 1 and 2 d^{-1} after the removal of the frequencies, f1 through f6, and daily harmonics, shows the presence of a few additional spikes at around the required S/N threshold (blue), suggesting further modes may be present in the star.

compare Figures 7.1 on page 157 showing all oscillations, and 7.4 after all prominent modes have been removed).

The nature of the modes was also investigated though consideration of variations in the time domain. When sampled over a period less than the mode lifetime, both the amplitude and phase of an oscillation will vary in a statistically forecastable manner, while the amplitude and phase of a sinusoidal oscillation will remain constant, with the exception of deviations caused by noise.

Assuming that the lower amplitude modes may be ignored, a timeseries of at least 25 days would be needed to resolve the two highest amplitude modes. Therefore in the timeseries of 970 days only at most around 40 independent values for the amplitude and phase of any single mode could be obtained; in fact fewer may be found as the fill of the timeseries is only around two-thirds. It has been suggested (Elsworth, private communicate) that at least 100 datapoints are necessary in order to be able to see the signature of a stochastically excited oscillation in a histogram of amplitude, or phase changes.

7.2 β Cephei stars - ν Eri

β Cephei stars are bright, hot, B stars, primarily on the main sequence, but encompassing a few sub-giants and giant stars. The stars undergo periodic pulsations of the order of 0.1 - 0.6

days with an amplitude of 0.01 - 0.3 magnitudes. The pulsations are driven by a κ mechanism process associated with the ionization of iron.

The β Cephei star ν Eri was one of the first stars other than the Sun for which a rotational splitting was detected. It was subject to an extensive observing campaign between October 2002, and February 2004 (Handler et al. 2004, Aerts et al. 2004, De Ridder et al. 2004, Jerzykiewicz et al. 2005), which detected a total of twelve independent frequencies between 5.62 and 7.91 d^{-1}, along with numerous combination frequencies at between 0.11 and 22.8 d^{-1}. In addition the study observed two lower frequency modes, establishing that ν Eri is both a β Cephei, and slowly pulsating B (SPB) star.

A study of ν Eri using data from SMEI was undertaken to confirm the suitability of β Cephei stars as objects of study for the the SMEI instrument. As the SMEI data runs from being concurrent with the last observation season of Handler, Aerts, De Ridder, Jerzykiewicz et al. through to approximately four and a half-years later it also gives a chance to investigate whether any changes in mode excitation could be observed.

7.2.1 Data

The SMEI data on ν Eri were taken between Julian Date 2452858.15 (2003 August 06) and 2454743.83 (2008 October 04), a total duration of 1886 days. During this time there were 11 observation seasons, each of approximately 60 days in duration, with gaps of approximately 120 days in duration between observation seasons. The fill when considered over the timeseries as a whole was 25.1%.

In processing these data each of the observations windows was constrained to have the same mean value, and a linear fitting to the window was subtracted from the data. By this means a substantial portion of the low-frequency power introduced by the SMEI instrument was suppressed. A plot of the original and processed timeseries is shown in Figure 7.5.

7.2.2 Results

The SMEI amplitude spectrum for ν Eri is seen in Figure 7.6 on page 164. The oscillations are clearly visible at between 5 and 6 d^{-1}, along with diurnal aliases at 1.0, 2.0 and 3.0 d^{-1}. The lump of power located at approximate 2.75 d^{-1} is an alias of the combination frequencies, which

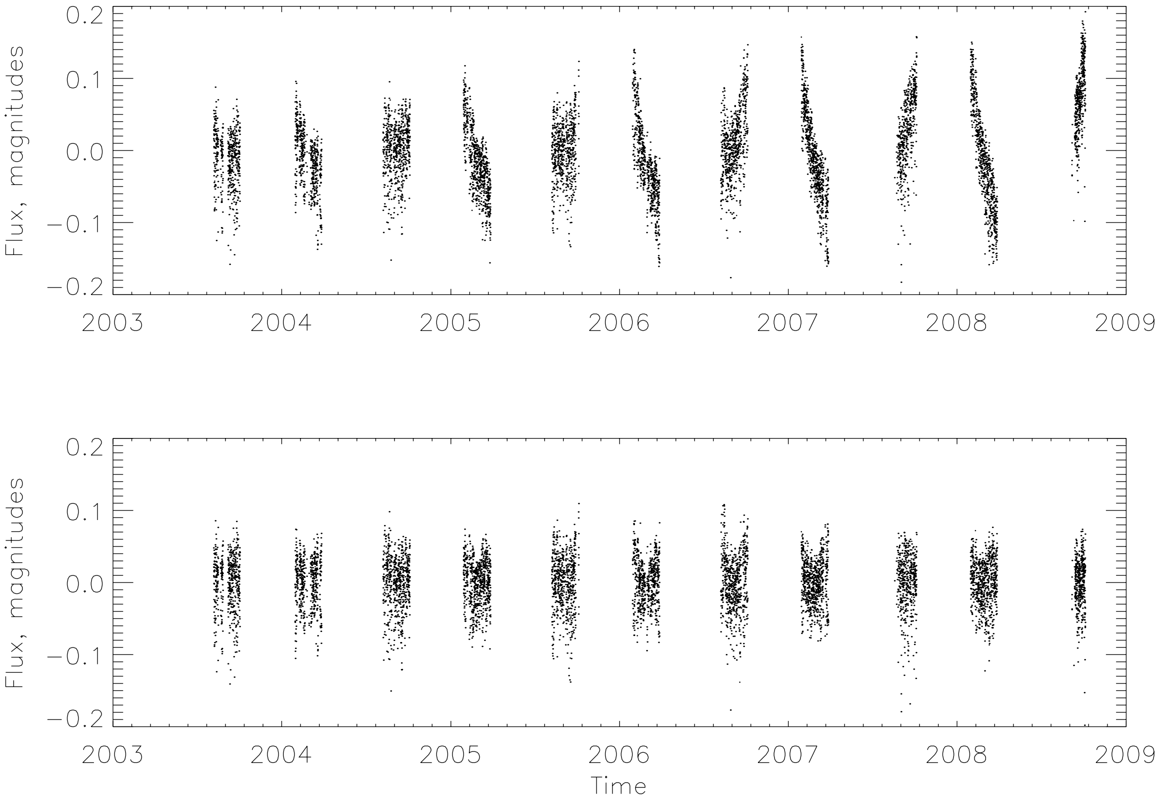

Figure 7.5: Timeseries of the β Cephei star ν Eri. Data pre-processing is shown in the upper plot, and after processing to remove linear trends in each observation in the lower plot.

in this case are above the Nyquist frequency, but due to the sampling have been reflected to lower frequencies (see Section 5.1.2 on page 86).

The highest frequency for which power has been detected in ν Eri by Jerzykiewicz et al. (2005) was located at approximately 22 d^{-1}. Figure 7.7 shows the amplitude spectrum extended out to 24 d^{-1} (approximately 3.4 times the Nyquist frequency). As the sampling of the SMEI data is not strictly regular, it can be seen that the features at approximately 11.4 d^{-1}, the location of the combination frequencies, have a higher amplitude than their reflections at approximately 2.75 d^{-1}.

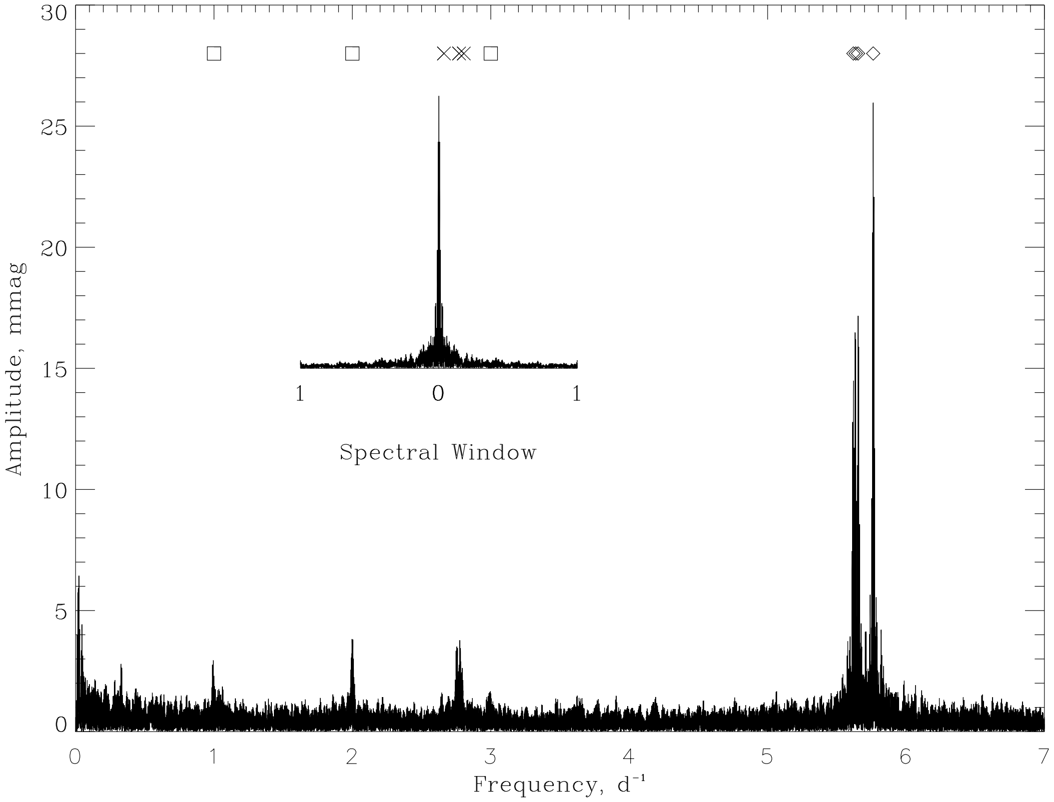

Figure 7.6: The amplitude spectrum of ν Eri. In this figure the independent frequencies have been noted by diamonds, aliases of the combination frequencies with crosses, and the diurnal artefacts introduced by the window function with squares.

Table 7.3 on page 167 reports on the frequencies observed in ν Eri. The convention established by the series of papers noted above in naming the frequencies has been followed. Frequencies and amplitudes are compared with the visual amplitude values given in Jerzykiewicz et al.

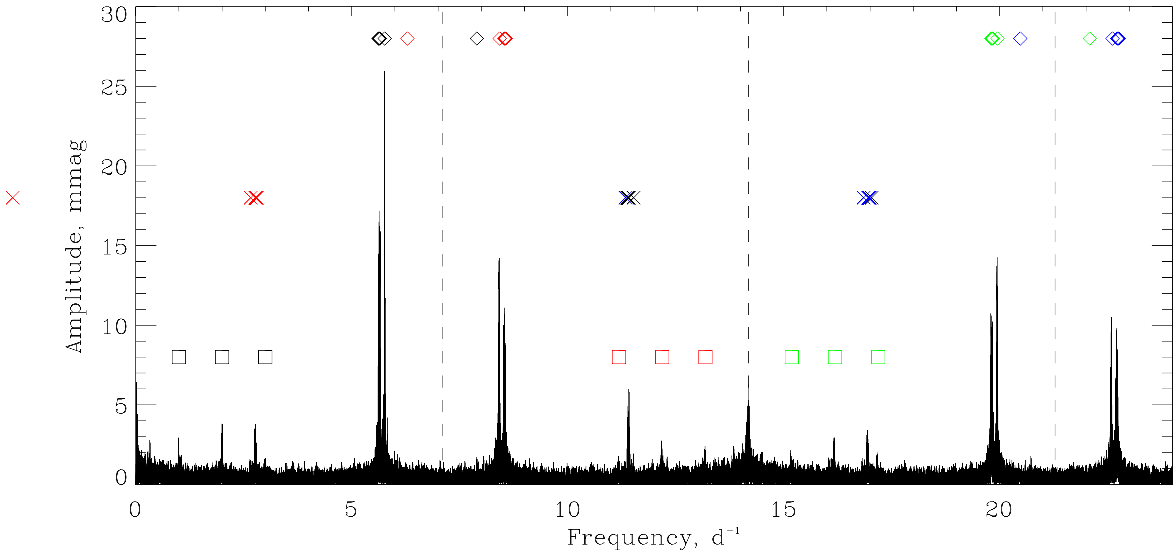

Figure 7.7: The amplitude spectrum of ν Eri, extended to several times the Nyquist critical sampling frequency. In this figure symbols denote the identification of the features, and colours the degree of the Nyquist with which they are associated. The independent frequencies have been noted by diamonds, aliases of the combination frequencies with crosses, and the diurnal artefacts introduced by the window function with squares. Features occurring at their 'true' frequency are shown in black, at aliases introduced by the first Nyquist frequency by red, by the second in green, and by the third in blue.

(2005). Here, we follow the convention established by the above series of papers, and only report on frequencies having a signal-to-noise of 4.0 or greater for an independent frequency, or 3.5 for a combination frequency (although no combination frequencies are seen at a signal-to-noise of between 3.5 and 4.0).

Having CLEANed this frequencies from the amplitude spectrum, the only feature noted in SMEI data other than the above frequencies and diurnal cycles was a spike at 0.328 d^{-1}. This feature appears to be co-incident with the anomalous feature noted in other SMEI timeseries, and therefore may be disregarded. A CLEANed version of the timeseries is shown in figure 7.8.

7.2.3 Discussion

There is excellent agreement between the frequency results seen in SMEI and the work of Jerzykiewicz et al. (2005), however the amplitudes observed by SMEI are systematically lower. Mode amplitudes are in general wavelength dependent, and for the R-band SMEI bandpass we should expect to see lower amplitudes to the previous observations which were made with a V-band filter.

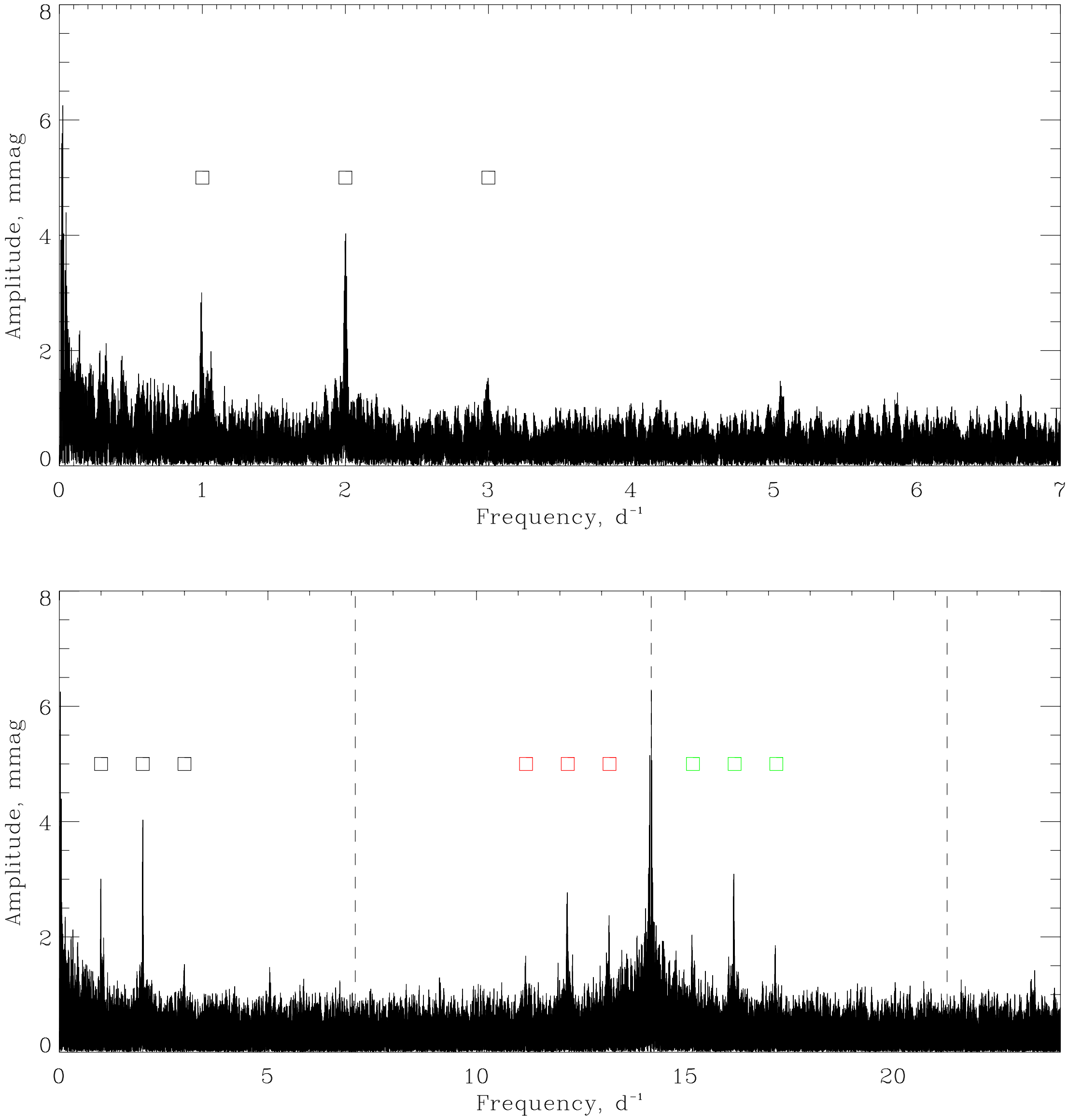

Figure 7.8: Amplitude Spectra of ν Eri, after all the significant features noted in Table 7.3 have been CLEANed. With the exception of noise at low-frequencies and diurnal cycles, no significant features are visible. In these diagrams the convention establish regarding colours and symbols as in Figures 7.6 on page 164 and 7.7 is followed.

Table 7.3: Frequencies observed in ν Eri. The naming convention established in Handler et al. (2004), and used in the follow up papers is maintained. Frequencies and amplitudes are compared with the results presented in Jerzykiewicz et al. (2005).

ID	Frequency (Jerzykiewicz) d^{-1}	Amplitude, A_v (Jerzykiewicz) mmag	Frequency (SMEI) d^{-1}	Amplitude (SMEI) mmag	Signal to Noise (SMEI)
Independent frequencies; significant in both					
F1	5.7632828(19)	40.8(1)	5.763250(4)	25.3(3)	73.1
F2	5.6538767(30)	27.1(1)	5.653876(6)	17.9(3)	45.7
F3	5.6200186(31)	24.5(1)	5.620012(6)	16.6(3)	46.7
F4	5.6372470(38)	22.3(1)	5.637229(7)	15.3(3)	39.8
F5	7.898200(32)	2.6(1)	7.89814(7)	1.6(3)	4.5
Combination frequencies, significant in both					
F1+F2	11.4171595(36)	8.8(1)	11.41712(2)	6.3(3)	16.6
F1+F3	11.3833014(36)	7.6(1)	11.38326(2)	5.0(3)	13.6
F1+F4	11.4005298(42)	7.2(1)	11.40048(2)	4.9(3)	13.7
2F1	11.5265656(27)	3.1(1)	11.52650(4)	2.3(3)	6.1
F1+F2+F3	17.037178(5)	2.5(1)	17.03714(7)	1.5(3)	4.0

A study of known β Cephei stars, with the intention to detect new modes of oscillation, and note any changes in the frequency of oscillation from those known has been undertaken using the SMEI data by Kym Goss and Ian Stevens. A further survey of a number of suitable candidate B stars for β Cephei class oscillations using SMEI data is also being performed by Kym Goss.

Chapter 8

Overview and Conclusions

The main focus of this thesis was to study individual stars across the HR diagram using the SMEI instrument, with the intent of characterising pulsational variability in these stars for the purposes of asteroseismology, and the determination of fundamental stellar parameters.

Chapters 2 and 3 of this thesis described the context of this study, in terms of the physics underlying the structure of stars, and within the science of asteroseismology. Asteroseismic variability will manifest in a number of different ways, and so a secure characterisation of the precise manner in which a star oscillates will allow a determination of the nature of the star.

8.1 The SMEI instrument, and analysis techniques

Chapter 4 of this thesis described the SMEI instrument. Five-year long photometric timeseries obtained from SMEI are available for a large number of the brightest stars in the sky. In general the data show a reasonable signal-to-noise ratio in comparison to other instruments of it's era, however it is not comparable to newer instruments such as CoRoT or Kepler. SMEI data show a number of anomalies associated with local effects of which any potential user should be aware. Annual and diurnal cycles are prominent in many data sets, which are speculated to be due respectively to imperfect cancellation of annual trends in the temperature of the instrument, stray light and a daily passage through the SAA.

It is important to note that the properties of SMEI data do not follow the expected statistics for broad concentrations of power. This introduces problems when searching for features which are spread over multiple bins of the power-spectrum. For example an anomalous, broad concentration of power at approximately 0.32 μHz is seen in a notable fraction of stars within 25° of the celestial equator.

The strength of the SMEI instrument comes in it's coverage. Time series are available on almost all stars in the sky brighter than magnitude 5 for a period of approximately five years, an . These stars are sometimes passed over in other observing campaigns which typically are limited in the number of targets they may observe and so concentrate upon targets known to show variability, or else observe only a small region of the sky. However, a limitation on the variability which may be observed is imposed by the Nyquist frequency, which places solar-like oscillators on the main-sequence outside of the observable range.

The results for stars which show sharp, sinusoidal oscillations at frequencies higher than 0.5 cycles per day seem to be robust, both statistically and in comparison to other observations of the same stars. There are a great number of stars with known oscillations which should be detectable with SMEI, as well as the potential for systematic surveys to detect new variables.

Chapter 5 of this thesis described the analysis techniques which are adopted for SMEI time-series. As the resolution of SMEI data is significantly greater than other comparable datasets the canonical 4.0 signal-to-noise test in amplitude was re-evaluated. It was shown that for such extended datasets the test should not be used, as the chances for at least one bin to show power at a signal-to-noise of above 4.0 will be approximately proportional to the number of bins.

8.2 Individual stars

For the K1.5III star Arcturus results are mixed. While initially the data suggested a prominent single mode of frequency 3.5 μHz, in a revised version of the processing pipeline no significant power at this frequency has been noted, and it is speculated that an error in the centroiding algorithm used in the earlier revision of the pipeline introduced power at this frequency. Assuming that the later data is reliable a limit of 0.438 ppt has been placed upon the amplitude of any single sinusoidal oscillation visible in Arcturus with a period shorter than approximately 5 days. This is contrary to expectations, as previous independent studies have seen an excess of power in this region.

For the first time we have been able to characterise variability in β UMi. We can robustly identify multi-periodic variability and give frequencies for each. However, the exact nature of the variability is unknown, and an interpretation of the spectrum may be made as showing either broad, presumably stochastically excited, or sharp, presumably κ mechanism excited oscillations.

Variability was also shown in the M giant star γ Crucis. Three prominent modes of oscillation were detected. As the modes are sharp in frequency it seems likely that γ Crucis does not show stochastic excitation. It may be that the apparent amplitude changes observed in semi-regular pulsating variable stars arise only as a result of beating between multi-mode oscillations.

Three further modes of oscillation to the three previously known have been detected in γ Doradus, the prototype star for γ Doradus class variable stars. The frequencies of these additional modes should allow theorists to better constrain models of the interior of the star.

The β Cephei star, ν Eri, has already been subject to an extensive observation programme in the early part of this century. SMEI has not been able to observe as many frequencies in the star at a high significance as the earlier observation programme, however the agreement between the determined frequencies is impressive.

8.3 Future projects

The results generated by SMEI for red giant stars have in many ways already been superseded by more accurate determinations from the CoRoT mission. Data from the NASA Kepler mission will also multiply by an order of magnitude the number of red giants stars for which an accurate determination of the oscillation parameters has been determined.

As the objects are rarer, the number of β Cephei stars which will be observed by Kepler is significantly lower than of red-giant stars, with only 12 long-cadence β Cephei targets. Therefore SMEI remains in a strong position to observe a substantial number of these objects, and a survey of known and likely β Cephei stars is being undertaken with SMEI data.

In general the five-year datasets of SMEI are a valuable resource for asteroseismology, being the longest comprehensive database of stellar variability available. As the objects under study are very bright, results generated from SMEI are well placed to be followed up by even fairly modest equipment.

Appendix A

Glossary

CCD A CCD, charge-coupled-device, is a photoelectric light sensor which is typically used in helio and asteroseismology to generate photometric observations of a star. Typically a single photon will release an electron in the plate, which will then be counted by the CCD.

CCDs are useful a useful tool as they are robust, being usable both on Earth and in space, and as the response function of an unsaturated CCD is linear to the input radiation - i.e., twice the number of photons will generate a signal twice the magnitude in the CCD (this is in contrast to photographic plates which has a logarithmic response function).

Full Width at Half Maximum A expression of the size (width) of a dispersed peak. Formally it is the difference between the two values of the dependent variable at the locations where the independent variable reaches a value of half that of the maximum (the 'peak'). For the Gaussian distribution this can be mathematically demonstrated to $2\sqrt{2\ln(2)}$, for the Lorentzian distribution it is the defining 'scale-parameter' of the distribution, Γ, and for the Sinc function it is 3.791, and for the Sinc^2 function it is 2.783.

Hipparcos Magnitude The Hipparcos magnitude is a measure of stellar brightness used by the 1989 Hipparcos space-based photometry mission. It represented the power seen through a broad band filter covering the spectral range 375-750 nm.

ICRS ICRS, the International Celestial Reference System, is a co-ordinate system which is approximately the same as equatorial co-ordinates. Formally the origin of the system is at the barycentre of the solar system with axes that are fixed relative to a number of extra-galactic quasars. These definitions were adopted such that the co-ordinate system are intended to be as close to 'fixed' with respect to space as possible.

Quaternions A generalisation of complex numbers into higher dimensions. Numbers of the form $a + b\mathrm{i} + c\mathrm{j} + d\mathrm{k}$, where $\mathrm{ij} = \mathrm{k}$, $\mathrm{jk} = \mathrm{i}$, $\mathrm{ki} = \mathrm{j}$ and $\mathrm{i}^2 = \mathrm{j}^2 = \mathrm{k}^2 = \mathrm{ijk} = -1$. Quaternions can provide a compact representation of a rotation, while avoiding some of the issues associated with a matrix representation, that is that the matrix is too powerful of a representation and can express not only rotation, but other transformations such as sheer, reflections and scalings.

Appendix B

Papers

The following chapter contains facsimile copies of papers released based on research undertaken as a part of my PhD.

In the case of the first paper, Section B.1, the text was primarily composed by Dr. William J. Chaplin in collaboration with the co-authors, based upon research conducted by myself. My name appears as first author due to the paper naming policies of the HiROS group.

In the case of the subsequent two papers, Section B.2 on page 179 and Section B.3 on page 183, the text was primarily written by myself, in collaboration with the co-authors.

Mon. Not. R. Astron. Soc. **382,** L48–L52 (2007)

doi:10.1111/j.1745-3933.2007.00387.x

Asteroseismology of red giants: photometric observations of Arcturus by SMEI

N. J. Tarrant, W. J. Chaplin,* Y. Elsworth, S. A. Spreckley and I. R. Stevens

School of Physics and Astronomy, University of Birmingham, Edgbaston, Birmingham B15 2TT

Accepted 2007 August 24. Received 2007 August 22; in original form 2007 June 11

ABSTRACT

We present new results on oscillations of the K1.5 III giant Arcturus (α Boo), from analysis of just over 2.5 yr of precise photometric observations made by the Solar Mass Ejection Imager on board the *Coriolis* satellite. A strong mode of oscillation is uncovered by the analysis, having frequency $3.51 \pm 0.03\ \mu$Hz. By fitting its mode peak, we are able to offer a highly constrained direct estimate of the damping time ($\tau = 24 \pm 1$ d). The data also hint at the possible presence of several radial-mode overtones, and maybe some non-radial modes. We are also able to measure the properties of the granulation on the star, with the characteristic time-scale for the granulation estimated to be $\sim 0.50 \pm 0.05$ d.

Key words: stars: individual: Arcturus – stars: oscillations.

A&A 483, L43–L46 (2008)
DOI: 10.1051/0004-6361:200809738

Astronomy
&
Astrophysics

L E

Oscillations in β Ursae Minoris

Observations with SMEI

N. J. Tarrant, W. J. Chaplin, Y. Elsworth, S. A. Spreckley, and I. R. Stevens

School of Physics and Astronomy, University of Birmingham, Edgbaston, Birmingham B15 2TT, UK
e-mail: `njt@bison.ph.bham.ac.uk`

Received 7 March 2008 / Accepted 9 April 2008

ABSTRACT

Aims. From observations of the K4III star β UMi we attempt to determine whether oscillations or any other form of variability is present.

Methods. A high-quality photometric time series of ≈1000 days in length obtained from the SMEI instrument on the Coriolis satellite is analysed. Various statistical tests were performed to determine the significance of features seen in the power density spectrum of the light curve.

Results. Two oscillations with frequencies 2.44 and 2.92 μHz have been identified. We interpret these oscillations as consecutive overtones of an acoustic spectrum, implying a large frequency spacing of 0.48 μHz. Using derived asteroseismic parameters in combination with known astrophysical parameters, we estimate the mass of β UMi to be 1.3 ± 0.3 $M_{\odot}$. Peaks of the oscillations in the power density spectrum show width, implying that modes are stochastically excited and damped by convection. The mode lifetime is estimated at 18 ± 9 days.

Key words. stars: individual: β UMi – stars: oscillations – stars: interiors – stars: fundamental parameters

A&A 492, 167–169 (2008)
DOI: 10.1051/0004-6361:200810952
©ESO 2008

Astronomy
&
Astrophysics

SMEI observations of previously unseen pulsation frequencies in γ Doradus

N. J. Tarrant, W. J. Chaplin, Y. P. Elsworth, S. A. Spreckley, and I. R. Stevens

School of Physics and Astronomy, University of Birmingham, Edgbaston, Birmingham, B15 2TT, UK
e-mail: `njt@bison.ph.bham.ac.uk`

Received 11 September 2008 / Accepted 22 September 2008

ABSTRACT

Aims. As g-mode pulsators, gamma-Doradus-class stars may naïvely be expected to show a large number of modes. Taking advantage of the long photometric time-series generated by the solar mass ejection imager (SMEI) instrument, we have studied the star gamma Doradus to determine whether any other modes than the three already known are present at observable amplitude.
Methods. High-precision photometric data from SMEI taken between April 2003 and March 2006 were subjected to periodogram analysis with the PERIOD04 package.
Results. We confidently determine three additional frequencies at 1.39, 1.87, and 2.743 d^{-1}. These are above and beyond the known frequencies of 1.320, 1.364, and 1.47 d^{-1}.
Conclusions. Two of the new frequencies, at 1.39 and 1.87 d^{-1}, are speculated to be additional modes of oscillation, with the third frequency at 2.743^{-1} a possible combination frequency.

Key words. stars: individual: γ Doradus – stars: oscillations – stars: early-type – stars: variables: general

References

C. Aerts, P. De Cat, G. Handler, U. Heiter, L. A. Balona, J. Krzesinski, P. Mathias, H. Lehmann, I. Ilyin, J. De Ridder, S. Dreizler, A. Bruch, I. Traulsen, A. Hoffmann, D. James, E. Romero-Colmenero, T. Maas, M. A. T. Groenewegen, J. H. Telting, K. Uytterhoeven, C. Koen, P. L. Cottrell, J. Bentley, D. J. Wright, and J. Cuypers. Asteroseismology of the β Cephei star ν Eridani - II. Spectroscopic observations and pulsational frequency analysis. MNRAS, 347: 463–470, January 2004. doi: 10.1111/j.1365-2966.2004.07215.x.

S. Aigrain, F. Favata, and G. Gilmore. Characterising stellar micro-variability for planetary transit searches. A&A, 414:1139–1152, February 2004. doi: 10.1051/0004-6361:20034039.

T. Appourchaux, T. Toutain, D. O. Gough, and A. Kosovichev. Testing the Statistical Significance of the Asymmetries of p-Mode Line Profiles: Application to the IPHIR Data. In R. K. Ulrich, E. J. Rhodes Jr., & W. Dappen, editor, *GONG 1994. Helio- and Astro-Seismology from the Earth and Space*, volume 76 of *Astronomical Society of the Pacific Conference Series*, page 314, 1995.

Thierry Appourchaux. The quest for solar g modes. A talk given at the GONG 2008 / SOHO XXI Meeting, August 11-15, 2008 - Boulder, Colorado, August 2008.

T. Arentoft, H. Kjeldsen, T. R. Bedding, M. Bazot, J. Christensen-Dalsgaard, T. H. Dall, C. Karoff, F. Carrier, P. Eggenberger, D. Sosnowska, R. A. Wittenmyer, M. Endl, T. S. Metcalfe, S. Hekker, S. Reffert, R. P. Butler, H. Bruntt, L. L. Kiss, S. J. O'Toole, E. Kambe, H. Ando, H. Izumiura, B. Sato, M. Hartmann, A. Hatzes, F. Bouchy, B. Mosser, T. Appourchaux, C. Barban, G. Berthomieu, R. A. Garcia, E. Michel, J. Provost, S. Turck-Chièze, M. Martić, J.-C. Lebrun, J. Schmitt, J.-L. Bertaux, A. Bonanno, S. Benatti, R. U. Claudi, R. Cosentino, S. Leccia, S. Frandsen, K. Brogaard, L. Glowienka, F. Grundahl, and

E. Stempels. A Multisite Campaign to Measure Solar-like Oscillations in Procyon. I. Observations, Data Reduction, and Slow Variations. ApJ, 687:1180–1190, November 2008. doi: 10.1086/592040.

T. Arentoft, H. Kjeldsen, and T. R. Bedding. Optimizing Weights for the Detection of Stellar Oscillations: Application to alpha Centauri A and B, and beta Hydri. *ArXiv e-prints*, January 2009.

A. Baglin, M. Auvergne, P. Barge, M. Deleuil, C. Catala, E. Michel, W. Weiss, and The COROT Team. Scientific Objectives for a Minisat: CoRoT. In M. Fridlund, A. Baglin, J. Lochard, & L. Conroy, editor, *ESA Special Publication*, volume 1306 of *ESA Special Publication*, page 33, November 2006.

L. A. Balona, K. Krisciunas, and A. W. J. Cousins. Gamma-Doradus - Evidence for a New Class of Pulsating Star. MNRAS, 270:905, October 1994.

C. Barban, J. M. Matthews, J. De Ridder, F. Baudin, R. Kuschnig, A. Mazumdar, R. Samadi, D. B. Guenther, A. F. J. Moffat, S. M. Rucinski, D. Sasselov, G. A. H. Walker, and W. W. Weiss. Detection of solar-like oscillations in the red giant star ϵ Ophiuchi by MOST spacebased photometry. A&A, 468:1033–1038, June 2007. doi: 10.1051/0004-6361:20066716.

T. Bedding and H. Kjeldsen. Observations of solar-like oscillations. In *Proceedings of SOHO 18/GONG 2006/HELAS I, Beyond the spherical Sun*, volume 624 of *ESA Special Publication*, October 2006.

T. R. Bedding, H. Kjeldsen, J. Reetz, and B. Barbuy. Measuring stellar oscillations using equivalent widths of absorption lines. MNRAS, 280:1155–1161, June 1996.

T. R. Bedding, L. L. Kiss, H. Kjeldsen, B. J. Brewer, Z. E. Dind, S. D. Kawaler, and A. A. Zijlstra. The light curve of the semiregular variable L_2 Puppis - II. Evidence for solar-like excitation of the oscillations. MNRAS, 361:1375–1381, August 2005. doi: 10.1111/j.1365-2966.2005.09281.x.

K. Belkacem, R. Samadi, M.-J. Goupil, L. Lefèvre, F. Baudin, S. Deheuvels, M.-A. Dupret, T. Appourchaux, R. Scuflaire, M. Auvergne, C. Catala, E. Michel, A. Miglio, J. Montalban,

A. Thoul, S. Talon, A. Baglin, and A. Noels. Solar-Like Oscillations in a Massive Star. *Science*, 324:1540–, June 2009. doi: 10.1126/science.1171913.

J. A. Belmonte, A. R. Jones, P. L. Palle, and T. Roca Cortes. Acoustic oscillations in the K2 III star Arcturus. Ap&SS, 169:77–84, July 1990. doi: 10.1007/BF00640689.

A. Blecha, G. Schaller, and A. Maeder. Fast pulsations in a Wolf-Rayet star. *Nature*, 360: 320–321, November 1992. doi: 10.1038/360320a0.

W. J. Borucki, D. G. Koch, J. Lissauer, G. Basri, T. Brown, D. A. Caldwell, J. M. Jenkins, J. J. Caldwell, J. Christensen-Dalsgaard, W. D. Cochran, E. W. Dunham, T. N. Gautier, J. C. Geary, D. Latham, D. Sasselov, R. L. Gilliland, S. Howell, D. G. Monet, and N. Batalha. KEPLER Mission Status. In *Transiting Extrapolar Planets Workshop*, volume 366 of *Astronomical Society of the Pacific Conference Series*, page 309, July 2007.

M.-P. Bouabid, K. Uytterhoeven, A. Miglio, J. Montalban, M.-A. Dupret, E. Niemczura, P. Mathias, A. Noels, and A. Grigahcene. Preliminary seismic study of the γ Doradus COROT target HD 49434. *Communications in Asteroseismology*, 157:290–291, December 2008.

M. Breger. Period Variations of Delta Scuti Stars. In J. A. Guzik & P. A. Bradley, editor, *American Institute of Physics Conference Series*, volume 1170 of *American Institute of Physics Conference Series*, pages 410–414, September 2009. doi: 10.1063/1.3246530.

M. Breger, J. Stich, R. Garrido, B. Martin, S. Y. Jiang, Z. P. Li, D. P. Hube, W. Ostermann, M. Paparo, and M. Scheck. Nonradial Pulsation of the Delta-Scuti Star Bu-Cancri in the Praesepe Cluster. A&A, 271:482, April 1993.

A.-M. Broomhall, W. J. Chaplin, G. R. Davies, Y. Elsworth, S. T. Fletcher, S. J. Hale, B. Miller, and R. New. Definitive Sun-as-a-star p-mode frequencies: 23 years of BiSON observations. MNRAS, 396:L100–L104, June 2009a. doi: 10.1111/j.1745-3933.2009.00672.x.

A.-M. Broomhall, W. J. Chaplin, Y. Elsworth, S. T. Fletcher, and R. New. Corrections of Sun-as-a-star p-mode frequencies for effects of the solar cycle. A&A, 503:241–245, August 2009b. doi: 10.1051/0004-6361/200912286.

A.-M. Broomhall, W. J. Chaplin, Y. Elsworth, S. T. Fletcher, and R. New. Is the Current Lack of Solar Activity Only Skin Deep? ApJ, 700:L162–L165, August 2009c. doi: 10.1088/0004-637X/700/2/L162.

K. I. T. Brown, D. F. Gray, and S. L. Baliunas. Long-Term Spectroscopic Monitoring of Arcturus. ApJ, 679:1531–1540, June 2008. doi: 10.1086/587783.

H. Bruntt. Asteroseismology with the WIRE satellite. *Communications in Asteroseismology*, 150:326, June 2007. doi: 10.1553/cia150s326.

H. Bruntt and D. L. Buzasi. High-precision photometry with the WIRE satellite . *Memorie della Societa Astronomica Italiana*, 77:278–+, 2006.

H. Bruntt, N. R. Evans, D. Stello, A. J. Penny, J. A. Eaton, D. L. Buzasi, D. D. Sasselov, H. L. Preston, and E. Miller-Ricci. Polaris the Cepheid Returns: 4.5 Years of Monitoring from Ground and Space. ApJ, 683:433–440, August 2008. doi: 10.1086/589565.

E. Budding and Osman Demircan. *Introduction to Astronomical Photometry.* Cambridge University Press, Cambridge, 2nd, illustrated, revised edition, 2007.

D. Buzasi. Platforms of opportunity: asteroseismology by Piggyback. In R. Pallavicini, G. Micela, & S. Sciortino, editor, *Stellar Clusters and Associations: Convection, Rotation, and Dynamos*, volume 198 of *Astronomical Society of the Pacific Conference Series*, pages 557–+, 2000.

D. Buzasi. Asteroseismic Results from WIRE (invited paper). In C. Aerts, T. R. Bedding, & J. Christensen-Dalsgaard, editor, *IAU Colloq. 185: Radial and Nonradial Pulsationsn as Probes of Stellar Physics*, volume 259 of *Astronomical Society of the Pacific Conference Series*, pages 616–+, 2002.

D. Cardini and A. Cassatella. Color, Rotation, Age, and Chromospheric Activity Correlations in Late-Type Main-Sequence Stars. ApJ, 666:393–402, September 2007. doi: 10.1086/519991.

A. J. Cenarro, R. F. Peletier, P. Sánchez-Blázquez, S. O. Selam, E. Toloba, N. Cardiel, J. Falcón-Barroso, J. Gorgas, J. Jiménez-Vicente, and A. Vazdekis. Medium-resolution Isaac Newton

Telescope library of empirical spectra - II. The stellar atmospheric parameters. MNRAS, 374: 664–690, January 2007. doi: 10.1111/j.1365-2966.2006.11196.x.

W. C. Chaplin, Y. Elsworth, G. R. Isaak, R. Lines, C. P. McLeod, B. A. Miller, R. New, and H. B. van der Raay. Observing the sun with the Birmingham Solar-Oscillations Network (BISON). *The Observatory*, 116:32–33, February 1996.

W. J. Chaplin. A Key to Understanding the Sun and Stars: The Birmingham Solar-Oscillations Network (BiSON). *Irish Astronomical Journal*, 24:103, July 1997.

W. J. Chaplin, Y. Elsworth, R. Howe, G. R. Isaak, C. P. McLeod, B. A. Miller, and R. New. The observation and simulation of stochastically excited solar P modes. MNRAS, 287:51–56, May 1997.

W. J. Chaplin, Y. Elsworth, G. R. Isaak, B. A. Miller, and R. New. Skew-symmetric solar P modes in low-l BiSON data. MNRAS, 308:424–430, September 1999.

William J. Chaplin. *Music of the Sun; the Story of Helioseismology.* One World, Oxford, first edition, 2006.

J. Christensen-Dalsgaard. On the Asteroseismic HR Diagram. In *GONG 1992. Seismic Investigation of the Sun and Stars*, volume 42 of *Astronomical Society of the Pacific Conference Series*, page 347, January 1993.

J. Christensen-Dalsgaard. *Lecture Notes on Stellar Oscillations.* Institut for Fysik og Astronomi, Aarhus Universitet, and Teoretisk Astrofysik Center, Danmarks Grundforskningsfond, fifth edition, March 2003.

J. Christensen-Dalsgaard and S. Frandsen. Stellar 5 min oscillations. Sol. Phys., 82:469–486, January 1983.

J. Christensen-Dalsgaard and D. O. Gough. On the interpretation of five-minute oscillations in solar spectrum line shifts. MNRAS, 198:141–171, January 1982.

J. Christensen-Dalsgaard, H. Kjeldsen, and J. A. Mattei. Solar-like Oscillations of Semiregular Variables. ApJ, 562:L141–L144, December 2001. doi: 10.1086/338194.

J. Christensen-Dalsgaard, T. Arentoft, T. M. Brown, R. L. Gilliland, H. Kjeldsen, W. J. Borucki, and D. Koch. The Kepler asteroseismic investigation. *Journal of Physics Conference Series*, 118(1):012039, October 2008. doi: 10.1088/1742-6596/118/1/012039.

J. Christensen-Dalsgaard, T. Arentoft, T. M. Brown, R. L. Gilliland, H. Kjeldsen, W. J. Borucki, and D. Koch. The Kepler mission. *Communications in Asteroseismology*, 158:328, July 2009.

L. da Silva, L. Girardi, L. Pasquini, J. Setiawan, O. von der Lühe, J. R. de Medeiros, A. Hatzes, M. P. Döllinger, and A. Weiss. Basic physical parameters of a selected sample of evolved stars. A&A, 458:609–623, November 2006. doi: 10.1051/0004-6361:20065105.

J. De Ridder, J. H. Telting, L. A. Balona, G. Handler, M. Briquet, J. Daszyńska-Daszkiewicz, K. Lefever, A. J. Korn, U. Heiter, and C. Aerts. Asteroseismology of the β Cephei star ν Eridani - III. Extended frequency analysis and mode identification. MNRAS, 351:324–332, June 2004. doi: 10.1111/j.1365-2966.2004.07791.x.

J. De Ridder, C. Barban, F. Carrier, A. Mazumdar, P. Eggenberger, C. Aerts, S. Deruyter, and J. Vanautgaerden. Discovery of solar-like oscillations in the red giant ϵ Ophiuchi. A&A, 448: 689–695, March 2006. doi: 10.1051/0004-6361:20053331.

J. De Ridder, C. Barban, F. Baudin, F. Carrier, A. P. Hatzes, S. Hekker, T. Kallinger, W. W. Weiss, A. Baglin, M. Auvergne, R. Samadi, P. Barge, and M. Deleuil. Non-radial oscillation modes with long lifetimes in giant stars. Nature, 459:398–400, May 2009. doi: 10.1038/nature08022.

J. Debosscher, L. M. Sarro, C. Aerts, J. Cuypers, B. Vandenbussche, R. Garrido, and E. Solano. Automated supervised classification of variable stars. I. Methodology. A&A, 475:1159–1183, December 2007. doi: 10.1051/0004-6361:20077638.

J. Debosscher, L. M. Sarro, M. López, M. Deleuil, C. Aerts, M. Auvergne, A. Baglin, F. Baudin, M. Chadid, S. Charpinet, J. Cuypers, J. De Ridder, R. Garrido, A. M. Hubert, E. Janot-Pacheco, L. Jorda, A. Kaiser, T. Kallinger, Z. Kollath, C. Maceroni, P. Mathias, E. Michel, C. Moutou, C. Neiner, M. Ollivier, R. Samadi, E. Solano, C. Surace, B. Vandenbussche, and W. W. Weiss. Automated supervised classification of variable stars in the CoRoT programme.

Method and application to the first four exoplanet fields. A&A, 506:519–534, October 2009. doi: 10.1051/0004-6361/200911618.

L. Decin, B. Vandenbussche, C. Waelkens, G. Decin, K. Eriksson, B. Gustafsson, B. Plez, and A. J. Sauval. ISO-SWS calibration and the accurate modelling of cool-star atmospheres. IV. G9 to M2 stars. A&A, 400:709–727, March 2003. doi: 10.1051/0004-6361:20021786.

F.-L. Deubner. Observations of low wavenumber nonradial eigenmodes of the sun. A&A, 44: 371–375, November 1975.

A. Domiciano de Souza, P. Kervella, S. Jankov, L. Abe, F. Vakili, E. di Folco, and F. Paresce. The spinning-top Be star Achernar from VLTI-VINCI. A&A, 407:L47–L50, August 2003. doi: 10.1051/0004-6361:20030786.

M.-A. Dupret, A. Grigahcène, R. Garrido, J. De Ridder, A. Moya, J.-C. Suárez, R. Scuflaire, M. Gabriel, and M.-J. Goupil. Theoretical Aspects of g-mode Pulsations in gamma Doradus Stars. *Memorie della Societa Astronomica Italiana*, 77:366, 2006a.

M.-A. Dupret, A. Grigahcène, R. Garrido, J. De Ridder, R. Scuflaire, and M. Gabriel. Application of time-dependent convection models to the photometric mode identification in gamma Doradus stars. *Memorie della Societa Astronomica Italiana*, 77:121, 2006b.

M.-A. Dupret, K. Belkacem, R. Samadi, J. Montalban, O. Moreira, A. Miglio, M. Godart, P. Ventura, H.-G. Ludwig, A. Grigahcène, M.-J. Goupil, A. Noels, and E. Caffau. Theoretical amplitudes and lifetimes of non-radial solar-like oscillations in red giants. volume 506, pages 57–67, October 2009. doi: 10.1051/0004-6361/200911713.

T. L. Duvall, Jr. and J. W. Harvey. Solar Doppler shifts: Sources of continuous spectra. In D. O. Gough, editor, *NATO ASIC Proc. 169: Seismology of the Sun and the Distant Stars*, pages 105–116, 1986.

W. A. Dziembowski, D. O. Gough, G. Houdek, and R. Sienkiewicz. Oscillations of α UMa and other red giants. MNRAS, 328:601–610, December 2001. doi: 10.1046/j.1365-8711.2001.04894.x.

A. J. Eddington. *The Internal Constitution of the Stars.* Cambridge University Press, 1926.

A. J. Eddington. *Stars and Atoms.* Oxford University Press, 1927.

Y. Elsworth, R. Howe, G. R. Isaak, C. P. McLeod, and R. New. Evidence from solar seismology against non-standard solar-core models. Nature, 347:536–539, October 1990. doi: 10.1038/347536a0.

C. J. Eyles, G. M. Simnett, M. P. Cooke, B. V. Jackson, A. Buffington, P. P. Hick, N. R. Waltham, J. M. King, P. A. Anderson, and P. E. Holladay. The Solar Mass Ejection Imager (Smei). Sol. Phys., 217:319–347, November 2003.

S. T. Fletcher, W. J. Chaplin, Y. Elsworth, J. Schou, and D. Buzasi. Frequency, splitting, linewidth and amplitude estimates of low-l p modes of α Cen A: analysis of Wide-Field Infrared Explorer photometry. MNRAS, 371:935–944, September 2006. doi: 10.1111/j.1365-2966.2006.10727.x.

P. J. Flower. Transformations from Theoretical Hertzsprung-Russell Diagrams to Color-Magnitude Diagrams: Effective Temperatures, B-V Colors, and Bolometric Corrections. ApJ, 469:355, September 1996. doi: 10.1086/177785.

S. Frandsen, F. Carrier, C. Aerts, D. Stello, T. Maas, M. Burnet, H. Bruntt, T. C. Teixeira, J. R. de Medeiros, F. Bouchy, H. Kjeldsen, F. Pijpers, and J. Christensen-Dalsgaard. Detection of Solar-like oscillations in the G7 giant star xi Hya. A&A, 394:L5–L8, October 2002. doi: 10.1051/0004-6361:20021281.

A. H. Gabriel, F. Baudin, P. Boumier, R. A. García, S. Turck-Chièze, T. Appourchaux, L. Bertello, G. Berthomieu, J. Charra, D. O. Gough, P. L. Pallé, J. Provost, C. Renaud, J.-M. Robillot, T. Roca Cortés, S. Thiery, and R. K. Ulrich. A search for solar g modes in the GOLF data. A&A, 390:1119–1131, August 2002. doi: 10.1051/0004-6361:20020695.

Rafael A. Garcia, Sylvaine Turck-Chieze, Sebastian J. Jimenez-Reyes, Jerome Ballot, Pere L. Palle, Antonio Eff-Darwich, Savita Mathur, and Janine Provost. Tracking Solar Gravity Modes: The Dynamics of the Solar Core. *Science*, 316(5831):1591–1593, 2007. doi: 10.1126/science.1140598. URL `http://www.sciencemag.org/cgi/content/abstract/316/5831/1591`.

S. J. George, I. R. Stevens, and S. A. Spreckley. Is Shedir Variable? *ArXiv e-prints*, May 2009.

L. Gizon and S. K. Solanki. Determining the Inclination of the Rotation Axis of a Sun-like Star. ApJ, 589:1009–1019, June 2003. doi: 10.1086/374715.

P. R. Goode. Solar Constant or Terrestrial Reflectance – Which Changes More? *AGU Spring Meeting Abstracts*, pages D8+, May 2007.

C. Gordon, D. Webb, and S. Wolpert. Isospectral plane domains and surfaces via Riemannian orbifolds. *Inventiones Mathematicae*, 110:1, 1992. doi: 10.1007/BF01231320.

D. F. Gray and K. I. T. Brown. The Rotation of Arcturus and Active Longitudes on Giant Stars. PASP, 118:1112–1118, August 2006. doi: 10.1086/507077.

R. E. M. Griffin and A. E. Lynas-Gray. The Effective Temperature of Arcturus. AJ, 117: 2998–3006, June 1999. doi: 10.1086/300878.

F. Grundahl, H. Kjeldsen, S. Frandsen, M. Andersen, T. Bedding, T. Arentoft, and J. Christensen-Dalsgaard. SONG: Stellar Oscillations Network Group . A global network of small telescopes for asteroseismology and planet searches. *Memorie della Societa Astronomica Italiana*, 77:458, 2006.

D. B. Guenther, T. Kallinger, M. Gruberbauer, D. Huber, W. W. Weiss, R. Kuschnig, P. Demarque, F. Robinson, J. M. Matthews, A. F. J. Moffat, S. M. Rucinski, D. Sasselov, and G. A. H. Walker. The Nature of p-modes and Granulation in Procyon: New MOST Photometry and New Yale Convection Models. ApJ, 687:1448–1459, November 2008. doi: 10.1086/592060.

J. A. Guzik, A. B. Kaye, P. A. Bradley, A. N. Cox, and C. Neuforge. Driving the Gravity-Mode Pulsations in γ Doradus Variables. ApJ, 542:L57–L60, October 2000. doi: 10.1086/312908.

G. Handler. Asteroseismology of Delta Scuti and Gamma Doradus Stars. *Journal of Astrophysics and Astronomy*, 26:241, June 2005. doi: 10.1007/BF02702332.

G. Handler. Confirmation of simultaneous p and g mode excitation in HD 8801 and γ Peg from time-resolved multicolour photometry of six candidate ‘hybrid’ pulsators. MNRAS, 398: 1339–1351, September 2009. doi: 10.1111/j.1365-2966.2009.15005.x.

G. Handler, R. R. Shobbrook, M. Jerzykiewicz, K. Krisciunas, T. Tshenye, E. Rodríguez, V. Costa, A.-Y. Zhou, R. Medupe, W. M. Phorah, R. Garrido, P. J. Amado, M. Paparó,

D. Zsuffa, L. Ramokgali, R. Crowe, N. Purves, R. Avila, R. Knight, E. Brassfield, P. M. Kilmartin, and P. L. Cottrell. Asteroseismology of the β Cephei star ν Eridani - I. Photometric observations and pulsational frequency analysis. MNRAS, 347:454–462, January 2004. doi: 10.1111/j.1365-2966.2004.07214.x.

J. Harvey. High-Resolution Helioseismology. In E. Rolfe and B. Battrick, editors, *Future Missions in Solar, Heliospheric & Space Plasma Physics*, volume 235 of *ESA Special Publication*, page 199, 1985.

A. P. Hatzes and W. D. Cochran. Long-period radial velocity variations in three K giants. ApJ, 413:339–348, August 1993. doi: 10.1086/173002.

A. P. Hatzes and W. D. Cochran. Short-period radial velocity variations of alpha Bootis: Evidence for radial pulsations. ApJ, 422:366–373, February 1994. doi: 10.1086/173731.

J. N. Heasley, K. Janes, B. Labonte, D. Guenther, D. Mickey, and P. Demarque. The Prospects for Asteroseismology from Ground-based Sites. PASP, 108:385, May 1996.

S. Hekker, C. Aerts, J. De Ridder, and F. Carrier. Pulsations detected in the line profile variations of red giants. Modelling of line moments, line bisector and line shape. A&A, 458: 931–940, November 2006. doi: 10.1051/0004-6361:20065755.

S. Hekker, T. Kallinger, F. Baudin, J. De Ridder, C. Barban, F. Carrier, A. P. Hatzes, W. W. Weiss, and A. Baglin. Characteristics of solar-like oscillations in red giants observed in the CoRoT exoplanet field. A&A, 506:465–469, October 2009. doi: 10.1051/0004-6361/200911858.

J. A. Högbom. Aperture Synthesis with a Non-Regular Distribution of Interferometer Baselines. A&AS, 15:417, June 1974.

P. Horowitz and H Winfield. *The Art of Electronics.* Cambridge University Press, Cambridge, second edition, 1989.

J. L. Innis, G. R. Isaak, R. I. Brazier, J. A. Belmonte, P. L. Palle, T. Rocacortes, and A. R. Jones. High precision velocity observations of Arcturus using the 7699 A line of potassium. In E. J. Rolfe, editor, *Seismology of the Sun and Sun-Like Stars*, volume 286 of *ESA Special Publication*, pages 569–573, December 1988.

M. J. Ireland, P. G. Tuthill, T. R. Bedding, J. G. Robertson, and A. P. Jacob. Multiwavelength diameters of nearby Miras and semiregular variables. MNRAS, 350:365–374, May 2004. doi: 10.1111/j.1365-2966.2004.07651.x.

M. Jerzykiewicz. Multiperiodicity and nonradial oscillations of the beta Cephei star 12 Lacertae. In H. A. Hill and W. A. Dziembowski, editors, *Nonradial and Nonlinear Stellar Pulsation*, volume 125 of *Lecture Notes in Physics, Berlin Springer Verlag*, pages 96–104, 1980. doi: 10.1007/3-540-09994-8_9.

M. Jerzykiewicz, G. Handler, R. R. Shobbrook, A. Pigulski, R. Medupe, T. Mokgwetsi, P. Tlhagwane, and E. Rodríguez. Asteroseismology of the β Cephei star ν Eridani - IV. The 2003-2004 multisite photometric campaign and the combined 2002-2004 data. MNRAS, 360: 619–630, June 2005. doi: 10.1111/j.1365-2966.2005.09088.x.

C. Karoff. *Observational asteroseismology.* PhD thesis, University of Aarhus, May 2008.

L. L. Kiss and T. R. Bedding. Red variables in the OGLE-II data base - I. Pulsations and period-luminosity relations below the tip of the red giant branch of the Large Magellanic Cloud. MNRAS, 343:L79–L83, August 2003. doi: 10.1046/j.1365-8711.2003.06931.x.

L. L. Kiss, K. Szatmáry, R. R. Cadmus, Jr., and J. A. Mattei. Multiperiodicity in semiregular variables. I. General properties. A&A, 346:542–555, June 1999.

H. Kjeldsen and T. R. Bedding. Amplitudes of stellar oscillations: the implications for asteroseismology. A&A, 293:87–106, January 1995.

H. Kjeldsen, T. R. Bedding, M. Viskum, and S. Frandsen. Solarlike oscillations in eta Boo. AJ, 109:1313–1319, March 1995. doi: 10.1086/117363.

David Koch and Alan Gould. Kepler mission, 2007. URL `http://kepler.nasa.gov/`.

C. Koen and L. Eyer. New periodic variables from the Hipparcos epoch photometry. MNRAS, 331:45–59, March 2002. doi: 10.1046/j.1365-8711.2002.05150.x.

B. V. Kukarkin, P. N. Kholopov, N. M. Artiukhina, V. P. Fedorovich, M. S. Frolov, V. P. Goranskij, N. A. Gorynya, E. A. Karitskaya, N. N. Kireeva, N. P. Kukarkina, N. E. Kurochkin, G. I. Medvedeva, N. B. Perova, G. A. Ponomareva, N. N. Samus, and S. Y. Shugarov. Catalogue of suspected variable stars. In *Moscow, Acad. of Sciences USSR Shternberg,1951 (1981)*, page 0, 1981.

D. W. Kurtz. Delta Scuti, Gamma DOR and roAp stars. *Delta Scuti Star Newsletter*, 10:28, October 1996.

D. W. Kurtz. Asteroseismology from Dome C. In *EAS Publications Series*, volume 25 of *Engineering and Science*, pages 95–101, 2007. doi: 10.1051/eas:2007079.

A. Kučinskas, P. H. Hauschildt, I. Brott, V. Vansevičius, L. Lindegren, T. Tanabé, and F. Allard. Broad-band photometric colors and effective temperature calibrations for late-type giants. II. Z ¡ 0.02. A&A, 452:1021–1038, June 2006. doi: 10.1051/0004-6361:20054431.

H. S. Leavitt and E. C. Pickering. Periods of 25 Variable Stars in the Small Magellanic Cloud. *Harvard College Observatory Circular*, 173:1–3, March 1912.

R. B. Leighton, R. W. Noyes, and G. W. Simon. Velocity Fields in the Solar Atmosphere. I. Preliminary Report. ApJ, 135:474, March 1962.

G. Lenain, R. Scuflaire, M.-A. Dupret, and A. Noels. The epsilon-mechanism in PMS and MS delta Scuti stars. *Communications in Asteroseismology*, 147:93–96, January 2006.

P. Lenz and M. Breger. Period04 User Guide. *Communications in Asteroseismology*, 146:53–136, June 2005. doi: 10.1553/cia146s53.

J. L. Linsky. Solar and stellar observations from the South Pole. In D. J. Mullan, M. A. Pomerantz, and T. Stanev, editors, *Astrophysics in Antarctica*, volume 198 of *American Institute of Physics Conference Series*, pages 205–217, 1989.

N. R. Lomb. Least-squares frequency analysis of unequally spaced data. Ap&SS, 39:447–462, February 1976. doi: 10.1007/BF00648343.

P. Mathias, E. Chapellier, M. Bouabid, E. Rodriguez, E. Poretti, M. Paparo, M. Hareter, P. De Cat, and L. Eyer. gamma Doradus stars in the COROT exoplanets fields: first inspection. *ArXiv e-prints*, September 2009.

J. M. Matthews, R. Kusching, D. B. Guenther, G. A. H. Walker, A. F. J. Moffat, S. M. Rucinski, D. Sasselov, and W. W. Weiss. No stellar p-mode oscillations in space-based photometry of Procyon. Nature, 430:51–53, July 2004. doi: 10.1038/nature02671.

W. J. Merline. *Observations of Small-Amplitude Oscillations in the Radial Velocity of Arcturus.* PhD thesis, AA(THE UNIVERSITY OF ARIZONA.), January 1995.

E. Michel, A. Baglin, W. W. Weiss, M. Auvergne, C. Catala, C. Aerts, T. Appourchaux, C. Barban, F. Baudin, M. Briquet, F. Carrier, P. Degroote, J. De Ridder, R. A. Garcia, R. Garrido, J. Gutiérrez-Soto, T. Kallinger, L. Lefevre, C. Neiner, E. Poretti, R. Samadi, L. Sarro, G. Alecian, L. Andrade, J. Ballot, O. Benomar, G. Berthomieu, P. Boumier, S. Charpinet, B. de Batz, S. Deheuvels, M.-A. Dupret, M. Emilio, J. Fabregat, W. Facanha, M. Floquet, Y. Frémat, M. Fridlund, M.-J. Goupil, A. Grotsch-Noels, G. Handler, A.-L. Huat, A.-M. Hubert, E. Janot-Pacheco, H. Kjeldsen, Y. Lebreton, B. Leroy, C. Martayan, P. Mathias, A. Miglio, J. Montalban, M. J. P. F. G. Monteiro, B. Mosser, J Provost, C. Regulo, J. Renan de Medeiros, I. Ribas, T. Roca Cortés, I. Roxburgh, J. Suso, A. Thoul, T. Toutain, D. Tiphene, S. Turck-Chieze, S. Vauclair, G. Vauclair, and K. Zwintz. First asteroseismic results from CoRoT. *Communications in Asteroseismology*, 156:73–87, December 2008.

D. Mozurkewich, J. T. Armstrong, R. B. Hindsley, A. Quirrenbach, C. A. Hummel, D. J. Hutter, K. J. Johnston, A. R. Hajian, N. M. Elias, II, D. F. Buscher, and R. S. Simon. Angular Diameters of Stars from the Mark III Optical Interferometer. AJ, 126:2502–2520, November 2003. doi: 10.1086/378596.

K. Murdoch, M. Clark, and J. B. Hearnshaw. The radial-velocity variability of Gamma Crucis. MNRAS, 254:27–29, January 1992.

J. R. Percy, J. B. Wilson, and G. W. Henry. Long-Term VRI Photometry of Small-Amplitude Red Variables. I. Light Curves and Periods. PASP, 113:983–996, August 2001. doi: 10.1086/322153.

M. A. C. Perryman, L. Lindegren, J. Kovalevsky, E. Hoeg, U. Bastian, P. L. Bernacca, M. Crézé, F. Donati, M. Grenon, F. van Leeuwen, H. van der Marel, F. Mignard, C. A. Murray, R. S. Le

Poole, H. Schrijver, C. Turon, F. Arenou, M. Froeschlé, and C. S. Petersen. The HIPPARCOS Catalogue. A&A, 323:L49–L52, July 1997.

W. D. Pesnell. A new driving mechanism for stellar pulsations. ApJ, 314:598–604, March 1987. doi: 10.1086/165089.

E. Poretti, E. Michel, R. Garrido, L. Lefèvre, L. Mantegazza, M. Rainer, E. Rodríguez, K. Uytterhoeven, P. J. Amado, S. Martín-Ruiz, A. Moya, E. Niemczura, J. C. Suárez, W. Zima, A. Baglin, M. Auvergne, F. Baudin, C. Catala, R. Samadi, M. Alvarez, P. Mathias, M. Paparò, P. Pápics, and E. Plachy. HD 50844: a new look at δ Scuti stars from CoRoT space photometry. A&A, 506:85–93, October 2009. doi: 10.1051/0004-6361/200912039.

Richard Powell. Atlas of the universe: The hertzsprung russell diagram, 2009. URL `http://www.atlasoftheuniverse.com/hr.html`.

William H. Press, Saul A. Teukolsky, William T. Vetterling, and Brian P. Flannery. *Numerical Recipes 3rd Edition: The Art of Scientific Computing.* Cambridge University Press, third edition, 2007.

A. Quirrenbach, D. Mozurkewich, D. F. Buscher, C. A. Hummel, and J. T. Armstrong. Angular diameter and limb darkening of Arcturus. A&A, 312:160–166, August 1996.

A. Retter, T. R. Bedding, D. L. Buzasi, H. Kjeldsen, and L. L. Kiss. Oscillations in Arcturus from WIRE Photometry. ApJ, 591:L151–L154, July 2003. doi: 10.1086/377211.

R. Samadi, M.-J. Goupil, E. Alecian, F. Baudin, D. Georgobiani, R. Trampedach, R. Stein, and Å. Nordlund. Excitation of Solar-like Oscillations: From PMS to MS Stellar Models. *Journal of Astrophysics and Astronomy*, 26:171, June 2005. doi: 10.1007/BF02702325.

R. Samadi, D. Georgobiani, R. Trampedach, M. J. Goupil, R. F. Stein, and Å. Nordlund. Excitation of solar-like oscillations across the HR diagram. A&A, 463:297–308, February 2007. doi: 10.1051/0004-6361:20041953.

F. X. Schmider, E. Fossat, J. Vernin, F. Martin, M. Azouit, K. Agabi, J. M. Clausse, and G. Grec. The Concordia Antarctic Station: an opportunity for asteroseismology and planetary search. In B. Battrick, F. Favata, I. W. Roxburgh, and D. Galadi, editors, *Stellar Structure and*

Habitable Planet Finding, volume 485 of *ESA Special Publication*, pages 219–224, January 2002.

C. Soubiran, O. Bienaymé, T. V. Mishenina, and V. V. Kovtyukh. Vertical distribution of Galactic disk stars. IV. AMR and AVR from clump giants. A&A, 480:91–101, March 2008. doi: 10.1051/0004-6361:20078788.

S. A. Spreckley. *A study of variable stars and search for extrasolar planets with the space based photometers SMEI and STEREO*. PhD thesis, UB (The University of Birmingham), October 2008.

S. A. Spreckley and I. R. Stevens. The period and amplitude changes of Polaris (α UMi) from 2003 to 2007 measured with SMEI. MNRAS, 388:1239–1244, August 2008. doi: 10.1111/j.1365-2966.2008.13439.x.

D. Stello, H. Kjeldsen, T. R. Bedding, and D. Buzasi. Oscillation mode lifetimes in ξ Hydrae: will strong mode damping limit asteroseismology of red giant stars? A&A, 448:709–715, March 2006. doi: 10.1051/0004-6361:20054016.

D. Stello, H. Bruntt, H. Preston, and D. Buzasi. Oscillating K Giants with the WIRE Satellite: Determination of Their Asteroseismic Masses. ApJ, 674:L53–L56, February 2008. doi: 10.1086/528936.

Y. K. Tang, S. L. Bi, and N. Gai. A new asteroseismic diagram of solar-like stars. A&A, 492: L49–L52, December 2008. doi: 10.1051/0004-6361:200809364.

N. J. Tarrant, W. J. Chaplin, Y. Elsworth, S. A. Spreckley, and I. R. Stevens. Asteroseismology of red giants: photometric observations of Arcturus by SMEI. MNRAS, 382:L48–L52, November 2007. doi: 10.1111/j.1745-3933.2007.00387.x.

M. Tassoul. Asymptotic approximations for stellar nonradial pulsations. ApJS, 43:469–490, August 1980. doi: 10.1086/190678.

K. Uytterhoeven, P. Mathias, E. Poretti, M. Rainer, S. Martín-Ruiz, E. Rodríguez, P. J. Amado, D. Le Contel, S. Jankov, E. Niemczura, K. R. Pollard, E. Brunsden, M. Paparó, V. Costa, J.-C. Valtier, R. Garrido, J. C. Suárez, P. M. Kilmartin, E. Chapellier, C. Rodríguez-López,

A. J. Marin, F. J. Aceituno, V. Casanova, A. Rolland, and I. Olivares. The γ Doradus CoRoT target HD 49434. I. Results from the ground-based campaign. A&A, 489:1213–1224, October 2008. doi: 10.1051/0004-6361:200809992.

F. van Leeuwen. Validation of the new Hipparcos reduction. A&A, 474:653–664, November 2007a. doi: 10.1051/0004-6361:20078357.

F. van Leeuwen, editor. *Hipparcos, the New Reduction of the Raw Data*, volume 350 of *Astrophysics and Space Science Library*, 2007b.

G. Walker, J. Matthews, R. Kuschnig, R. Johnson, S. Rucinski, J. Pazder, G. Burley, A. Walker, K. Skaret, R. Zee, S. Grocott, K. Carroll, P. Sinclair, D. Sturgeon, and J. Harron. The MOST Asteroseismology Mission: Ultraprecise Photometry from Space. PASP, 115:1023–1035, September 2003. doi: 10.1086/377358.

K. Zwintz and W. Weiss. Asteroseismology with the HST Fine Guidance Sensors: the Microvariability Survey. In T. Teixeira and T. Bedding, editors, *The Third MONS Workshop: Science Preparation and Target Selection*, page 111, April 2000.